Organic materials for magnesium batteries

Kwakernaak, M.C.

DOI
10.4233/uuid:a1c440ad-ee44-4fec-846e-9b5c2cd18769

Publication date
2026

Document Version
Final published version

Citation (APA)
Kwakernaak, M. C. (2026). *Organic materials for magnesium batteries*. [Dissertation (TU Delft), Delft University of Technology]. https://doi.org/10.4233/uuid:a1c440ad-ee44-4fec-846e-9b5c2cd18769

Important note
To cite this publication, please use the final published version (if applicable).
Please check the document version above.

Organic materials for magnesium batteries

Markus C. Kwakernaak

Organic materials for magnesium batteries

Dissertation

for the purpose of obtaining the degree of doctor
at Delft University of Technology
by the authority of the Rector Magnificus Prof.dr.ir. T.H.J.J. van der Hagen,
chair of the board for Doctorates
to be defended publicly on
Wednesday 7 January 2026 at 12:30

by

Markus Cornelis KWAKERNAAK
Master of Science in Chemistry, Leiden University, the Netherlands
born in Capelle aan den IJssel, the Netherlands

This dissertation has been approved by the promotors.

Composition of the doctoral committee:

Rector magnificus,	chairperson
Dr. E.M. Kelder	Delft University of Technology, promotor
Dr. W.F. Jager	Delft University of Technology, copromotor

Independent members:

Prof.dr. S.J. Picken	Delft University of Technology
Prof.dr. F.C. Grozema	Delft University of Technology
Prof.dr. D. Brandell	Uppsala University, Sweden
Prof.dr. H. Sakaebe	Kyushu University, Japan
Dr. G.L.M.M. Verbist	TNO Eindhoven
Prof.dr. J.H. van Esch	Delft University of Technology, reserve member

Contents

1
Introduction

1.1 A very brief history

All species on Earth leave footprints behind on the planet. ~2.7 billion years ago oxygen producing cyanobacteria formed in the oceans.[1–3] At first this oxygen reacted with reducing molecules and elements in the ocean and atmosphere, after which oxygen started to appear free in the atmosphere. This altered the composition of Earth's atmosphere so much, that the first mass extinction event took place. Oxygen replaced methane in the atmosphere. Methane is a potent greenhouse gas, so this resulted in a drop in global temperatures. The cyanobacteria had such a profound footprint on the Earth, that it shifted the entire planetary ecosystem. 850 million years ago, the first plants started to inhabit terrestrial habits.[4] This had again a profound effect on atmospheric oxygen levels, since more space was now available for photosynthesis. This increased the oxygen level above 10%.[5]

Not all organisms can trigger such big events on Earth, but they all have footprints. Every tree alters the atmosphere, every Apex predator let prey populations shrink with every meal. Early in human history, we, as hunter-gatherers, had a similar footprint compared to other animals of the same size.[6] With the advent of agriculture and a growing population, human environmental footprint started to get bigger, we cut away trees to generate fields for farming. Urbanization and the emergence of the first empires enabled trade of goods. Domesticated animals were raised for food in places far from where their evolutionary ancestors came from.[7] Forever diverting the evolutionary paths of many species. However, this increasingly bigger footprint was all based on energy and materials from the biosphere, which always meant that the growth was in some balance with the biosphere. If this balance was not in check, famine and depopulation would occur. In extreme cases, entire populations disappeared from areas.[8]

This all changed during the industrial revolution in the late 18th century. Humanity started to tap into energy and material resources outside the biosphere and inside the geosphere, fossil fuels.[9] The combustion of coal, oil and natural gas generates carbon dioxide and heat. CO_2 escapes into the atmosphere, while the heat can be used for warmth, performing work or generating electricity. Global use of fossil fuels have grown exponentially since the industrial revolution.[10] The energy and materials that we obtain from fossil fuels have greatly contributed to the wealth and well-being of societies around the planet.[11]

1.2 The climate problem

The exponential increase in fossil fuel consumption has also let to exponentially more CO_2 emissions into the atmosphere. Since the emission rate is far higher than the rate at which the biosphere can absorb CO_2,[12,13] it accumulates in the atmosphere, where the concentration CO_2 has increased from 280 ppm in the late 18th century[14] to 410 ppm in 2019.[15] CO_2 is a greenhouse gas that will trap heat in the atmosphere. A higher concentration of greenhouse gasses in the atmosphere will increase the atmospheric temperature on Earth, causing the climate to shift. The increase in atmospheric CO_2 is so rapid, that the climate shift is also rapid. Far too fast for most ecosystems to adapt to the new conditions. A rapid shift in climate patterns are often followed by mass extinction events.

Also, polar ice caps will melt and terrestrial ice will than contribute to a rise in the sea level, threatening coastal settlements and cities, impacting around 2.4 billion people

directly from this. Changing weather patterns will also make agriculture more challenging, impacting the entire world population.[15]

To mitigate the problems caused by climate change, it is vital for atmospheric CO_2 levels to stop increasing. In 2015 at the United Nations Climate Conference near Paris, world governments agreed to keep the rise in average global temperature below 2°C and preferably limit it to 1.5°C.[16] Although not forbidding greenhouse gas emissions, realistically, nations will only reach this goal if they stop emitting CO_2. It makes sense to focus efforts on the biggest source of CO_2, which is energy consumption from fossil fuels.[17] This can either be direct consumption of fuels for heating or transportation, or indirect through electricity generated by fossil fuels. If all this energy was generated from renewable or sustainable sources, most CO_2 emissions would stop. Methane is another potent greenhouse gas that is emitted on a large scale, but a large part is also emitted due to fossil fuel extraction and utilization.[17] Governments have made different pledges and timelines in which they will reduce and eliminate CO_2 emission, their net-zero targets. Most advanced economies have pledged to reach net-zero in 2050, China pledged 2060, while India has pledged 2070.[18] In 2020 the average global surface temperature had already risen to ~1.26°C (Fig 1), bold actions are therefore needed.

1.3 Energy

When we take a closer look at the available sustainable and renewable energy sources, they can be divided in 2 groups, solar[19] and wind[20] are intermittent, while nuclear,[21] biomass[22] and hydro[23] are more stable sources of energy. Biomass is constrained in its capacity, since there is not enough available space on Earth to feed all people, have healthy ecosystems and generate enough energy for our societies. Although biomass is a good option to overcome peak demands in electricity generation. Biomass should however be primarily used for the production of valuable chemicals. Hydropower can deliver stable amounts of electricity over longer periods of time, but it is constrained to very specific geographic places. Currently, nuclear energy is the backbone of electricity production in many places around the world. This can be expanded upon, but the main drawbacks of nuclear energy are its high price, complex

engineering challenges, safety and waste management. That leaves wind and solar energy, which are intermittent sources of electricity. They are however very cheap and environmentally benign. The main drive for wind and solar is their versatility in location options. Most nations on the planet have suitable areas for large scale electricity generation by wind or solar. Taking a look at climate policies from different nations tells you that wind and solar are going to be the biggest sources of electricity in the latter half of the 21th century in many places.[24] Many nations are already well under way to make this a reality.

This leaves a very big problem that still needs to be solved, the intermittency of wind and solar. Already, nations in the European Union are seeing that on some days, their renewable energy generation is higher than is needed and on some days there is almost

Observed global mean surface temperature change
Relative to 1850–1900 using four datasets
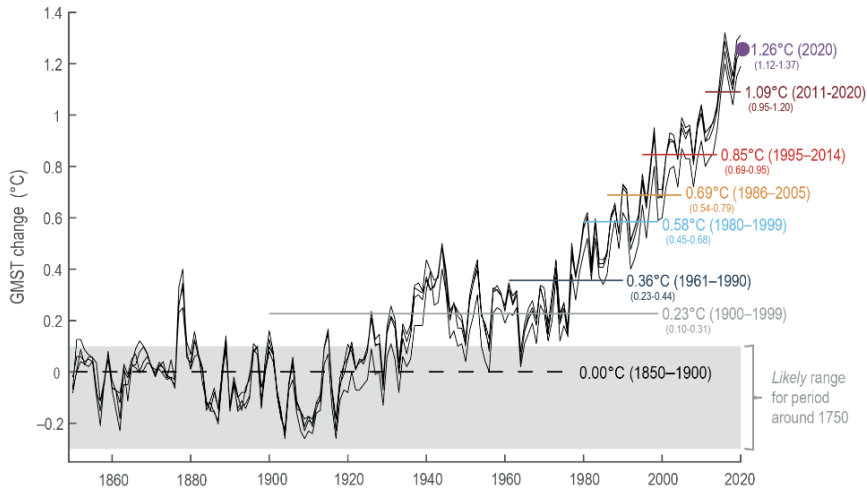
Figure 1. Observed global mean surface temperature change (GMST) from different datasets. The temperatures on the y-axes are relative to the average temperatures of 1850-1900. The area highlighted in grey is the estimated temperature range for 1750, before the industrial revolution. Figure 1.12 in IPCC, 2021: Chapter 1, In: Climate Change 2021: the physical science basis.

non being generated. This also leads to wild price fluctuations on the energy markets from day to day.[25] Currently, this is solved by exporting electricity on high production days, while gas turbines deliver electricity on low production days. Although export and import of renewable energy across borders are an important way to smooth out electricity production and demand, it is not sufficient to solve the intermittency of wind and solar when the majority of countries are relying on them. The volumes are simply too big.

1.4 Electricity storage

A new solution is therefore needed to store the excess electricity from one moment, and deliver it for consumption on other moments, electricity storage. A few technologies have already proven themselves as viable energy storage solutions. Pumped hydro,[26] where the elevation difference of 2 water reservoirs is utilized, accounts for 160 GW, 90% of installed capacity in 2021. Grid-scale batteries accounted for 16 GW of installed capacity in 2021.[27] Batteries are more versatile than pumped hydro, since they are not geographically constrained. Most grid-scale batteries in 2021 are lithium-ion batteries, and this will be the case in the coming years.[18] If governments go ahead with their energy and climate policies in the coming years, demand for electricity storage will grow dramatically. When governments are on track with their net-zero targets, the International Energy Agency has calculated, the world will need 680 GW of grid-scale batteries in 2030.[18]

1.5 Lithium-ion batteries

Like said earlier, in the short term future, lithium-ion batteries will make up the vast majority of grid-scale battery capacity. Although prices have fallen in the last decade, the price of lithium-ion batteries is now largely dictated by mineral prices.[18] The most precious materials being lithium, cobalt and nickel.[28] Another problem is competition with other applications. Lithium-ion batteries are already used in small electronics, but they are expected to be used in the vast majority of automobiles in the later part of this century.[29] Also, lithium-ion batteries have rather short lifetimes compared to other energy infrastructure.[28] This all puts pressure on the price and implementation of lithium-ion based grid-scale storage.

A lithium-ion battery is composed of an anode, an electrolyte and a cathode (Fig 2).[28] Generally, the anode is made from graphite, while other materials can be used for specialty applications. The electrolyte is composed of lithium salts, such as $LiPF_6$, $LiBF_6$ and $LiClO_4$, dissolved in an organic solvent (ethylene carbonate, dimethyl carbonate and diethyl carbonate). The cathode is made from $LiCoO_2$ (LCO), $LiFePO_4$, (LFP), $LiMn_2O_4$ (LMO), $LiNiCoAl_2$ (NCA) or $LiNi_xMn_yCo_zO_2$ (NMC). Specific combinations will result in lithium-ion batteries with desired properties. For example, LCO is commonly used for its high capacity, while LFP is used for its safety profile and lifetime, while having a lower capacity. Both the cathode and anode operate through an intercalation mechanism. When the battery is fully charged, metallic lithium is stored between the graphene sheets in the anode. Upon full discharge of the battery, lithium cations are stored in the cathode crystal structure. Although lithium-ion batteries are known for their high capacity, commercialized systems operate far from the thermodynamic maximum that a pure lithium battery can. This has to be done mainly because of issues that result in a low cycle life, the amounts of times a battery can charge and discharge.
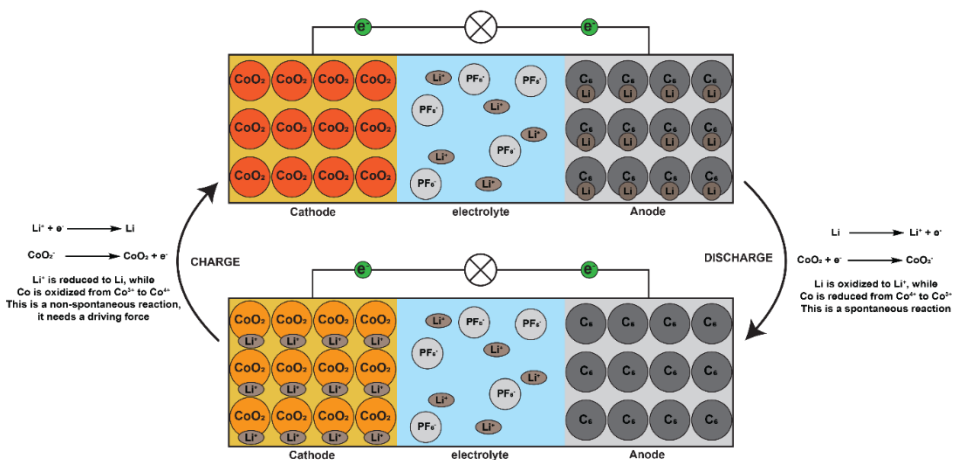

Figure 2. Schematic overview of a lithium-ion battery, with LCO as cathode and graphite as cathode.

Lithium-ion batteries can be produced in modules that can be connected in parallel or series.[28] This can result in a small battery that operates a personal electronic device, or it can be expanded to a grid-scale battery. This makes lithium-ion batteries flexible enough for a wide range of applications.

Cycle lifetime, safety concerns and cost are the main drawbacks of grid-scale lithium-ion batteries.[30] When LCO is used, the battery can do 500-1000 full charge and discharge cycles, while with LFP, this can be increased to 2500 cycles. After these amounts of cycles, the capacity has faded to 90% compare to the original capacity. Although one can still use the battery after this point, more defects start to occur and the capacity fading is accelerated. If the grid-scale battery is used to its full potential once every day, the lifetime of LCO is just ~1.4 – 2.8 years until the capacity has faded to 90%. LFP can do better with ~6.8 years. Proper and advanced battery monitor systems can expand the lifetime of a lithium-ion battery, but the problem of capacity fading still remains.

Safety is already a concern for small lithium-ion battery, this becomes a bigger issue when scaling up to an electric automobile, but in a grid-scale lithium-ion battery this takes on new proportions. The safety concerns are mainly due to the volatile organic electrolyte.[31] When a battery module self-discharges, enough heat can be formed for the electrolyte to vaporize. This builds up the pressure inside the module, which will rupture. The escaping hot vapour comes in contact with oxygen, which initiates a fire.

The price of lithium-ion battery modules has greatly decreased in the last decade. In 2013, it was priced ~$732/kWh, while in 2021 this has decreased to ~$141/kWh.[32] Due to economic and geopolitical pressures, the price has slightly increased between 2021 and 2022. This was the first time in many years that the price of lithium-ion batteries increased. Demand for lithium-ion batteries is set to increase in the coming decade. Many new applications will see mass adoption, the electric automobile for example. Therefore it should be noted that mineral prices are predicted to increase, since the supply of rare battery minerals in finite, while demand will increase. A great decrease in lithium-ion battery prices is therefore unlikely.

Although not all details about lithium-ion batteries have been included in this introduction, a picture emerges that lithium-ion batteries cannot supply all the energy storage demands that will come in the future. Applications were a high energy density is required, like personal electronics and electric automobiles, will need to use lithium-ion batteries in the coming decades. Other applications, where energy density is of lesser importance, but cost and safety are important, need to use different battery chemistries. New high energy density batteries can still be discovered in the future, which work with abundant or renewable materials, but that is a much harder task.

1.6 Sustainable battery chemistries

If one thinks from the top down, and forgets about the chemical limitations, grid-scale batteries need to have certain properties. They should be durable and have a long lifetime. Coal-fired power plants can operate for over 30 years if properly maintained,[33] while wind and solar farms have an estimated lifetime of 20-30 years.[33] The primary use of a grid-scale battery is to store excess wind and solar energy, so a lifetime of 20-30 years is minimal. If the battery is used at a solar farm and is used to store solar energy for the night, it needs to be charged and discharge almost 11 000 times over 30 years. Over 30

years, the solar farm will lose ~20% of its output,[34] so a connected grid-scale battery should still have 80% of its capacity after 30 years. The battery should be safe and non-flammable and its contents are preferably environmentally benign. The materials used should be abundant, renewable and easily sourced from many places around the world. The costs should be very low, a battery will always increase the price of the electricity without adding additional value, so the cost really matters. Therefore, material cost and large scale production should be cheap and easy.

Taking this into consideration, one can look at possible battery chemistries and start from that. For a non-flammable and safe battery, water is a great choice for an electrolyte.[35] An anode can be based on earth abundant metals. Sodium, magnesium, aluminium, potassium, calcium and iron are all abundant rock-forming metals that can be mined in many places in the world.[36] Cathodes can be based on abundant transition metal oxides,[37] or organic materials,[38] which are renewable. Literature already provides great examples of such systems.[37,38]

1.7 Organic cathodes

Organic materials are both abundant and renewable. If used for durable applications, fossil feedstock's provide abundant organic materials, while biomass provides renewable organic materials. Both anodes and cathodes have been successfully made with organic materials as the active compound.[39] Especially organic cathodes are promising, as they can be very stable in electrochemical environments and provide a great specific capacity and a decent potential against most metals.[38] Different chemical bonds in the organic molecules can be used to store electrochemical energy, these are repeatedly reduced and oxidized.[40]

The most investigated type is based on carbonyl chemistry.[41] Naphthalene and perylene derivatives are part of the rylene family of polyaromatic compounds and are a commonly investigated family of molecules for cathodes. In particular naphthalene and perylene diimides are of interest for their electrochemical properties. It has been shown that lithium and sodium can react with the carbonyl groups of the perylene/naphthalene diimide.[42] A cation is then chelated in an enolate while the electrons are stored in the elaborate aromatic system. The electrochemical potential of these compounds is determined by the electron density of the aromatic system. Electron donating or withdrawing substituents can then be employed to obtain a very specific electron density.[43] Perylenes and naphtalenes can undergo supramolecular interactions through π-π stacking.[44] This could potentially result in electron conductive properties, when the π-orbitals can successfully overlap.

Organic molecules can suffer from solubility in the electrolyte, fading the battery capacity in the process.[42] One needs to take into account all the different derivatives the molecule forms during electrochemical cycling. A common way to solve this problem is by polymerization of the small organic molecule. However, extensive polymerization can negatively impact the kinetics of the material. By controlling the extent of polymerization, a compromise can be found between solubility and preserving good kinetics.[45]

1.8 Aqueous electrolytes

A good electrolyte conducts ions, while having a high resistance towards electron conductivity.[46] Like mentioned before, grid-scale batteries need to be very safe and the electrolyte choice is a big component in that. Lithium-ion batteries use an organic solvent with salts dissolved in it, which is highly flammable.[47] Water is a safer option for an electrolyte and conveniently it is also very abundant and cheap. Aqueous electrolytes are known for a long time, the first electrochemical battery, the voltaic pile, made by Alessandro Volta, used brine as an electrolyte between copper and zinc plates.[48]

A big downside to a water-based electrolyte is it electrochemical stability window. At room temperature this is 1.23 V.[49] This hampers most aqueous electrolytes for use in high capacity batteries. Another issue is anodic stability against water. Earlier, we have determined that sodium, magnesium, aluminium, potassium, calcium and iron are the metals that are interesting for grid-scale batteries. Sodium and potassium react very violently with water. Magnesium, calcium and aluminium react less violent, but still react over time. Only iron will be stable against water.

A solution for this problem has been found, water-in-salt electrolytes.[49] In these electrolytes, the concentration of salt is so high, one can speak about a brine. The high concentration of salt expands the potential stability window of water to ~3 V in a lithium-ion battery.[50] It also helps with the anodic stability. The water molecules are not free moving, they are tightly bound to ions. This dims their reactivity towards the reactive metals. The key here, it too still use water as an electrolyte, but to change its properties with the salts.

1.9 Redox flow battery

In this introduction, the design of a grid-scale battery has not been mentioned yet. Typical batteries that people are familiar with, are modular with a solid cathode and anode. The lithium-ion battery is a good example of this. When the battery is fully charged, all energy in stored in the anode. This modular design has its advantages, it is easy to expand and it can be manufactured on a large scale. For smaller scale applications, like electronics or electric automobiles, a modular design works very well. You can choose the output voltage and current by stacking the modules in parallel or in series.

In grid-scale batteries, this is less important, while other factors of a modular design become limiting. Every cell needs to be individually packaged and needs individual outlets. This is all wasted space and material. When one cell in a stack is not properly working anymore, it can degrade the performance of other cells. A redox flow battery design solves many of these issues. In a redox flow cell, the cathode and anode materials are not solid, but in solution in two separate compartments, the catholyte and anolyte.[51,52] These solutions are then pumped between a common membrane and two different current collectors (Fig 3). At the current collectors, the redox reaction takes place, the membrane facilitates charge compensation through ion transport. The compartments can be as large as required and practically feasible. In a redox flow battery, the energy storage is decoupled from the size of electrochemical cell. The size of the current collectors and the membrane, together with the pump speed, dictate the kinetics of the redox reaction, which in turn determines the amount of electricity that can be generated or stored per unit of time.
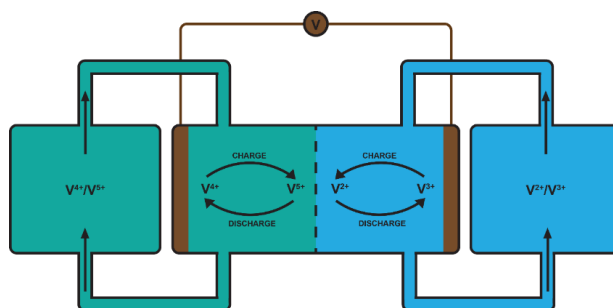
Figure 3. A schematic overview of a vanadium redox flow battery.

Redox flow batteries offer great advantages over regular batteries. Theoretically, they do not self-discharge, since the catholyte and anolyte can be physically separated by closing off a compartment.[52] Like said before, the total storage capacity is decoupled from the amount of power it can produce, which creates flexibility in designs. Also, the lifetime of a redox flow battery is very long, >30 years.[53,54] This is because all redox reactions take place in solution. There is no need for solid to solution transitions.

A lot of laboratory scale redox flow batteries have been made, and some larger scale pilots have been constructed. At the end of 2022, in Dalian, China, the largest so far, went online on the grid. It can deliver 100 MW with a capacity of 400 MWh. It is an aqueous vanadium redox flow battery, the most investigated redox flow chemistry.[55,56] When this battery is discharged, V^{3+} is reduced to V^{2+} in the anolyte, while V^{4+} is oxidized to V^{5+} in the catholyte. Although vanadium is an expensive metal, the long lifetime of the battery results in low overall cost.

There are, however, also reasons why vanadium chemistry is not optimal for large scale applications. Its abundance on earth is quite low, 0.015% of the crust,[57] and it can be toxic for humans and ecosystems.[58] Organic materials and abundant metals can also be used in a redox flow battery, a lot of research is ongoing on this topic.[51]

1.10 Motivation and outline of this thesis
To fulfil the climate goals, agreed in Paris in 2015, humanity needs to decarbonize its way of living. More specifically, stop the burning of fossil fuels and fossil derived chemicals. The majority of material from fossil sources is used for direct energy consumption or electricity generation. Moving to renewable energy is the most important step we need to take to reach our goals. At the moment of writing, solar and wind energy are the most abundant sources of renewable energy humanity can tap into. They are cheap and clean, but they are also intermittent. Therefore, in the coming decades, we need to develop large scale electricity storage. Chemical batteries are the most versatile technology we can deploy, but this comes at a time where batteries are needed in a large array of applications, like electronics and electric automobiles. At the moment, lithium-ion batteries, although not perfect, are best suited for large grid-scale batteries. Materials used in lithium-ion batteries are common, but not abundant on Earth. To fulfil all future demand for energy storage, we need different battery chemistries, preferably at lot of them. This will decrease demand for lithium-ion batteries, decreasing their price. Also, large scale deployment of grid-scale batteries raises safety and health concerns. Lithium-

ion batteries are amazing high energy density batteries, but our focus should now be on durable and safe battery chemistries.

Chapter 2, 3 and 4 will zoom in on a very promising organic cathode material, perylene diimide. **Chapter 2** will elaborate on novel reaction conditions to synthesize perylene diimides. The original conditions have been known for decades and are quite harsh. It uses molten imidazole or refluxing DMF between 140-160 °C with a zinc catalyst. We have found new and mild conditions to prepare perylene diimides. Under specific circumstances, one can already prepare the compound at room temperature in DMSO and water with DBU as a base. In a more general approach, the perylene diimide can be prepare at 60 °C with DMF and DBU, or at 100 °C with DMSO and K_2CO_3. The latter only using renewable or abundant additives. **Chapter 3** uses similar conditions mentioned in chapter 2, to make perylene diamic acid salts. These salts are highly soluble in basic solutions, which is highly unusual for perylene derivatives. Upon controlled acidification, perylene diamic acid salts are protonated and hydrolysed, making them very hydrophobic. They then stack in supramolecular polymers and form a hydrogel. Perylene diamic acid salts might be interesting molecules to use in an aqueous redox flow battery. **Chapter 4** will take a close look at modifications of perylene diimides. These modifications can alter the HOMO and LUMO of the perylene molecule, which impact it potential versus metals in a battery setup. This can be very useful, since it allows for cathode design with full control over the potential.

Chapter 5 and 6 will take a look at a new material in battery research, alginate. Alginate is well known in the food- and pharmaceutical industries. It is a polysaccharide, obtained for algae, making it a renewable source. The saccharides in this polymer are equipped with carboxylate side groups that make the polymer anionic. Divalent and trivalent cations can bind with the carboxylates, crosslinking the polymers in the process. The cations are bound to the polymer in varying strengths. **Chapter 5** describes magnesium alginate as a new electrolyte for aqueous magnesium batteries. Magnesium cations are loosely bound to the alginate backbone, this enables magnesium conductivity in the material. We also found that magnesium alginate stabilizes metallic magnesium against reacting with water, a very relevant finding. **Chapter 6** takes a look at iron(III) alginate and manganese(II) alginate as electrodes in a battery. Alginate is used to trap the ions into the material to prevent dissolution. Iron is a very abundant metal, while manganese is quite abundant. They both have a low toxicity for the environment, if a spill were to occur.

1.11 References

(1)   Kasting, J. F. What Caused the Rise of Atmospheric O2? *Chem. Geol.* **2013**, *362*, 13–25. https://doi.org/10.1016/j.chemgeo.2013.05.039.
(2)   Bachan, A.; Kump, L. R. The Rise of Oxygen and Siderite Oxidation during the Lomagundi Event. *Proc. Natl. Acad. Sci.* **2015**, *112* (21), 6562–6567. https://doi.org/10.1073/pnas.1422319112.
(3)   Olejarz, J.; Iwasa, Y.; Knoll, A. H.; Nowak, M. A. The Great Oxygenation Event as a Consequence of Ecological Dynamics Modulated by Planetary Change. *Nat. Commun.* **2021**, *12* (1), 3985. https://doi.org/10.1038/s41467-021-23286-7.
(4)   Knauth, L. P.; Kennedy, M. J. The Late Precambrian Greening of the Earth. *Nature* **2009**, *460* (7256), 728–732. https://doi.org/10.1038/nature08213.
(5)   Canfield, D. E. The Early History of Atmospheric Oxygen: Homage to Robert M. Garrels. *Annu. Rev. Earth Planet. Sci.* **2005**, *33* (1), 1–36. https://doi.org/10.1146/annurev.earth.33.092203.122711.
(6)   Gowdy, J. Our Hunter-Gatherer Future: Climate Change, Agriculture and Uncivilization. *Futures* **2020**, *115*, 102488. https://doi.org/10.1016/j.futures.2019.102488.
(7)   Zeder, M. A. Core Questions in Domestication Research. *Proc. Natl. Acad. Sci.* **2015**, *112* (11), 3191–3198. https://doi.org/10.1073/pnas.1501711112.

(8)   Lima, M. Climate Change and the Population Collapse during the "Great Famine" in Pre-Industrial Europe. *Ecol. Evol.* **2014**, *4* (3), 284–291. https://doi.org/10.1002/ece3.936.

(9)   Fernihough, A.; O'Rourke, K. H. Coal and the European Industrial Revolution. *Econ. J.* **2021**, *131* (635), 1135–1149. https://doi.org/10.1093/ej/ueaa117.

(10)   *Fossil Fuels - Our World in Data*. https://ourworldindata.org/fossil-fuels (accessed 2023-04-25).

(11)   Holechek, J. L.; Geli, H. M. E.; Sawalhah, M. N.; Valdez, R. A Global Assessment: Can Renewable Energy Replace Fossil Fuels by 2050? *Sustainability* **2022**, *14* (8), 4792. https://doi.org/10.3390/su14084792.

(12)   Chapin III, F. S.; Randerson, J. T.; McGuire, A. D.; Foley, J. A.; Field, C. B. Changing Feedbacks in the Climate–Biosphere System. *Front. Ecol. Environ.* **2008**, *6* (6), 313–320. https://doi.org/10.1890/080005.

(13)   Canadell, J. G.; Le Quéré, C.; Raupach, M. R.; Field, C. B.; Buitenhuis, E. T.; Ciais, P.; Conway, T. J.; Gillett, N. P.; Houghton, R. A.; Marland, G. Contributions to Accelerating Atmospheric CO2 Growth from Economic Activity, Carbon Intensity, and Efficiency of Natural Sinks. *Proc. Natl. Acad. Sci.* **2007**, *104* (47), 18866–18870. https://doi.org/10.1073/pnas.0702737104.

(14)   Cao, L.; Caldeira, K. Atmospheric CO2 Stabilization and Ocean Acidification. *Geophys. Res. Lett.* **2008**, *35* (19). https://doi.org/10.1029/2008GL035072.

(15)   Climate Change 2021: The Physical Science Basis.

(16)   *The Paris Agreement | UNFCCC*. https://unfccc.int/process-and-meetings/the-paris-agreement (accessed 2023-04-25).

(17)   Ritchie, H.; Roser, M.; Rosado, P. CO₂ and Greenhouse Gas Emissions. *Our World Data* **2020**.

(18)   World Energy Outlook 2022.

(19)   Kabir, E.; Kumar, P.; Kumar, S.; Adelodun, A. A.; Kim, K.-H. Solar Energy: Potential and Future Prospects. *Renew. Sustain. Energy Rev.* **2018**, *82*, 894–900. https://doi.org/10.1016/j.rser.2017.09.094.

(20)   Blanco, M. I. The Economics of Wind Energy. *Renew. Sustain. Energy Rev.* **2009**, *13* (6), 1372–1382. https://doi.org/10.1016/j.rser.2008.09.004.

(21)   Bodansky, D. *Nuclear Energy: Principles, Practices, and Prospects*; Springer Science & Business Media, 2007.

(22)   Klass, D. L. *Biomass for Renewable Energy, Fuels, and Chemicals*; Elsevier, 1998.

(23)   Paish, O. Small Hydro Power: Technology and Current Status. *Renew. Sustain. Energy Rev.* **2002**.

(24)   *A European Green Deal*. https://commission.europa.eu/strategy-and-policy/priorities-2019-2024/european-green-deal_en (accessed 2023-04-25).

(25)   Soini, V. Wind Power Intermittency and the Balancing Power Market: Evidence from Denmark. *Energy Econ.* **2021**, *100*, 105381. https://doi.org/10.1016/j.eneco.2021.105381.

(26)   Ibrahim, H.; Ilinca, A.; Perron, J. Energy Storage Systems—Characteristics and Comparisons. *Renew. Sustain. Energy Rev.* **2008**, *12* (5), 1221–1250. https://doi.org/10.1016/j.rser.2007.01.023.

(27)   *Grid-Scale Storage – Analysis*. IEA. https://www.iea.org/reports/grid-scale-storage (accessed 2023-04-25).

(28)   Li, M.; Lu, J.; Chen, Z.; Amine, K. 30 Years of Lithium-Ion Batteries. *Adv. Mater.* **2018**, *30* (33), 1800561. https://doi.org/10.1002/adma.201800561.

(29)   Swart, P.; Dewulf, J.; Biernaux, A. Resource Demand for the Production of Different Cathode Materials for Lithium Ion Batteries. *J. Clean. Prod.* **2014**, *84*, 391–399. https://doi.org/10.1016/j.jclepro.2014.01.056.

(30)   Han, X.; Ouyang, M.; Lu, L.; Li, J.; Zheng, Y.; Li, Z. A Comparative Study of Commercial Lithium Ion Battery Cycle Life in Electrical Vehicle: Aging Mechanism Identification. *J. Power Sources* **2014**, *251*, 38–54. https://doi.org/10.1016/j.jpowsour.2013.11.029.

(31)   Wang, Q.; Jiang, L.; Yu, Y.; Sun, J. Progress of Enhancing the Safety of Lithium Ion Battery from the Electrolyte Aspect. *Nano Energy* **2019**, *55*, 93–114. https://doi.org/10.1016/j.nanoen.2018.10.035.

(32)   *Lithium-ion Battery Pack Prices Rise for First Time to an Average of $151/kWh*. BloombergNEF. https://about.bnef.com/blog/lithium-ion-battery-pack-prices-rise-for-first-time-to-an-average-of-151-kwh/ (accessed 2023-04-26).

(33)   Fthenakis, V.; Kim, H. C. Land Use and Electricity Generation: A Life-Cycle Analysis. *Renew. Sustain. Energy Rev.* **2009**, *13* (6), 1465–1474. https://doi.org/10.1016/j.rser.2008.09.017.

(34)   Virtuani, A.; Caccivio, M.; Annigoni, E.; Friesen, G.; Chianese, D.; Ballif, C.; Sample, T. 35 Years of Photovoltaics: Analysis of the TISO-10-KW Solar Plant, Lessons Learnt in Safety and Performance—Part 1. *Prog. Photovolt. Res. Appl.* **2019**, *27* (4), 328–339. https://doi.org/10.1002/pip.3104.

(35)   Pasta, M.; Wessells, C. D.; Huggins, R. A.; Cui, Y. A High-Rate and Long Cycle Life Aqueous Electrolyte Battery for Grid-Scale Energy Storage. *Nat. Commun.* **2012**, *3* (1), 1149. https://doi.org/10.1038/ncomms2139.

(36)   Offerman, S. E. *Critical Materials: Underlying Causes and Sustainable Mitigation Strategies*; World Scientific series in current energy issues; World Scientific: New Jersey, 2018.

(37) Desilvestro, J.; Haas, O. Metal Oxide Cathode Materials for Electrochemical Energy Storage: A Review. *J. Electrochem. Soc.* **1990**, *137* (1), 5C-22C. https://doi.org/10.1149/1.2086438.

(38) Lyu, H.; Sun, X.-G.; Dai, S. Organic Cathode Materials for Lithium-Ion Batteries: Past, Present, and Future. *Adv. Energy Sustain. Res.* **2021**, *2* (1), 2000044. https://doi.org/10.1002/aesr.202000044.

(39) Iordache, A.; Delhorbe, V.; Bardet, M.; Dubois, L.; Gutel, T.; Picard, L. Perylene-Based All-Organic Redox Battery with Excellent Cycling Stability. *ACS Appl. Mater. Interfaces* **2016**, *8* (35), 22762–22767. https://doi.org/10.1021/acsami.6b07591.

(40) Xu, D.; Liang, M.; Qi, S.; Sun, W.; Lv, L.-P.; Du, F.-H.; Wang, B.; Chen, S.; Wang, Y.; Yu, Y. The Progress and Prospect of Tunable Organic Molecules for Organic Lithium-Ion Batteries. *ACS Nano* **2021**, *15* (1), 47–80. https://doi.org/10.1021/acsnano.0c05896.

(41) Han, X.; Chang, C.; Yuan, L.; Sun, T.; Sun, J. Aromatic Carbonyl Derivative Polymers as High-Performance Li-Ion Storage Materials. *Adv. Mater.* **2007**, *19* (12), 1616–1621. https://doi.org/10.1002/adma.200602584.

(42) Sharma, P.; Damien, D.; Nagarajan, K.; Shaijumon, M. M.; Hariharan, M. Perylene-Polyimide-Based Organic Electrode Materials for Rechargeable Lithium Batteries. *J. Phys. Chem. Lett.* **2013**, *4* (19), 3192–3197. https://doi.org/10.1021/jz4017359.

(43) Kumar, S.; Shukla, J.; Kumar, Y.; Mukhopadhyay, P. Electron-Poor Arylenediimides. *Org. Chem. Front.* **2018**, *5* (14), 2254–2276. https://doi.org/10.1039/C8QO00256H.

(44) Görl, D.; Zhang, X.; Würthner, F. Molecular Assemblies of Perylene Bisimide Dyes in Water. *Angew. Chem. Int. Ed.* **2012**, *51* (26), 6328–6348. https://doi.org/10.1002/anie.201108690.

(45) Jin, Z.; Cheng, Q.; M. Evans, A.; Gray, J.; Zhang, R.; Tong Bao, S.; Wei, F.; Venkataraman, L.; Yang, Y.; Nuckolls, C. π-Conjugated Redox-Active Two-Dimensional Polymers as Organic Cathode Materials. *Chem. Sci.* **2022**, *13* (12), 3533–3538. https://doi.org/10.1039/D1SC07157B.

(46) Robinson, R. A.; Stokes, R. H. *Electrolyte Solutions: Second Revised Edition*; Courier Corporation, 2002.

(47) Arbizzani, C.; Gabrielli, G.; Mastragostino, M. Thermal Stability and Flammability of Electrolytes for Lithium-Ion Batteries. *J. Power Sources* **2011**, *196* (10), 4801–4805. https://doi.org/10.1016/j.jpowsour.2011.01.068.

(48) Abetti, P. A. The Letters of Alessandro Volta. *Electr. Eng.* **1952**, *71* (9), 773–776. https://doi.org/10.1109/EE.1952.6437680.

(49) Chen, J.; Vatamanu, J.; Xing, L.; Borodin, O.; Chen, H.; Guan, X.; Liu, X.; Xu, K.; Li, W. Improving Electrochemical Stability and Low-Temperature Performance with Water/Acetonitrile Hybrid Electrolytes. *Adv. Energy Mater.* **2020**, *10* (3), 1902654. https://doi.org/10.1002/aenm.201902654.

(50) Suo, L.; Borodin, O.; Gao, T.; Olguin, M.; Ho, J.; Fan, X.; Luo, C.; Wang, C.; Xu, K. "Water-in-Salt" Electrolyte Enables High-Voltage Aqueous Lithium-Ion Chemistries. *Science* **2015**, *350* (6263), 938–943. https://doi.org/10.1126/science.aab1595.

(51) Wei, X.; Pan, W.; Duan, W.; Hollas, A.; Yang, Z.; Li, B.; Nie, Z.; Liu, J.; Reed, D.; Wang, W.; Sprenkle, V. Materials and Systems for Organic Redox Flow Batteries: Status and Challenges. *ACS Energy Lett.* **2017**, *2* (9), 2187–2204. https://doi.org/10.1021/acsenergylett.7b00650.

(52) Weber, A. Z.; Mench, M. M.; Meyers, J. P.; Ross, P. N.; Gostick, J. T.; Liu, Q. Redox Flow Batteries: A Review. *J. Appl. Electrochem.* **2011**, *41* (10), 1137–1164. https://doi.org/10.1007/s10800-011-0348-2.

(53) Yuan, X.-Z.; Song, C.; Platt, A.; Zhao, N.; Wang, H.; Li, H.; Fatih, K.; Jang, D. A Review of All-Vanadium Redox Flow Battery Durability: Degradation Mechanisms and Mitigation Strategies. *Int. J. Energy Res.* **2019**, *43* (13), 6599–6638. https://doi.org/10.1002/er.4607.

(54) Kwabi, D. G.; Ji, Y.; Aziz, M. J. Electrolyte Lifetime in Aqueous Organic Redox Flow Batteries: A Critical Review. *Chem. Rev.* **2020**, *120* (14), 6467–6489. https://doi.org/10.1021/acs.chemrev.9b00599.

(55) Parasuraman, A.; Lim, T. M.; Menictas, C.; Skyllas-Kazacos, M. Review of Material Research and Development for Vanadium Redox Flow Battery Applications. *Electrochimica Acta* **2013**, *101*, 27–40. https://doi.org/10.1016/j.electacta.2012.09.067.

(56) Skyllas-Kazacos, M.; Rychik, M.; Robins, R. G.; Fane, A. G.; Green, M. A. New All-Vanadium Redox Flow Cell. *J. Electrochem. Soc.* **1986**, *133* (5), 1057. https://doi.org/10.1149/1.2108706.

(57) Fleischer, M. *Recent Estimates of the Abundances of the Elements in the Earth's Crust*; U.S. Department of the Interior, Geological Survey, 1953.

(58) Domingo, J. L. Vanadium: A Review of the Reproductive and Developmental Toxicity. *Reprod. Toxicol.* **1996**, *10* (3), 175–182. https://doi.org/10.1016/0890-6238(96)00019-6.

2

Room temperature synthesis of perylene diimides facilitated by high amic acid solubility

Abstract

A novel protocol for the synthesis of perylene diimides (PDIs), by reacting perylene dianhydride (PDA) with aliphatic amines is reported. Full conversions were obtained at temperatures between 20 and 60°C, using DBU as the base in DMF or DMSO. A "green" synthesis of PDIs, that runs at higher temperatures, was developed using K_2CO_3 in DMSO. The reaction sequence for the imidization process, *via* perylene amic acid intermediates (PAAs), has been confirmed experimentally aided by the synthesis and full characterization of stable model amic acid salts and amic esters. Kinetic studies, using absorption spectroscopy, have established that PDI formation proceeds *via* fast amic acid formation, followed by a slow conversion to imides. Solubility of the intermediate PAA salts is found to be low and rate-limiting. Based on this finding, quantitative PDI synthesis at room temperature was achieved by diluting the reaction mixture with water, the solvent in which PAA salts have better solubility. Thus, the otherwise harsh synthesis of PDIs has been transformed into an extremely convenient functional group tolerant and highly efficient reaction that runs at room temperature.

2.1 Introduction

Perylene-3,4,9,10-tetracarboxylic acid derivatives (PTCAs) form a class of organic dyes and pigments, from which perylene- 3,4,9,10-tetracarboxylic diimides (PDIs) are the most abundantly used representatives.[1] These compounds have very benign optical properties, which has resulted in large scale application of PDIs as dyes and pigments.[2] Moreover, PDIs are well-suited for utilization as functional materials, mostly in the optoelectronic domain.[3–5] Current research efforts are focused on the use of PDIs as non-fullerene acceptors in photovoltaics,[6–8] light harvesting antenna molecules,[9–15] electrode materials in batteries,[16–18] fluorescent probes[19,20] and photocatalysts for the dehalogenation of aromatic compounds.[21]

Despite this long history and intense interest by scientists from a wide range of disciplines, the synthesis of PDIs is generally performed under harsh conditions, with limited functional group tolerance.[22] PDIs are routinely synthesized by the "Langhals method", reacting perylene-3,4,9,10-tetracarcoxylic dianhydride (PDA) with primary amines in molten imidazole at 140–180°C, using zinc acetate as a catalyst.[23,24] This method has been the gold standard for decades and has proven itself to be very reliable and universally applicable. Nevertheless, a milder, greener and more user-friendly synthesis would be desirable, in order to make more PDIs accessible to a larger scientific audience.

The harsh conditions in the "Langhals method" appear to originate from either the low reactivity of the amic acid intermediates, the low solubility of starting compounds and intermediates, or both. The more soluble bay-halogenated PDAs generally undergo imidization reactions at milder conditions, typically using organic acids as catalyst and (co)solvent,[25] while the imidization of 4-substituted naphthyl anhydrides proceeds at even milder conditions,[26] typically in refluxing ethanol. These observations suggest that solubility is the major driver for applying harsh reaction conditions in the current PDI syntheses.

Greener methods for PDI synthesis have been reported recently, notably a solvent-less method using a twin screw extruder[27] and a method in which water at high temperatures and elevated pressure is used.[28] Both methods work particularly well for aliphatic amines and are definitely green(er). Still these reactions require high temperatures, which limits functional group tolerance. Interestingly, when using water at milder temperatures, around 60°C, PDIs are not formed in significant quantities. Instead, perylene-3,4-dicarboxylic acid monoanhydride-9,10-dicarboxylic acid monoimide (PMAMIs) are the major reaction products.[29] Most likely, anhydride ring opening by hydroxide ions,[30] resulting in the formation of adjacent dicarboxylates on the perylene scaffold is responsible for the observed PMAMI formation.[28,31–34] It should be mentioned nevertheless, that partial hydrolysis of PDA to perylene-3,4-dicarboxylic monoanhydride-9,10-dicarboxylates, followed by a selective imidization at the anhydride position is a highly beneficial reaction that has been exploited for efficient syntheses of aliphatic PMAMIs and N-desymmetrized PDIs.[35–37]
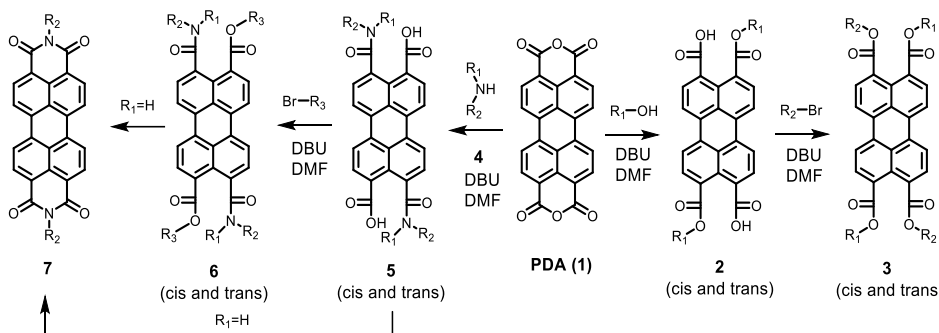
Scheme 1. *Room temperature synthesis of PTEs (3) PDAAs (5), PDAEs (6) and PDIs (7)*.

In contrast to imidization, esterification of PDA has been achieved at mild reaction conditions,[38,39] even at room temperature,[40] see Scheme 1. In the first step of this reaction an alcohol opens the anhydride in the presence of the strong base DBU. The perylene-3,9-dicarboxylic acid-4,10-dicarboxylic dialkyl esters 2 resulting from the first reaction step are highly soluble and subsequently react with an alkyl halide in a slower rate-determining step to produce perylene-3,4,9,10-tetracarboxylic tetra-alkyl esters (PTEs 3) in almost quantitative yields. Interestingly, in a variation of this reaction, the synthesis of an imide at room temperature, postulated to proceed *via* an amic acid, has been reported. Although the reported synthetic procedure, exploiting a 3-day aminolysis reaction, may not be the most practical one, this finding suggests that PDI synthesis at mild reaction conditions is a realistic option.[40]

Additional information suggesting that PDI synthesis at low temperatures is feasible, comes from mechanistic studies on naphthalene-1,8-dicarboxylic amic acid (NMAA)[41] and naphthalene-1,3,4,8-tetracarboxylic diamic acid (NDAA).[42,43] NMAA has been synthesized by a reaction of naphthalene-1,8- dicarboxylic anhydride (NMA) with butyl amine at low temperatures.[44] At high pH values in water, NMAA forms the corresponding imide, naphthalene-1,8-dicarboxylic imide (NMI), while at low pH values the anhydride NMA is formed. These reactions are reversible and already proceeds at appreciable rates at temperatures as low as 30°C. These studies suggest that formation of PDIs from PDA *via* corresponding amic acids may take place at low temperatures and high pH values, provided that a suitable polar solvent is identified. This may not be a trivial event in the light of the low solubility of most PTCA derivatives. Also it should be mentioned that the chemistry of PTCAs may differ from those of the corresponding naphthalene derivatives in other aspects than solubility. For example perylene-3,4,9,10-tetracarboxilic acid chloride has never been prepared[24] whereas the analogous naphthyl-1,8-di[45] and 1,3,4,8-tetracid chlorides[46] are readily available by conventional means.

In this work we report the synthesis of PDIs by reacting PDA with primary aliphatic amines at low temperatures, in a manner analogous to the synthesis of PTEs depicted in Scheme 1. Reaction conditions for the imidization of PDA under "standard" conditions, with DBU as the base in the solvent DMF, were optimized. In addition an entirely green synthesis of PDIs, using DMSO and K_2CO_3, was developed. To identify the reactive intermediates formed during the imidization reaction, stable model amic acids have been synthesized by the reaction of PDA with secondary amines. The (photo) physical

properties of these compounds were determined and their spectra were compared with those of the reaction intermediates to support the proposed mechanism of imide formation. A kinetic model of the imidization reactions has been constructed and tested by monitoring imidization reactions in real time. Based on the mechanistic insights obtained from these experiments the reaction conditions were optimized further to achieve quantitative imide formation at room temperature.

2.2 Results and discussion
2.2.1 General reaction and proposed reaction mechanism
When secondary amines were reacted with PDA 1, using the synthetic protocol for the synthesis of PTEs, perylene-3,4,9,10- tetracarboxylic-diamic esters PDAE **6** were formed *via* perylene-3,4,9,10-tetracarboxylic-diamic acid PDAA **5**, see Scheme 1. Both compounds have been isolated and fully characterized, vide infra. When primary amines were employed, using the same procedure, however, PDIs **7** were obtained in appreciable yields. The fact that PDIs are formed is not surprising as such, since amic acids and amic esters are known to react further to form imides. The observation that this reaction takes place at room temperature already was surprising to us and clearly indicates that PDI synthesis can be performed at very mild conditions.

Next, it is worthwhile to establish whether alkylation of amic acids, i.e. amic ester formation, is a prerequisite for efficient imide formation. Reactions from amic esters to imides have been reported in the context of polyimide formation. This work, however, involved the synthesis of five-membered phthalimides and these imidization reaction have been performed by "brute force". To the best of our knowledge, neither the temperature nor the solvent dependence of such reactions have been explored.[47] In another work the alkylation of a perylene-3,4-monoamic acid has been reported. This reaction resulted in a double alkylation at the carboxylate and the amide nitrogen,[48] but imide formation was not reported.

Whether the imide formation using our original procedure proceeds *via* the amic acid **5**, the amic ester **6**, or possibly both has been investigated by reacting **1** with 2-ethyl-hexyl amine **4b**, in the presence and in the absence of butyl bromide. For both reactions PDI **7b** was isolated, in yields of 60% and 25%, respectively, see Table 2 entries 3 and 4. This outcome demonstrated convincingly that addition of an alkylating reagent significantly increased the yield of PDI **7b**, and thereby proofs that imidization via PDAE **6** is the faster route to form PDIs.[49]

Although significantly higher yields have been obtained by adding an alkylating reagent, we decided to further develop mild imidization reactions without the use of alkylating reagents. This choice has been made because alkylation requires an extra reaction step, uses a highly reactive alkylating reagent and thereby severely limits functional group tolerance. As for the reaction without an alkylating reagent, the imide formation itself already has a conversion around 50%,[50] and that is a good starting point for obtaining satisfactory yields after optimizing the reaction conditions. It should be noted that the use of alkylating reagents for highly unreactive systems, such as electron deficient or sterically hindered amines, is still a viable option.

The detailed reaction schemes for the imidization reactions, starting from PDA **1** or model compound perylene-3,4-dicarboxylic anhydride-9,10-dicarboxylic dibutyl ester PMADE

11,[51,52] are depicted in Schemes 2 and 3. The imidization reaction of PMADE **11** is included in this work, because this reaction proceeds *via* a single amic acid intermediate compound **12**, and yields reaction products, perylene-3,4-dicarboxylic monoimide-9,10-dicarboxylic diesters (PMIDEs **13**), that are soluble in common organic solvents. The more complex imidization of PDA (**1**) proceeds through four intermediates; compound **8**, *cis*- and *trans*-**5** and compound **9**. In addition, the resulting PDIs **7** generally are not soluble in organic solvents, which prevents easy identification of the reaction product(s).

2.2.2 Synthesis and characterization of model amic acids
In order to validate the reaction mechanism depicted in Schemes 2 and 3, the potassium salts of the amic acids **12a**, **5a** and **9a** were synthesized and characterized. These compounds are model compounds for the intermediate amic acid salts in the imidization reaction. Potassium salts were synthesized, because these compounds are easier to isolate and characterize than the corresponding DBU salts. It has been reported that hydrolysis of structurally similar amic acids yield anhydrides under acidic conditions.[41,48] Under basic conditions amic acids derived from primary amines form imides, but this reaction is blocked for amic acids derived from secondary amines. Therefore amic acids salts **K12a**, **K25a** and **K9a** are expected to be stable under basic conditions.

At room temperature the formation of the amic acid salt **K12a** from PMADE **11** proceeds within 60 minutes, as the pale reaction mixture, in which PMADE **11** is sparsely soluble, is converted to a bright orange solution. Isolation of compound **K12a** was achieved by precipitation, using water-free conditions, see entry 1, Table 3. Formation of the perylene monoamide triester **14a**, a thermally and hydrolytically stable compound, was accomplished by adding butylbromide to the reaction mixture. This reaction is highly efficient and without any purification efforts compound **14a** was isolated in 86% yield, see entry 2 in Table 3. Compounds **K12a** and **14a** were characterized by NMR, absorption and emission spectroscopy and mass spectrometry. These techniques provided solid proof of the molecular structure of these compounds, see SI. With the successful synthesis and characterization of compounds **K12a** and **14a** it has been proven that the amic acid **12** in an intermediate in the imidization of PMADE **11**, which strongly supports the validity of Scheme 3. Also, the synthesis and spectral characterization of **K12a** facilitates the identification of other perylene monoamic acid diesters salts of **12**.
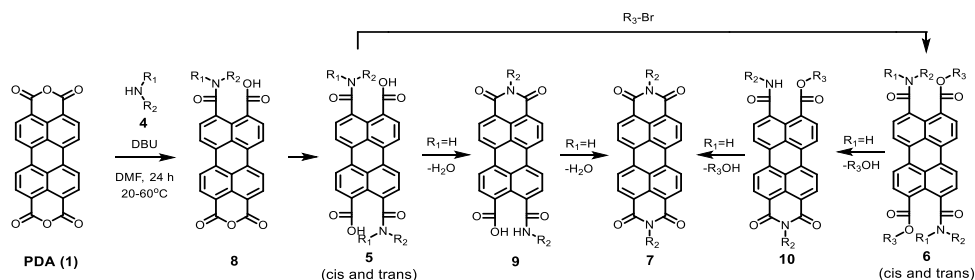

Scheme 2. *Imidization reaction starting from PDA (**1**) including all anticipated intermediates.*
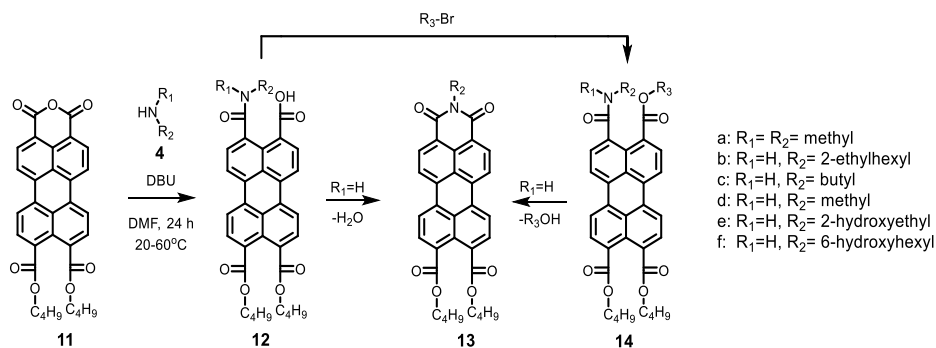
Scheme 3. *Imidization reaction starting from PMADE (11) including all anticipated intermediates.*

When PDA **1** is reacted with dimethylamine **4a** soluble amic acids are formed even faster. The initial reaction mixture, a red suspension, is transformed to a deep orange viscous liquid within 20 minutes. Amic acid salt **K₂5a** was isolated by precipitation in dry acetone, see entry 1, Table 2. The dibasic salt **K₂5a** is soluble in polar solvents, including water, and exhibits an absorption spectrum that is very similar to that of PTE **3** and perylene-3,4,9,10-tetracarboxylate.[30] When butylbromide was added after formation of PDAA **5a**, PDAE **6a** was obtained in 76% yield, virtually free of contaminants, see Table 2, entry 2 and Fig. S1 and S2 in the SI. The *cis* and *trans* regioisomers of compound **6a** were not distinguishable in the ¹H NMR spectrum. Broadening of the resonances of the aromatic protons is the sole indication of the presence of two isomers, a result that is in line with the ¹H NMR spectrum reported for a similar amic acid,[53,54] see Fig. S1. The ¹³C NMR spectrum, however, clearly revealed the formation of two isomers by the presence of two amide and two carboxylate carbons. Also the number of aromatic carbons atoms in the ¹³C NMR spectrum exceeds the 10 expected for either the *cis* or the *trans* isomer, see Fig. S2. The successful isolation of compounds **K₂5a** and **6a** confirms that diamic acid salt of **5** is an intermediate in the imidization of PDA and supports the reaction mechanism in Scheme 2.
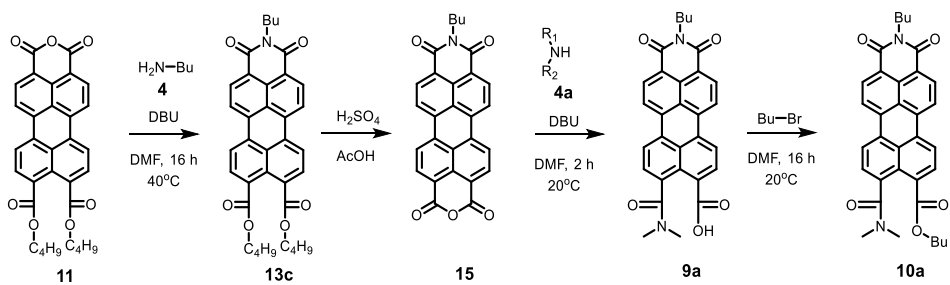
Scheme 4. *Synthesis of model compounds K9a and 10a.*

Model compounds **K9a** and **10a** were synthesized according to Scheme 4. This synthesis starts with the imidization of compound **11** using our mild imidization protocol and produced **13c** in almost quantitative yield. Cleavage of the ester functionalities in concentrated sulfuric acid gave compound **15** in high yield.[54,55] Ring opening, using dimethylamine **4a**, yielded model compound **K9a**, that was isolated via an anhydrous

precipitation. The hydrolytically stable and highly soluble compound **10a** was obtained from **K9a** *in situ*, by addition of bromobutane. The identity of compounds **10a** and **K9a** was unambiguously proven by NMR spectroscopy and mass spectrometry, see SI.

To provide proof of the intermittency of compound **9** in the imidization reaction we have reacted compound **15** with butylamine under standard conditions (DBU, DMF) to form compound **9c** *in situ*, see Scheme S1. The conversion of this compound to PDI **7c** was followed by absorption spectroscopy, *vide infra*, and this experiment has confirmed the intermediary of compound **9c** in Scheme 2.
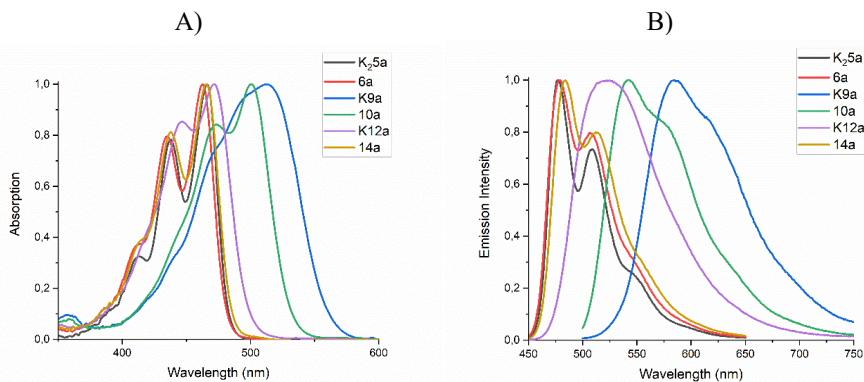

Figure 1. *a) Normalized UV-Vis absorption and b) Normalized fluorescence emission spectra of Compounds 3, K₂5a, 6a, K9a, 10a, K12a and 14a in Ethanol.*

The absorption and emission spectra of the amic acid salts **K₂5a**, **K9a**, **K12a** were recorded in water, DMF and ethanol, see Fig. S14 and S16, while the spectra of the corresponding apolar model compounds **6a**, **10a** and **14a** were recorded in ethanol and chloroform, see Fig. S15. The spectra of all compounds in the common solvent EtOH are presented in Fig. 1, while photo physical data are presented in Table S2. The absorption spectra of compounds **3**, **13c** and **7c** in chloroform are depicted in Fig. S3. The spectra in this Figure serve as a point of reference, for the spectra expected for molecularly dissolved perylene diamic acids, perylene monoamic acid monoimides and perylene diimides, respectively.

The absorption spectra in ethanol of diamic acid salt **K₂5a**, diamic ester **6a** and the diester monoamic ester **14a** resemble that of tetraester **3**, with a clear vibronic structure and absorption maxima around 470 and 440 nm. Substitution of a butyl ester by a dimethyl amide (**3** to **14a**, **6a**) resulted in ~2 nm blue shifts per substitution, whereas substitution of an amic ester by an amic acid salt (**6a**, **14a** to **12a**, **5a**) resulted in ~3 nm red shifts per substitution. The absorption of the monoamic ester diester **10a** is 32 nm red shifted as compared to tetraester **3**, see also Fig. S3. The absorption spectra of the amic acid salts **K12a** and **K9a** are red shifted and show a diminished vibrational structure, as compared to their amic ester analogues. Amic acids, obtained after protonation of their potassium salts, exhibit blue shifted absorption spectra, but are too unstable for full characterization, see Fig. 8, S12 and S13.

Table 1. *Spectral data of amic acid salts K_25a and $K9a$ in different solvents*

Compound	Solvent	λ_{abs}	λ_{em}	Φ_F
K$_2$5a	DMF	475, 443	487	0.16
K$_2$5a	EtOH	466, 438	477.5, 509	0.93
K$_2$5a	H$_2$O[a]	463, 435	475, 505	1.0
K9a	DMF	521	581	0.14
K9a	EtOH	513	584	0.65
K9a	H$_2$O[a]	505	591	0.19

[a] 0.01 M K$_2$CO$_3$

Since the amic acid salts of **5** and **9** are intermediates in the PDI synthesis, it is worthwhile to investigate the (photo) physical data of compounds **K$_2$5a** and **K9a** in different solvents, see Table 1. Surprisingly, these amic acid salts have poor solubility in DMF, the solvent used for the imide formation, while solubility in water is much higher. Fluorescence quantum yields of compound **K$_2$5a** are very high in water and ethanol, which indicates that this dianionic compound is molecularly dissolved. In DMF, however, the fluorescence quantum yield is a meagre 0.16. For compound **K9a** the structure-less absorption and emission spectra, as compared to those of compound **10a** and **13c**, may be indicative for aggregate formation. Fluorescence quantum yields are high in ethanol, but in DMF and water quantum yields of 0.14 and 0.19 reflect substantial quenching. Solutions of **K9a** in water form a strong foam layer after shaking, which indicates that this compound acts as a surfactant and presumably forms micelles. The corresponding DBU salts of **5a** and **9a** have not been isolated, but spectra from diluted reaction mixtures containing these DBU salts have been recorded. Absorption and emission spectra as well as fluorescence quantum yields taken from these reaction mixtures closely resemble those of the corresponding potassium salts.

To determine the relative rates of the reaction steps in the imidization process, we have reacted PDA **1** with butyl amine **4c** at room temperature and monitored the reaction by sampling the reaction mixture at regular intervals. Subsequently, these samples were diluted and analyzed by absorption spectroscopy. Highly fluorescent yellow solutions were obtained after 20 minutes of reaction, both in water and chloroform, as seen in Fig. S4. This result indicates that all PDA had reacted, and that all reaction products are soluble, both in water and chloroform. The absorption and emission spectra of the reaction product closely resembled those of diamic acid salt **K$_2$5a**, indicating that the reaction product is the DBU salt of **5c**. Amic acid formation using K$_2$CO$_3$ in DMSO, proceeded at a similar rate.

Upon heating the reaction to 60°C, the amount of diamic acid salt **5c** slowly decreased. It is anticipated that the DBU salt of **9c** is formed. However, this compound has not been identified in the absorption spectra. Poor solubility of compound **9c** in chloroform, the solvent used for dilution, along with the presence of considerable quantities of compounds **5c** and **7c**, may be the reason for this. The formation of PDI **7c**, however, is clearly visible when the imidization reaction is performed, see Fig. S4.[56]

In summary, these preliminary studies of the reaction of PDA **1** with butylamine **4c**, revealed a fast formation of diamic acid **5c** in 15–20 minutes at room temperature. At prolonged reaction times and elevated temperatures, typically a few hours at 60°C, the

concentration of diamic acid **5** decreased and monoamic acid monoimide **9c** was formed (but not detected). Subsequently the formation of PDI **7c** has been observed. It was concluded that the fast ring opening reactions, forming amic acid **5c**, and the subsequent slow imidization processes, forming intermediate **9c** and eventually the PDI **7c**, are decoupled processes that take place at markedly different time scales.

2.2.3. Reaction optimization by variation of reaction conditions

After validation of Scheme 3 and the establishment of the relative rates of the reaction steps, the imidization reaction was optimized by changing the reaction parameters. The reaction of PDA **1** with 2-ethyl-hexyl amine **4b** was chosen for this purpose, because the product of this reaction, PDI **7b**, is highly soluble in chloroform and conveniently characterized by NMR spectroscopy. Isolation of the reaction product was extremely convenient; pouring the reaction mixture in water, filtering the precipitate and washing the product with dilute base to remove water-soluble amic acids, yielded pure PDI.[57]

Using the standard conditions (4 molar equivalents of amine and DBU and DMF as the solvent), increasing the reaction yields was achieved by increasing the temperature to 60°C or the reaction time to 7 days, see entries 5 and S1 in Tables 2 and S1. From a practical point of view the elevated temperature is preferred. In the original work by Langhals,[10] Zinc Acetate $Zn(OAc)_2$ was used to catalyze the reaction. In our experiments $Zn(OAc)_2$ leads to higher yields at room temperature, but addition of this compound no longer has a pronounced effect at elevated temperatures, see entries 2 and 3 in Table S1. Therefore, and also because we want to keep the reactions clean and simple, we refrain from the addition of $Zn(OAc)_2$. In summary, the optimized imidization proceeds at 60°C, achieves quantitative yields and takes approximately 24 hours.

Our next objective is to convert the mild, convenient and efficient imidization reaction into a green(er) and more sustainable process.[58] This has been accomplished by substitution of the solvent DMF and the base DBU by greener alternatives. Substitution of toxic DMF by DMSO, a non-toxic solvent with similar physical properties, did not affect the reaction yields (entry 6, Table 2). With regard to the substitution of DBU by organic bases, it was observed that DBU is distinctly the best base for this reaction, as was the case for the PTE formation as well.[59] Reaction with TEA or DIPEA, resulted in significantly lower yields, typically around 20–25% after 24 hours at 60°C, entry S4, Table S1. Since most organic bases have toxicity issues similar to those of DBU, substitution of DBU by organic bases was not explored further. Finally, the use of the non-toxic inorganic base K_2CO_3 in combination with DMSO, was investigated. At 60°C, significantly lower yield were observed than with DBU as a base, see entry S5, Table S1. By raising the reaction temperature to 100°C, however, the decreased reaction rate was fully compensated for and the reaction gave quantitative yields, see entry 7 in Table 2. This result demonstrates that an entirely green and sustainable process for the imidization of PDA has been developed. Apart from starting material PDA **1**, the amine **4b** and the reaction product PDI **7b**, all inherent to this reaction, the solvent and other reactant are non-toxic and environmentally benign.

Table 2. *Formation of PDIs **7** from the reaction of PDA **1** with different amines, using various reaction conditions.*

Entry	PDA	Reagents	Base	Solvent	Conditions	Yield, in %
1	PDA (**1**) 0.5 mmol	**4a** 2 mmol	K_2CO_3 2 mmol	DMSO 4 mL	24h RT	**$K_2$5a** 66%
2	PDA (**1**) 0.5 mmol	**4a** 2 mmol BuBr 2 mmol	DBU 2 mmol	DMF 4 mL	24h RT	**6a** 76%
3	PDA (**1**) 0.5 mmol	**4b** 2 mmol	DBU 2 mmol	DMF 4 mL	24h RT	**7b** 25%
4	PDA (**1**) 0.5 mmol	**4b** 2 mmol BuBr 4 mmol	DBU 2 mmol	DMF 4 mL	24h RT	**7b** 60%
5	PDA (**1**) 0.5 mmol	**4b, 4c, 4d**[a]. **4f** 2 mmol	DBU 2 mmol	DMF 4 mL	24h 60°C	**7b, 7c, 7d, 7f** >97%
6	PDA (**1**) 0.5 mmol	**4b, 4c** 2 mmol	DBU 2 mmol	DMSO 4 mL	24h 60°C	**7b, 7c** >97%
7	PDA (**1**) 0.5 mmol	**4b, 4c, 4d**[a], **4e**[b], **4f** 2 mmol	K_2CO_3 2 mmol	DMSO 4 mL	24h 100°C	**7b, 7c, 7d, 7e, 7f** >97%
8	PDA (**1**) 0.5 mmol	**4b, 4c** 1.1 mmol	K_2CO_3 2 mmol	DMSO 4 mL	24h 100°C	**7b**, 93% **7c**, >97%
9	PDA (**1**) 0.5 mmol	**4e** 2 mmol	DBU 2 mmol	DMF 4 mL	8h RT	**7e** >97%
10	PDA (**1**) 0.5 mmol	**4b**[c], **4c, 4d, 4f** 2 mmol	DBU 2 mmol	DMSO 4 mL H_2O[d] 4 mL	24h RT	**7b, 7c, 7d** >97% **7f** 90%

[a] First hour kept at RT. [b] At 80°C. [c] 2 mL of water added. [d] Water added to the reaction after half an hour.

Next, imidization reactions of PDA **1** were undertaken using the amines **4c**–**4f**. The PDIs obtained by these reactions bear small alkyl chains (**7c**–**7d**), or hydroxyalkyl chains (**7e**–**7f**) and only the PDIs **7c** and **7f** are sparsely soluble in chloroform.[60] With butylamine **4c**, the room temperature reaction was incomplete, but the yield of **7c**, (48%) was considerably higher than that of **7b** (25%). By increasing the reaction temperature to 60°C, the reaction yielded **7c** in quantitative yield, both in DMF and DMSO. Using the green conditions, DMSO as a solvent and K_2CO_3 as a base, quantitative yields were obtained at 100°C, see entries 5–7 and S6 in Tables 2 and S1. In order to make the DMSO/K_2CO_3 reaction entirely green, the excess of amine was limited to 10%. After facilitating the amic acid formation, by stirring one hour at room temperature, the reaction mixture was heated to 100°C and PDI **7c** was isolated in quantitative yield, see entry 8 Table 2. With this modification only minute amounts of unreacted amine are present in the final reaction mixture. This procedure of forming the amic acid at room temperature prior to imidization at higher temperatures, may also be extremely suited for working with volatile or expensive amines.

In the synthesis of **7d**, methylamine **4d** dissolved in methanol was used as a reactant. The room temperature reaction yielded **7d** in 89% yield. When the reaction was stirred at room temperature for 1 hour, to ensure amic acid formation and prevent evaporation of the amine, quantitative yields were obtained for the DBU reactions at 60°C as well as the K_2CO_3 reaction at 100°C, see entries 5,7 and S7 in Tables 2 and S1.19 For the reaction

Table 3. *Reaction of amines 4a-4f PMADE 11*.

Entry	Perylene anhydride	Reagents	Base	Solvent	Reaction conditions	Product and yield, in %
1	PMADE (**11**) 0.19 mmol	**4a** 0.38 mmol	K_2CO_3 0.38 mmol	DMSO 2 ml	24h RT	**K12a** 61%
2	PMADE (**11**) 0.19 mmol	**4a** 0.38 mmol BuBr 0.76 mmol	DBU 0.38 mmol	DMF 2 ml	24h RT	**14a** 86%
3	PMADE (**11**) 0.19 mmol	**4b** 0.38 mmol	DBU 0.38 mmol	DMF 2 ml	24h RT	**13b** 55%
4	PMADE (**11**) 0.19 mmol	**4c** 0.38 mmol	DBU 0.38 mmol	DMF 2 ml	24h RT	**13c** 65%
5	PMADE (**11**) 0.19 mmol	**4d** 0.38 mmol	DBU 0.38 mmol	DMF 2 ml	24h RT	**13d** 75%
6	PMADE (**11**) 0.19 mmol	**4e** 0.38 mmol	DBU 0.38 mmol	DMF 2 ml	24h RT	**13e** 80%
7	PMADE (**11**) 0.19 mmol	**4f** 0.38 mmol	DBU 0.38 mmol	DMF 2 ml	24h RT	**13f** 75%

with 6-amino-1-hexanol **4f**, the yield of the DMF/DBU reaction was 66% at room temperature. Quantitative yields are obtained by raising the temperature to 60°C, while the K_2CO_3 reaction gave quantitative yields at 100°C, see entries 5, 7 and S8 in Tables 2 and S1.

The imidization reaction with ethanolamine **4e** proceeded much faster and quantitative conversion at room temperature was achieved after 8 hours already. When this reaction was sampled and diluted in water, the resulting absorption spectra clearly showed that amic acid formation and imidization both take place at room temperature and that amic acid formation and imidization are no longer decoupled. The initial rise in the concentration of amic acid **5e** is reversed within 20 minutes and a broad structure-less
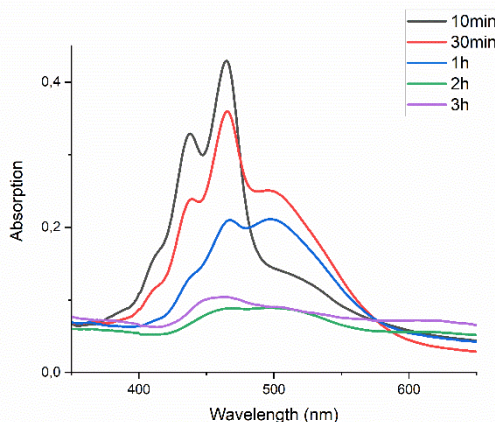

Figure 2. *UV-Vis spectra of the reaction of PDA (**1**) with ethanolamine (**4e**) in DMF using DBU as the base. Spectra were taken from samples of the reaction mixture diluted in water. The baseline is lifted due to the presence of insoluble PDA **1** and/or PDI **7e**. Absorptions do not accurately scale with concentrations in the reaction mixture due to sampling from a heterogeneous reaction mixture.*

red-shifted absorption emerges, which closely resembles that of compound **9a**, see Fig. 2 an S16. Also, a purple precipitate originating from PDI **7e** is formed upon diluting the reaction mixture in water early in the reaction. For the same reaction in DMSO, using K_2CO_3 as the base, amic acid formation took place within 20 minutes, but imidization was not observed at room temperature, see Fig. S6. For this reaction quantitative yields were obtained at 80°C, see entries 7 and 9, Table 2.

The mild imidization reaction with model compound PMADE **11** and the aliphatic amines **4b**–**4f** was also examined. Reactions were performed at room temperature and yields, after purification by column chromatography are displayed in Table 3. Purity and identity of compounds **13b**–**f** were conveniently proven by NMR spectroscopy. From the reported yields in Table 3 it is concluded that in all cases the reaction yields are well over 50% at room temperature, and that ethanolamine **4e** is the most reactive amine. These room temperature yields correlate well with those obtained for the bisimides and may be indicative for the reactivity of the amines in the imidization of perylene anhydrides. By increasing the reaction temperatures to 40°C, quantitative yields can be obtained overnight, as demonstrated with the synthesis of compound **13c**, *vide supra*.

In summary, the reactions of PDA **1** with all aliphatic amines are very convenient and quantitative yields are obtained with DBU in DMF or DMSO at 60°C and with K_2CO_3 in DMSO at 100°C. Quantitative PDI formation resulted in a convenient workup in which the filtrate is transparent, virtually colorless and free from PTCA derivatives. These results indicate that these reaction conditions are universally applicable for aliphatic amines. For all reactions the ring opening by the amines is fast while the imidization from the amic acid intermediates is rate-determining. Therefore, differences in amine reactivity must be due to differences in rates of imidization of the respective amic acids.

2.2.4. Reaction kinetics; modelling and measuring

Based on the reaction sequence for the imidization of PDA in Scheme 2, a kinetic model has been constructed. With this kinetic model the reaction mechanism can be validated and the rate constants for the different reaction steps determined. Furthermore, this model may also help to understand why our novel synthetic approach produces PDIs at room temperature already. In addition, factors that limit the rate of the imidization step, can be identified and potentially resolved to make the process even faster at mild and green conditions.

The imidization of PDA consists of 4 reaction steps, two consecutive second-order amic acid forming ring opening reactions, followed by two intramolecular consecutive first-order imidization reactions, see eqn (1). These consecutive reaction steps are identical by mechanism and their rate constants should have near-identical values, i.e. $k_1 \approx k'_1$ and $k_2 \approx k'_2$. It should also be noted that the stable amic acids salts K_2**5a** and **K9a**, have been synthesized and characterized, which facilitated easy identification of analogous amic acid intermediates.

$$1 \xrightarrow{k_1} 8 \xrightarrow{k'_1} 5 \xrightarrow{k_2} 9 \xrightarrow{k'_2} 7 \qquad eq\ 1$$
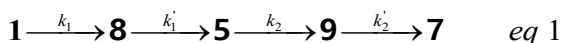
Bimolecular ring opening reactions to form amic acids are fast, *vide supra*, and we have observed that these ring opening reactions are generally decoupled from the slower unimolecular imidization reactions. Therefore, both reactions, the amic acid formation

24

from *vide supra* to *vide supra* and the imidization from *vide supra* to *vide supra*, will be described separately.

The first part of the reaction, from PDA to diamic acid **5**, is treated in detail in the SI. In deriving the kinetic equations, we assume that compound **1** is insoluble, whereas compound **8** will be somewhat soluble. Therefore, the conversion from PDA **1** to compound **8** is the rate-limiting step in this sequence. Accumulation of compound **8**, whose spectroscopic signature in molecular solutions is expected to be close to that of compound **9**, apart from a ~4 nm blue shift,[37] is not anticipated. The rate of consumption of compound **1** and the rate of formation of compound **5** according to eqn (S3) and (S8), are identical and depicted in Fig. S7. Experimental data, shown in Fig. S3 and S6, do not resemble those in Fig. S7, most likely because the data used for constructing Fig. S3 and S6, were obtained from sampling inhomogeneous reaction mixtures.

Compounds **5** and **9**, participating in the second part of the reaction, are partly soluble in the reaction medium, as indicated by the deep red color that is developed throughout the reaction. Eqn (2)–(4) describe the rates of the individual reaction steps.

$$\frac{d[\mathbf{5}]}{dt} = -2k_2[\mathbf{5}] \qquad\qquad \text{eq 2}$$

$$\frac{d[\mathbf{9}]}{dt} = 2k_2[\mathbf{5}] - k_2'[\mathbf{9}] \qquad \text{eq 3}$$

$$\frac{d[\mathbf{7}]}{dt} = k_2'[\mathbf{9}] \qquad\qquad \text{eq 4}$$

Solutions for eqn (2)–(4) are given by eqn (5)–(7).[61]

$$[\mathbf{5}] = [\mathbf{5}]_0 \exp^{-2k_2 t} \qquad\qquad\qquad \text{eq 5}$$

$$[\mathbf{9}] = \frac{2k_2[\mathbf{5}]_0}{k_2' - 2k_2} (\exp^{-2k_2 t} - \exp^{-k_2' t}) \qquad\qquad \text{eq 6}$$

$$[\mathbf{7}] = [\mathbf{5}]_0 \left\{ 1 + \frac{1}{k_2 - 2k_2'} \left[k_2' \exp^{-2k_2 t} - 2k_2 \exp^{-k_2' t} \right] \right\} \qquad \text{eq 7}$$

The kinetic model for the imidization of PMADE **11** or PMAMI **15**, in which the same reaction rate constants k_1 and k_2 are employed, is described in the SI (eqn (S9)–(S15)).

A graphical representation of the composition of the reaction mixture, according to eqn (5)–(7), is given in Fig. 3. The decay of the diamic acid **5** follows first order kinetics, the amic acid monoimide **9** is an intermediate whose concentration builds up to nearly 50% and subsequently declines, while the formation of PDI **7** distinctly lags behind the disappearance of compound **5**. Experimental data, to support our kinetic model have not been obtained so far. Qualitatively the consumption of compound **5c** and formation of compound **7c** have been demonstrated but detection, let alone quantification of the amount of compound **9c** has not been achieved.
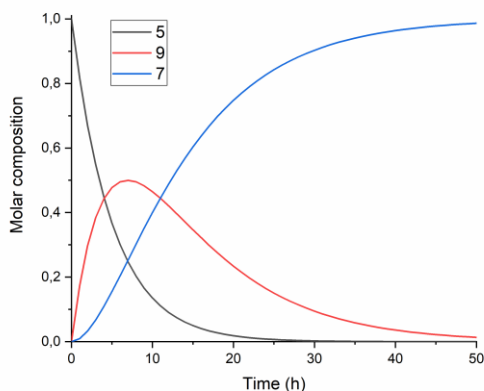
Figure 3. Consumption of diamic acid **5**, formation and disappearance of reaction intermediate **9** and formation of PDI **7** according to equations 5-7.

It should be noted that the amic acid salts of compounds **5** and especially **9** have limited solubility in DMF and DMSO and form aggregates and precipitates at the high concentrations used for the standard reactions. Thus solubility and possibly the type of aggregation of the amic acid salts of **5** and **9**,[62–64] will govern the rate of the imidization reaction. The solubility and aggregation behavior of these salts depends on the reaction temperature, the solvent, the substituent R_2 and the counter ions. Therefore, we anticipate that these are the major factors that determine rates of imide formation.
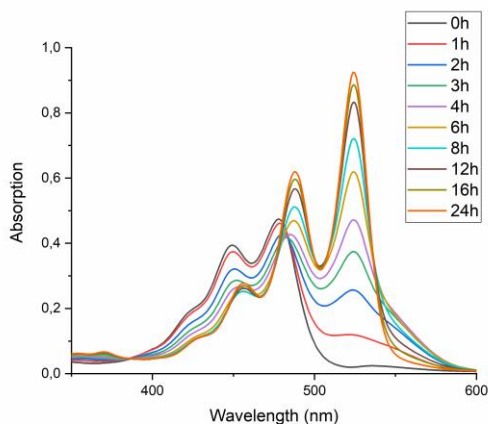
Figure 4. Absorption spectra as a function of time of the reaction of the DBU salt of diamic acid **5c** in DMF at room temperature (20ºC) at concentrations around 10^{-5} M.

To test the hypothesis that solubility of amic acid salts limits the rate of imidization reaction, we decided to perform the second stage of this reaction in a highly diluted medium. The imidization reaction with butylamine **4c** at room temperature was conducted under standard conditions (DMF, DBU) for 30 minutes, until the formation of the diamic acid **5c** was completed. At this stage the reaction mixture was a thick orange slurry, a

clear indication that the amic acid salts derived from compound **5c** did not fully dissolve. By strongly diluting the reaction mixture with DMF, reaching concentrations in the 10^{-5} molar range,[65] the remainder of the reaction at room temperature was followed *in situ* by absorption spectroscopy, see Fig. 4.[66] While the normal reaction reaches 48% conversion in 24 hours, the diluted reaction reaches this conversion in approximately 6 hours and achieves a near-quantitative conversion in 24 hours. The diamic acid salt of **5c**, absorbing at 438 and 466 nm, is consumed swiftly, and a broad absorption (extending up to 600 nm), which closely resembles the absorption of model compound **K9a**, emerges. In time this broad absorption, which originates from the salt of compound **9c**, builds up and disappears, while eventually PDI **7c**, with distinct absorptions at 488 and 524 nm, is formed. At the end of the reaction a clear, brightly fluorescent solution that contains PDI **7c** is obtained. The good solubility of PDI **7c** in DMF is really surprising, although it is obvious that these solutions are oversaturated.[67]
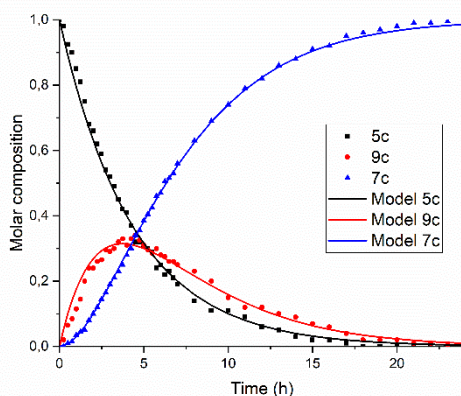
Figure 5. *Composition of the reaction mixture obtained from the data displayed in Figure 4. Solid lines represent the fitting curves obtained using equations 5-7. The solid squires, balls and triangles are concentrations of compounds **5c**, **9c** and **7c**, respectively obtained by analyzing the absorption spectra.*

In Fig. 5, the composition of the reaction mixture as a function of time is displayed. For determining the composition of the reaction mixture, it was assumed that the spectrum taken at t = 0 is that of the DBU salt of **5c** and that the spectrum taken after 24 hours is from **7c**. Relative concentrations of **5c** and **7c** were determined by manual fitting of the absorption spectra. The remaining absorption spectrum, obtained by subtracting the contributions from compounds **5c** and **7c**, is assigned to reaction intermediate **9c**. The fitting was done such that the absorption spectra of compound **9c** were consistent throughout the series, and closely resembled the spectra that we have previously obtained from compound **K9a**, see Fig. S14. Using this procedure, determining the concentration of PDI **7c** is fairly consistent and reliable. However, for determining [**5c**] and [**9c**] independently this procedure is not suited.[68]
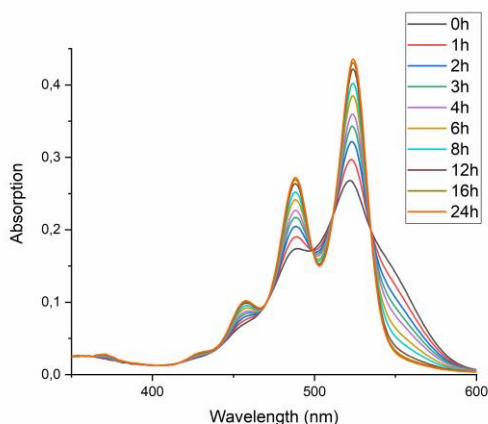
Figure 6. *Absorption spectra as a function of time of the reaction of the DBU salt of amic acid monoimide **9c** in DMF at concentrations around 5*10⁻⁶ M. The starting compound **9c** already contains traces of the product **7c**. The sharp isosbestic points clearly indicate the presence of only two compounds; **9c** and **7c**.*

The experimental data in Fig. 5 resemble those predicted by our model depicted in Fig. 3, qualitatively; the monotonic decrease of compound **5c**, the delayed formation of compound **7c** and the intermediate formation of compound **9c** are clearly visible. The curve fitting of the data in Fig. 5 was accomplished by using values for the rate constants k_2 and k'_2 of 3×10^{-5} s^{-1} and 8×10^{-5} s^{-1}, respectively. The blue curve for the formation of PDI **7** was constructed by taking identical values for k_2 and k'_2 of 5×10^{-5} s^{-1}. We anticipate that these seemingly different values for the rate constants k_2 and k'_2 are artefacts that emerged because the concentrations of diamic acid **5c** and the monoamic acid **9c** could not be determined independently.
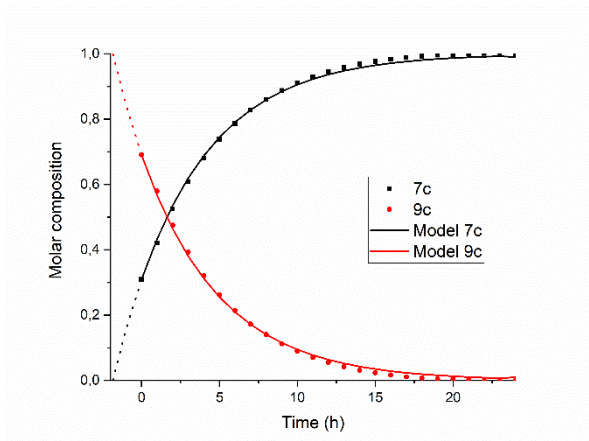
Figure 7. *Composition of the reaction mixture obtained from the data displayed in Figure 6. Solid lines represent the theoretical fitting curves obtained using a first-order decay obtained using equations S11 and S12.*

28
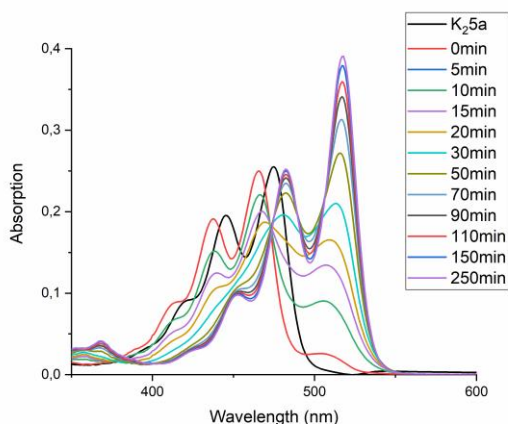
Figure 8. *Absorption spectra of compound* **$K_2$5a** *(black) in DMF and* **5a** *(red), formed after acidification with 1 drop 1N HCl. In the time-dependent absorption spectra the reaction from* **5a** *(λ_{max}= 466 and 438 nm) via compound* **8a** *to compound* **1** *(λ_{max}= 517.5 and 482 nm) is visible. Please note that the first spectrum after acidification already contains traces of compound* **8a**.

To find out if this assumption is correct, the rate constant k'_2 was determined independently by monitoring the reaction from compound **9c** to **7c**. To this end, monoanhydride **15** was reacted with butylamine **4c** under standard conditions for 30 minutes to form compound **9c** quantitatively, see Scheme S1. After dilution with DMF, the conversion from intermediate **9c** to PDI **7c** by a first order process was monitored, see Fig. 6 and 7. In Fig. 6 three isosbestic points at 499, 512 and 535 nm are observed, which proofs that **9c** is converted to **7c** directly. The rate constant k'_2 was determined to be 5×10^{-5} s^{-1}, as demonstrated in Fig. 7. In addition this reaction rate constant was also determined from the reaction of monoamic acid diester **12c** to PMIDE **13c**, see Fig. S9 and S10. The imidization rate constant for this reaction had the same value, 5×10^{-5} s^{-1}. Combining these results it is obvious that the rate constants k_2/k'_2 for the transformation of an amic acid to an imide on the perylene scaffold has a value of 5×10^{-5} s^{-1} and is not significantly affected by the substituent(s) at the opposing peri-position(s). It is also concluded that kinetic measurements, starting from compound **5c** are not appropriate for determining k_2 and k'_2 independently. With the assumption that $k_2 = k'_2$, however, the reaction rate constant can be determined from such kinetic measurements. To investigate the stability of amic acids under acidic conditions, dilute solutions of the model amic acid salts **$K_2$5a**, **K9a** and **K12a** in DMF were acidified with HCl. In line with the reported behavior of naphthyl-1,8-dicarboxylic amic acids, perylene amic acids were highly unstable.[69] Protonation was visible by a distinct 9 nm blue shift in the absorption spectrum and formation of **5a** was immediately followed by the appearance of an absorption around 505 nm, see Fig. 8. After 30 minutes the spectrum of PDA **1**, the end product of the acid decomposition process, became visible and the reaction was finished within 5 hours. From this experiment, the spectrum of the so far undetected monoamic acid monoanhydride **8a** was obtained, by subtracting the spectra of compounds **5a** and **1** from those of the reaction mixture, in a procedure similar to the one used to analyze the imidization of compound **5c**, see Fig. S11. It appears that compound **8a** is molecularly dissolved, as its absorption spectrum exhibits weak vibrational structure and is neither

broadened nor red shifted.[70] Similar experiments, monitoring the acid catalyzed anhydride formation from amid acids **9a** and **12a** are depicted in Fig. S12 and S13. For these reactions clear and unambiguous isosbestic points were observed, due to the absence of reaction intermediates. PDA, PMAMI and PMADE, formed by amic acid hydrolysis, were molecularly dissolved in DMF and formed highly fluorescent oversaturated solutions. Rate constants for these reactions were not determined, because pH values, on which these reaction rates depend, have not been determined.

Finally it should be noted that fast anhydride formation from amic acids, implies that workup of reaction products in the PDI synthesis must be performed under basic conditions, until all amic acids are removed. Otherwise anhydrides are formed that cannot be removed.

2.2.5. Room temperature imidization

The dilution experiments depicted in Fig. 4–7 have demonstrated that imidizations of PDA proceed at room temperature and have low activation barriers for imide formation. The overall reaction rate under standard conditions is limited by the solubility of the intermediate amic acid salts of **5** and **9**. At high dilution[71] the imide formation for the DBU reaction in DMF is strongly accelerated, with a rate constants k_2 around 5×10^{-5} s^{-1}. This allows the reaction to proceed to a >97% conversion in 24 hours at room temperature. It appears, from visual inspection of the reaction mixtures, that the DBU salts of the amic acids **5** and **9** have better solubility, as compared to the potassium salts, and this increased solubility may be the cause of the apparent DBU catalysis of the imidization reaction.

Our findings, that the rate of imidization is limited by the solubility of the amic acid salts **5** and **9**, and that dilution has a highly beneficial effect on the overall reaction rate, can be readily exploited for improving the synthesis of PDIs. Taking into account that amic acids **5** and **9** have higher solubility in water (as compared to DMF and DMSO) and that for imidization of NMA and NDA water is an excellent solvent, dilution with water appears to be a viable option to increase the imidization rate even further.

When the synthesis of PDI **7c** was started employing the normal reaction protocol (DBU in DMSO) quantitative formation of PDAA **5c** was achieved within an hour at room temperature. Subsequently, one equivalent of water (4 ml) was added, resulting in instantaneous dissolution of the DBU salt of **5c** to form a deep red solution.[72] After 24 hours of reaction at room temperature, PDI **7c** was obtained in quantitative yield, entry 10 Table 1. It should be noted that this reaction has a 50% yield without water addition. Water is the ideal solvent to add, because in our synthetic protocol water should be added anyway for separating the solid product from the reaction mixture. For amines **4b**, **4d** and **4f**, the same procedure, adding water after amic acid formation was examined. For the formation of **7d**, imide formation was quantitative as well, while for the formation of **7f**, the yield was high, 90%, but not quantitative. For the formation of **7b**, we only added 2 mL of water because the long hydrophobic 2-ethyl-hexyl tails limit water solubility. The yield for this reaction was quantitative.[73]

These results imply that aliphatic PDIs can be synthesized in quantitative yields at room temperature, without (**7e**) or with the addition of water (**7b–7d**). When stable aliphatic amines, such as **4b–4f** are used, synthesis at 60–100°C is a reliable and practical option.

As it has been reported that PDI synthesis with amino acids under Langhals conditions does not affect the stereochemistry of the appended amino acid,[74,75] the 60–100°C "high temperature" synthesis is appropriate for these compounds as well. However, when temperature sensitive amines are used, imidization at room temperature will be the preferred route.

2.3 Discussion

In this work, we have demonstrated that imidization of PDA, contrary to previous experience, is a process that is conveniently and efficiently performed at moderate temperatures, if need be at room temperature. The first step of the process, formation of diamic acid, is facile and fast in DMF or DMSO with all bases that we have explored. Conditions for PDAA synthesis found in the literature are generally harsh,[76] but structurally similar amic acids, such as 1,8-naphthyl-dicarboxylic amic acids and 1,3,4,8-naphthyl-tetracarboxylic diamic acids, have been synthesized under much milder conditions.[44] Also the formation of compound **2**, the ester analogue of perylene diamic acid **5**, is a process that runs at extremely mild conditions. Therefore the observation that amic acid formation is the easy step in the imide synthesis is not very surprising and in line with our expectations.

Imide formation from amic acids, on the other hand, is anticipated to be much more difficult to achieve. It is reasonable to assume that limited solubility of PTCA derivatives is a major factor necessitating the high temperatures in the conventional PDI syntheses, since imidization from more soluble analogous (di)anhydride substrates is reported at lower temperatures.[25,26] The activation barrier for the imidization step has been largely unexplored, since all PDI forming reactions have been performed far above room temperature. In contrast to the data obtained from synthetic sources, mechanistic research on the reactivity of 1,8-naphthyl-dicarboxylic amic acids in water indicates that the activation barriers for analogous imidization reactions are low. The conversion from napththyl amic acids to naphthyl imides is a process that takes place reversibly at temperatures as low as 30°C. These data suggest that in water, a solvent in which PTCA derivatives tend to be poorly soluble, imidization is a process with a low activation barrier. So if polar solvents in which perylene amic acids are soluble can be found, imidization reactions of PDA may proceed at low temperatures.

Our experiments, in which diamic acid salts of **5** were fully dissolved in DMF at high dilution, gave full conversion to PDI **7** at room temperature. This proofs that amic acid salt solubility is the major rate limiting factor for the imidization of PDA. Absorption spectra taken at high dilution have clearly demonstrated that all reaction products and intermediates are visible. The diamic acid salts of **5** and even PDI **7** are molecularly dissolved, but monoimide amic acid salts of **9** still forms aggregates at these high dilutions. This finding suggests that the solubility of compound **9** is the major factor limiting the imidization rate. Since we have observed that the solubility of compound **5** is also limited under the standard reaction conditions, the solubility of this compound may be rate limiting as well. For amic acid salts of **5** and **9** it has been observed that potassium salts are less soluble than DBU salts and this solubility difference correlates with a lower reactivity of the reactions when K_2CO_3 is used. Another case where high solubility and high reactivity are correlated is the unusual fast reaction of ethanolamine **4e** with PDA under standard conditions. The more intense red color of the reaction mixture observed in this synthesis obviously reflects a higher solubility of the intermediate amic acid salts.

Once more, the rate for this reaction is higher when DBU is used as the base. Based on these observations, we conclude that the rate enhancing effect of DBU primarily originates from the higher solubility of the DBU amic acid salts in the reaction medium.

For optimal results, in terms of materials used and rate of the reaction, the bimolecular amic acid formation from PDA is best performed at high concentrations, using only a small excess of amine in as little solvent as possible. For this reaction DMF and DMSO are the only useful solvents identified so far. The second step, the unimolecular imide formation, is limited by the solubility of the amic acid salts and therefore dilution with an appropriate polar solvent is required to speed up this part of the reaction. Enhancing the yield has been proven by strongly diluting the reaction mixture with DMSO or DMF. By adding just one equivalent amount of water the same result, *i.e.* quantitative PDI formation at room temperature, was obtained as well. The use of water in this respect is extremely beneficial, as water is green, cheap and is already used for precipitating the reaction product PDI 7 out of the solution. Further reaction optimization along these lines will be the subject of coming research in our group.

Looking ahead further, attractive opportunities emerge in broadening the scope of the mild imidization reactions. For example in terms of the amines and anhydrides used as starting compounds. It is known from literature that aromatic amines are less nucleophilic and generally have lower yields in imidization reactions.[23,24,27,28] Preliminary results of reactions on PMADE 11 have shown that at elevated temperatures aromatic imides can be formed.[77] Reactions of NDI with butyl amine demonstrated the formation of dibutyl NDI at room temperature already. In the literature this reaction is reported in DMF or acetic acid at temperatures above 100°C.[78,79] Attaching delicate and sensitive (bio)molecules, such as amino terminated nucleic acids and proteins, to strongly fluorescent perylene anhydride moieties like compound 11 is another attractive prospect of our novel synthetic procedure. Very mild reaction conditions can be employed, which is advantageous in view of the high value and limited stability of NH_2-terminated biomolecules. An additional advantage of the mild imidization protocol is that every step of the process can be monitored and examined in great detail using absorption spectroscopy. This facilitates optimization of the reaction by tuning the individual reaction steps.

2.4 Conclusions
The imidization of PDA 1 has been converted from a harsh "molten imidazole" process, performed at 140–180°C, into a highly practical, efficient process that runs at strongly decreased temperatures. When using primary aliphatic amines, DBU and either DMF or DMSO as the solvent, full conversion within 24 hours is achieved in the temperature range between 20–60°C. By using K_2CO_3 in DMSO, a truly green and user-friendly synthesis has been developed at reaction temperatures between 80–100°C.

The reaction sequence for the imidization process via various amic acid intermediates, as displayed in Scheme 2, has been confirmed experimentally, aided by the synthesis and full characterization of stable model amic acid salts and amic esters. The formation of diamic acid salts is a fast process that is completed within 30 minutes. Conversion from amic acids to imides is rate determining, due to the low solubility of the intermediate amic acid salts. Diluting the reaction mixture after amic acid formation, strongly increases the reaction rates. The reaction rate constant for the imidization process in DMF was

determined to be 5×10^{-5} s^{-1} at 20°C. An improved synthesis, that yields quantitative conversion at room temperature, was developed by adding water after amic acid is formed. An equivalent amount of water is enough to solubilize these amic acids and run the reaction to completion.

Finally, the convenience of the novel synthetic protocol needs to be emphasized. A protective atmosphere, special equipment and advanced synthetic skills are no longer required. When run at the proper temperature, full conversion is obtained and work-up comes down to product precipitation in water followed by a simple filtration. Current research efforts are focused on broadening the scope of our synthetic protocol by exploring the synthesis of aromatic PDIs and the use of delicate, temperature sensitive amines.

2.5 Experimental
2.5.1 Materials
The compound perylene-3,4-dicarboxylic monoanhydride-9,10-dicarboxylic dibutyl ester (**11**) was synthesized according to literature procedures.[51] All other reagents utilized in the syntheses were used as received from the manufacturers, unless otherwise stated. The solvents used were of reagent grade. PDA, 97% purity, was obtained from Sigma Aldrich.

2.5.2. Instrumentation and characterization
The NMR spectra were recorded with 400 MHz pulsed Fourier transform NMR spectrometer in CDCl$_3$, DMSO-d6 or MeOH-d4 at room temperature. The chemical shift values are given in ppm and J values in Hz. High-resolution mass spectra were collected on an AccuTOF GCv 4G, JMS-T100GCV, Mass spectro- meter (JEOL, Japan). The FD/FI probe (FD/FI) was equipped with an FD Emitter, Carbotec (Germany), FD 10 μm. Typical measurement conditions were as follow: Current rate 51.2 mA min^{-1} over 1.2 min; Counter electrode −10 kV; Ion source 37 V. The samples were prepared in dichloromethane. Absorption measurements were performed using a PerkinElmer Lambda 365 UV−Vis spectrophotometer. Photoluminescence studies were done in Jobin Horiba SPEX Fluorolog 111 Spectrofluorometer. For quantum yield measurements, the formula for optically dilute solutions was used.[80] Fluorescence quantum yields were determined by the comparative method using perylene-3,4,9,10-tetracarboxylic tetrabutylester (ΦF = 0.95 in CH$_2$Cl$_2$) and N,N′-di(1-hexylheptyl)perylene-3,4,9,10-tetracarboxy bisimide (ΦF = 0.99 in CHCl$_3$) and perylene-3,4,9,10-tetracarboxylic tetrapotassium salt (ΦF = 1.0 in water) as reference compounds.[30] Melting points (uncorrected) were recorded on a Gallenkamp melting point apparatus.

Kinetic measurements were performed on the formation of imides from amic acids at low concentrations in 3 mL quartz cuvettes with a 10 mm pathway. Reactions from the anhydrides **1**, **11** or **15** to the amic acid salts of **5c**, **12c** and **9c** were performed at room temperature at the smaller scale (200 or 100 mg starting compound) in DMF using DBU as the base at the conditions specified in the synthetic section. For the synthesis of **9c**, 100 mg of **15**, 2.0 equivalents of DBU and amine in 2 mL DMF were used.

After 1 hour of reaction a droplet of the reaction mixture was diluted with DMF and a few droplets of this solution were added to a cuvette placed in a dual beam

spectrophotometer. Absorption spectra were taken at room temperature every 5 minutes over a period of 24 hours.

2.5.3. Synthesis

Perylene-3,4,9,10-tetracarboxylic acid 3,9-dimethylamide dipotassium salt (and its 3,10 isomer) $K_2 5a$

In a 50 mL round bottom flask equipped with a magnetic stirring bar, PBA **1** (200 mg, 0.51 mmol), K_2CO_3 (564 mg, 4.08 mmol) and dimethylamine hydrochloride (**4a**, 166 mg, 2.09 mmol) were suspended in 4 mL DMSO. The suspension was stirred for 2 hours at 60°C. The reaction mixture was cooled to room temperature. Methanol (10 mL) was added under vigorous stirring and subsequently, acetone (200 mL) was added. The precipitate was filtered off and washed with acetone. The yellow solid was dissolved in methanol (20 mL) and filtered to remove the remaining K_2CO_3. The organic solvent was removed from the filtrate by rotary evaporation. This yielded a yellow solid that was dried in a vacuum oven.

Yield: 188 mg, 0.34 mmol, 66 %. ^{1}H-NMR (δH [ppm], MeOD, 400 MHz): 8.40 (2H, *J=8 Hz*, d), 8.38 (2H, *J=8 Hz*, d), 7.79 (2H, *J=8 Hz*, d), 7.51 (2H, *J=8 Hz*, d), 3.10 (6H, s), 3.05 (6H, s). MS (ESI): [M]$^{2-}$ Calculated for $C_{28}H_{20}N_2O_6$, 240.0666; found: 240.0668 [KM]$^-$ Calculated for $C_{28}H_{20}KN_2O_6$: 519.0964; found: 519.0965.]. MP > 350°C.

*Perylene-3,4,9,10-tetracarboxylic acid 3,9-dimethylamide 4,10-dibutyl ester and perylene-3,4,9,10-tetracarboxylic acid 3,10-dimethylamide 4,9 dibutyl ester **6a***

In a 50 mL round bottom flask equipped with a magnetic stirring bar, PBA **1** (200 mg, 0.51 mmol), DBU (621 mg, 4.08 mmol) and dimethylamine hydrochloride (**4a**, 166 mg, 2.04 mmol) were suspended in 4 mL DMF. The suspension was stirred for 1 hours at 60°C. 1-Bromobutane (699 mg, 5.10 mmol) was added and the reaction mixture was left to stir for 18 hours at 60°C. The mixture was cooled to room temperature. Water (40 mL) was added under strong stirring, which caused a precipitation of the crude product. The reaction product was filtered and the obtained solid was washed extensively with water, until almost no colour was observed in the filtrate, yielding an orange solid that was dried in a vacuum oven.

Yield: 230 mg, 0.39 mmol, 76%. ^{1}H-NMR (δH[ppm], CDCl$_3$, 400 MHz): 8.24 (4H, m), 7.86 (4H, *J=8 Hz*, d), 7.52 (2H, *J=8 Hz*, d), 4.33 (4H, *J=8 Hz*, t), 4.15 (6H, s), 3.12 (6H, s), 1.82 (4H, *J=8 Hz*, quin), 1.52 (4H, m), 1.01 (6H, *J=8 Hz*, t). ^{13}C-NMR (δC[ppm], CDCl$_3$, 101 MHz): 172.13, 172.09, 169.04, 169.02, 133.60, 133.29, 132.73, 131.12, 130.43, 129.44, 129.28, 128.82, 128.32, 127.81, 127.66, 120.97, 120.80, 120.75, 77.04, 76.72, 65.37, 39.80, 35.06, 30.68, 19.30, 13.83. LC-MS: t = 6.44, m/z calc: 594.27; found: 594.84 [M]. MS (FD): [M]$^+$ Calculated for $C_{36}H_{38}N_2O_6$, 594.2730; found: 594.2764, [M$_2$]$^+$ Calculated for $C_{72}H_{77}N_4O_{12}$ 1188.5460; found: 1188.5600. MP = 190-198°C

*Synthesis of perylene-3,4,9,10-tetracarboxylic acid diimides **7***

Standard reactions were performed using 200 mg of PDA. Under optimal conditions larger scale reactions for synthetic purposed were performed, using up to 5 grams of PDA. Reaction yields were independent of the scale.

In a 50 mL round bottom flask equipped with a magnetic stirring bar, PDA 1 (200 mg, 0.51 mmol), base (DBU or K_2CO_3, 2.04 mmol) and amine 4 (2.04 mmol) were suspended

in 4 mL solvent. Reactions with methylamine **4d** used a 40% solution in MeOH and were stirred for one hour at RT prior to heating. The suspension was stirred for 24 hours at the desired temperature. The reaction mixture was cooled to room temperature. Water (40 mL) was added under strong stirring, which caused a precipitation of the crude product. The precipitate was left to settle for a maximum of 24 hours. The reaction product was filtered and the obtained solid was washed extensively with 0.01 M K_2CO_3 until almost no color was observed in the filtrate and subsequently with water. When the reaction involved the more hydrophobic amine 4b, the filtrate was washed two more times with dilute HCl (1 M, 10 mL) and two more times with demineralized water (25 mL). The solid was dried in a vacuum oven.

DBU/DMSO water addition:
After addition of the reagents, the suspension was stirred for 1 hour at room temperature. Subsequently 4 mL of water was added (2mL for the synthesis of 7b) and the reaction mixture was stirred for another 23 hours at room temperature. Workup as described above.

N,N′-Di(2-ethylhexyl) perylene-3,4,9,10-tetracarboxylic acid diimide **7b**
DBU/DMF method, RT, from 200 mg PDA: Purple solid, yield 79 mg, 0.13 mmol, 25%. DBU/DMF method, 60 °C, from 1.00 g (2.55 mmol) PDA: Purple solid, yield 1.534 g, 2.50 mmol, 98%. K_2CO_3/DMSO method, 100 °C, from 1.00 g (2.55 mmol) PDA: Purple solid, yield 1.548 g, 2.52 mmol, 99%. DBU/DMSO water addition, from 200 mg PDA: Purple solid, yield 307 mg, 0.50 mmol, 98%.

^{1}H-NMR (δH[ppm], CDCl₃, 400 MHz): 8.61 (4H, *J=8 Hz*, d), 8.52 (4H, *J=8 Hz*, d), 4.14 (4H, m), 1.97 (2H, m), 1.42-1.32 (18H, m), 0.96 (6H, *J=8 Hz*, t), 0.90 (6H, *J=8 Hz*, t). ^{13}C-NMR (δC[ppm], CDCl₃, 101 MHz): 163.70, 134.44, 131.35, 126.30, 123.25, 122.98, 44.34, 37.96, 30.77, 28.71, 24.08, 23.08, 14.10, 10.64.

N,N′-dibutyl perylene-3,4,9,10-tetracarboxylic acid diimide **7c**
DBU/DMF method, RT, from 200 mg PDA: Purple solid, yield 123 mg, 0.24 mmol, 48%. DBU/DMF method, 60 °C, from 1.00 g (2.55 mmol) PDA: Purple solid, yield 1.249 g, 2.49 mmol, 98%. K_2CO_3/DMSO method, 100 °C, from 1.00 g (2.55 mmol) PDA: Purple solid, yield 1.239 g, 2.47 mmol, 97%. DBU/DMSO water addition, from 200 mg PDA: Purple solid, yield 249 mg, 0.50 mmol, 98%.

^{1}H NMR (δH[ppm], CDCl₃, 400 MHz): δ 8.74 (4H, *J=8 Hz*, d), 8.67 (4H, *J=8 Hz*, d), 4.23 (4H, *J=8Hz*, t), 1.74 (4H, *J=8 Hz*, quin), 1.47 (4H, *J=8 Hz*, sex), 0.99 (6H, *J=8 Hz*, t).

N,N′-dimethyl perylene-3,4,9,10-tetracarboxylic Diimide **7d**
DBU/DMF method, RT, from 200 mg PDA: Red solid, yield 180 mg, 0.43 mmol, 84%. DBU/DMF method, RT, from 200 mg PDA: Red solid, yield 210 mg, 0.50 mmol, 98%. K_2CO_3/DMSO method, 100 °C, from 200 mg PDA: Red solid, yield 207 mg, 0.49 mmol, 92%. DBU/DMSO water addition, from 200 mg PDA: Red solid, yield 214 mg, 0.51 mmol, 100%.

^{1}H-NMR (δH[ppm], D$_2$SO$_4$, 400 MHz): 9.15 (4H, *J=8 Hz*, d), 9.10 (4H, *J=8 Hz*, d), 3.93 (6H, s). FTIR: 742, 808, 850, 863, 1021, 1053, 1127, 1156, 1184, 1237, 1284, 1326, 1358, 1400, 1446, 1507, 1578, 1594, 1659, 1698.

*N,N'-di-(2-hydroxyethyl) perylene-3,4,9,10-tetracarboxylic acid diimide **7e***
DBU/DMF method, RT, 1.00 g (2.55 mmol) PDA: Dark purple solid, yield 1.196 g, 2.40 mmol, 98%. K$_2$CO$_3$/DMSO method, 80 °C, 1.00 g (2.55 mmol) PDA: Dark purple solid, yield 1.177 g, 2.36 mmol, 97%.

^{1}H-NMR (δH[ppm], D$_2$SO$_4$, 400 MHz): 9.21-9.07 (8H, m), 5.64 (4H, *J=8 Hz*, t), 4.85 (4H, *J=8 Hz*, t).

*N,N'-di-(6-hydroxyhexyl) perylene-3,4,9,10-tetracarboxylic acid diimide **7f***
DBU/DMF method, RT, 200 mg PDA: Purple solid, yield 199 mg, 0.34 mmol, 66%. DMF/DBU method, 60°C, 200 mg PDA: Purple solid, yield 297 mg, 0.50 mmol, 97%. K$_2$CO$_3$/DMSO method, 100°C, 200 mg PDA: Purple solid, yield 296 mg, 0.50 mmol, 97%. DBU/DMSO water addition, 200 mg PDA: Purple solid, yield 270 mg, 0.46 mmol, 90%.

^{1}H-NMR (δH[ppm], CDCl$_3$, 400 MHz): 8.77 (4H, *J=8 Hz*, d), 8.72 (4H, *J=8 Hz*, d), 4.37 (4H, *J=8 Hz*, t), 4.25 (4H, *J=8 Hz*, t), 8.69 (8H, m), 1.50 (8H, m).

*N-(butyl)perylene-3,4,9,10-tetracarboxylic acid 3,4-imide 9-dimethylamide potassium salt **K9a***
In a 25 mL round bottom flask equipped with a magnetic stirring bar, PMIMA **15 (**50 mg, 0.11 mmol), K$_2$CO$_3$ (650 mg, 0.47 mmol) and dimethylamine hydrochloride (**4a**, 20 mg, 0.25 mmol) were suspended in 1 mL DMSO. The suspension was stirred for 2 hours at 60ºC. The mixture was cooled to room temperature. Methanol (1 mL) was added under vigorous stirring and subsequently 20 mL of a 1:1 acetone/petroleum ether mixture was added. The precipitate is filtered off and washed with acetone/petroleum ether. The purple solid was dissolved in ethanol (5 mL) and filtered to remove the remaining K$_2$CO$_3$. The organic solvent was removed from the filtrate by rotary evaporation. This yielded a yellow solid that was dried in a vacuum oven.

Yield: 64 mg, 0.12 mmol, 107.2%. ^{1}H-NMR (δH[ppm], MeOD, 400 MHz): 8.59-8.45 (6H, m), 7.88 (1H, *J=8 Hz*, d), 7.59 (1H, *J=4 Hz*, d), 4.16 (2H, *J=8 Hz*, t), 3.13 (3H, s). 3.10 (3H, s), 1.73 (2H, *J=8 Hz*, quin), 1.47 (2H, *J=8 Hz*, sex), 1.02 (3H, *J=8 Hz*, t). MS (ESI): [M]$^-$ Calculated for C$_{28}$H$_{20}$N$_2$O$_6$, 240.0666; found: 240.0668 [KM]$^-$ Calculated for C$_{30}$H$_{23}$N$_2$O$_5$, 491.1612; found: 491.1598. MP > 350°C.

*N-(butyl)perylene-3,4,9,10-tetracarboxylic acid 3,4-imide 9-dimethylamide 10-butylester **10a***
In a 25 mL round bottom flask equipped with a magnetic stirring bar, PMIMA **15 (**50 mg, 0.11 mmol), DBU (680 mg, 0.45 mmol), 0.47 mmol) and dimethylamine hydrochloride (**4a**, 20 mg, 0.25 mmol) were suspended in 1 mL DMF. The suspension was stirred for 1 hours at 60ºC. 1-Bromobutane (153 mg, 1.12 mmol) was added and the reaction mixture was left to stir for 3 hours at 60ºC. The mixture was cooled to room temperature. Water (10 mL) was added under strong stirring, which caused a precipitation of the crude product. The suspension was transferred to a separation funnel and chloroform (10 mL)

was added. The organic layer was collected, and washed two times with salt solution (10 mL, 2 M NaCl). The organic layer was collected and dried on Na_2SO_4. After filtration, the organic solvent was removed by rotary evaporation, yielding a red solid.

Yield: 53 mg, 0.097 mmol, 77%. ^{1}H-NMR (δH[ppm], CDCl$_3$, 400 MHz): 8.63 (2H, $J=8$ Hz, d), 8.46 (4H, m), 7.95 (1H, $J=8$ Hz, d), 7.63 (1H, $J=8$ Hz, d), 4.35 (2H, $J=8$ Hz, t), 4.22 (2H, $J=8$ Hz, t), 3.18 (3H, s), 3.13 (3H, s), 1.84 (2H, m), 1.75 (2H, m), 1.47 (2H, m), 1.01 (6H, m). ^{13}C-NMR (δC[ppm], CDCl$_3$, 101 MHz): 168.56, 163.38, 163.34, 135.33, 135.14, 132.43, 131.51, 131.01, 130.90, 129.92, 129.22, 127.84, 125.48, 122.68, 122.44, 121.55, 121.31, 121.22, 120.94, 65.74, 40.24, 39.84, 35.12, 30.67, 30.20, 20.44, 19.31, 13.87, 13.85. LC-MS: t = 6.92, m/z calc: 548.23; found: 548.75 [M]. MS (FD): [M]$^+$ Calculated for $C_{34}H_{32}N_2O_5$, 548.2311; found: 548.2326, [M$_2$]$^+$ Calculated for $C_{68}H_{62}N_4O_{10}$, 1096.4622; found: 1096.4767. MP = 153-154°C.

*Perylene-3,4,9,10-tetracarboxylic acid 3-dimethylamide 9,10- dibutylester potassium salt **K12a***
In a 25 mL round bottom flask equipped with a magnetic stirring bar, PMADE **11 (**50 mg, 0.096 mmol), K_2CO_3 (56 mg, 0.4019 mmol) and dimethylamine hydrochloride (**4a**, 17 mg, 0.21 mmol) were suspended in 1 mL DMSO. The suspension was stirred for 2 hours at 60ºC. The mixture was cooled to room temperature. While vigorously stirring, methanol (1 mL) was added. Subsequently, 20 mL of a 1:1 acetone/petroleum ether mixture was added. The resulting yellow precipitate was left to settle and filtered off. The yellow solid was dissolved in ethanol (5 mL) and filtered to remove the remaining K_2CO_3. The organic solvent was removed from the filtrate by rotary evaporation. This yielded a yellow solid that was dried in a vacuum oven.

Yield: 35 mg, 0.063 mmol, 61%. ^{1}H-NMR (δH[ppm], MeOD, 400 MHz): 8.40 (2H, $J=8$ Hz, d), 8.36 (2H, $J=4$ Hz, d), 7.76 (2H, $J=8$ Hz, d), 7.81 (1H, $J=8$ Hz, d), 7.51 (1H, $J=8$ Hz, d), 4.30 (4H, $J=8$ Hz, t), 3.12 (3H, s), 3.08 (3H, s), 1.78 (4H, $J=8$ Hz, quin), 1.52 (4H, $J=8$ Hz, sex), 1.01 (6H, $J=8$ Hz, t). MS: (ESI): [M]$^-$ Calculated for $C_{34}H_{32}NO_7$, 566.2148; found: 566.2165, [KM$_2$]$^-$ Calculated for $C_{68}H_{62}KN_2O_{14}$, 1171.4000; found: 1171.3961. MP > 350°C.

*Synthesis of perylene-3,4,9,10-tetracarboxylic acid-3,4-monoimide-9,10-dibutylesters **13***
In a 25 mL round bottom flask equipped with a magnetic stirring bar, PMADE **11**, (100 mg, 0.19 mmol), DBU (58 mg, 0.38 mmol)) and amine (**4**, 0.38 mmol) are suspended in 2 mL DMF. The reaction mixture was stirred at room temperature for 24 hours. Afterwards the clear solution was poured in a sodium bicarbonate solution (20 mL, 1 M) and left for at least 30 minutes. The resulting suspension was filtered on a paper filter and the solid was washed with water until the filtrate was colorless. The solid was dried in a vacuum oven and the product was dissolved in DCM and subsequently purified using normal phase column chromatography (SiO$_2$/ DCM/MeOH).

*N-(2-ethylhexyl)perylene-3,4,9,10-tetracarboxylic acid 3,4-imide 9,10-dibutylester **13b***
Column chromatography on silica/ 0.5% MeOH in DCM. red waxy solid.
Yield: 66 mg, 0.10 mmol 55%. ^{1}H-NMR (δH[ppm], CDCl$_3$, 400 MHz): 8.41 (2H, d, 8 Hz), 8.20 (2H, d, 4 Hz), 8.17 (2H, d, 4 Hz), 7.97 (2H, $J=8$ Hz, d), 4.36 (4H, $J=8$ Hz, t), 4.11 (2H, m), 1.96 (1H, $J=8$ Hz, sep), 1.82 (4H, $J=8$ Hz, quin), 1.53 (4H, $J=8$ Hz, sex), 1.42-1.32 (8H, m), 1.02 (6H, $J=8$ Hz, t), 0.96 (3H, $J=8$ Hz, t), 0.90 (3H, $J=8$ Hz, t). ^{13}C-

NMR (δC[ppm], CDCl$_3$, 101 MHz): 168.20, 163.78, 135.06, 131.86, 131.78, 131.18, 130.15, 129.04, 128.93, 128.83, 125.67, 122.37, 121.95, 121.60, 77.31, 76.99, 76.67, 65.54, 44.18, 37.97, 30.78, 30.62, 28.71, 24.09, 23.08, 19.25, 14.09, 13.79, 10.64. MS (FD): [M]$^+$ Calculated for C$_{40}$H$_{43}$NO$_6$, 633.3090; found: 633.3073. MP = 178°C.

N-(butyl)perylene-3,4,9,10-tetracarboxylic acid 3,4-imide 9,10-dibutylester **13c**
Column chromatography on silica/ 0.5% MeOH in DCM. red waxy solid.
Yield: 71 mg, 0.12 mmol, 65%. ^{1}H-NMR (δH[ppm], CDCl$_3$, 400 MHz): 8.17 (2H, *J=8 Hz*, d), 7.91 (2H, *J=8 Hz*, d), 7.84 (4H, m), 4.36 (4H, *J=8 Hz*, t), 4.12 (2H, *J=8 Hz*, t), 1.82 (4H, *J=8 Hz*, quin), 1.74 (2H, *J=8 Hz*, quin), 1.52 (6H, m), 1.03 (9H, m). ^{13}C-NMR (δC[ppm], CDCl$_3$, 101 MHz): 168.12, 163.15, 134.61, 131.67, 131.47, 130.73, 129.97, 128.81, 128.47, 128.44, 125.21, 122.14, 121.67, 121.27, 77.33, 77.01, 76.70, 65.56, 40.26, 30.64, 30.17, 20.43, 19.28, 13.86, 13.82. MS (FD): [M]$^+$ Calculated for C$_{38}$H$_{39}$NO$_7$, 577.2464; found: 577.2443. MP = 265°C.

N-(methyl)perylene-3,4,9,10-tetracarboxylic acid 3,4-imide 9,10-dibutylester **13d**
Column chromatography on silica/ 1.0% MeOH in DCM. red waxy solid.
Yield: 77 mg, 0.14 mmol, 75%. ^{1}H-NMR (δH[ppm], CDCl$_3$, 400 MHz): 8.32 (2H, *J=8 Hz*, d), 8.11 (2H, *J=8 Hz*, d), 8.07 (2H, *J=8 Hz*, d), 7.93 (2H, *J=8 Hz*, d), 4.35 (4H, *J=8 Hz*, t), 3.50 (3H, s), 1.81 (4H, *J=8 Hz*, quin), 1.51 (4H, *J=8 Hz*, sex), 1.01 (6H, *J=8 Hz*, t). ^{13}C-NMR (δC[ppm], CDCl$_3$, 101 MHz): 168.15, 163.53, 135.09, 131.83, 131.69, 131.02, 130.13, 128.96, 128.66, 128.63, 125.52, 122.37, 121.63, 121.48, 77.30, 76.99, 76.67, 65.57, 30.61, 26.98, 19.25, 13.79. MS (FD): [M]$^+$ Calculated for C$_{33}$H$_{29}$NO$_6$, 535.1995; found: 535.1983. MP = 263°C.

N-(2-hydroxyethyl)perylene-3,4,9,10-tetracarboxylic acid 3,4-imide 9,10-dibutylester **13e**
Column chromatography on silica/ 0.5 to 2.5% MeOH in DCM. red waxy solid.
Yield: 82 mg, 0.14 mmol, 80%. ^{1}H-NMR (δH[ppm], CDCl$_3$, 400 MHz): 7.92 (2H, *J=8 Hz*, d), 7.69 (2H, *J=8 Hz*, d), 7.59 (2H, *J=8 Hz*, d), 4.36-4.31 (6H, m), 4.03 (2H, *J=4 Hz*, t), 2.89 (br, 1H), 1.84 (4H, *J=8 Hz*, quin), 1.54 (4H, *J=8 Hz*, sex), 1.04 (6H, *J=8 Hz*, t). ^{13}C-NMR (δC[ppm], CDCl$_3$, 101 MHz): 168.00, 163.73, 134.40, 131.68, 130.84, 130.63, 129.84, 128.46, 127.95, 127.95, 124.61, 122.12, 120.99, 120.98, 77.33, 77.01, 76.69, 65.62, 61.27, 42.72, 30.63, 19.28, 13.84. MS (FD): [M]$^+$ Calculated for C$_{34}$H$_{31}$NO$_7$, 565.2101; found: 565.2100. MP = 305°C.

N-(6-hydroxhexyl)perylene-3,4,9,10-tetracarboxylic acid 3,4-imide 9,10-dibutylester **13f**
Column chromatography on silica/ 0.5 to 2% MeOH in DCM. red waxy solid.
Yield: 88 mg, 0.14 mmol, 75%. ^{1}H-NMR (δH[ppm], CDCl$_3$, 400 MHz): 8.09 (2H, *J=8 Hz*, d), 7.84 (2H, *J=8 Hz*, d), 7.80 (2H, *J=8 Hz*, d), 7.75 (2H, *J=8 Hz*, d), 4.36 (4H, *J=8 Hz*, t), 4.08 (2H, *J=8 Hz*, t), 3.86 (2H, *J=8 Hz*, t), 1.83 (6H, m), 1.76 (2H, m), 1.64 (2H, m), 1.52 (6H, m), 1.03 (6H, *J=8 Hz*, t). ^{13}C-NMR (δC[ppm], CDCl$_3$, 101 MHz): 168.11, 163.11, 134.57, 103.66, 129.96, 128.74, 128.37, 128.30, 125.06, 122.17, 121.47, 121.19, 65.58, 62.70, 40.22, 32.56, 30.64, 27.88, 26.64, 25.22, 19.28, 13.83. MS (FD): [M]$^+$ Calculated for C$_{38}$H$_{39}$NO$_7$, 621.2727; found: 621.2703. MP = 195°C.

Perylene-3,4,9,10-tetracarboxylic acid 3-dimethylamide 4,9,10- tributylester **14a**
In a 25 mL round bottom flask equipped with a magnetic stirring bar, PMADE **11 (**100 mg, 0.19 mmol), DBU (117 mg, 0.77 mmol) and dimethylamine hydrochloride (**4a**, 31

mg, 0.38 mmol) were suspended in 2 mL DMF. The suspension was stirred for 1 hours at 60°C. 1-Bromobutane (131 mg, 0.96 mmol) was added and the reaction mixture was left to stir for 18 hours at 60°C. The mixture was cooled to room temperature. Water (40 mL) was added under strong stirring, which caused a precipitation of the crude product. The reaction product was filtered and the obtained solid was washed extensively with water, until almost no colour was observed in the filtrate, yielding a yellow solid that was dried in a vacuum oven.

Yield: 103 mg, 0.17 mmol, 86%. ^{1}H-NMR (δH[ppm], CDCl$_3$, 400 MHz): 8.06 (4H, m), 7.92 (2H, m), 7.90 (1H, *J=8 Hz*, d), 7.75 (1H, *J=8 Hz*, d), 7.42 (1H, d), 4.34 (6H, *J=8 Hz*, t), 3.15 (3H, s), 3.13 (3H, s), 1.87-1.76 (6H, m), 1.57-1.48 (6H, m), 1.05-0.99 (9H, m). ^{13}C-NMR (δC[ppm], CDCl$_3$, 101 MHz): 171.92, 168.90, 168.65, 134.11, 133.22, 133.07, 132.63, 130.92, 130.41, 130.31, 130.00, 129.68, 129.31, 128.89, 128.83, 128.69, 128.43, 127.75, 121.42, 121.33, 120.95, 120.68, 65.49, 65.23, 39.80, 35.08, 30.66, 19.29, 13.80. LC-MS: t = 7.07, m/z calc: 623.29; found: 623.82 [M]. MS (FD): [M]$^+$ Calculated for C$_{38}$H$_{41}$NO$_7$, 623.2883; found: 623.2886. MP = 124-127°C.

N-(2-butyl)perylene-3,4,9,10-tetracarboxylic acid 3,4-imide 9,10-anhydride **15**
Concentrated sulfuric acid (7 mL) was added to a 50 mL round bottom flask, closed off with a drying tube charged with calcium chloride. **13c** (298 mg, 0.517 mmol) was then dissolved by stirring at room temperature for a few minutes. The mixture was left to stir at room temperature overnight. The strongly acidic mixture was slowly poured on ice. After the ice melted, the obtained suspension was filtered and dried by air and further dried in a vacuum oven. This yielded a red solid.

Yield: 215 mg, 93%. ^{1}H-NMR (δH[ppm], CDCl$_3$, 400 MHz): 8.81 (8H, m), 4.26 (2H, *J=8 Hz*, t), 1.76 (2H, *J=8 Hz*, quin), 1.49 (2H, *J=8 Hz*, sex), 1.00 (3H, *J=8 Hz*, t).

2.6 Supporting information
2.6.1. Kinetic Measurements
Analysis of the absorption spectra was performed using MS Excel. For the simple reactions (from **12c** to **13c** or **9c** to **7c**), the first spectrum (obtained at t=0) was assumed to be from the starting compound (amic acid) and the last spectrum (obtained at t= 24h) was from the product (imide). Cleanup of the spectrum of the starting compound may be required, because the startingcompound already contains small amounts of the reaction product. This cleanup generallycomes down to subtracting a fraction of the product spectrum from the starting compound spectrum. The spectra of the reaction mixtures were simulated by a linear combination of the spectra from the starting compound and the reaction product:

Spectrum reaction mixture= x*Spectrum starting compound+(1-x)* Spectrum product

$0 \leq x \leq 1$

The best fit was obtained when the simulated spectra, calculated according to the formula above, were identical to the experimental spectra. This was visualized by subtracting the simulated spectrum from that of the reaction mixture. A flat base line should result and if need be this process is automated by requiring the choice of x such that the sum of all absorption data points is minimized.

For the more complex reaction from diamic acid **5c** to diimide **7c** via the intermediate **9c**, finding the composition of the reaction mixture was less accurate. Here we assume that the first spectrum (obtained at t=0) was from the starting compound (diamic acid **5c**) and the last spectrum (obtained at t= 24h) was from the product (diimide **7c**). The spectrum from the reaction intermediate **9c** was unknown, but is expected to resemble that of compound **9a**. Cleanup of the spectrum of the starting compound may be required, because the starting compound already contains a little of the intermediate product **9c**. This cleanup generally comes down to flattening the spectrum of compound **5c** above 520 nm.

Simulated reaction mixture= x*Spectrum **5c**+ y*Spectrum **9c** +(1-(x+y))* **7c**

$0 \leq (x+y) \leq 1$

Since the spectrum of **9c** is unknown, various values of x and 1-(x+y) are tested. By subtracting
x*5c+ (1-(x+y))*7c from the spectrum of the reaction mixture, the spectrum of y*9c is obtained. Doing this in such a manner that the spectrum of **9c** is consistent in shape and resembling that of **9a**, resulted in values of x and y for the different reaction times and thereby the molecular composition. This process is more complex, less accurate (in independently finding x and y) and cannot be automated easily.

2.6.2. Kinetic modelling
In the first part of the reaction from PDA **1** to the diamic acid **5**, all steps are second order reactions, as described by Equations S1-3.

$$\frac{d[\mathbf{1}]}{dt} = -2k_1[\mathbf{1}][\mathbf{4}] \approx -k[\mathbf{4}]; \quad k << k_1[\mathbf{1}] \qquad eq\ S1$$

$$\frac{d[\mathbf{8}]}{dt} = k[\mathbf{4}] - k_1'[\mathbf{8}][\mathbf{4}] \qquad eq\ S2$$

$$\frac{d[\mathbf{5}]}{dt} = k_1'[\mathbf{8}][\mathbf{4}] \qquad eq\ S3$$

Because PDA **1** is insoluble (in DMF or DMSO), the conversion to compound **8** is not a second order reaction but a heterogeneous reaction. This reaction is best described as a pseudo-first order reaction, whose rate scales with the concentration of amine **4**. The apparent rate constant for this reaction k is much smaller than $k_1[\mathbf{1}]$. Equations S1 and S3 describe the consumption of PDA **1** and the formation of diamic acid **5**. For setting up Eqs S4-S8, we have made the assumption that compound **8**, to some extent, is soluble in the reaction mixture and will be consumed by a fast second-order reaction. This reaction consumes a second molecule of amine **4** , which results in the relation between [**1**] and [**4**] formulated in Equation S4.

$$[\mathbf{4}] = 2[\mathbf{1}]_0 + 2[\mathbf{1}]) \qquad\qquad eq\ S4$$

$$\frac{d[\mathbf{1}]}{dt} = -k(2[\mathbf{1}]_0 + 2[\mathbf{1}]) \qquad\qquad eq\ S5$$

$$[\mathbf{1}] = 2[\mathbf{1}]_0 \exp^{-2kt} - [\mathbf{1}]_0 \qquad\qquad eq\ S6$$

$$\frac{d[\mathbf{8}]}{dt} = k[\mathbf{4}] - k_1'[\mathbf{8}][\mathbf{4}] \approx o \qquad\qquad eq\ S7$$

$$[\mathbf{5}] = 2[\mathbf{1}]_0 - 2[\mathbf{1}]_0 \exp^{-2kt} \qquad\qquad eq\ S8$$

The rates of consumption of compound **1** and the rate of formation of compound **5** according to Equations S6 and S8, are depicted in Figure S11. Experimental data concerning the formation of **5c** and **5e** are obtained from UV experiments are depicted in Figures S4b and S8b, respectively. These experimental data, which demonstrate that formation of amic acid **5** is completed in 15-20 minutes, are crude due to non-reproducible sampling from a heterogeneous reaction mixture and do not correlate well with the prediction from our model.

The imide forming reactions from **9** to **7** and **12** to **13** are first-order reactions. The reaction rate constants for these reactions should be very similar and equal k_2 and k'_2 from the reactions that forms PDI **7** from amic acid **5**. The formation of compounds **7** and **13** and the consumption of compounds **9** and **12** are described by simple exponential functions, as illustrated for the latter reaction in Eqs. S9-S12.

$$\frac{d[\mathbf{9}]}{dt} = -k_2[\mathbf{9}] \qquad\qquad eq\ S9$$

$$\frac{d[\mathbf{7}]}{dt} = k_2[\mathbf{7}] \qquad\qquad eq\ S10$$

$$[\mathbf{9}] = [\mathbf{9}]_0 \exp^{-k_2 t} \qquad\qquad eq\ S11$$

$$[\mathbf{7}] = [\mathbf{9}]_0 (1 - \exp^{-k_2 t}) \qquad\qquad eq\ S12$$

$$\frac{d[\mathbf{12}]}{dt} = -k_2[\mathbf{12}] \qquad\qquad eq\ S9$$

$$\frac{d[\mathbf{13}]}{dt} = k_2[\mathbf{13}] \qquad\qquad eq\ S13$$

$$[\mathbf{12}] = [\mathbf{12}]_0 \exp^{-k_2 t} \qquad\qquad eq\ S14$$

$$[\mathbf{13}] = [\mathbf{12}]_0 (1 - \exp^{-k_2 t}) \qquad\qquad eq\ S15$$

2.6.3. Graphs and Figures
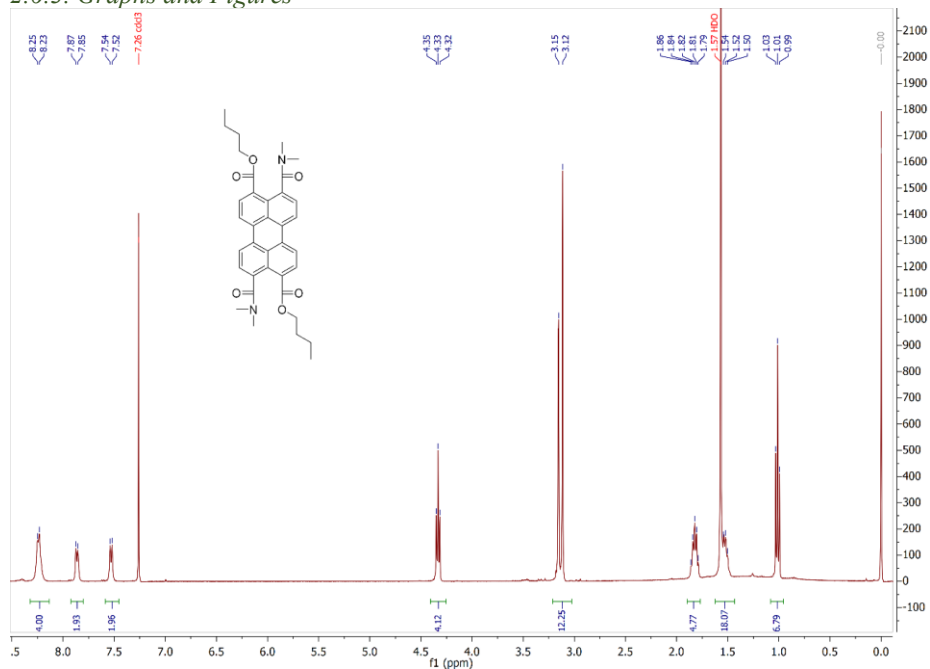
Figure S1. ^1H Spectrum of compound **6a**.
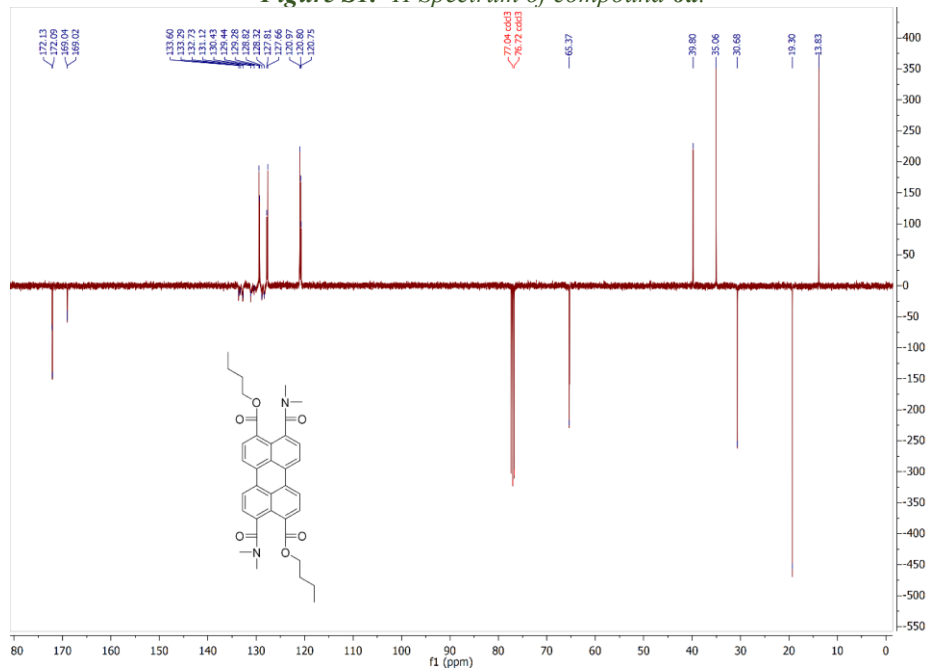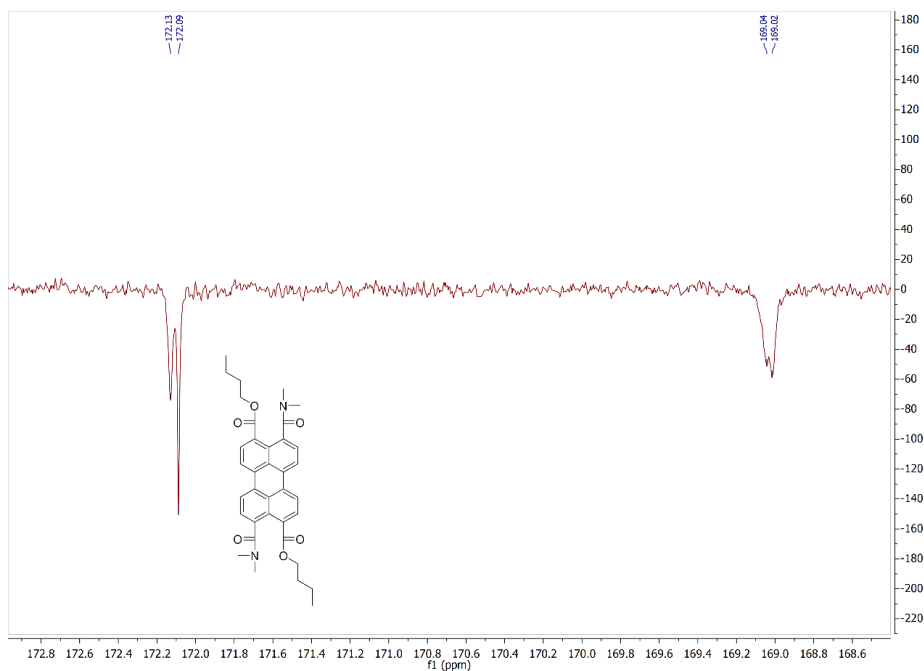
Figure S2*. ^{13}C Spectrum of compound **6a**.*
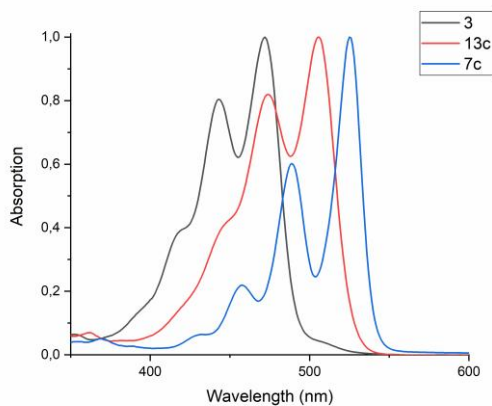
Figure S3. *Normalized absorption spectra of compounds **3**, **13c** and **7c** in Chloroform. All compounds are molecularly dissolved and these spectra are representative for PTEs PMIDEs (and corresponding amic esters and amic acids) and PDIs.*
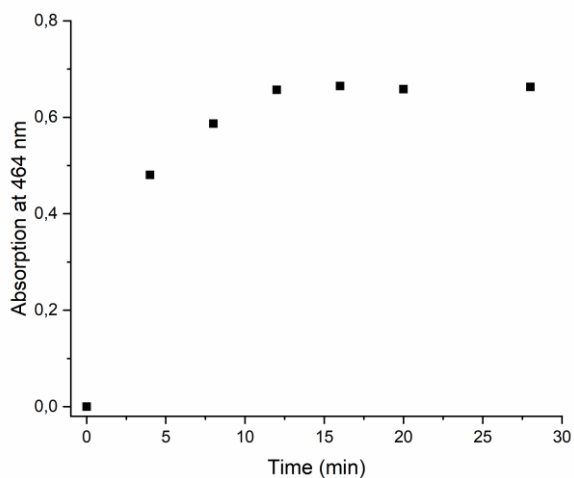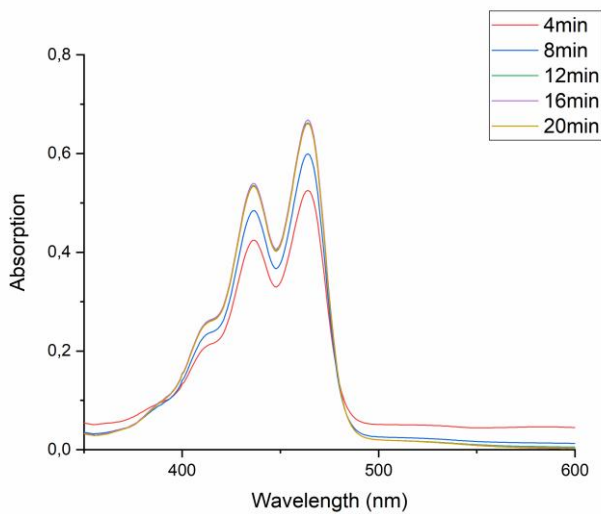
Figure S4*.a: Absorption spectra taken by adding a fixed volume of the reaction of PDA with amine **4c** (Solvent DMF, base DBU, room temperature) in water at regular intervals. The compound that is visible is compound **5c**. The baseline is shifted, in particular at short reaction times, due to the presence of insoluble PDA. b: Absorption at 464 nm, corrected for the shifted baseline, as a function of time.*
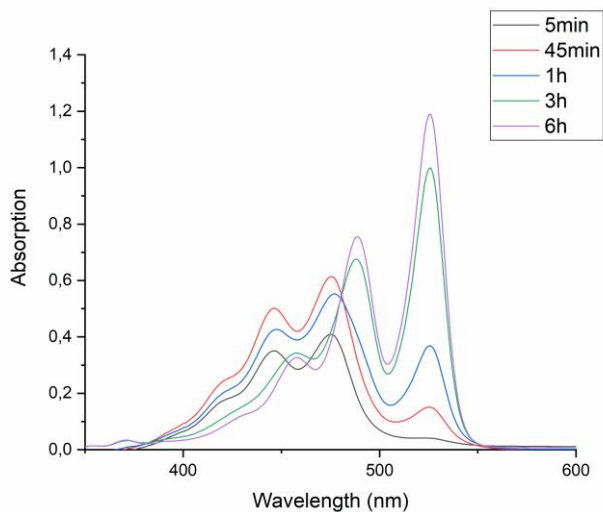
Figure S5*. Absorption spectra taken by adding a fixed volume of the reaction of PDA with amine **4c** (solvent DMF, base DBU, temperature 60ºC) in chloroform at regular intervals. The compounds that are visible are the DBU salt of **5c**, **(HDBU)₂5c** (446 and 475 nm) and **7c** (489 and 526 nm).*
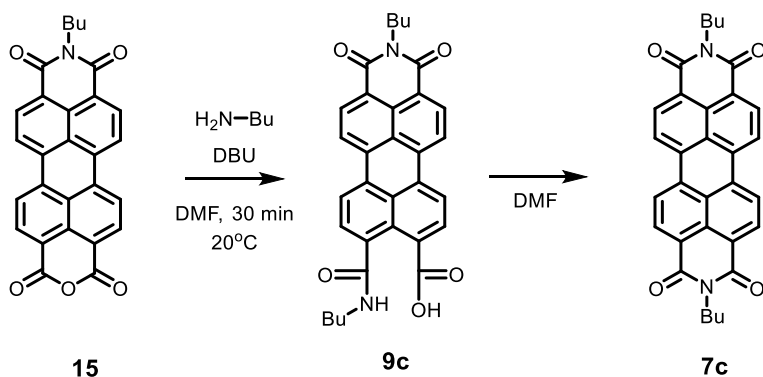
Scheme S1. *Imidization of compound **15** using butylamine **4c** via amic acid **9c**. The last step of this reaction has been monitored using absorption spectroscopy.*
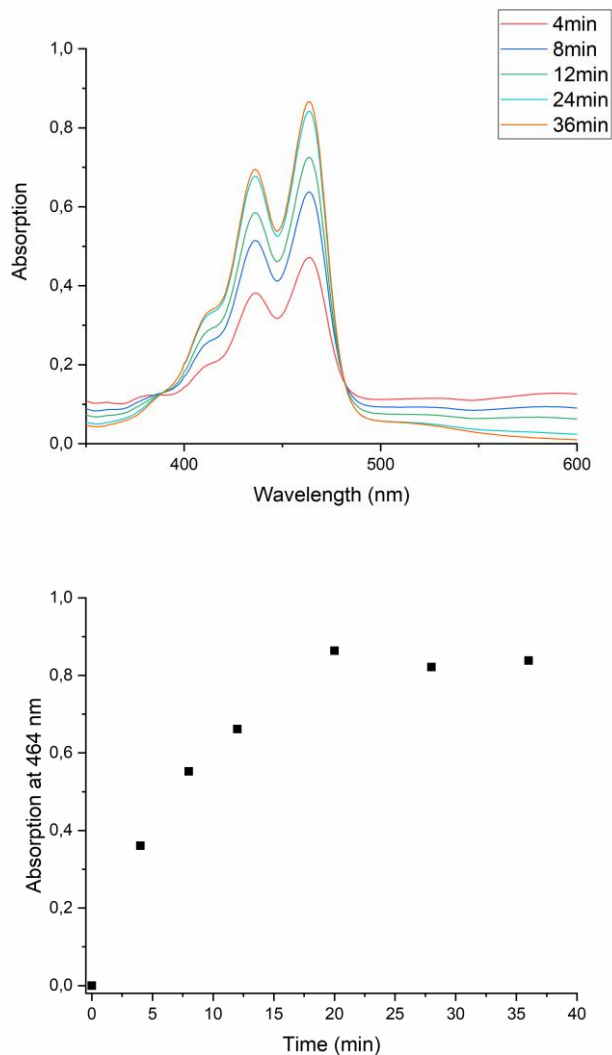
Figure S6*. a: Absorption spectra taken by adding a fixed volume of the reaction of PDA with amine 4e (Solvent DMSO, base K2CO3, room temperature) in water at regular intervals. The compound that is visible is compound 5e. The baseline is shifted due to the presence of insoluble PDA. b: Absorption at 464 nm, corrected for the shifted baseline, as a function of time.*
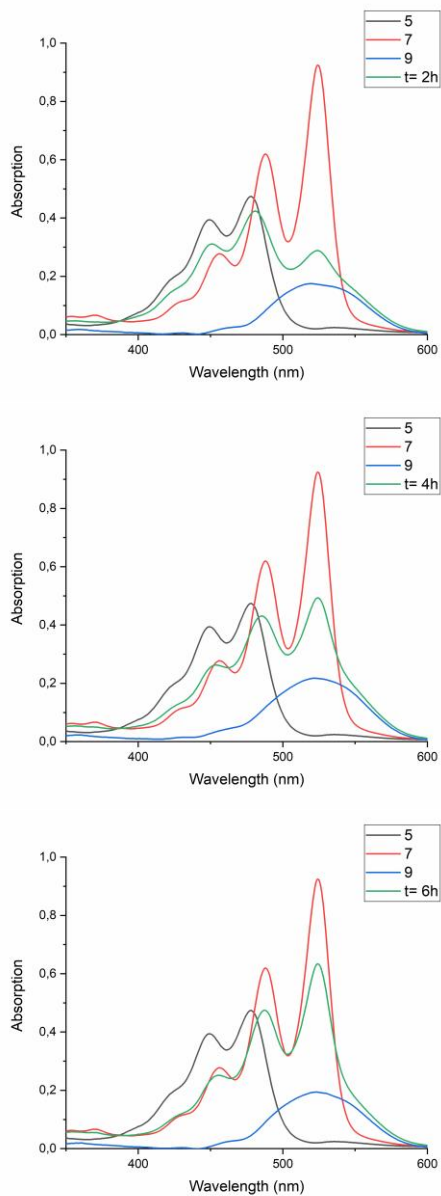
Figure S7*. Spectra taken from the imidization of the DBU salt of **5c** in DMF taken 2, 4 and 6 hours, after diluting the reaction mixture (in green). The spectra of starting compound, the DBU salt of **5c** (black) and final product **7c** (red) are depicted as well. After subtracting the contributions of starting compound, the DBU salt of **5c**, and product **7c** from that of the reaction mixture, the broad, the contributions of the intermediate, the DBU salt of **9c**, are revealed (blue). In this manner the composition of the reaction mixture is determined.*
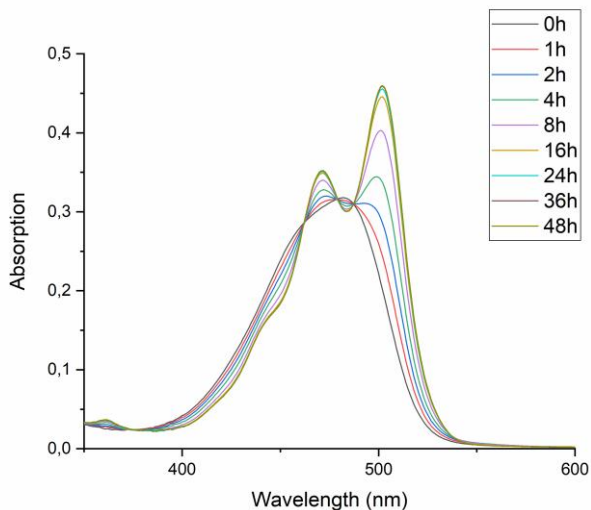
Figure S8. *Absorption spectra as a function of time of the reaction of the DBU salt of amic acid 12c in DMF at concentrations around 1*10-5 M. Isosbestic points are observed at 462, 479 and 487 nm.*
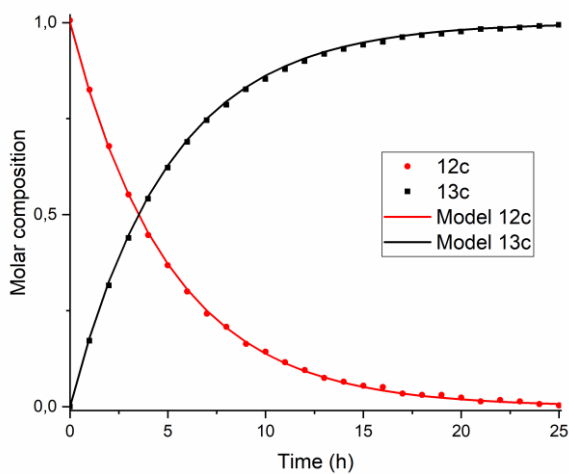
Figure S9. *Composition of the reaction mixture obtained from the data displayed in Figure S9. Solid lines represent the theoretical fitting curves obtained using a first-order decay obtained using equations S14 and S15.*
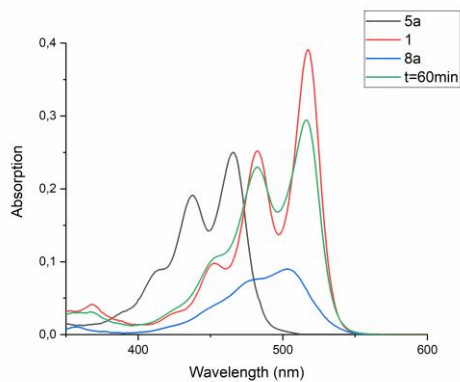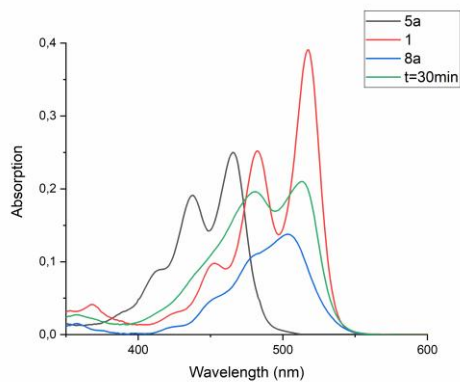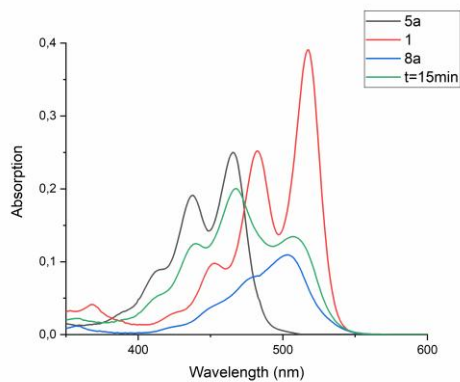
*Figure S10. Spectrum taken from the acid hydrolysis of compound **5a** in DMF after 15, 30 and 60 minutes of reaction (blue). The spectra of starting compound **5a** (black) and final product **1** (red) are depicted as well. are after subtracting the contributions of starting compound **5a** and product **1** from the absorption spectra of the reaction mixture (green), the contributions of the intermediate **8a** are revealed (blue).*
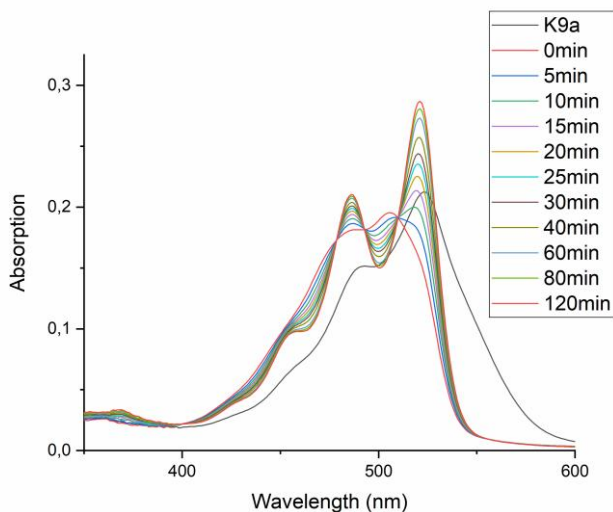
Figure S11*. Absorption spectra of compound **K9a** (black) in DMF and **9a** (red), formed after acidification with 1 drop 1N HCl. In the time-dependent absorption spectra the reaction from **9a** (λ_{max}= 506 nm) to compound **15** (λ_{max}= 521 and 486 nm) is visible. Please note that the first spectrum after acidification already contains (traces of) compound **15**. Isosbestic points are observed at 479, 493 and 510 nm.*
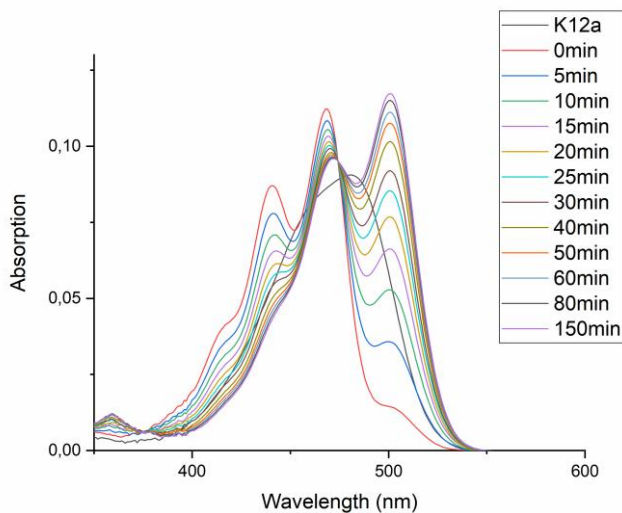
Figure S12*. Absorption spectra of compound K12a (black) in DMF and 12a (red), formed after acidification with 1 drop 1N HCl. In the time-dependent absorption spectra the reaction from 12a (λmax= 468 and 441 nm) to compound 11 (λmax= 472 and 501 nm) is visible. Please note that the first spectrum after acidification already contains (traces of) compound 11. An isosbestic points is observed at 475 nm.*

2.6.4. Synthesis
Table S1

Entry	Perylene anhydride	Amine	Base	Solvent	Reaction conditions	Yield, in % (conversion)
S1	PDA (**1**) 0.5 mmol	**4b** 2 mmol	DBU 2 mmol	DMF 4 ml	168h RT	**7b** 87%
S2	PDA (**1**) 0.5 mmol	**4b** 2 mmol	Zn(Ac)$_2$, 0.6 mmol DBU, 2 mmol	DMF 4 ml	24h RT	**7b** 52%
S3	PDA (**1**) 0.5 mmol	**4b** 2 mmol	Zn(Ac)$_2$, 0.6 mmol DBU, 2 mmol	DMF 4 ml	24h 60˚C	**7b** 78%
S4	PDA (**1**) 0.5 mmol	**4b** 2 mmol	TEA 2 mmol	DMSO 4 ml	24h 60˚C	**7b** 20%
S5	PDA (**1**) 0.5 mmol	**4b** 2 mmol	K$_2$CO$_3$ 2 mmol	DMSO 4 ml	24h 60˚C	**7b** 32%
S6	PDA (**1**) 0.5 mmol	**4c** 2 mmol	DBU 2 mmol	DMSO 4 ml	24h RT	**7c** 52%
S7	PDA (**1**) 0.5 mmol	**4d** 2 mmol	DBU 4 mmol	DMF 4 ml	24h 60˚C	**7d** 89%
S8	PDA (**1**) 0.5 mmol	**4f** 2 mmol	DBU 2 mmol	DMF 4 ml	24h RT	**7f** 66%
S9	PDA (**1**) 0.5 mmol	**4f** 2 mmol	DBU 2 mmol	DMF 4 ml	24h 60˚C	**7f** >97%
S10	PDA (**1**) 0.5 mmol	**4f** 2 mmol	K$_2$CO$_3$ 2 mmol	DMSO 4 ml	24h 100˚C	**7f** >97%
S11	PDA (**1**) 0.5 mmol	**4c** 2 mmol	DBU 2 mmol	DMSO 4 ml water 4 ml	24h 60˚C	**7c** 75%

2.6.5. UV-VIS absorption and fluorescence spectra
Table S2. Spectral data of amic acids, amic acid salts and amic esters

Compound	Solvent	λ_{abs}	λ_{em}	ϕ_F
3	EtOH	468, 440	485, 515	0.86
K$_2$5a	DMF	475, 443	487	0.16
K$_2$5a	EtOH	466, 438	477.5, 509	0.93
K$_2$5a	Water[a]	463, 435	475, 505	1.0
6a	CHL	466, 438	482, 511.5	0.88
6a	EtOH	463, 435	479, 507	0.85
K9a	DMF	521	581	0.14
K9a	EtOH	513	584	0.65
K9a	Water[b]	505	591	0.19
10a	CHL	507, 477,5	530, 566	0.73
10a	EtOH	501, 472	542	0.66
K12a	DMF	481	522	0.19
K12a	EtOH	472, 447	522	0.96
K12a	Water[b]	468, 444	524	~0.6[c]
14a	CHL	470, 441.5	487, 517	0.92
14a	EtOH	466, 438	484, 512	0.87

a: 0.1 M K$_2$CO$_3$ b: 0.01 M K$_2$CO$_3$ c: inaccurate due to low solubility
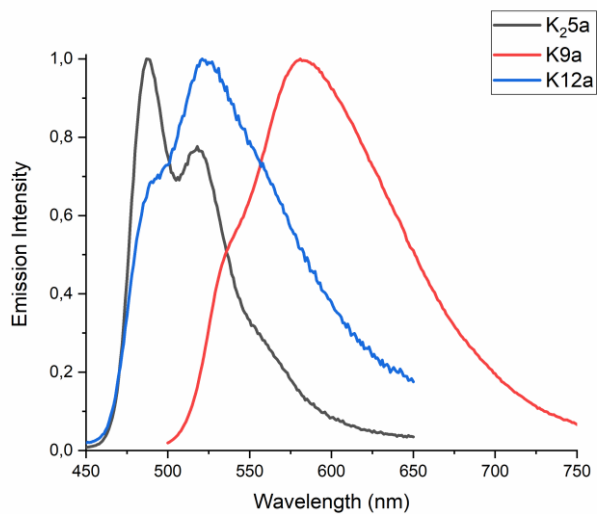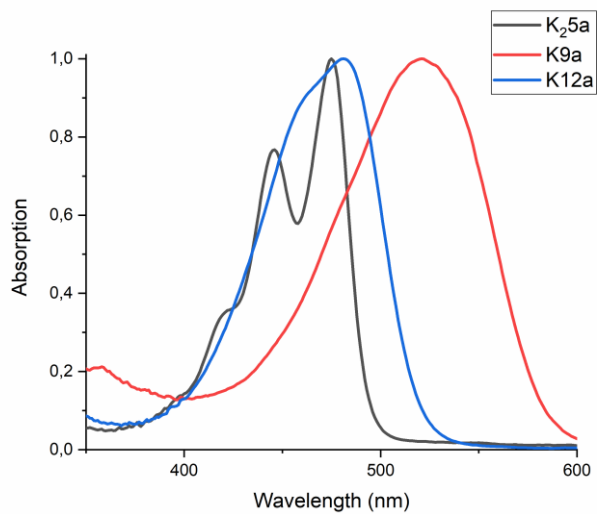
Figure S13. *a) Normalized UV-Vis absorption and b) normalized fluorescence emission spectra of the amic acid salts **$K_2$5a**, **K9a** and **K12a** in DMF.*
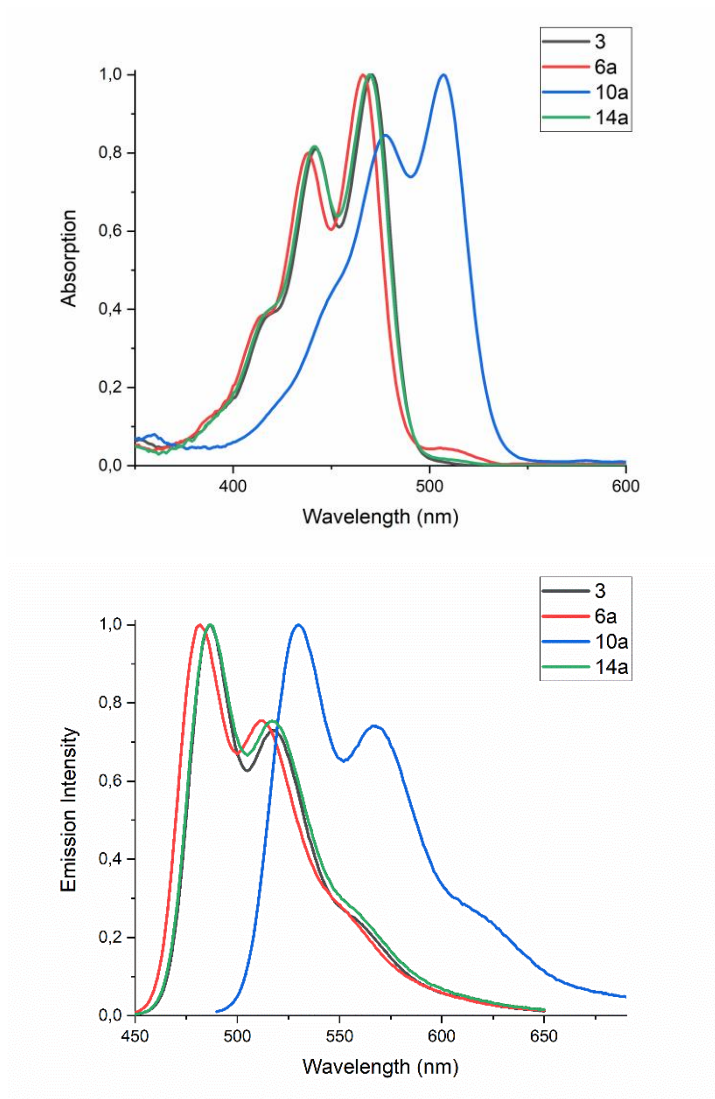
Figure S14. *a) Normalized UV-Vis absorption and b) normalized fluorescence emission spectra of amic esters **6a**, **10a** and **14a** along with PTE **3** in chloroform.*
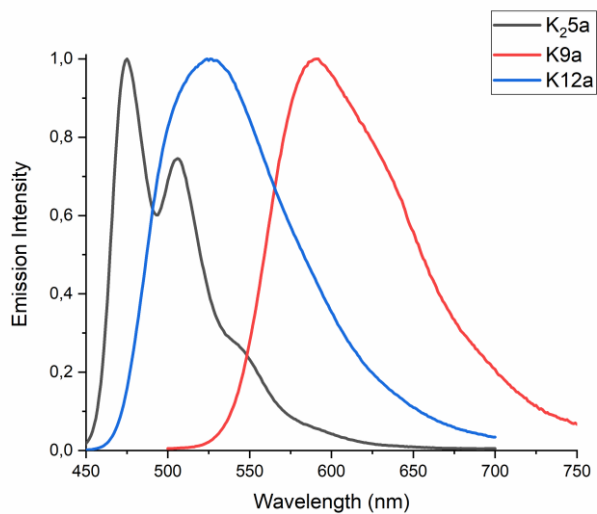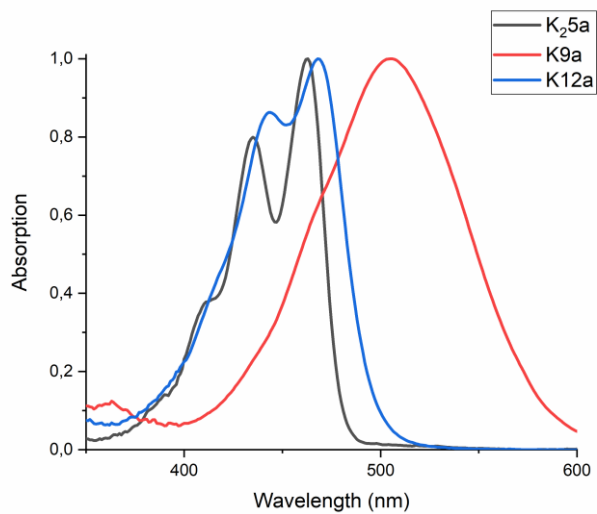
Figure S15. *a) Normalized UV-Vis absorption and b) normalized fluorescence emission spectra of the amic acid salts **K₂5a**, **K9a** and **K12a** in water.*

2.6.6. NMR
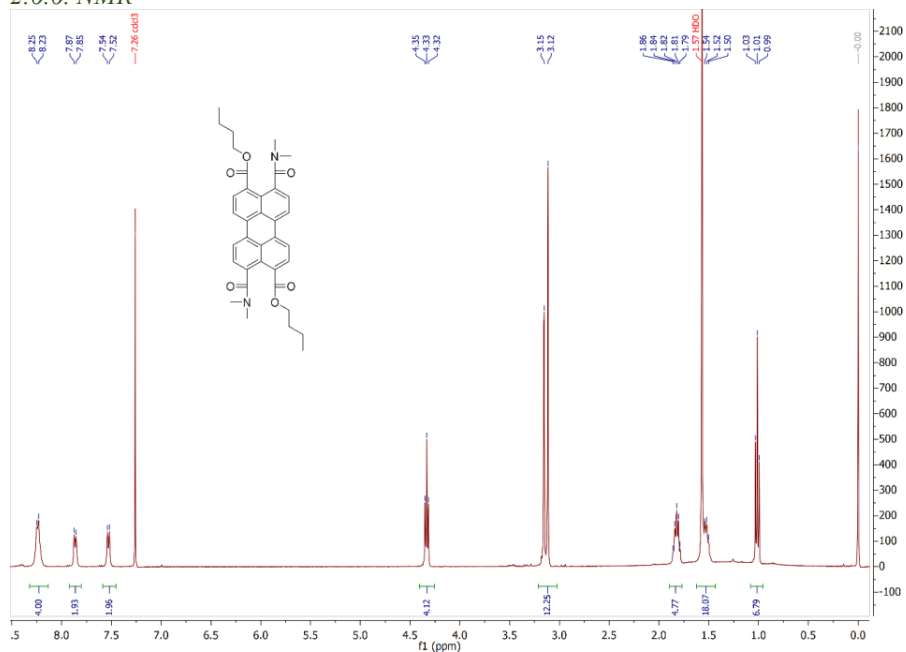
Figure S16. ^1H NMR spectrum of **6a** in CDCl$_3$.
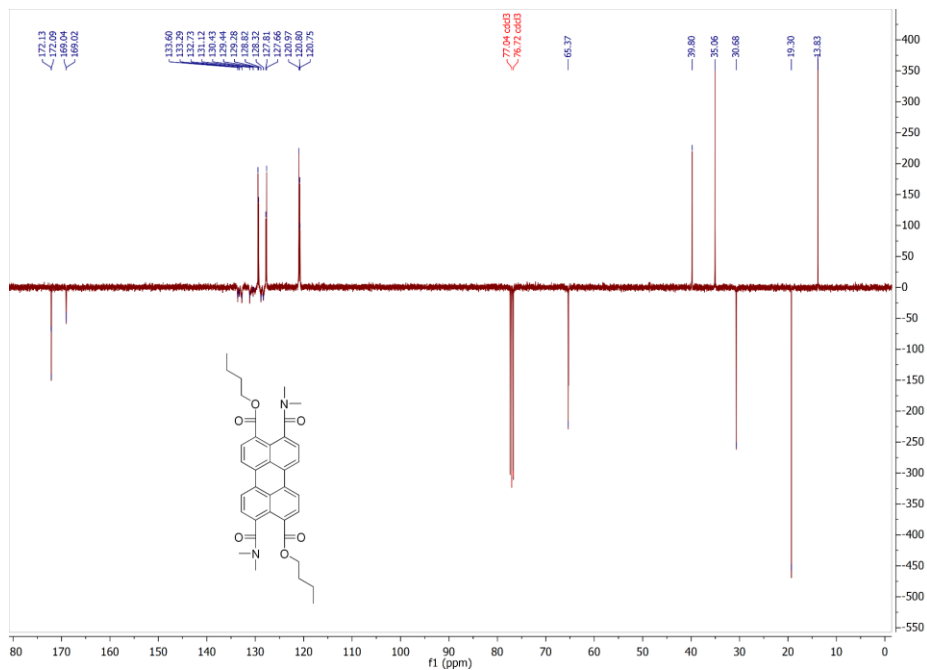
Figure S17. ^{13}C- NMR spectrum of **6a** in CDCl$_3$.

Figure S18. *^1H NMR spectrum of **7b** in CDCl₃.*

Figure S19. *^{13}C- NMR spectrum of **7b** in CDCl₃.*
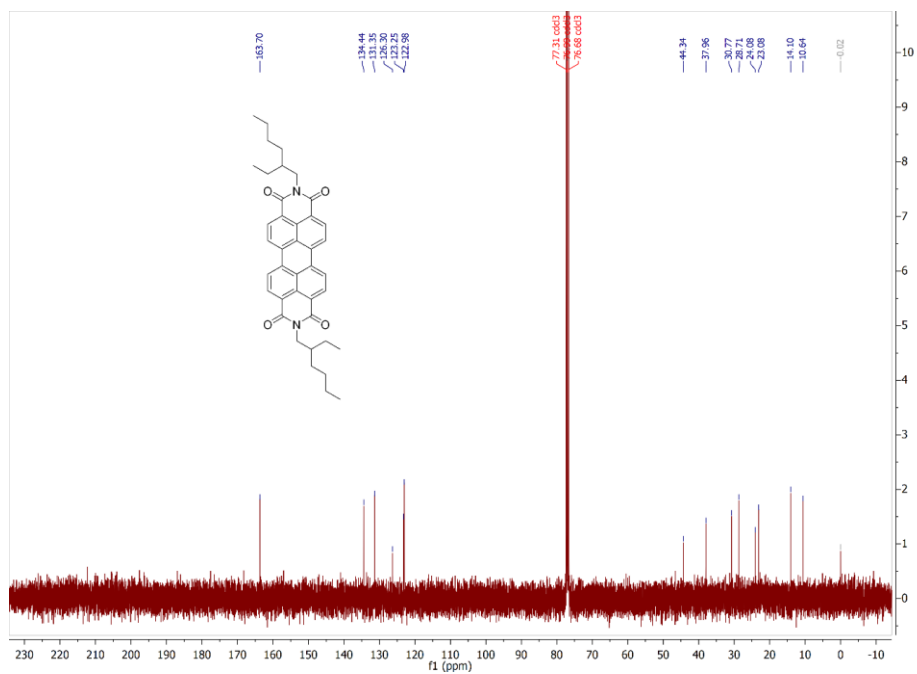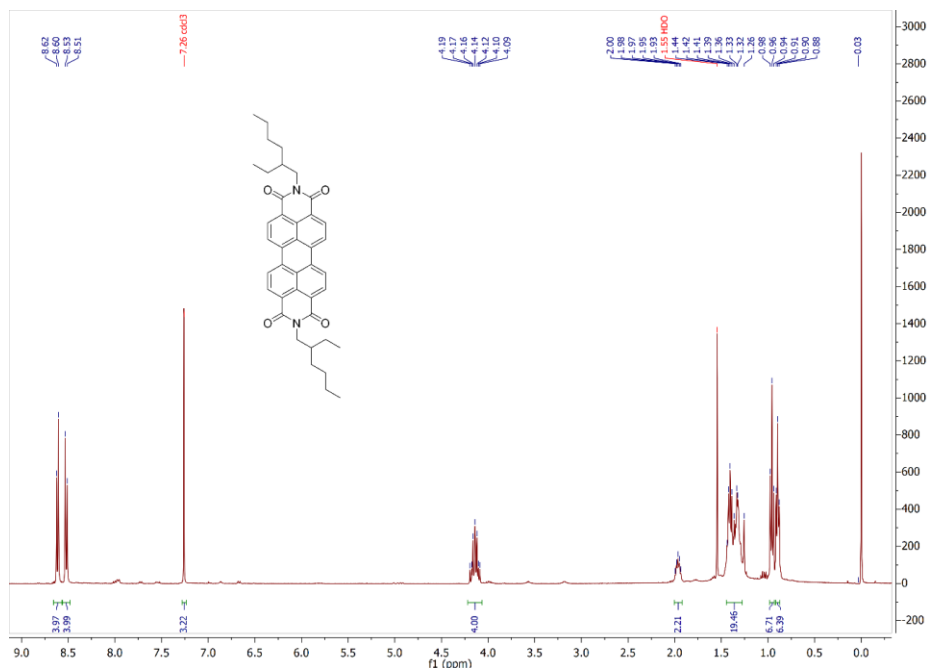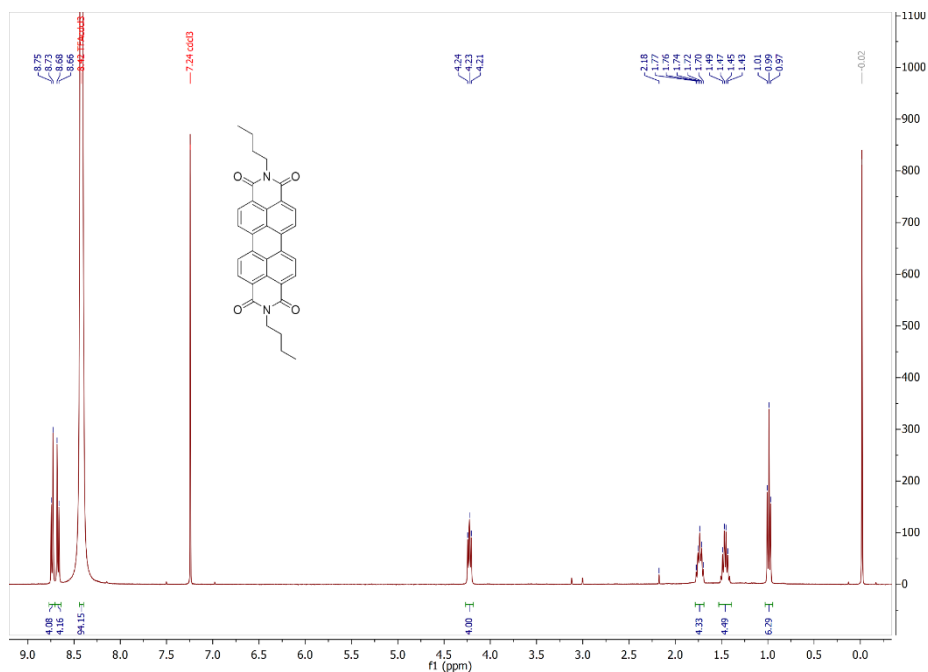
Figure S20. *^{1}H NMR spectrum of **7c** in CDCl$_3$ (with 1 drop of TFA).*
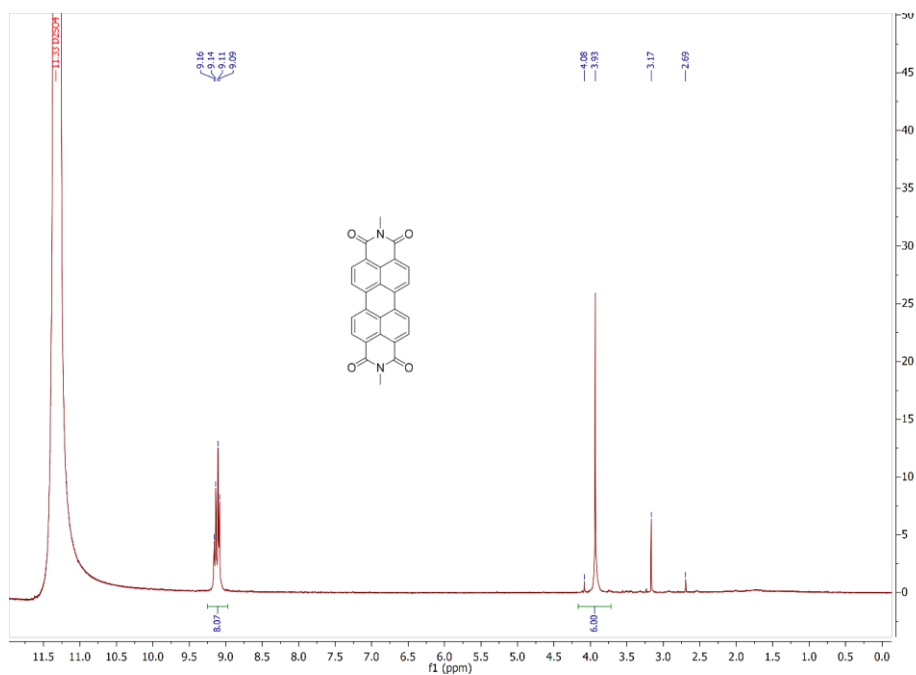
Figure S21. *^{1}H NMR spectrum of **7d** in D$_2$SO$_4$.*
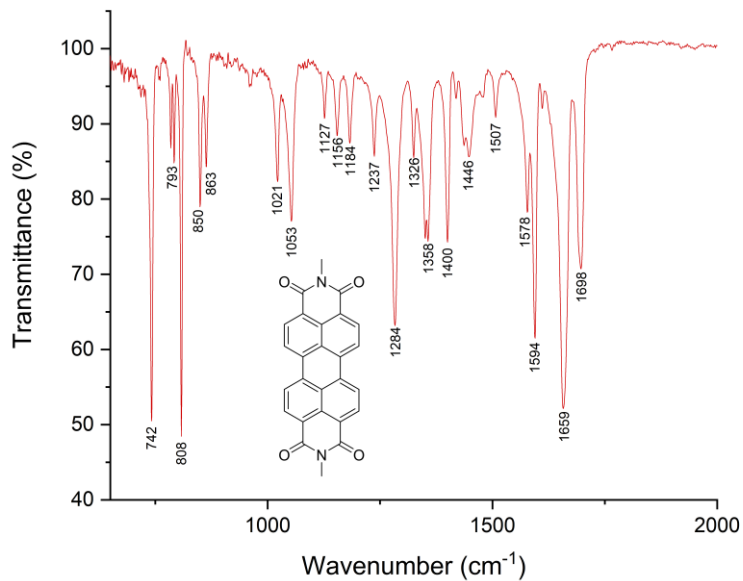
Figure S22. *FTIR spectrum of **7d**.*
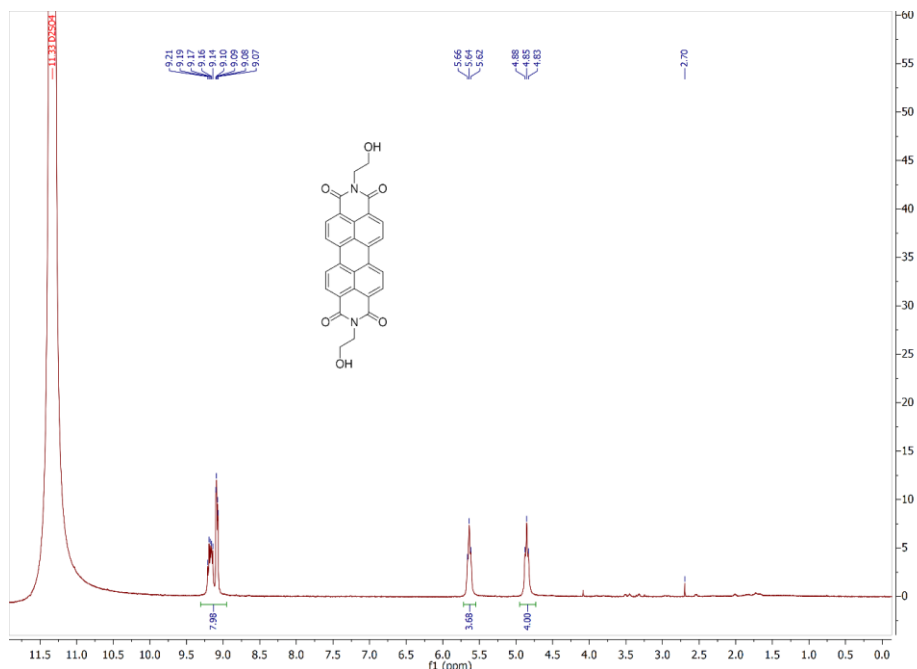
Figure S23. *¹H NMR spectrum of **7e** in D₂SO₄. The splitting pattern of the aromatic protons suggests aggregation.*

Figure S24. *¹H NMR spectrum of **7f** in CDCl₃ (with 1 drop of TFA).*

Figure S25. *¹H NMR spectrum of **9a** in MeOD. NMR contains methanol and water from the solvent, DMSO, and traces of compound **5a**.*
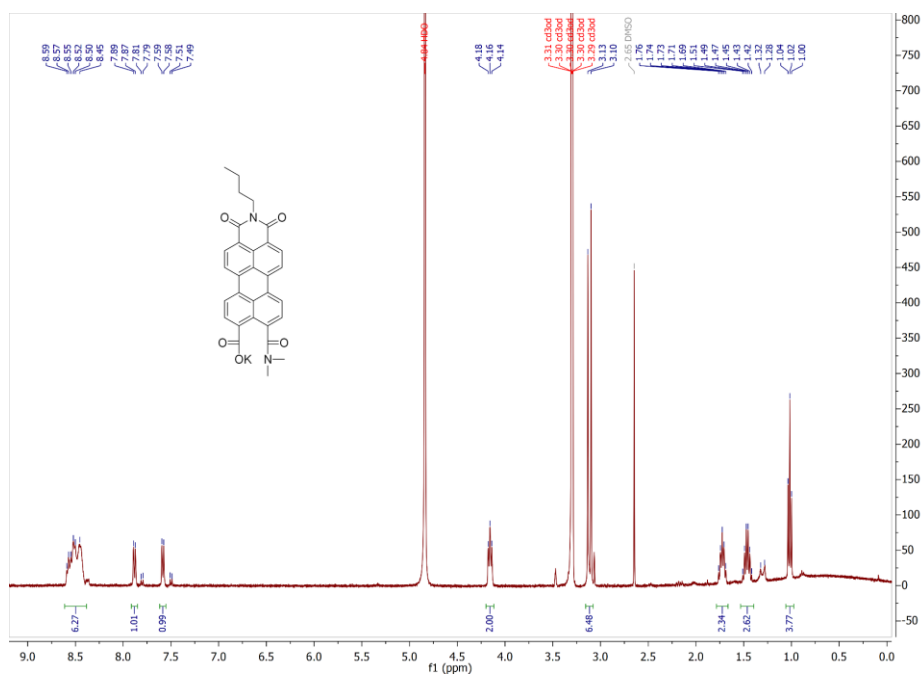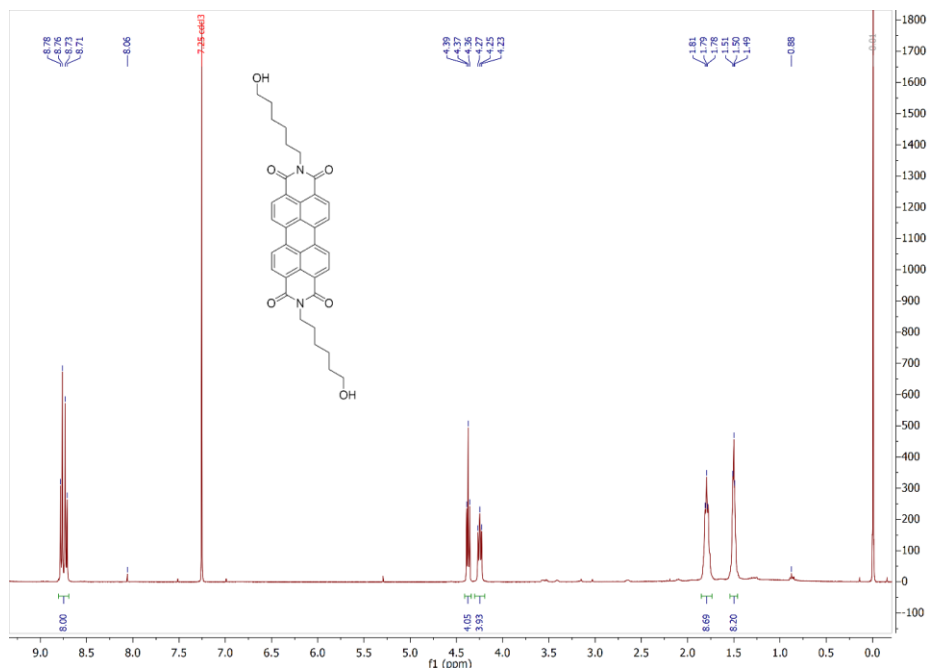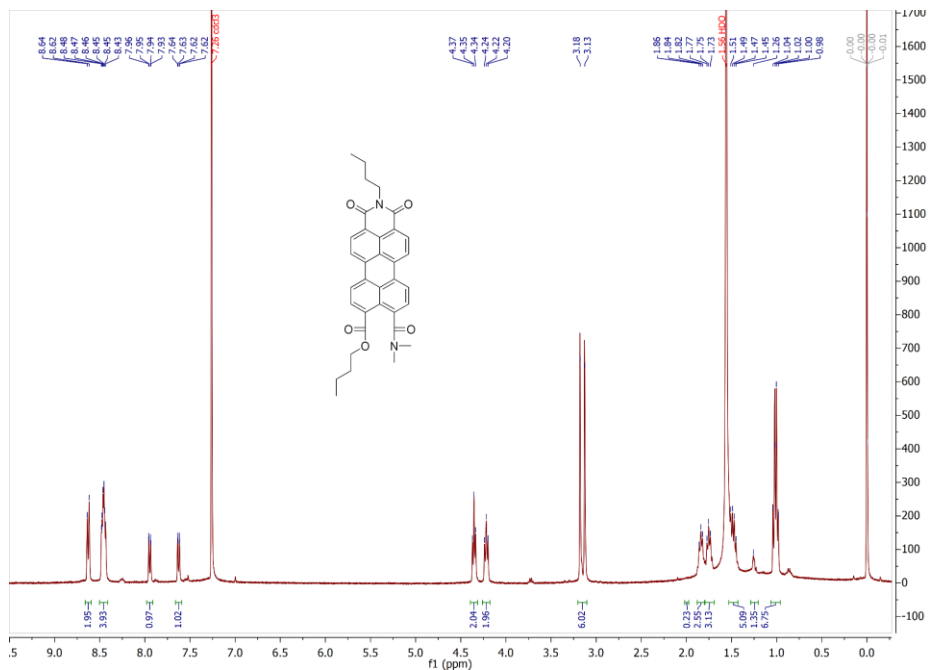
Figure S26. *¹H NMR spectrum of **10a** in CDCl₃.*
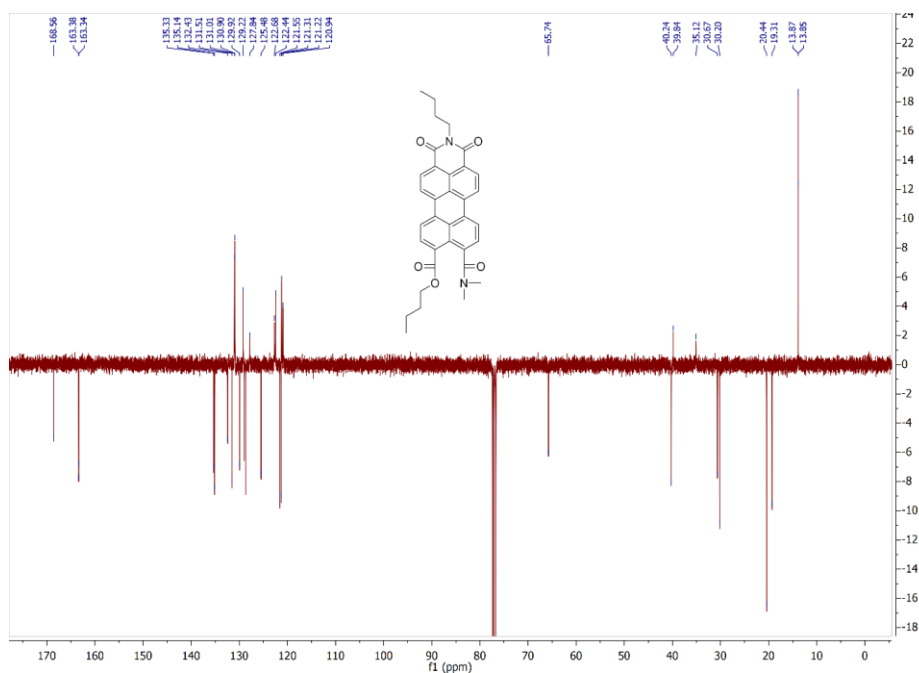
Figure S27. *¹³C- NMR spectrum of **10a** in CDCl₃.*
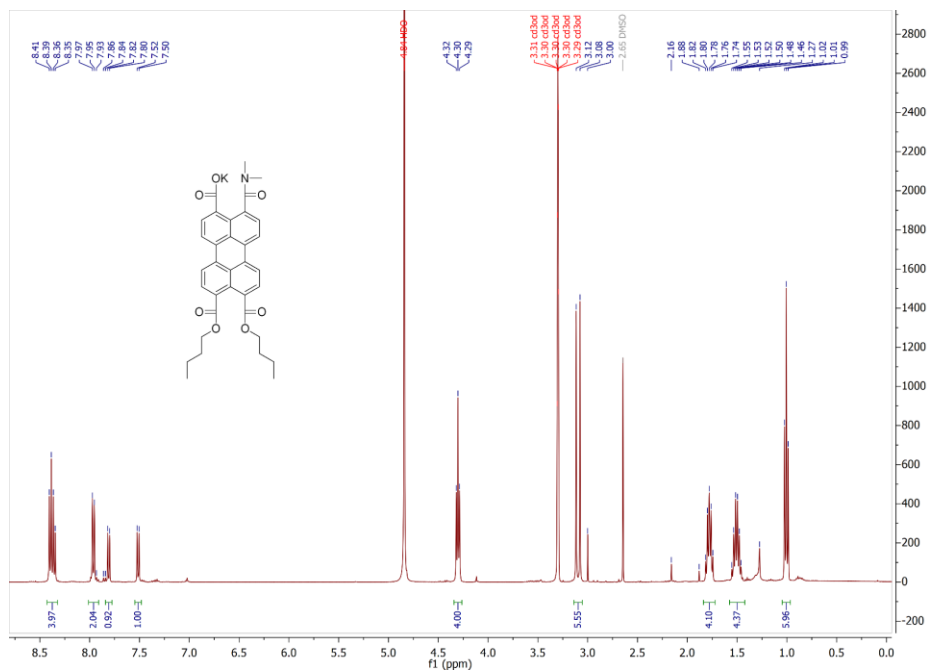
Figure S28. *¹H NMR spectrum of **K12a** in MeOD.*
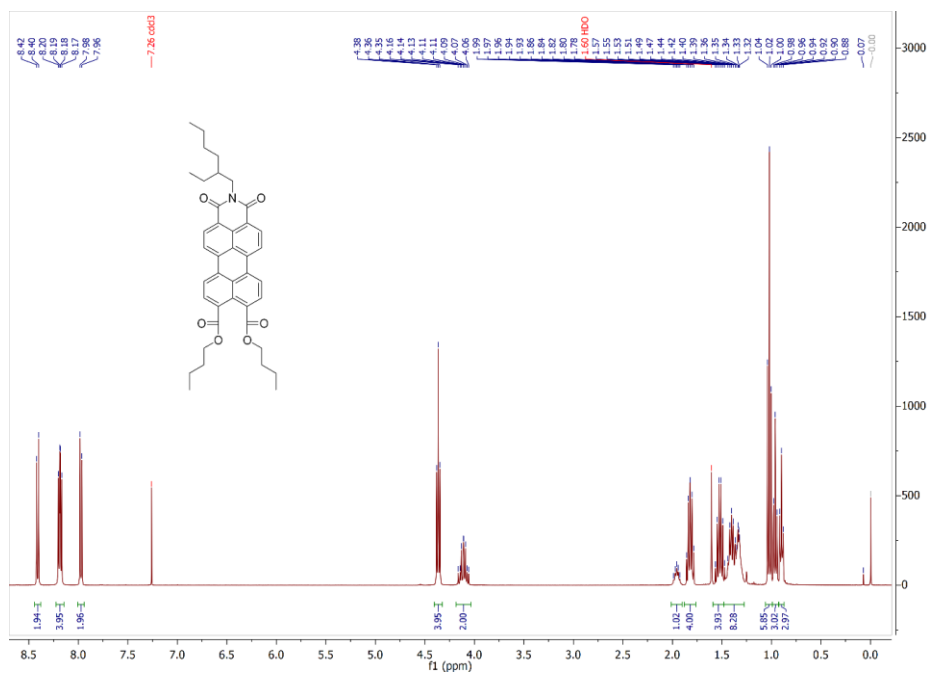
Figure S29. *¹H NMR spectrum of **13b** in CDCl₃.*
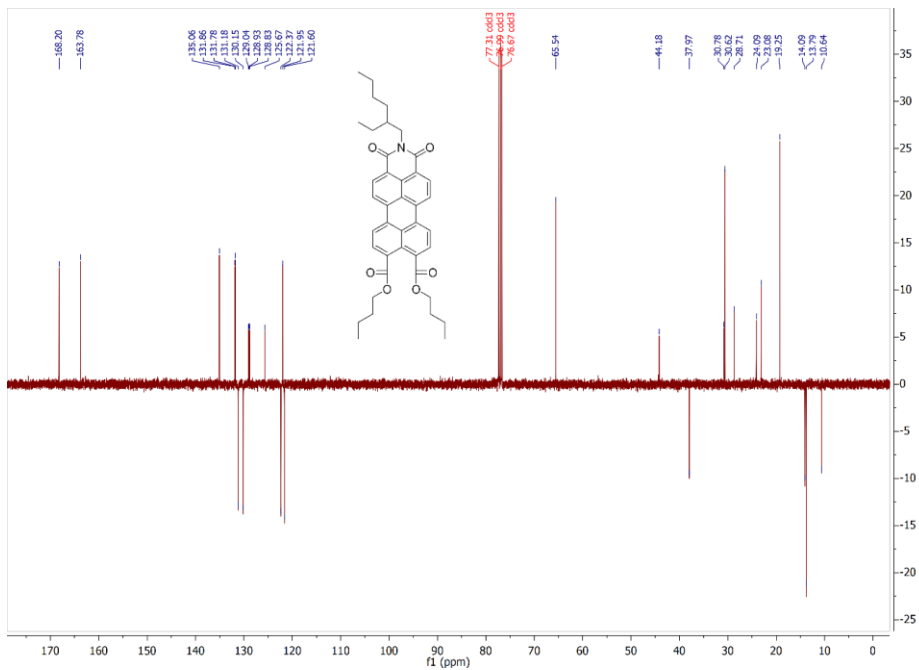
Figure S30. *¹³C- NMR spectrum of **13b** in CDCl₃.*
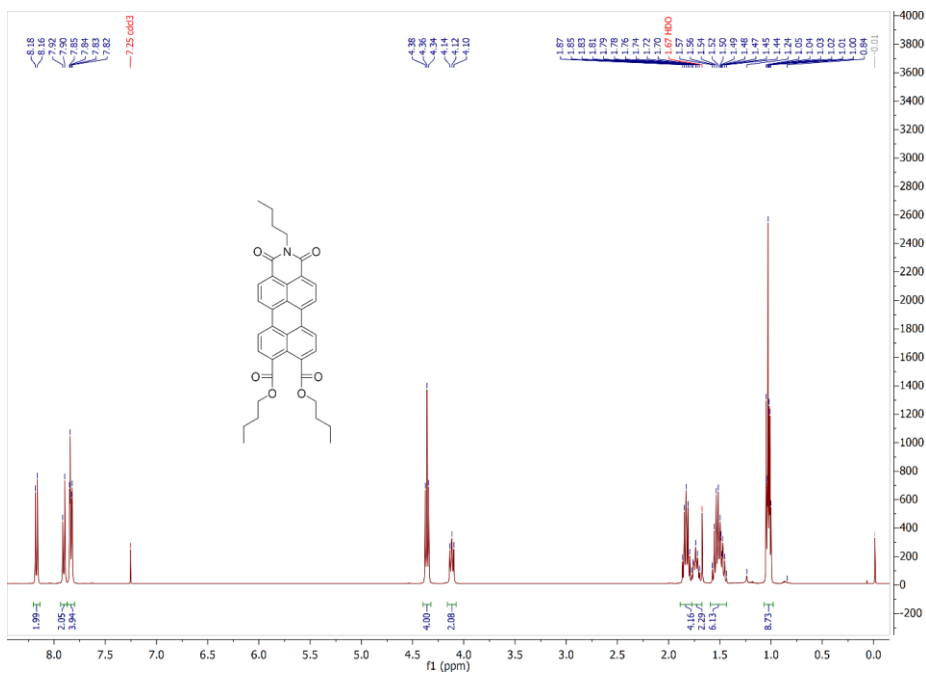
Figure S31. *¹H NMR spectrum of 13c in CDCl₃.*
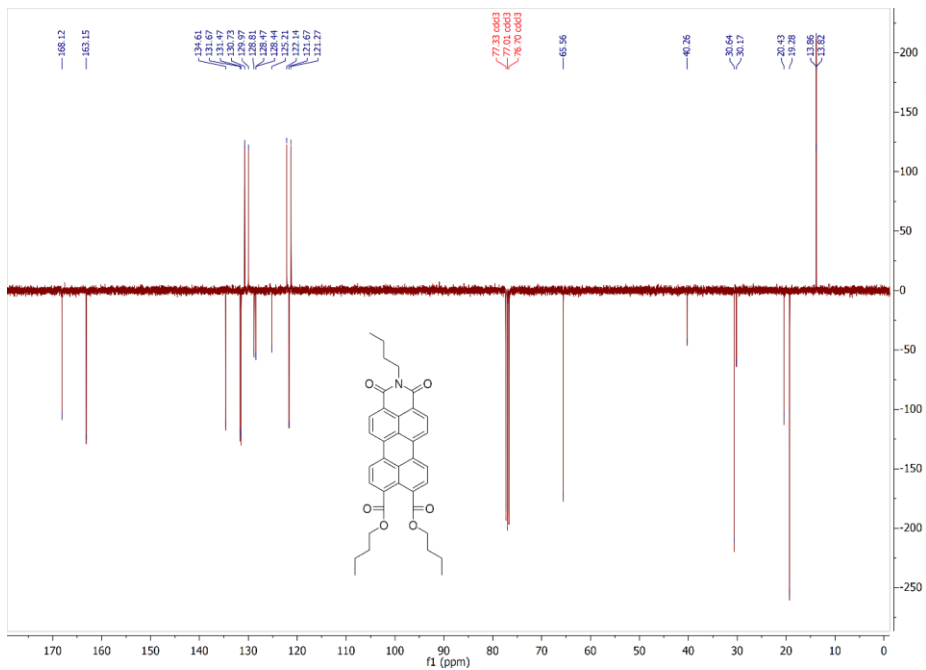
Figure S32. *¹³C- NMR spectrum of **13c** in CDCl₃.*
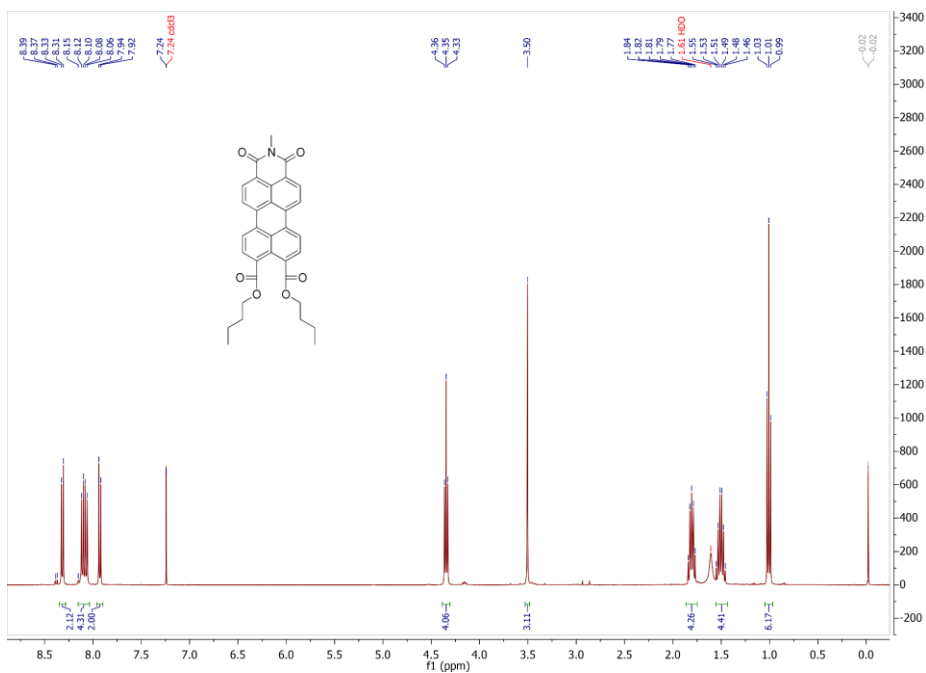
Figure S33. *¹H NMR spectrum of **13d** in CDCl₃.*
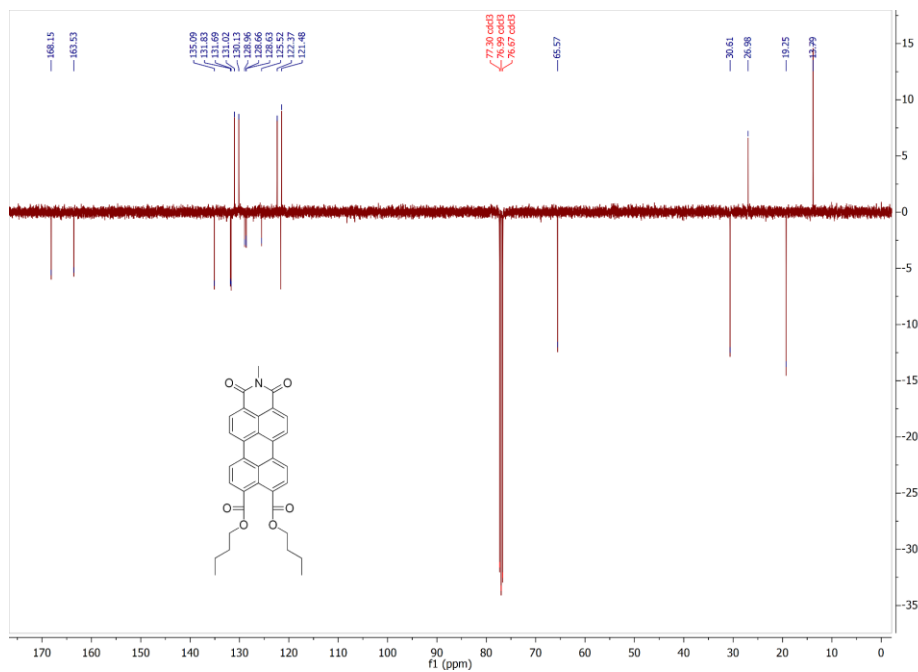
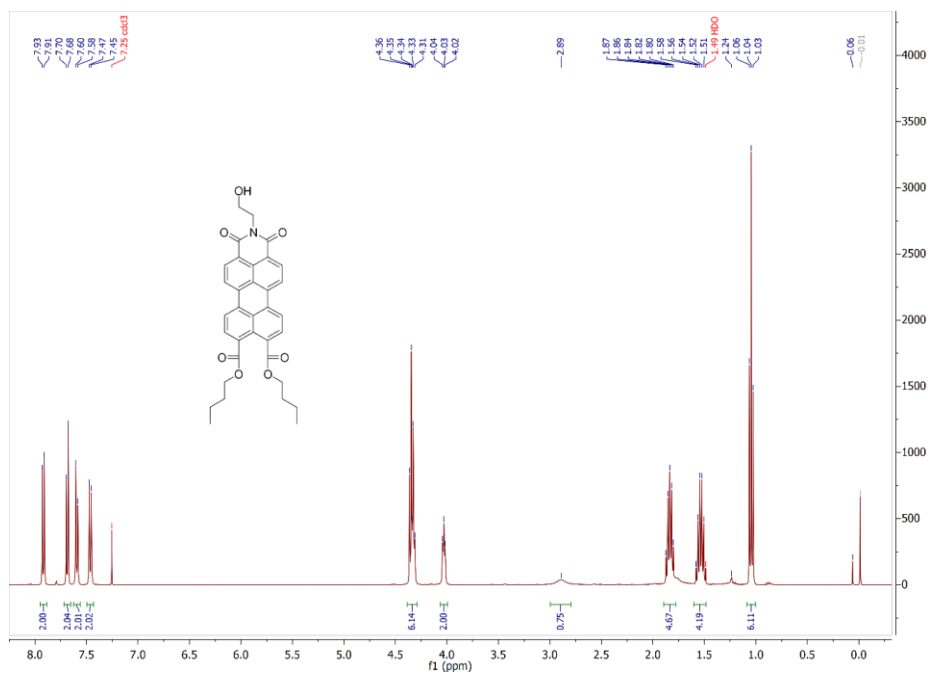***Figure S34.*** *^{13}C- NMR spectrum of **13d** in CDCl₃.*

Figure S35. *^{1}H NMR spectrum of **13e** in CDCl₃.*

Figure S36. *^{13}C- NMR spectrum of **13e** in CDCl₃.*

Figure S37. *^1H NMR spectrum of **13f** in CDCl₃.*
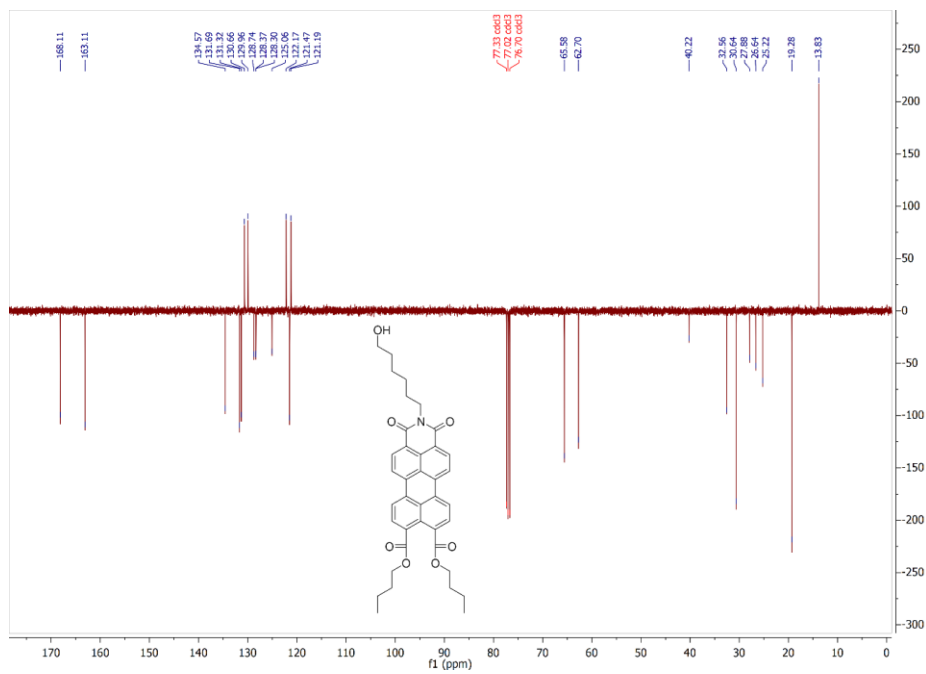
Figure S38. *¹³C- NMR spectrum of **13f** in CDCl₃.*
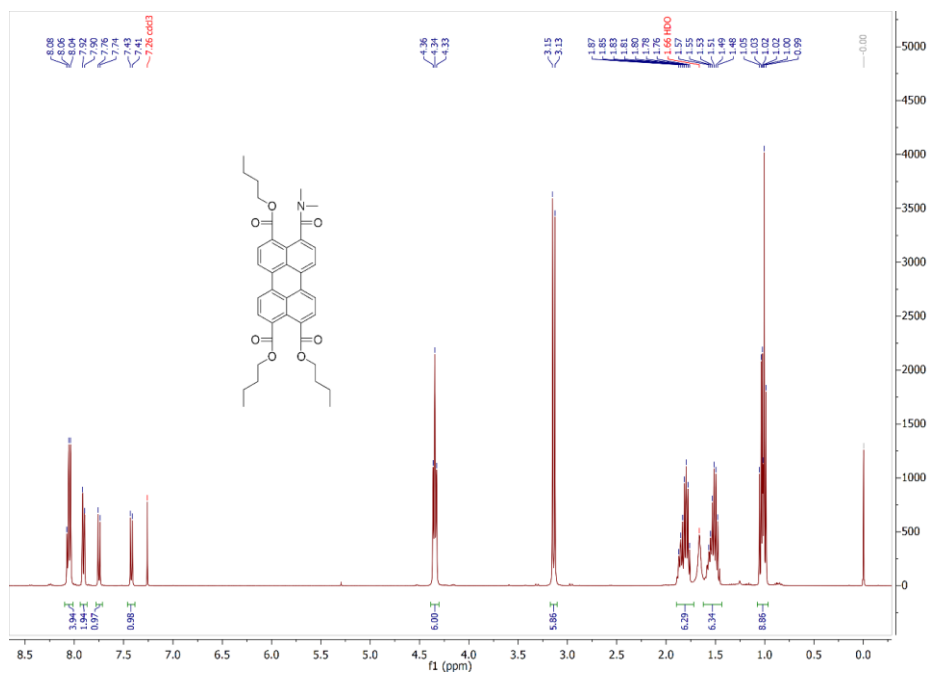
Figure S39. *¹H NMR spectrum of **14a** in CDCl₃.*
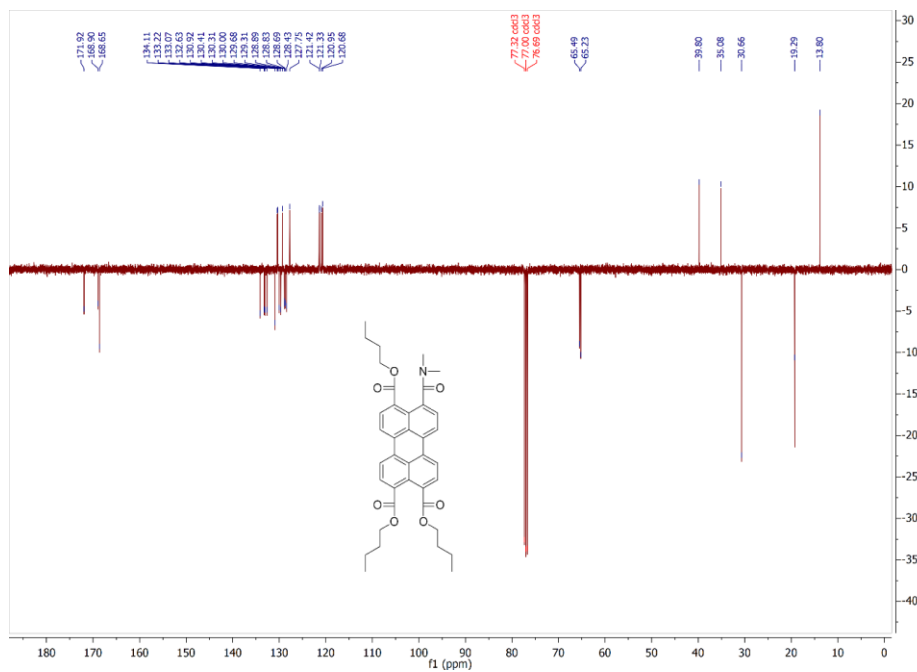
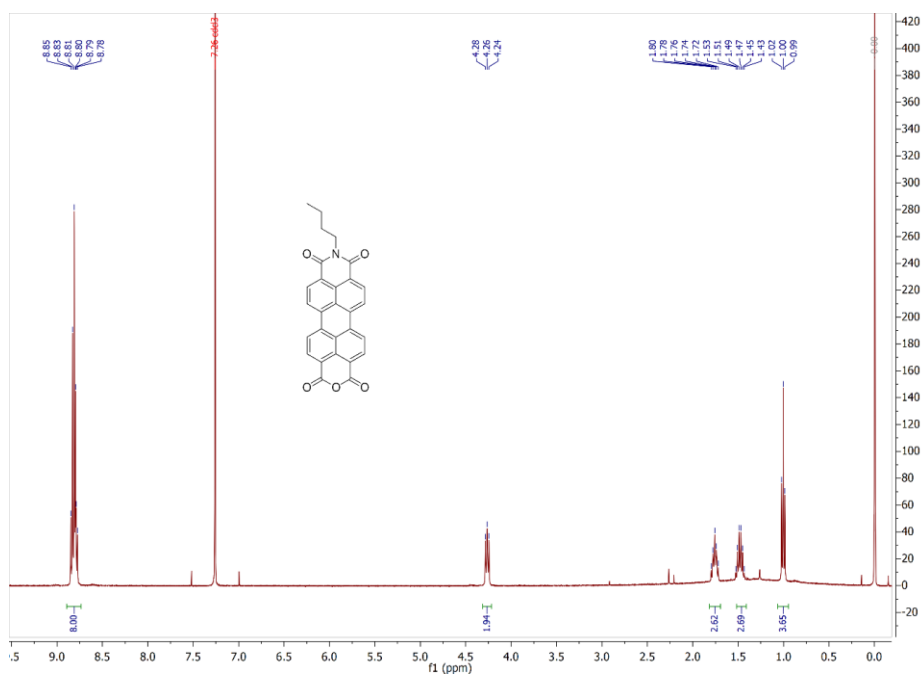***Figure S40.*** *¹³C- NMR spectrum of **14a** in CDCl₃.*

Figure S41. *¹H NMR spectrum of **15** in CDCl₃ (with 1 drop of TFA).*

2.7 References and notes

(1) Kardos, M. Über Einige Aceanthrenchinon- Und 1.9-Anthracen-Derivate. *Berichte Dtsch. Chem. Ges.* **1913**, *46* (2), 2086–2091. https://doi.org/10.1002/cber.191304602126.

(2) Herbst, W.; Hunger, K.; Wilker, G. *Industrial organic pigments: production, properties, applications*; Wiley-VCH: Weinheim, 2004.

(3) Würthner, F. Perylene Bisimide Dyes as Versatile Building Blocks for Functional Supramolecular Architectures. *Chem Commun* **2004**, No. 14, 1564–1579. https://doi.org/10.1039/B401630K.

(4) Langhals, H. Control of the Interactions in Multichromophores: Novel Concepts. Perylene Bis-Imides as Components for Larger Functional Units. *Helv. Chim. Acta* **2005**, *88* (6), 1309–1343. https://doi.org/10.1002/hlca.200590107.

(5) Huang, C.; Barlow, S.; Marder, S. R. Perylene-3,4,9,10-Tetracarboxylic Acid Diimides: Synthesis, Physical Properties, and Use in Organic Electronics. *J. Org. Chem.* **2011**, *76* (8), 2386–2407. https://doi.org/10.1021/jo2001963.

(6) Nielsen, C. B.; Holliday, S.; Chen, H.-Y.; Cryer, S. J.; McCulloch, I. Non-Fullerene Electron Acceptors for Use in Organic Solar Cells. *Acc. Chem. Res.* **2015**, *48* (11), 2803–2812. https://doi.org/10.1021/acs.accounts.5b00199.

(7) Liu, Z.; Wu, Y.; Zhang, Q.; Gao, X. Non-Fullerene Small Molecule Acceptors Based on Perylene Diimides. *J. Mater. Chem. A* **2016**, *4* (45), 17604–17622. https://doi.org/10.1039/C6TA06978A.

(8) Zink-Lorre, N.; Font-Sanchis, E.; Sastre-Santos, Á.; Fernández-Lázaro, F. Perylenediimides as More than Just Non-Fullerene Acceptors: Versatile Components in Organic, Hybrid and Perovskite Solar Cells. *Chem. Commun.* **2020**, *56* (27), 3824–3838. https://doi.org/10.1039/D0CC00337A.

(9) Kelley, R. F.; Shin, W. S.; Rybtchinski, B.; Sinks, L. E.; Wasielewski, M. R. Photoinitiated Charge Transport in Supramolecular Assemblies of a 1,7,N,N'-Tetrakis(Zinc Porphyrin)-Perylene-3,4:9,10-Bis(Dicarboximide). *J. Am. Chem. Soc.* **2007**, *129* (11), 3173–3181. https://doi.org/10.1021/ja0664741.

(10) Hurenkamp, J. H.; Browne, W. R.; Augulis, R.; Pugžlys, A.; Loosdrecht, P. H. M. van; Esch, J. H. van; Feringa, B. L. Intramolecular Energy Transfer in a Tetra-Coumarinperylene System: Influence of Solvent and Bridging Unit on Electronic Properties. *Org. Biomol. Chem.* **2007**, *5* (20), 3354–3362. https://doi.org/10.1039/B711681K.

(11) Fujitsuka, M.; Harada, K.; Sugimoto, A.; Majima, T. Excitation Energy Dependence of Photoinduced Processes in Pentathiophene−Perylene Bisimide Dyads with a Flexible Linker. *J. Phys. Chem. A* **2008**, *112* (41), 10193–10199. https://doi.org/10.1021/jp805350d.

(12) Wasielewski, M. R. Self-Assembly Strategies for Integrating Light Harvesting and Charge Separation in Artificial Photosynthetic Systems. *Acc. Chem. Res.* **2009**, *42* (12), 1910–1921. https://doi.org/10.1021/ar9001735.

(13) Blas-Ferrando, V. M.; Ortiz, J.; Bouissane, L.; Ohkubo, K.; Fukuzumi, S.; Fernández-Lázaro, F.; Sastre-Santos, Á. Rational Design of a Phthalocyanine–Perylenediimide Dyad with a Long-Lived Charge-Separated State. *Chem. Commun.* **2012**, *48* (50), 6241–6243. https://doi.org/10.1039/C2CC31087B.

(14) Frischmann, P. D.; Mahata, K.; Würthner, F. Powering the Future of Molecular Artificial Photosynthesis with Light-Harvesting Metallosupramolecular Dye Assemblies. *Chem. Soc. Rev.* **2013**, *42* (4), 1847–1870. https://doi.org/10.1039/C2CS35223K.

(15) Dubey, R. K.; Inan, D.; Sengupta, S.; Sudhölter, E. J. R.; Grozema, F. C.; Jager, W. F. Tunable and Highly Efficient Light-Harvesting Antenna Systems Based on 1,7-Perylene-3,4,9,10-Tetracarboxylic Acid Derivatives. *Chem. Sci.* **2016**, *7* (6), 3517–3532. https://doi.org/10.1039/C6SC00386A.

(16) Frischmann, P. D.; Gerber, L. C. H.; Doris, S. E.; Tsai, E. Y.; Fan, F. Y.; Qu, X.; Jain, A.; Persson, K. A.; Chiang, Y.-M.; Helms, B. A. Supramolecular Perylene Bisimide-Polysulfide Gel Networks as Nanostructured Redox Mediators in Dissolved Polysulfide Lithium–Sulfur Batteries. *Chem. Mater.* **2015**, *27* (19), 6765–6770. https://doi.org/10.1021/acs.chemmater.5b02955.

(17) Iordache, A.; Delhorbe, V.; Bardet, M.; Dubois, L.; Gutel, T.; Picard, L. Perylene-Based All-Organic Redox Battery with Excellent Cycling Stability. *ACS Appl. Mater. Interfaces* **2016**, *8* (35), 22762–22767. https://doi.org/10.1021/acsami.6b07591.

(18) Ranque, P.; George, C.; Dubey, R. K.; van der Jagt, R.; Flahaut, D.; Dedryvère, R.; Fehse, M.; Kassanos, P.; Jager, W. F.; Sudhölter, E. J. R.; Kelder, E. M. Scalable Route to Electroactive and Light Active Perylene Diimide Dye Polymer Binder for Lithium-Ion Batteries. *ACS Appl. Energy Mater.* **2020**, *3* (3), 2271–2277. https://doi.org/10.1021/acsaem.9b01225.

(19) Weil, T.; Vosch, T.; Hofkens, J.; Peneva, K.; Müllen, K. The Rylene Colorant Family—Tailored Nanoemitters for Photonics Research and Applications. *Angew. Chem. Int. Ed.* **2010**, *49* (48), 9068–9093. https://doi.org/10.1002/anie.200902532.

(20) Aigner, D.; Freunberger, S. A.; Wilkening, M.; Saf, R.; Borisov, S. M.; Klimant, I. Enhancing Photoinduced Electron Transfer Efficiency of Fluorescent PH-Probes with Halogenated Phenols. *Anal. Chem.* **2014**, *86* (18), 9293–9300. https://doi.org/10.1021/ac502513g.

(21) Ghosh, I.; Ghosh, T.; Bardagi, J. I.; König, B. Reduction of Aryl Halides by Consecutive Visible Light-Induced Electron Transfer Processes. *Science* **2014**, *346* (6210), 725–728. https://doi.org/10.1126/science.1258232.

(22) Nowak-Król, A.; Würthner, F. Progress in the Synthesis of Perylene Bisimide Dyes. *Org. Chem. Front.* **2019**. https://doi.org/10.1039/C8QO01368C.

(23) Langhals, H. Synthese von Hochreinen Perylen-Fluoreszenzfarbstoffen in Großen Mengen – Gezielte Darstellung von Atrop-Isomeren. *Chem. Ber.* **1985**, *118* (11), 4641–4645. https://doi.org/10.1002/cber.19851181138.

(24) Langhals, H. Cyclic Carboxylic Imide Structures as Structure Elements of High Stability. Novel Developments in Perylene Dye Chemistry. *HETEROCYCLES* **1995**, *40* (1), 477. https://doi.org/10.3987/REV-94-SR2.

(25) Würthner, F.; Sautter, A.; Schilling, J. Synthesis of Diazadibenzoperylenes and Characterization of Their Structural, Optical, Redox, and Coordination Properties. *J. Org. Chem.* **2002**, *67* (9), 3037–3044. https://doi.org/10.1021/jo011133l.

(26) Esteban-Gómez, D.; Fabbrizzi, L.; Licchelli, M.; Sacchi, D. A Two-Channel Chemosensor for the Optical Detection of Carboxylic Acids, Including Cholic Acid. *J. Mater. Chem.* **2005**, *15* (27–28), 2670–2675. https://doi.org/10.1039/B502869H.

(27) Cao, Q.; Crawford, D. E.; Shi, C.; James, S. L. Greener Dye Synthesis: Continuous, Solvent-Free Synthesis of Commodity Perylene Diimides by Twin-Screw Extrusion. *Angew. Chem. Int. Ed.* **2020**, *59* (11), 4478–4483. https://doi.org/10.1002/anie.201913625.

(28) Baumgartner, B.; Svirkova, A.; Bintinger, J.; Hametner, C.; Marchetti-Deschmann, M.; Unterlass, M. M. Green and Highly Efficient Synthesis of Perylene and Naphthalene Bisimides in Nothing but Water. *Chem. Commun.* **2017**, *53* (7), 1229–1232. https://doi.org/10.1039/C6CC06567H.

(29) Nagao, Y.; Misono, T. Synthesis and Reactions of Perylenecarboxylic Acid Derivatives. VIII. Synthesis of N-Alkyl-3,4:9,10-Perylenetetracarboxylic Monoanhydride Monoimide. *Bull. Chem. Soc. Jpn.* **1981**, *54* (4), 1191–1194. https://doi.org/10.1246/bcsj.54.1191.

(30) Langhals, H.; Karolin, J.; Johansson, L. B.-Å. Spectroscopic Properties of New and Convenient Standards for Measuring Fluorescence Quantum Yields. *J. Chem. Soc. Faraday Trans.* **1998**, *94* (19), 2919–2922. https://doi.org/10.1039/a804973d.

(31) PMAMI Was Obtained after Acid Work-up, Which Converts a Dicarboxylic Acid into an Anhydride.

(32) At Low Temperatures Imide Formation Is Prevented, Because Amic Acid Formation from Dicarboxylates Requires Elevated Temperatures.

(33) Using a 40% Methylamine Solution in Refluxing Water, a Quantitative PDI Synthesis Was Reported, Which Makes Sense in View of the Extremely High Concentration and the Huge Excess of the Amine.

(34) Stang, P. J.; Cao, D. H.; Saito, S.; Arif, A. M. Self-Assembly of Cationic, Tetranuclear, Pt(II) and Pd(II) Macrocyclic Squares. x-Ray Crystal Structure of [Pt2+(Dppp)(4,4'-Bipyridyl).Cntdot.2-OSO2CF3]4. *J. Am. Chem. Soc.* **1995**, *117* (23), 6273–6283. https://doi.org/10.1021/ja00128a015.

(35) Formation of Monoimides from Perylene Dicarboxylate Monoanhydride Has Been Reported.

(36) Tröster, H. Untersuchungen zur Protonierung von Perylen-3,4,9,10-tetracarbonsäurealkalisalzen. *Dyes Pigments* **1983**, *4* (3), 171–177. https://doi.org/10.1016/0143-7208(83)80015-1.

(37) Kaiser, H.; Lindner, J.; Langhals, H. Synthese von nichtsymmetrisch substituierten Perylen-Fluoreszenzfarbstoffen. *Chem. Ber.* **1991**, *124* (3), 529–535. https://doi.org/10.1002/cber.19911240319.

(38) Hassheider, T.; Benning, S. A.; Kitzerow, H.-S.; Achard, M.-F.; Bock, H. Color-Tuned Electroluminescence from Columnar Liquid Crystalline Alkyl Arenecarboxylates. *Angew. Chem. Int. Ed.* **2001**, *40* (11), 2060–2063. https://doi.org/10.1002/1521-3773(20010601)40:11<2060::AID-ANIE2060>3.0.CO;2-H.

(39) Dubey, R. K.; Westerveld, N.; Grozema, F. C.; Sudhölter, E. J. R.; Jager, W. F. Facile Synthesis of Pure 1,6,7,12-Tetrachloroperylene-3,4,9,10-Tetracarboxy Bisanhydride and Bisimide. *Org. Lett.* **2015**, *17* (8), 1882–1885. https://doi.org/10.1021/acs.orglett.5b00562.

(40) Kelber, J.; Bock, H.; Thiebaut, O.; Grelet, E.; Langhals, H. Room-Temperature Columnar Liquid-Crystalline Perylene Imido-Diesters by a Homogeneous One-Pot Imidification–Esterification of Perylene-3,4,9,10-Tetracarboxylic Dianhydride. *Eur. J. Org. Chem.* **2011**, *2011* (4), 707–712. https://doi.org/10.1002/ejoc.201001346.

(41) de Barros, T. C.; Filho, P. B.; Loos, M.; Politi, M. J.; Chaimovich, H.; Cuccovia, I. M. Formation and Decomposition of N-Alkylnaphthalimides: Experimental Evidences and Ab Initio Description of the Reaction Pathways. *J. Phys. Org. Chem.* **2011**, *24* (5), 385–397. https://doi.org/10.1002/poc.1768.

(42) Kim, M. B.; Dixon, D. W. Hydrolysis of Aliphatic Naphthalene Diimides: Effect of Charge Placement in the Side Chains. *J. Phys. Org. Chem.* **2008**, *21* (9), 731–737. https://doi.org/10.1002/poc.1334.

(43) Shukla, D.; Meyer, D. M.; Ahearn, W. G. Aromatic Amic Acid Salts and Compositions. WO2011149699A1, December 1, 2011. https://patents.google.com/patent/WO2011149699A1/en (accessed 2023-04-02).

(44) Barros, T. C.; Molinari, G. R.; Berci Filho, P.; Toscano, V. G.; Politi, M. J. Photophysical Properties of N-Alkylnaphthalimides and Analogs. *J. Photochem. Photobiol. Chem.* **1993**, *76* (1), 55–60. https://doi.org/10.1016/1010-6030(93)80173-7.

(45) Mason, F. A. CCLXXVIII.—Derivatives of 1 : 8-Naphthalic Acid. Part I. The Preparation and Properties of 1 : 8-Naphthalyl Chloride. *J. Chem. Soc. Trans.* **1924**, *125* (0), 2116–2119. https://doi.org/10.1039/CT9242502116.

(46) Strey, K.; Voss, J. EPR Studies on Carboxylic Esters. Part 15.1 Spin Density Distribution in the Radical Anions of Naphthalenecarboxylic Esters. *J. Chem. Res. Synop.* **1998**, No. 3, 110–111. https://doi.org/10.1039/A706189G.

(47) Kim, Y.; Ree, M.; Chang, T.; Ha, C. S.; Nunes, T. L.; Lin, J. S. Rodlike/Flexible Polyimide Composite Films Prepared from Soluble Poly(Amic Diethyl Ester) Precursors: Miscibility, Structure, and Properties. *J. Polym. Sci. Part B Polym. Phys.* **1995**, *33* (14), 2075–2082. https://doi.org/10.1002/polb.1995.090331409.

(48) Feiler, L.; Langhals, H.; Polborn, K. Synthesis of Perylene-3,4-Dicarboximides — Novel Highly Photostable Fluorescent Dyes. *Liebigs Ann.* **1995**, *1995* (7), 1229–1244. https://doi.org/10.1002/jlac.1995199507164.

(49) This Higher Reactivity of Amic Esters Is Attributed by Us to the Higher Solubility of Amic Esters as Compared to Amic Acids, Vide Infra.

(50) With 25% of PDI Isolated, the Conversion of the Imidization Reaction Is Expected to Be at Least 50%, as the Remainder of the Reaction Mixture Consists Mainly of Perylene Monoimide Monoamic Acid 9b (~5(0)%) and Lesser Amounts of Perylene Diamic Acid 5b (~25%). See Also the "Reaction Kinetics" Section in This Manuscript.

(51) Xue, C.; Sun, R.; Annab, R.; Abadi, D.; Jin, S. Perylene Monoanhydride Diester: A Versatile Intermediate for the Synthesis of Unsymmetrically Substituted Perylene Tetracarboxylic Derivatives. *Tetrahedron Lett.* **2009**, *50* (8), 853–856. https://doi.org/10.1016/j.tetlet.2008.11.084.

(52) Wang, R.; Shi, Z.; Zhang, C.; Zhang, A.; Chen, J.; Guo, W.; Sun, Z. Facile Synthesis and Controllable Bromination of Asymmetrical Intermediates of Perylene Monoanhydride/Monoimide Diester. *Dyes Pigments* **2013**, *98* (3), 450–458. https://doi.org/10.1016/j.dyepig.2013.04.006.

(53) The ^{1}H NMR Spectrum of Compound 6a Is Similar to the One Reported for a Similar Perylene Diamic Acid. For These Compounds the Cis and Trans Isomers Could Not Be Distinguished Either.

(54) Kunz, V.; Stepanenko, V.; Würthner, F. Embedding of a Ruthenium(II) Water Oxidation Catalyst into Nanofibers via Self-Assembly. *Chem. Commun.* **2014**, *51* (2), 290–293. https://doi.org/10.1039/C4CC08314H.

(55) Generally Chlorosulfonic Acid or Sulfuric Acid Are Used for This Transformation. Mixtures of Acetic Acid and Sulfuric Acid Have Been Used at Elevated Temperatures.

(56) When Sampled in Water the Formation of 7c Was Deduced from an Elevated Baseline in the Absorption Spectra and a Purple Solid Precipitate in the Reaction Mixture.

(57) For PDI 7b We Initially Used an Alternative Workup Procedure, Involving Extraction with Chloroform, Followed by Filtration. However, This Procedure Was Tedious Less Efficient and Only Suitable for Soluble PDIs.

(58) Anastas, P.; Eghbali, N. Green Chemistry: Principles and Practice. *Chem Soc Rev* **2010**, *39* (1), 301–312. https://doi.org/10.1039/B918763B.

(59) For the Synthesis of PTEs in Acetonitrile, We Have Attempted to Replace DBU by Other Tertiary Amines, but None of These Bases Gave Satisfactory Yields. In This Specific Case, Apart from the Solubility of the Intermediate Salts, Base Strength May Also Have Been Critical.

(60) Demmig, S.; Langhals, H. Leichtlösliche, lichtechte Perylen-Fluoreszenzfarbstoffe. *Chem. Ber.* **1988**, *121* (2), 225–230. https://doi.org/10.1002/cber.19881210205.

(61) *Encyclopedia of Physical Organic Chemistry, 5 Volume Set*; Wang, Z., Ed.; John Wiley & Sons, Inc.: Hoboken, NJ, USA, 2016. https://doi.org/10.1002/9781118468586.

(62) Hecht, M.; Würthner, F. Supramolecularly Engineered J-Aggregates Based on Perylene Bisimide Dyes. *Acc. Chem. Res.* **2021**, *54* (3), 642–653. https://doi.org/10.1021/acs.accounts.0c00590.

(63) Chen, Z.; Lohr, A.; Saha-Möller, C. R.; Würthner, F. Self-Assembled π-Stacks of Functional Dyes in Solution: Structural and Thermodynamic Features. *Chem. Soc. Rev.* **2009**, *38* (2), 564–584. https://doi.org/10.1039/B809359H.

(64) Wang, H.; Kaiser, T. E.; Uemura, S.; Würthner, F. Perylene Bisimide J-Aggregates with Absorption Maxima in the NIR. *Chem. Commun.* **2008**, No. 10, 1181–1183. https://doi.org/10.1039/B717407A.

(65) Extinction Coefficient of Diamic Acids like $K_2$5a Are 33000 M^{-1} cm^{-1}.

(66) In Fig. 5 It Is Clearly Visible That the First Spectrum Primarily Contains Compound $K_2$5c. Absorption above 500 nm, Indicates That Compound K9c Is Already Present in the Reaction Mixture. The Last Spectrum Consists Mostly of Compound 7c, but the Tail in the Absorption above 500 nm May Indicate That Not All K9c Has Been Consumed.

(67) PDA, PDIs and PMAMIs Are Virtually Insoluble in DMF. When These Compounds Are Formed in Situ by Reaction in DMF, Oversaturated Solutions Are Formed. These Compound Are Molecularly Dissolved and Highly Fluorescent, but Precipitate in Due Time.

(68) Extracting the Relative Concentrations of 5c, 9c and 7c from the Absorption Spectra Has Been Performed Manually in a Few Independent Runs. In All Cases the Relative Concentration of 7c Was Consistent. The Relative Concentrations of 5c and 9c, on the Other Hand, Showed a Larger Variation between the Different Runs.

(69) Souza, B. S.; Mora, J. R.; Wanderlind, E. H.; Clementin, R. M.; Gesser, J. C.; Fiedler, H. D.; Nome, F.; Menger, F. M. Transforming a Stable Amide into a Highly Reactive One: Capturing the Essence of Enzymatic Catalysis. *Angew. Chem.* **2017**, *129* (19), 5429–5432. https://doi.org/10.1002/ange.201701306.

(70) The Apparent Isosbestic Point at 473 Nm Is Confusing. Close Inspection of the Spectra Shows That an Isosbestic Point for Compounds 5a and 1 Is Found at This Wavelength, but That the Extinction Coefficient of the Reaction Intermediate 8a at 473 nm Is Slightly Higher.

(71) The High Dilution Used Here Comes down to 1 Gram of PDA in 750 mL DMF.

(72) Water Addition Was Also Accompanied by a Spontaneous ~23 °C Rise in Temperature. This Temperature Increase Was Short-Lived and Has Not Contributed to the Increased Yield.

(73) For the "Green" Reaction, with K_2CO_3 and DMSO, Adding 4 mL of Water after 1 Hour Increased Solubility, but the Orange Potassium Salt of Compound 5c Did Not Fully Dissolve. Continuation of the Reaction at Room Temperature Did Result in a Higher PDI Yield, ~75%, but the Reaction Yield Was Not Quantitative.

(74) Xu, Y.; Leng, S.; Xue, C.; Sun, R.; Pan, J.; Ford, J.; Jin, S. A Room-Temperature Liquid-Crystalline Phase with Crystalline π Stacks. *Angew. Chem. Int. Ed.* **2007**, *46* (21), 3896–3899. https://doi.org/10.1002/anie.200604607.

(75) Gershberg, J.; Radić Stojković, M.; Škugor, M.; Tomić, S.; Rehm, T. H.; Rehm, S.; Saha-Möller, C. R.; Piantanida, I.; Würthner, F. Sensing of Double-Stranded DNA/RNA Secondary Structures by Water Soluble Homochiral Perylene Bisimide Dyes. *Chem. Weinh. Bergstr. Ger.* **2015**, *21* (21), 7886–7895. https://doi.org/10.1002/chem.201500184.

(76) Boccia, A. C.; Lukeš, V.; Eckstein-Andicsová, A.; Kozma, E. Solvent- and Concentration-Induced Self-Assembly of an Amphiphilic Perylene Dye. *New J. Chem.* **2020**, *44* (3), 892–899. https://doi.org/10.1039/C9NJ05674B.

(77) For the Reaction of 11 with 4-Dimethylamino Aniline Using DBU in DMF under Argon, a 60% Yield Was Obtained after Reacting Overnight at 60 °C.

(78) Matsunaga, Y.; Goto, K.; Kubono, K.; Sako, K.; Shinmyozu, T. Photoinduced Color Change and Photomechanical Effect of Naphthalene Diimides Bearing Alkylamine Moieties in the Solid State. *Chem. – Eur. J.* **2014**, *20* (24), 7309–7316. https://doi.org/10.1002/chem.201304849.

(79) Saha, S.; Sahoo, P. Luminescence Turn-on Response of Naphthalene Diimide Based Chemosensor with Formaldehyde: A Novel Stratagem for Estimation of Formaldehyde in Storage Fish Samples. *Bioorg. Med. Chem. Lett.* **2021**, *49*, 128287. https://doi.org/10.1016/j.bmcl.2021.128287.

(80) Lakowicz, J. R. *Principles of Fluorescence Spectroscopy*, 3rd ed.; Springer: New York, 2006.

3

Perylene dianhydride hydrogels obtained from highly accessible perylene-3,4,9,10-tetracarboxylic diamic acids precursors.

Abstract

A novel class of perylene-based hydrogelators, perylene amic acid salts, which form hydrogels upon protonation by a unique mechanism, is reported. A detailed study of this gelation process was conducted on a series of perylene diamic acid potassium salts derived from cyclic secondary amines, whose structure was systematically varied. Upon slow protonation all compounds formed deeply coloured hydrogels with respectable mechanical properties, which showed profound syneresis over time. The gelation process was investigated using time-dependant UV-VIS and H-NMR, cryo-TEM and rheology measurements, and based on the obtained data a unique gelation mechanism is proposed. Very weak gels are formed almost instantaneously by π-π stacking of hydrophobic amid acids that are formed by protonation. Subsequently, a slower amine elimination process forms anhydrides that, due to their planarity and lack of steric hindrance, form much stronger hydrogels. It was found that the rate of anhydride formation primarily determines the hydrogel properties and that hydrogels from amic acids that decompose slower have superior mechanical properties. We also conclude that the formation of hydrogels from perylene amic acid salts and their ester analogues has been observed for different classes of compounds and is quite universal.

3.1 Introduction

Perylene-3,4,9,10- teracarboxylic acid derivatives (PTCAs) are a class of aromatic dyes and pigments from which perylene-3,4,9,10-tetracarboxylic diimides PDIs are the most abundantly exploited representatives.[1] These compounds are produced on an industrial scale and applied as dyes and pigments,[2] for instance for colouring plastics and for automotive applications in paints. Due to their benign optoelectronic properties, potential applications in PV,[3–7] photocatalysis[8–16] and organic batteries[13,17,18] have been identified and this forms a major motivation for the current research efforts. For example, the current boom in non-fullerene acceptors for bulk heterojunction solar cells is largely driven by the development of novel PDIs and PDI-based polymers.[19]

Due to their hydrophobic nature and tendency to self-assemble by π-π stacking[20–24] non-bay substituted PDIs, have been employed as hydrogelators. The self-assembly process that forms hydrogels is induced by converting charged and water-soluble PDIs into non-charged insoluble PDIs, which is most conveniently achieved by altering the pH. Well-known are amino acid appended PDIs,[25–29] that have a free carboxylate at the amino acid residues and therefore, these compounds are negatively charged and water soluble at high pH values. Hydrogels are formed upon step-wise protonation of gelator salts in solution upon lowering the pH. In some cases the chirality of the appended amino acids is expressed in the ordering of the PDI molecules in the gel fibres.[30,31]

The mechanism of gel formation for PDI based hydrogels is similar in all reported cases; neutralisation of the carboxylic moieties of the hydrogelator ions, which induces self-assembly of the PDI moieties by hydrophobic interactions. The rate of forming insoluble molecules, can be controlled by the manner at which the pH is modulated. For example, by using buffers of a predefined pH value, or by using a lactone hydrolysis reaction that decreases the pH by a slow release of a carboxylic acid.[32–34] The rate of aggregate formation and the ordering of the PDI molecules in π-π-stacks is also influenced by the nature of the pending group at the imide position of the PDI gelator molecules.[24] Both factors will influence the final structure and physical properties of the resulting hydrogel.

In this work, perylene-3,4,9,10-diamic acid salts will be introduced as a novel type of perylene tetracarboxylic based hydrogelator. Amic acids are composed of an amide and an acid group in close proximity and these compounds are formed by the reaction of amines with anhydrides. Amic acids obtained from primary amines are the intermediates in the synthesis of imides.[35–39] In the well-known synthesis of polyimides, using aromatic diamines and pyromilitic anhydride, first amic acids are formed at modest temperatures and subsequently solutions of these soluble polymers are cast in films.[40] Lastly, the imidization reaction is performed at high temperatures.
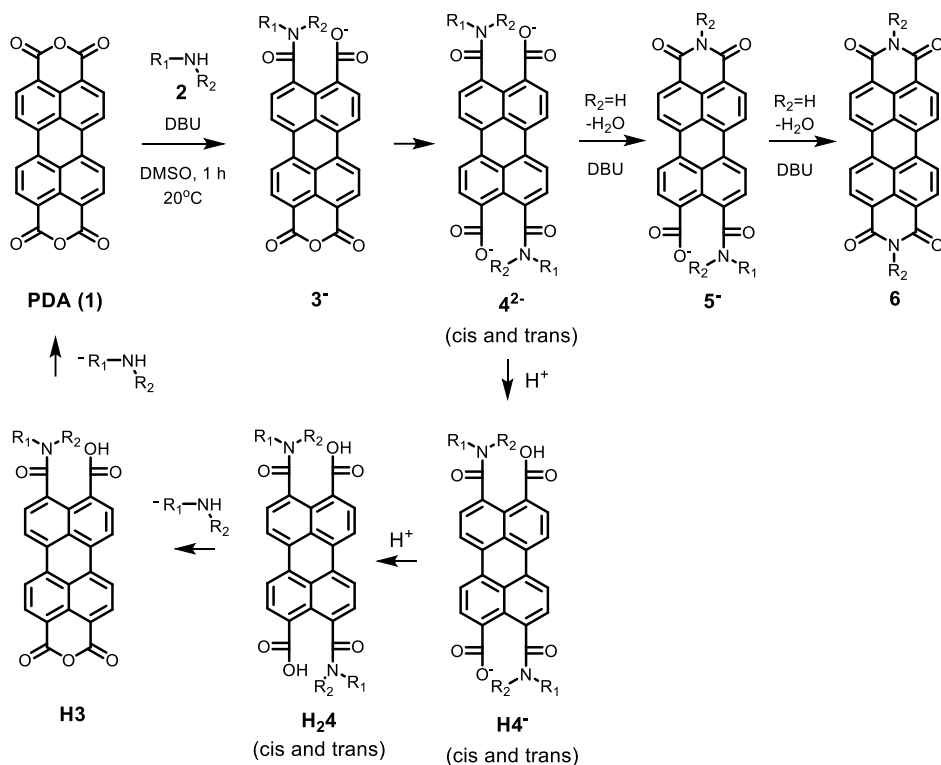
Scheme 1.

Recently we have reported a very mild synthesis of aliphatic PDIs **6**, in which the amic acid salt intermediates **4²⁻** already react at room temperature to form the corresponding imides (Scheme 1).[39] When secondary amines are employed, however, the resulting amic acid salts are stable against further imidization, and conveniently isolated. Under acidic conditions, however, these aliphatic perylene amic acids quickly hydrolyse to form PDA **1**. For aliphatic naphthalene amic acids, acid-induced hydrolysis reactions have been reported.[41,42] Nome and Menger *et al.* examined this reaction in greater detail and concluded that the rate of hydrolysis is dependent on the pH and intramolecular catalysis by an adjacent carboxylic acid group.[42]

When aqueous solutions of perylene-3,4,9,10-diamic acid salts **4²⁻** are acidified the formation of highly coloured hydrogels are observed. Upon lowering the pH, uncharged and insoluble amic acids will be formed that undergo self-assembly. Subsequently, the amic acids in these self-assembled structures react to form perylene-3,4,9,10-tetracarboxylic acid dianhydride (PDA). According to this scenario the molecular structure of the amic acid controls the initial self-assembly process as well as the rate of decomposition of the amic acid. However, the final hydrogels are composed of PDA and thus identical in chemical composition, regardless of the molecular structure of the amic acid precursor. Compared to the conventional PDI gel formation the formation of hydrogels from perylene diamic acids proceeds by a unique two-steps gelation mechanism.

In this manuscript we will investigate this exceptional gelation mechanism in detail, by employing a series of PDAAs in which the structure of the appended amine is systematically varied. We will investigate the scope of the gel formation, characterize the formed hydrogels, critically evaluate the proposed mechanism of gel formation and establish gelator structure versus gel property relationships. For the latter we will determine amic acid decomposition rates for the gelator molecules. In addition to perylene diamic acids, we also report on perylene monoimide monoamic acids (PMIMAAs) as gelator molecules. For hydrogel formation from these molecules, the gelation mechanism consists of the same steps, neutralization of the amic acid followed by self-assembly and anhydride formation.

3.2 Results and discussion
3.2.1. Synthesis and Characterization of perylene amic acids
The syntheses of perylene-3,4,9,10-diamic acids salts **K₂4a-K₂4f**, perylene-3,4-imide-9,10-amic acids salts **K5a-K5f** and perylene-3,4-amic acid-9,10-diesters acid salt **K9a** are depicted in Scheme 1 and described in the SI. In these syntheses K_2CO_3 was used as a base, instead of DBU, because the potassium salts of the amic acids, i.e. **K₂4 K5** and **K9** were easier to isolate than the corresponding non-crystalline DBU salts. Elevated temperatures of 60°C were used because secondary amines react slower than primary amines, presumably due to steric reasons. We used a series of cyclic piperazine, piperidine, morpholine and pyrrolidine bases **2a-2e**, along with **2f** as an acyclic reference, in order to identify correlations between the molecular structure of the gel precursor and the hydrogel that is formed. Cyclic amines have been selected because amic acids derived from these amines exhibit slower decomposition reactions, which appears to be beneficial for the formation of strong hydrogels.
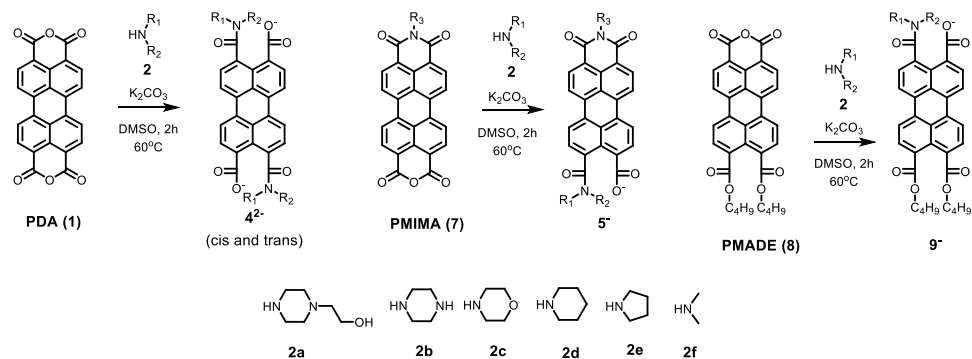
Scheme 2. *Synthesis of amic acids salts* **K₂4a-f**, **K5a-f** *and* **K9a**.

The potassium salts **K₂4a-K₂4f** have been characterised by NMR, absorption and emission spectroscopy. The ¹H and ¹³C NMR spectra of compound **K₂4a** in CD₃OD are shown in Figures 1 and S22-25. In the proton NMR the presence of two isomers is not clearly visible in the aromatic part of the spectrum, most likely due to strong overlap of the spectra of both isomers. In the aliphatic region the methylene units of the hydroxyethyl groups attached to the piperazine ring are visible as two sharp triplets at 2.59 and 3.67 ppm. The 6 protons on the piperazine rings exhibit a complex coupling pattern. Integration of the multiplet resonances demonstrates that all protons attached to the
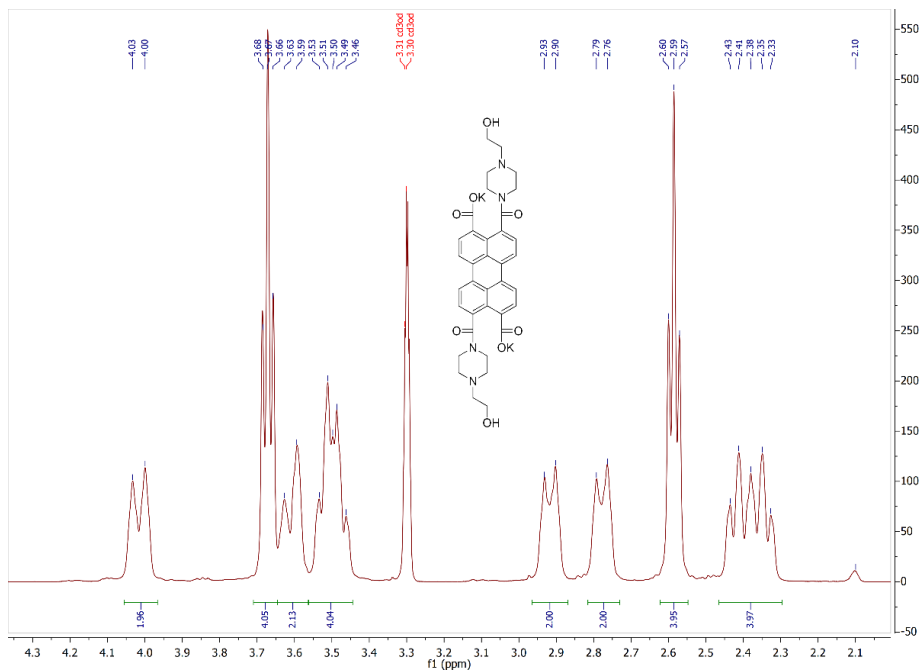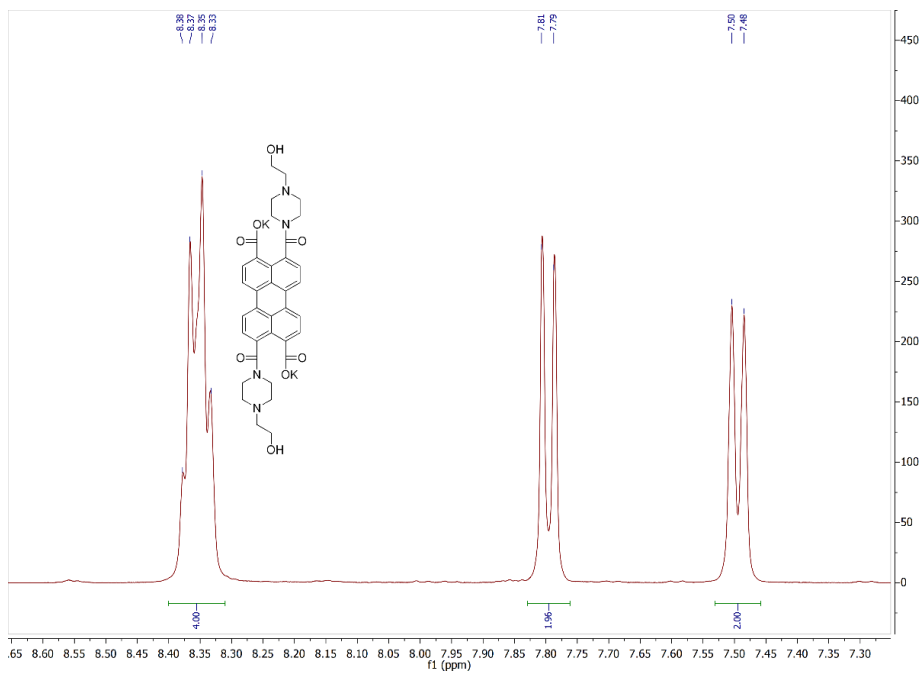
Figure 1. *¹H NMR spectrum for **K₂4a**, enlarging the aromatic (top) and the aliphatic part (bottom).*

piperazine ring have different chemical shifts and are individually visible. This observation indicates that both the inversion of the six-membered piperazine ring and the rotation over the perylene amide bond at the peri-position are slow on the NMR timescale. A slow rotation over the amide bond is already apparent in the ^{1}H NMR spectrum of **K$_2$4f**, were the two methyl peaks are split between two singlets at 3.05 en 3.10 ppm (figure S40). The carbon NMR spectrum reveals that **K$_2$4a** indeed is a mixture of cis and trans isomers in a 1:1 ratio. For the carboxylate and amide carbonyl carbons, at 175.7 and 171.3 ppm, respectively, double resonances are observed and the total number of resonances in the aromatic region is 20, as expected for a mixture of cis and trans isomers. UV-Vis spectra are in accordance to those previously reported for the dimethylamine derived amic acids. **K$_2$4f**, **K5f** and **K9f** (Fig S1)[39]. All compounds are soluble in water, ethanol, chloroform and DMF. However, **K$_2$4** has the highest solubility in water and the lowest in chloroform, while **K5** shows the reversed trend. It should be noted that diamic acid salts **K$_2$4** are highly soluble in water; for compound **K$_2$4a** the solubility exceeds 5 g/l, which is remarkable in view of the low solubility of non-bay substituted perylene diimides, which is remarkable for the highly hydrophobic perylene scafold.[43,44]

3.2.2. Gel formation experiments

In our attempts to isolate PMDAAs by acidification of amic acid salts in aqueous media we serendipitously discovered that this procedure leads to the formation of highly coloured, pudding-like hydrogels. Amic acid salt containing solutions were obtained by reacting an amine with PDA for one hour at 60°C with DMF as the solvent and DBU as the base[45] (Scheme 1). The obtained highly fluorescent solutions were poured in a tenfold excess of water. Subsequently, 1 M HCl was added dropwise until the intense green fluorescence of the amic acid salt disappeared and the solutions turned dark red. This procedure resulted in gel formation, not only for amic acids but also for their ester analogues.[i] All reaction mixtures contained 0.05 M gelator (0.5-1% w/w) and gelation times between 0.5 en 24 hours have been observed, depending on the chemical structure of the hydrogelator, see Table S1. Gels from different precursors were transparent and had colours ranging from deep burgundy red in most cases to orange-red. Reaction mixtures obtained in DMSO, using K$_2$CO$_3$ as the base, also yielded gels using the same procedure, but these gels generally were not as intensely coloured and less transparent. In time, the gels started to sweat and contract but this was a slow process. Most of the gels were stable enough to remove them from the mould and make pudding-sized objects, see Figure S18.

We noticed that for some compounds adding acid resulted in formation of gel particles or even crystalline material and homogeneous gels could not be made in this manner. To prevent premature gel formation due to a fast pH decrease, we also made hydrogels from reaction mixtures by adding freshly prepared glucono-δ-lactone (GdL) solution. GdL hydrolyses in water forming D-gluconic acid and the decrease of pH in time is depicted in Figure S17. In this manner the pH slowly deceases and for all compounds the gelation process occurs by neutralisation of the amic acid salt followed by PDA formation at a rate that is in part regulated by the GdL decomposition. It should also be mentioned that due to the excess amine and DBU the crude reaction mixture is strongly buffered. Using GdL, good hydrogels were obtained from virtually all precursors that were attempted, Table S2. It was also noted that the shrinkage or syneresis that is usually observed when acid is used in excess can be strongly reduced, when only a small excess of acid is used. By adding GdL we noted that all precursors yield deeply coloured homogeneous gels.

Following these crude gelation experiments, in which cosolvents and additional reagents were present along with the hydrogelator, we decided to use pure amic acids salts derived from a series of cyclic secondary amines, depicted in Scheme 2. In this series of gelator molecules, the size and the polarity of the amines are systematically tuned. Cyclic amines have been employed because the rate of hydrolysis of the derived amic acids are lower than those for amic acids derived from corresponding linear non-cyclic amines, possibly for steric reasons. It was observed, in the crude experiments using crude reaction mixtures, that a lower hydrolysis rate has a positive effect on the gelation process. Gelation of **K₂4f** was investigated as a control experiment.

Gel formation was investigated by lowering the pH of a solution of **K₂4a- K₂4e** in a 0.05 M GdL solution. The critical gel concentrations (CGCs) were determined and depicted in Table 1. In contrast to the gels formed from crude reaction mixtures, that contain 10% of a polar cosolvent and buffering amines, the gels formed in pure water exhibit substantial syneresis, i.e. the gel starts shrinking isotropically after formation. As syneresis of **K₂4a- K₂4e** started soon after the gel was set, performing classical inversion experiments is not feasible in all cases. Instead it was determined if gels made from **K₂4a- K₂4e** were capable of holding their original shape after being aged for 24 hours, which can be considered a pseudo inversion experiment. From Table 1 it is clear that gelators **K₂4a** and **K₂4b** stand out with very low CGCs around $1*10^{-5}$ M. These values in the same order of magnitude as those observed for amino acid derived PDI hydrogels that were prepared under similar conditions.[25,27,29,30,32] For hydrogels prepared from compounds **K₂4c- K₂4e** the observed CGCs are at least one order of magnitude higher, and these gels tend to crumble in time, rather than shrink. Comparing this to the kinetic experiments in the previous section, a trend can be observed: hydrogels made with hydrophilic amines (**K₂4a** and **K₂4b**) have a slower hydrolysis, a lower CGC and show no crumbling. The opposite can be seen for hydrogels made from hydrophobic amines (**K₂4c-K₂4e**). In Figure 2, the gels formed from compound **K₂4c**, 24 hours after formation, are depicted. The higher shrinkage of the more concentrated gels and the formation of transparent gels with a modest optical density at lower gel loading are clearly visible. The same experiments were performed for **K5a**, but the PMIMAA formed only very weak and crumbling hydrogels. **K₂4f** was unable to form a hydrogel under these circumstances. An alternative method of hydrogel formation that we investigated was by pouring the amic acid salts in a buffer solutions. Compounds **K₂4a-K₂4c** (0.5-0.05 M) form stable hydrogels in an ascorbic acid buffer (0.5-0.25 M, pH 4), compounds **K₂4d** and **K₂4e** precipitate under the same conditions. Syneresis of these gels is slower compared to the gels formed using GdL. A similar trend is observed when using an acetic acid buffer (<0.3 M, pH 4).

Table 1.** Summary of the critical gel concentrations in mg/ml and mmol/L of **K₂4a-K₂4e

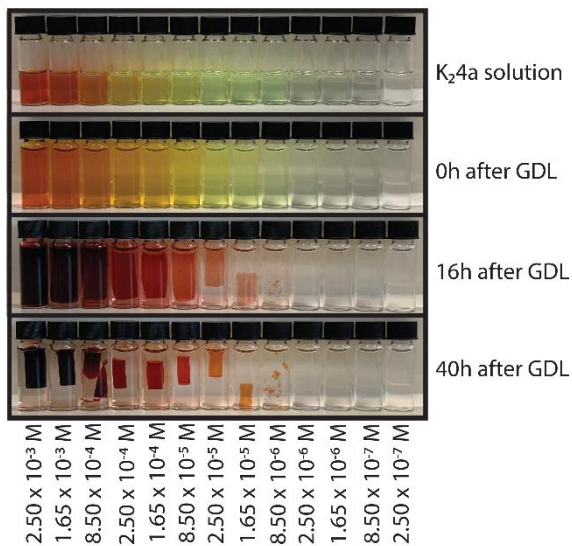|	CGC (mg/ml)	CGC (M)	Gelation time@conditions
K₂4a	0.008	$1.2 * 10^{-5}$	5h50
K₂4b	0.007	$1.0 * 10^{-5}$	>7h, <16h
K₂4c	0.06	$1.9 * 10^{-4}$	1h50
K₂4d	0.26	$4.1 * 10^{-4}$	50min
K₂4e	0.25	$4.0 * 10^{-4}$	40min

Figure 2. *dilutions of* **K₂4a** *up to 40 hours after addition of 0.05 M GdL. The strong syneresis at high gelator concentrations is clearly visible. Concentrations are from left to right 2.50 * 10⁻³ – 2.50 * 10⁻⁷ M.*

3.2.3. Rheology

The mechanical properties of 1 mM hydrogels of **K₂4a-K₂4e** were examined by oscillatory rheology at 20 °C. In time-sweep experiments the elasticity (G') and loss (G'') moduli were measured over time. The highest observed G' and G'' values are summarized in table 2. For all compounds **4a-e** G' was larger than G'', indicating viscoelastic behavior. The time at which the value of G' and G'' reaches the highest point corresponds well with the time it takes to perform a successful gel inversion experiment for all gels. In the first few minutes of the experiments, all gels gain a G' higher than G'', indicating the formation of a gel. The mechanical properties of the early gels that consist of amic acids are very weak with loss moduli G' of a few pascals. This is followed by a slow and steady increase in the mechanical properties, presumably as a consequence of amic acid decomposition. Compound **4a** exhibits the highest values for G', approximately 480 Pa (Figure 3). This value is in the same order of magnitude as PDI hydrogels reported in literature, although PDI hydrogels generally are made at higher concentrations.[25,27,29,30,32] At the end of the time sweep experiment, the mechanical properties start to decline. An exception to this behavior is observed for **4b**, where the decline is not detected in the time scope of the experiment. For gels **4a** and **4c-e**, G' remains larger than G'' during the decline. The drop in mechanical properties is most likely caused by the gel syneresis that has also been observed in the gel forming experiments. This causes the gel to detach from the plate and results in poorly reproducible experiments and less reliable data. Although all gels are composed of PDA **1** after hydrolysis, the rheology for all hydrogels shows different mechanical properties. More hydrophilic amines (**K₂4a** and **K₂4b**) show higher maximum strengths and a longer time to go through hydrolysis and syneresis, compared to amic acids with more hydrophobic amines (**K₂4c-K₂4e**). Again, this shows that amic acids with faster hydrolysis, amic acids with hydrophobic amines, have a lower mechanical strength.

Rheology of **K5a** showed that very weak hydrogels are formed with 25 Pa as the maximum loss modulus. It showed a similar syneresis as the diamic acids **K₂4a-K₂4e**.

Table 2. summary of G' and G'' values, the maximum G'/G'' ratio and the time at which the maximum of G/G'' was reached (gelation time) for 1 mM gels of K₂4a-e in 0.05 mM GdL.

Gelator (at 1 mM)	G' (Pa)$_{max}$	G'' (Pa)$_{max}$	G'/G''$_{max}$	Gelation Time (s)
K₂4a	477	7.5	64	32.300
K₂4b	670	6.5	103	16610
K₂4c*	3.3	0.2	17	10593
K₂4d	274	11	25	995
K₂4e	35	1.4	27	980
* Large quantities of a well specified K_2CO_3 contamination were present in the sample which are known to affect gelation. The observed values for G'/G'' may not be representative as a result.				
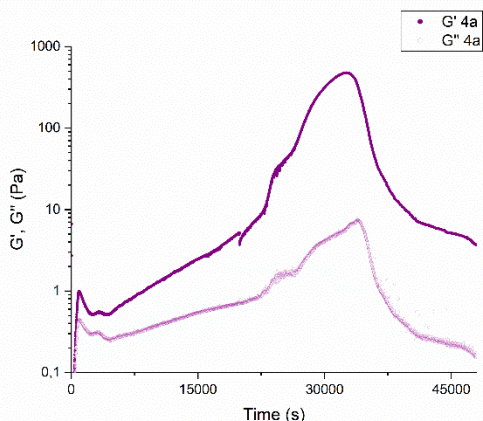
Figure 3. Rheological time-sweeps of G' and G'' of 1 mM aqueous gels of K₄4a prepared with 0.05 M GdL.

3.2.4. Kinetics of amic acid to anhydride decomposition

The rate of the amic acid decomposition was measured in a series of UV experiments, because it was observed the kinetics of this process has a profound effect on the gel formation. The kinetics of naphthalene amic acid hydrolysis in aqueous solutions has been reported in the literature. For these naphthalene compounds, the starting material, intermediates and product are soluble in water at 10^{-5} M concentrations.[41,42] However, this is not applicable for perylene diamic acids, because PDA will aggregate and gelate in water, even at low concentrations. Therefore, amic acid decomposition was monitored at room temperature in DMF, a solvent in which all compounds are soluble and aggregation of amic acids and the formed PDA does not occur.[46,47] The hydrolysis is depicted in Scheme 1 and the absorption spectra taken after addition of HCl to a solution of **K₂4a** (as a function of time) are depicted in Figure 4. Upon the addition of acid the amic acid **H₂4a** is formed instantaneously, which is clearly visible by a 10 nm blue shift in absorption and the disappearance of fluorescence. Subsequently decomposition of both

amic acid units takes place and via the monoanhydride monoamic acid **H3a**, PDA **1** is formed. Because the hydrolysis of PDAA **H$_2$4a** takes place in two steps and because the absorption spectra of the compounds involved (**H$_2$4**, **H3** and **1**) strongly overlap, accurate rate constants cannot be determined from these experiments. However, the relative rates have been determined and for this process and the order of the decomposition rates is: **H$_2$4c > H$_2$4e/H$_2$4d > H$_2$4a H$_2$4b**. As mentioned before, hydrolysis rates for these cyclic amic acids are markedly lower than those for acyclic dimethylamine-derived amic acid **H$_2$4f**.
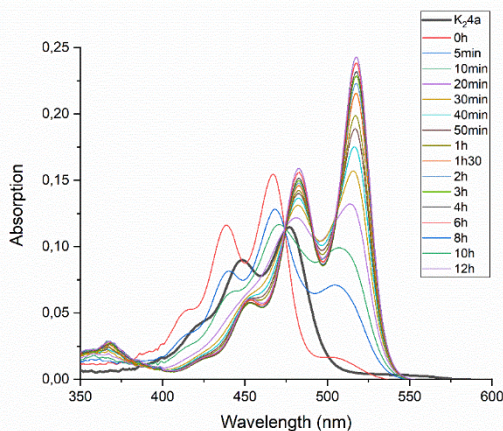
Figure 4. *Absorption spectra of the acidification and hydrolysis of amic acid **4a** with 50 μl 3M HCl in DMF at room temperature. The black line represents **K$_2$4a** before acidification. The final spectrum at 12 hours represents PDA **1**.*
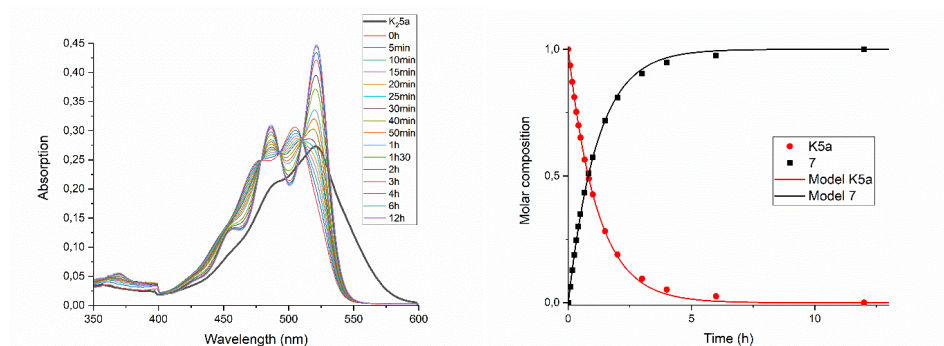
Figure 5. *Absorption spectra of compound **K5a** (black, λ_{max}= 522 nm) in DMF and **5a** (red, λ_{max}= 506 nm), formed after acidification with 50 μl 3M HCl. In the time-dependent absorption spectra the reaction from **5a** to compound **7** (λ_{max}= 521 and 486 nm) is visible. Isosbestic points are observed at 479, 492 and 510 nm.*

In order to determine accurate rate constants for the amic acid hydrolysis, as a function of the molecular structure of the attached secondary amine, the hydrolysis of PMIMAA **H5a** was investigated, as depicted in Scheme 3. This hydrolysis is a clean process and the spectra in Figure 5 exhibit clear isosbestic points at 479, 493 and 510 nm. Rate

constants for the PMIMAAs **H5a-H5e**, depicted in Table 3, are in line with the results obtained from the decomposition of the PDAAs **H₂4a-H₂4e**. To substantiate the claim that cyclic amines the lower hydrolysis rate for cyclic amines, **H5f** was also hydrolysed under the same conditions (Fig S10). The rate of hydrolysis was determined at $3.0*10^{-3}$ s^{-1}. This result implies that, with the notable exception of **K5c**, we can confirm that the hydrolysis of amic acids derived from cyclic amines is a slower process.

Table 3.

Compound	5a	5b	5c	5d	5e	5f
Reaction rate[a]	$2.4*10^{-4}$	$1.5*10^{-4}$	$3.7*10^{-3}$	$4.5*10^{-4}$	$9.4*10^{-4}$	$3.0*10^{-3}$

a: reaction rates k' in s^{-1}
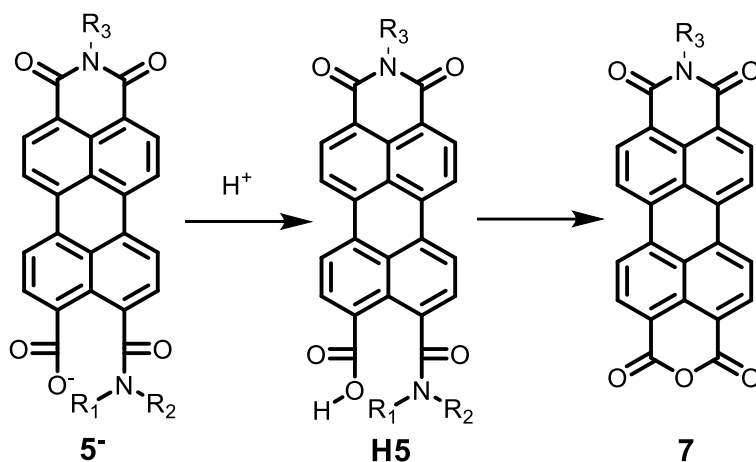
Scheme 3. *Hydrolysis of PMIMAA* **K5**

3.2.5. Gelation observed with NMR and UV-VIS

In order to investigate hydrogel formation at the molecular level , ^{1}H NMR spectra were taken as a function of time during the gelation of **K₂4a** in a pH 4 CD₃COOD/NaOD buffer. This system was chosen because we did not have fully deuterated GdL, and because we have previously demonstrated that proper hydrogel formation takes place in pH 4 buffers.

NMR spectra taken before and after acidification (at 1 minute intervals) are depicted in Figure 6. From these NMR spectra it is clearly visible that acidification induces aggregation of the amic acids, as the aromatic protons shift, broaden and finally disappear in 10 minutes. Proton shifts and broadening is also observed for the aliphatic protons, but in contrast to their aromatic counterparts, the aliphatic resonances do not disappear. This observation indicates that primarily the aromatic part of hydrogelator **H₂4a** is immobilised and the aromatic proton resonances are broadened to a large extent.
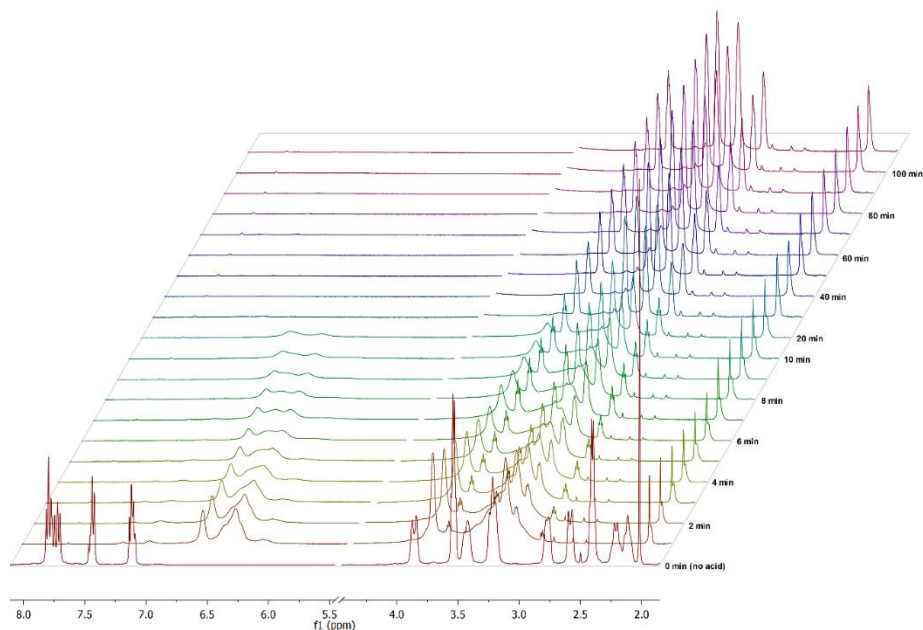
Figure 6. NMR measurement of **K₂4a** in deuterated acetic acid buffer at pH 4.

This is a clear indication of π-π stacking of the aromatic perylene moieties. After 30 minutes the aggregation process of the neutral protonated species **H₂4a** is followed by hydrolysis, that eventually forms PDA **1** and piperazine **2a**, see Scheme 1. The protons of aggregated PDA are not visible in the proton NMR, which makes perfect sense, since PDA will form more rigid and better ordered stacks than either **H₂4a** or **H5a**. The presence of piperazine **2a**, however, is clearly visible in the NMR by the emergence of sharp and intense resonances in the aliphatic region of the spectrum. The resonances below 2.7 ppm, present in the spectrum of **K₂4a**, are absent in the spectrum, which is consistent with the spectra of compound **2a** that was recorded independently (fig S42). Obviously the high field resonances observed in the spectrum of **H₂4a** are caused by strong shielding induced by the perylene skeleton. In the equivalent non-deuterated system gel formation took place in about 1 hour and 45 minutes.

3.2.6. UV-VIS
The gelation process of compound **K₂4a** was monitored by UV-Vis spectroscopy as well. Because the gelation already takes place at very low concentrations ~10^{-4}-10^{-5} M, absorption spectra can be recorded at convenient optical densities using a 1 mm pathway cuvette. For this experiment GdL was used to lower the pH and this experiment was performed under the same conditions as for the standard gel preparation, see gel formation experiments. The absorption spectra taken at different time intervals are depicted in Figure 7. In the first hour, the absorption maxima at 465 and 439 nm of the molecularly dissolved amic acid salt gradually decreases. In contrast to the kinetic experiments that were performed in DMF, the blue-shifted absorption of **H₂4a** has not been observed, which implies that this compound is not molecularly dissolved in water. Instead, a broad, red-shifted and profoundly less intense absorption emerges around 482 nm, which most likely originates from aggregated **H₂4a.** The absorption remains fairly stable for the
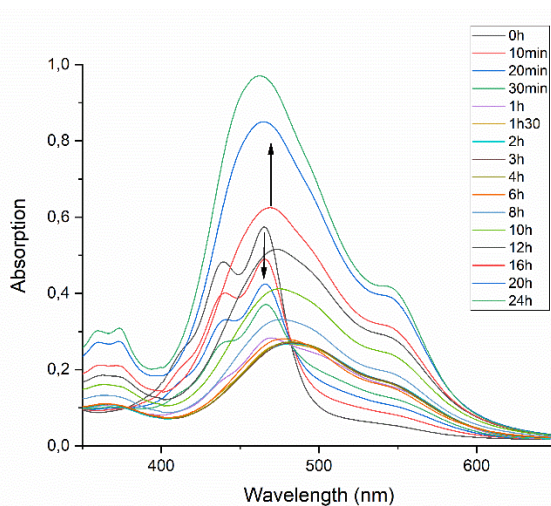
Figure 7: absorptions of an aqueous gel of K₂4a with 0.05 M GdL monitored over 24 hours. One spectrum was taken every 10 minutes for the first two hours, then one spectrum every 40 minutes for the remaining 22 hours.

following 5 hours. Subsequently the absorption grows in intensity and gradually shift to the blue to 462 nm. The final spectra obtained after 20-24 hours remain stationary, apart from increases in intensity induced by syneresis, and therefore is expected to be the spectra of fully aggregated PDA.

During the first hour the decrease of the structured absorption spectrum of **K₂4a** is indicative of protonation of this compound and the aggregation of the compounds **H4a⁻** and **H₂4a** that have been formed upon protonation. Formation of these aggregated species takes place in one hour and this is consistent with rheology experiments that demonstrate the formation of a very soft ~1 Pa gel in this timeframe. The aggregation process is accompanied by a ~60% loss of absorption intensity and this phenomenon may be indicative of the formation of unordered and rather lose aggregated structures. After 5 hours the absorption spectra increase in intensity and this may indicate that hydrolysis takes place. It is known for molecularly dissolved perylenes that the extinction coefficients increases twofold, going from a tetraester to a diimide via the monoimide diester, while the absorption wavelength is red-shifted.[20,48] This behaviour has also been demonstrated for the acid induced decomposition of **H₂4** to **1** in DMF, as illustrated in Figure 4. In our case we are looking at aggregated structures and the exact ordering of the perylene molecules in the aggregates will either induce red shifts (J-aggregates) or blue shifts (H-aggregates) and may also influence the absorption intensities. The red-shifts, anticipated on the formation of PDA **1** have not been observed, which may be the case because the type of aggregation may have changed as a consequence of the chemical transformation that took place. The anticipated increase in intensity has been observed and it is likely that this increase has been enhanced by changing the aggregation; we anticipate that PDA forms tighter aggregates than PDAAs (larger π-system intensity increase). Finally it should be noted that a small part of the intensity increase is due to the shrinking of the gel.

3.2.7. Visualization by Cryo-TEM measurements

Gelation from small molecules is usually induced by aggregation to form bundles with large aspect ratios that are cross-linked. In Figure 8a a cryo TEM image of the gel formed with compound K_24a (c= 0.5 mM) and GdL (c= 0.025 M) is depicted. In Figure 8a it is visible that the gel is homogeneous and consists of long cross-linked fibres. Upon analysis of the fibres, it was shown that "single-stranded" fibres range in thickness from 3.5 nm to 6.5 nm, while the dimensions of a single molecule of perylene are 0.5 by 1.25 nm. This means that the smallest fibres already contain multiple stacks of perylene, and providing that the fibres consist of PDA molecules only, the number of single PDA strands in a fibre would be in the order of 10-30. In Figure 8b a gel is depicted that was formed by neutralizing a K_24a solution with a few drops of 1.0 M HCl. The gels structure is similar, consisting of cross-linked fibres, but the fibrilous network in this sample clearly is less homogeneous. The fibres appear to be thicker with smaller mesh sizes and some areas are almost devoid of fibres. Also the presence of larger spherical chunks of material are visible in Figure 8b. It appears that the slower gel formation, that is achieved by a slower and more homogeneous lowering of the pH by using GdL, has resulted in more homogeneous gels. When comparing amic acids K_24a-K_24e, where a slower hydrolysis results in a mechanically stronger and more stable hydrogel, this is an additional effect on the gel formation that should not be underestimated.
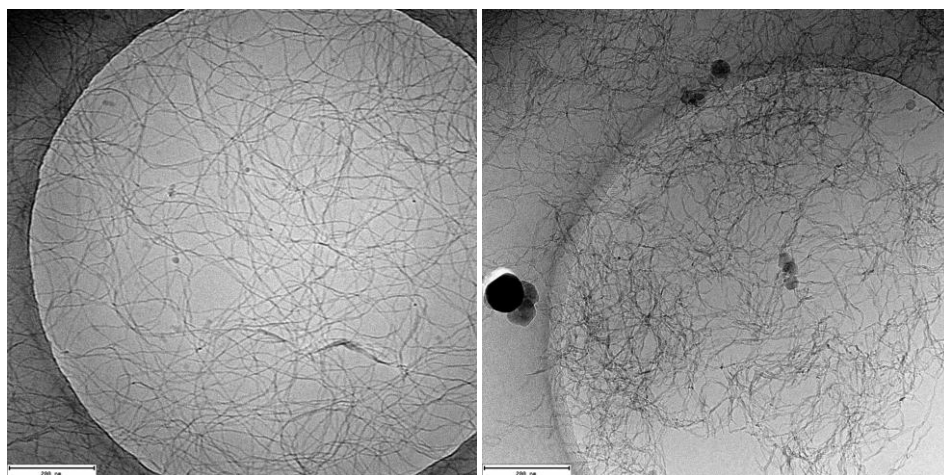

Figure 8. *Left Figure 8a. Cryo-TEM image of the hydrogel formed with K_24a (c= 0.5 mM) and GdL (0.025 M), right Figure 8b. Hydrogel from the same compound prepared by adding a few drops of a 1.0 M HCl solution, right.*

3.2.8. Proposed gelation mechanism.

In this section we will propose a detailed mechanism for the gelation of amic acid salts 4^{2-}. Along with this mechanism we will discuss the experimental data that (dis)favour this gelation mechanism. Upon slow acidification of a solution of 4^{2-}, which is typically the case when GdL is used, 4^{2-} gets protonated and $H4^-$ will be formed. This compound will have a decreased solubility in aqueous media and formd non-fluorescent aggregates, probably dimers or micelles.[49,50] This is expected because the formation of larger rigid aggregates is energetically unfavourable due to a high charge density on the stacks. Upon further protonation H_24 will be formed and this neutral species will be entirely insoluble in water and is expected to form long fibrous aggregates. In order to accommodate this

stacking the piperazine amide units should be placed at the axial position with respect to the perylene plane. Also due to steric hindrance the perylene units should be rotated with respect to each other along the stack axis, at an extent depending on the bulk of the amic acid substituents. Bundling of multiple stacks or the formation of cross-links of the fibres seems unlikely at this stage, because the amic acid functionalities are fairly compatible with the water phase. In the cases of piperazine-functionalized amic acids, protonation of the piperazine amine may be another argument that opposes bundling and cross-linking of the fibres at this stage. Rheology experiments indicate that the initially formed aggregated structures, presumable those build up from $H_2 4$, are very weak gels with moduli in the 1 Pa range. It remains unknown what effect the presence of both cis and trans amic acids have on the aggregation process. It is conceivable that the gelator self-sorts in different stacks, in a process that removes some of the steric hindrance of the piperazine amide group, see Scheme S2. but it is also possible they co-assemble in the same stack. Rate and reversibility of aggregation determines the extend of self-sorting and the eventual quality of the gels. In the final highly symmetric PDA-gel, the effect of self-sorting will have disappeared

In time, either during further acidification by GdL or at a stable pH in buffered solutions, hydrolysis of the amic acid takes place, forming $H3$ initially and finally PDA 1. The rates of this process in aggregates formed of $H_2 4$ and $H3$ is has not been determined experimentally, but most likely these rates are proportional to the rates measured for $K_2 4a$-$K_2 4e$ in DMF, unless steric factors in these stacks play a decisive role. The transformation from an amic acid to an anhydride will promote the aggregation process, because the anhydride functionality is planar and much smaller than the amic acid, thereby decreasing steric hindrance of the aggregation process. Due to this the fibres will become more rigid. Due to the disappearance of the large and deplanarizing carboxylic acid and piperazine amide groups, the less hydrophilic nature of the anhydride group and the formation of more ordered rigid π-π stacks, bundling and further cross-linking of the fibres will mostly take place at this stage.

Experimental evidence favouring this mechanism can be found in various experiments. The dimerization or micellization of $H4^-$ will remain hypothetical, as we have not attempted to make this species specifically. Aggregation upon acidification, either of $H4^-$ or $H_2 4$ is evident from the disappearance of fluorescence upon acidification. Also, the 10 nm blue shift that is observed upon formation of $H_2 4$ from 4^{2-} is not observed in water, which indicates that 4^{2-} is not molecularly dissolved in water and thus has aggregated instantaneously. The aggregation of $H_2 4$ is a more certain bet and supported by various experiments. To start with, it is known that all neutral PTCA derivatives are hydrophobic and not soluble in polar solvents like water. The structurally related perylene diamic esters are the relevant examples. It is also known that non-bay substituted uncharged PTCAs will form aggregates by π-π stacking[23].

Experimental evidence for the aggregation of $H_2 4$ is found in the NMR experiments in acetate buffer, where acidification leads to an immediate strong broadening of specifically the resonances in the aromatic part of the amic acid spectrum. UV broadening upon acidification and the immediate disappearance of fluorescence upon acidification provide further support for the occurrence of an aggregation process. The slow gel formation, evidenced from macroscopic experiments and the slow development of mechanical strength observed in the rheology experiments are indications that aggregated amic acid

are not the constituents of the final gel. The self-assembled structures formed from **H₂4** are too weak to form the strong gels that are finally obtained.

Experimental evidence for the decomposition comes from different sources. First of all hydrolysis of the structurally similar naphthyl amic acids in water have been reported and the kinetics of this process was determined by UV-Vis experiments. The decomposition of the perylene amic acids **H₂4a-H₂4e** was demonstrated in DMF and here too the kinetics of this process has been determined using absorption spectroscopy. Direct evidence for decomposition during gel formation in water comes from the NMR experiments with **H₂4a** in a pH 4 acetate buffer. The release of ethanolpiperazine **2a** at the later stages of the gelation process is clearly visible in this experiment. UV-Vis absorption experiments using **H₂4a** and GdL in water reveal the formation of PDA **1** at the later stages of the process. Although **H₂4a**, **H3a** and **1** are all aggregated and their absorption spectra depend on the exact type of aggregation, the formation of **1** from **H₂4a** is evident from the large increase of the absorption intensity. Finally the rheology experiments exhibit strong increases in mechanical strength of the gels on time frames for the different gelators that coincide with the hydrolysis rates of these respective gelator molecules.

We have demonstrated the hydrogels were also formed from PMIMAA salts like **K5a** and **K9**, by following a similar two-step mechanism of aggregation upon amic acid neutralisation, followed by hydrolysis to form anhydride. However, the gels formed from these gelators have inferior mechanical properties. Several factors may be identified to explain this phenomenon. To start with, due to the amphiphilic nature of these molecules, the gelation process does not start from a molecularly dissolved solution, as is the case for **K₂4**, but from aggregates in aqueous solution, for example micelles. Upon protonation, the morphology changes to fibrous stacks, which can trigger precipitation, since the protonated PMIMAA will have a low solubility. If protonation could be done even slower and more controlled, this hurdle may be overcome. The final structure is different and the butyl imide and dibutyl ester functionality may hamper the stacking and cross-linking process.

3.3 Conclusions
A novel class of perylene-based hydrogelators has been discovered; perylene diamic acid salts, perylene monoamic acid salts with either an imide or a diester functionality at the opposite peri position. In addition the ester analogues of perylene diamic acid salts form hydrogels as well. In all cases hydrogels are formed straight from crude reaction mixtures by protonation of the amic acid and subsequent decomposition to form anhydrides.

For a more detailed study a series of perylene diamic acid potassium salts were synthesised and their gelation behaviour was investigated in water. The investigated compounds had amic acid functionalities derived from cyclic secondary amines, whose structure was systematically varied. All compounds successfully gelated into hydrogels upon slow protonation. The obtained hydrogels show respectable mechanical properties and profound synerisis over time. The gelation process was investigated using time-dependant UV-VIS and ¹H-NMR, cryo-TEM and rheology. It was found that hydrogels from amic acids with more hydrophilic amides hydrolyse slower and have superior mechanical properties compared to more hydrophobic amides. We propose that the perylene amic acid already aggregates to some extend in water. When the acidity of the solution increases, the amic acids are protonated, lowering the charge of the aggregate,

promoting further aggregation. This is followed by hydrolysis of the amide which will eliminate steric hindrance between monomers, increasing the supramolecular interactions between the monomers, and again promoting aggregation. Slower protonation and hydrolysis will result in longer aggregates that have a more homogenous distribution, which enhances the mechanical properties. Thus, forming hydrogels that have the same molecular composition, but with greatly different properties. We also conclude that the formation of hydrogels from perylene amic acid salts and their ester analogues is quit universal and has been observed for different classes of compounds.

3.4 Experimental

3.4.1. Synthesis of K₂4a-k₂4e

To a 500 mL round bottom flask, DMSO (20 mL), PDA (1.00 g, 2.55 mmol), K_2CO_3 (2.80 g, 20.39 mmol) and the appropriate amine (10.20 mmol) were added. The resulting slurry is stirred for 2 hours at 60 ºC. After reaction completion, the mixture is left to cool to room temperature. This is followed by the addition of methanol (10 mL) under strong stirring. The mixture is then poured into acetone (200 mL) to precipitate the product. The solids are filtered off and dissolved in methanol (10 mL) again. The precipitation in acetone (200 mL) is repeated. This yields potassium amic acid salts $K_2$4a-$K_2$4e as yellow/orange solids.

$K_2$4a: Yield: 1.208 g, 65%
$K_2$4b: Yield: 0.784 g, 48%
$K_2$4c: Yield: 0.688 g, 42%
$K_2$4d: Yield: 0.977 g, 60%
$K_2$4e: Yield: 1.121 g, 72%

3.4.2. Gelation of K₂4a-K₂4e

A solution of $K_2$4 with double the desired hydrogel concentration is prepared in distilled water. Also a solution of 0.1 mM GdL is freshly prepared, or an acidic buffer is prepared. The two solutions are mixture in equal amounts. When using GdL, this yields a fluorescent solution that will turn into a non-fluorescent red solution within an hour. GdL needs to be prepared immediately before addition to $K_2$4, since its hydrolysis will start when in contact with water, lowering the pH. When an acidic buffer is used instead of GdL, a non-fluorescent red solution is formed almost immediately. The solution is left to stand and will form a hydrogel, after which it will undergo syneresis, according to the times noted in table 1.

3.4.3. Synthesis of the gelator solutions for crude gelation experiments.

For the amic acid preparation a stock solution consisting of 10 mL of DMF and 760 mg, 5mmol DBU was prepared. PDA 100 mg (0.25 mmol) was suspended in 2.1 mL stock solution (containing 1.0 mmol, 4 eq) DBU. To this solution 1.0 mmol, 4 eq of amine 2 was added. The reaction mixture was stirred overnight at room temperature.

For the ester preparation a stock solution consisting of 10 mL of DMF and 10 mmol, 1.52 g DBU was prepared. PDA 100 mg (0.25 mmol) was suspended in 2.2 mL stock solution (containing 2.0 mmol, 8 eq) DMF. To this solution 2.0 mmol, 8 eq alcohol 101 was added. The reaction mixture was stirred overnight at room temperature.

For the gelation experiments 18 mL of demi water was added to the reaction mixture containing the hydrogelator 4 or 100. 3.0 mL of this solution was added to a 5 mL asperine tube. Depending on the amine (diamine or monoamine) used for preparing 4, 0.5 M freshly prepared Gdl solution was added (1.05 or 0.7 mL). To the solution containing the

ester gelator 100, 0.8 mL 0.5M Gdl solution was added. The hydrogelator concentration in the final mixture ~1*10 M.

3.5 Supporting information
3.5.1. Synthesis and gelation of amic acids from crude reaction mixtures
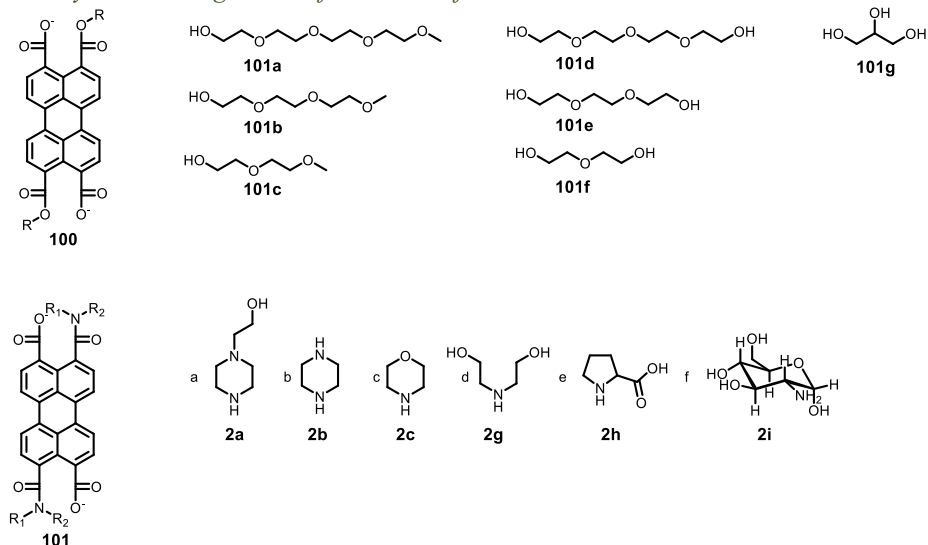
Scheme S1. *Synthesized amic acids from crude reaction mixtures.*

Compounds **100a-g** and **4a-f** have been prepared in DMF with DBU as the base under the usual synthetic conditions, see experimental section (crude gelation experiments). The reaction mixtures were diluted with 9 volumes of water and from these 12.5 mM solutions hydrogels were prepared by addition of 1.2 to 1.5 equivalents of a freshly prepared 0.5 M Gdl solution. Stable gels (inverted test tube) form within 2 hours and most of them shrink within 24 hours. However, in some cases, syneresis is not observed and gels remain unchanged for days/weeks. This phenomenon is not understood by us yet, but it appears that apart from the chemical structure of the hydrogelator, the amount of added GdL seems to play a role. This is so because for the same hydrogelator syneresis and stable gels are formed under very similar, near identical conditions. A dilution series conducted with gelator **4b** revealed that the critical gel concentration (CGC) of crude gels from reaction mixtures are similar to those of the pure gels made from the respective potassium salts **K24** in water.

By mixing gelator molecules **4** and **100** in various combinations in a 1:1 ratio (12.5 mM total) good hydrogels were obtained. Some shrank, some did not shrink. Preparing a hydrogel with **K₄X** the perylene tetracarboxylic acid salt of perylene tetracarboxylic acid was not successful; upon acidification a precipitate was formed. It also did not work in mixtures.

Addition of 1 M HCl to a solution of gelator did not always yield stable gels. For example compound **101a** and **101b** yielded gels, whereas **101c** and **101d** yielded inhomogeneous gel-like materials and a precipitate respectively. It is anticipated that a large pH gradient

leads may lead to premature amic acid decomposition and uncontrolled precipitation of PDA from the solution.

Scheme S2. Self-sorting of cis and trans diamic acids.

3.5.2. UV-VIS spectra

A)   B)

Figure S1. a) Normalized UV-Vis absorption and b) Normalized fluorescence emission spectra of Compounds **K₂4f, K5f** and **K9f** in Ethanol.
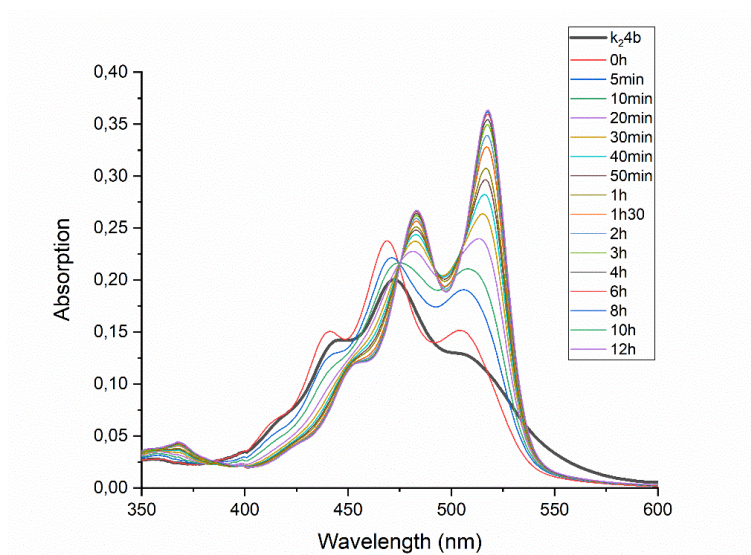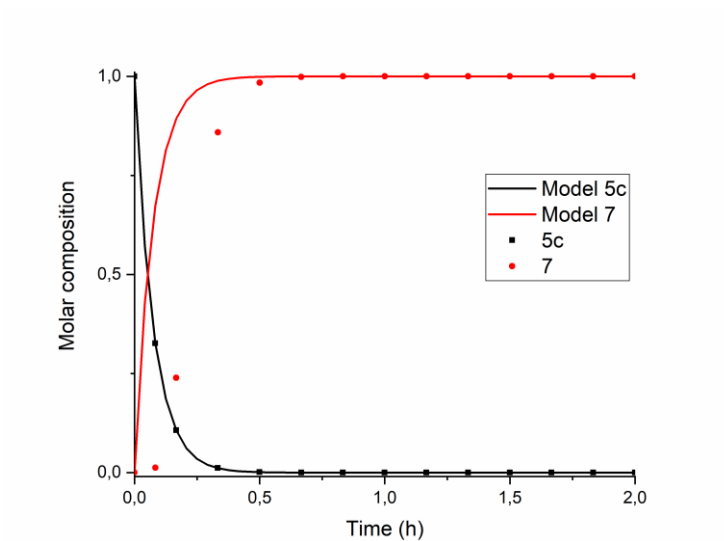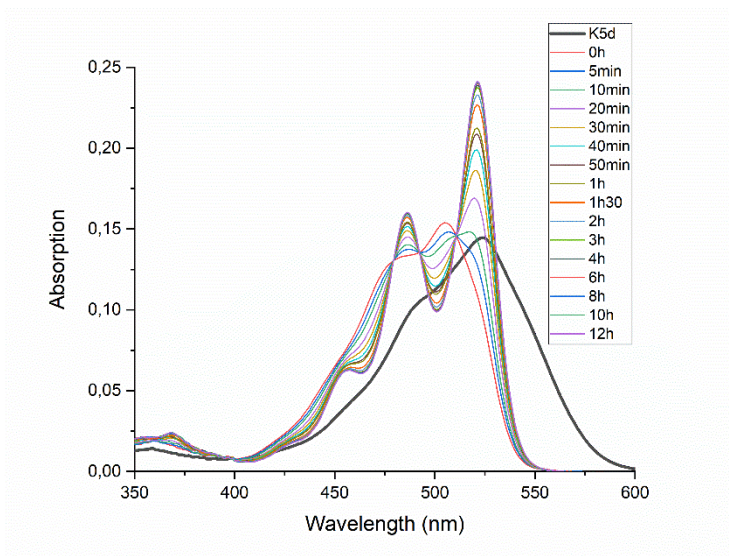
Figure S2. *Absorption spectra of the acidification and hydrolysis of amic acid **4b** with 50 μl 3M HCl in DMF at room temperature. The black line represents **K₂4b** before acidification. The final spectrum at 12 hours represents PDA **1**.*
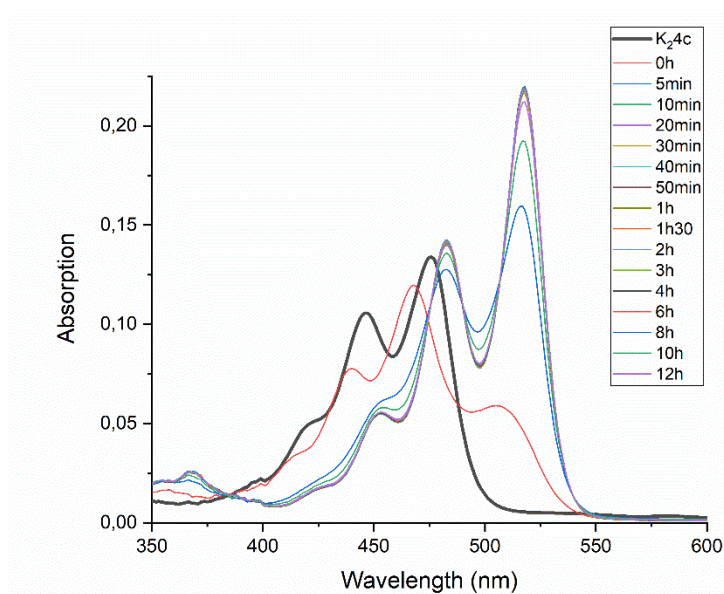
Figure S3. *Absorption spectra of the acidification and hydrolysis of amic acid **4c** with 50 μl 3M HCl in DMF at room temperature. The black line represents **K₂4c** before acidification. The final spectrum at 12 hours represents PDA **1**.*
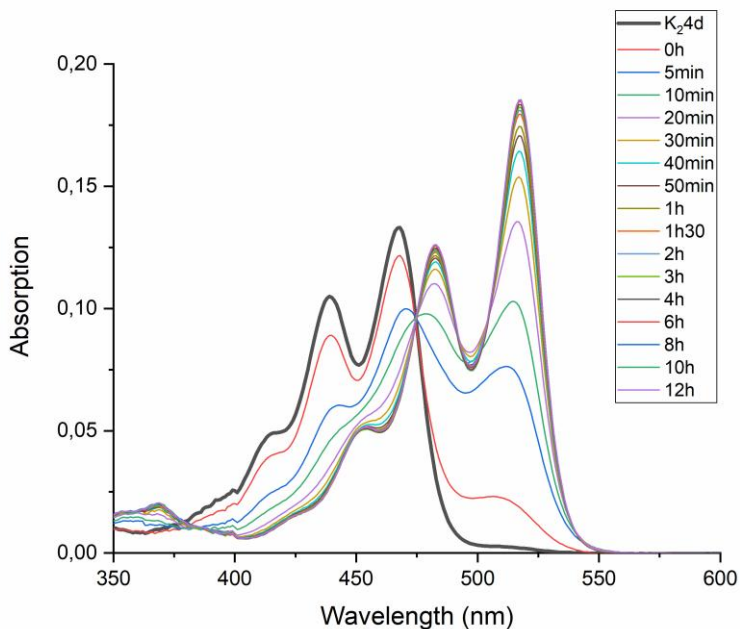
Figure S4. *Absorption spectra of the acidification and hydrolysis of amic acid **4d** with 50 μl 3M HCl in DMF at room temperature. The black line represents **K₂4d** before acidification. The final spectrum at 12 hours represents PDA **1**.*
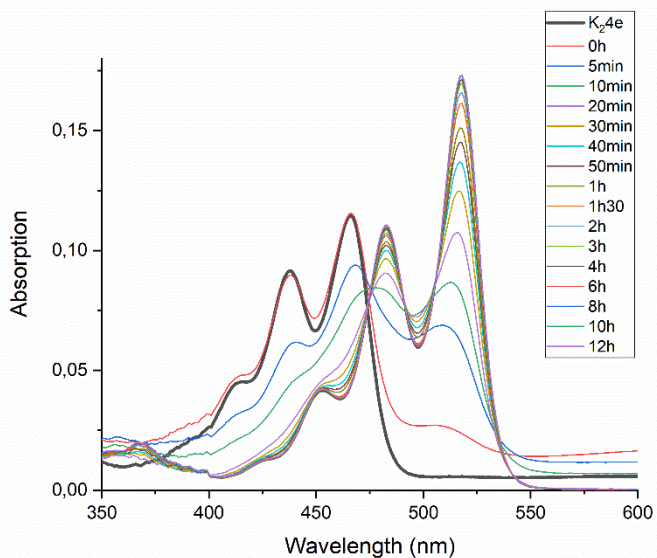
Figure S5. *Absorption spectra of the acidification and hydrolysis of amic acid **4e** with 50 μl 3M HCl in DMF at room temperature. The black line represents **K₂4e** before acidification. The final spectrum at 12 hours represents PDA **1**.*
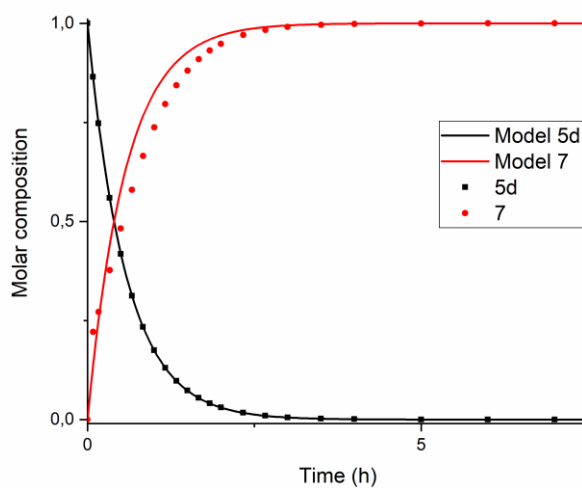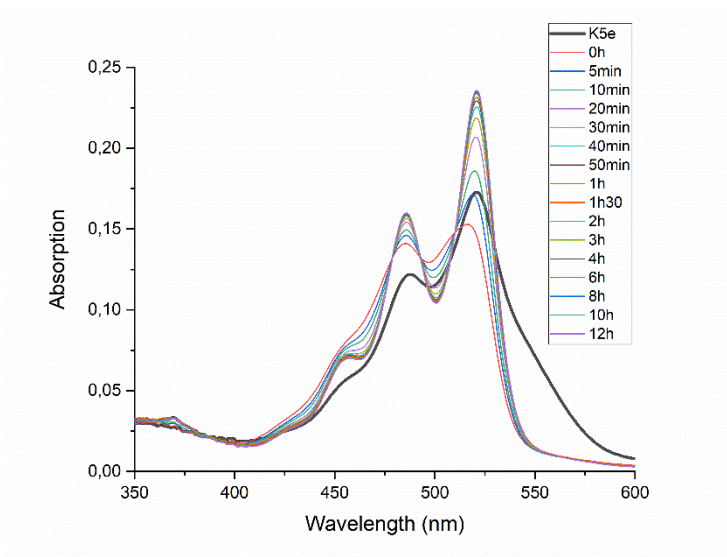
A)
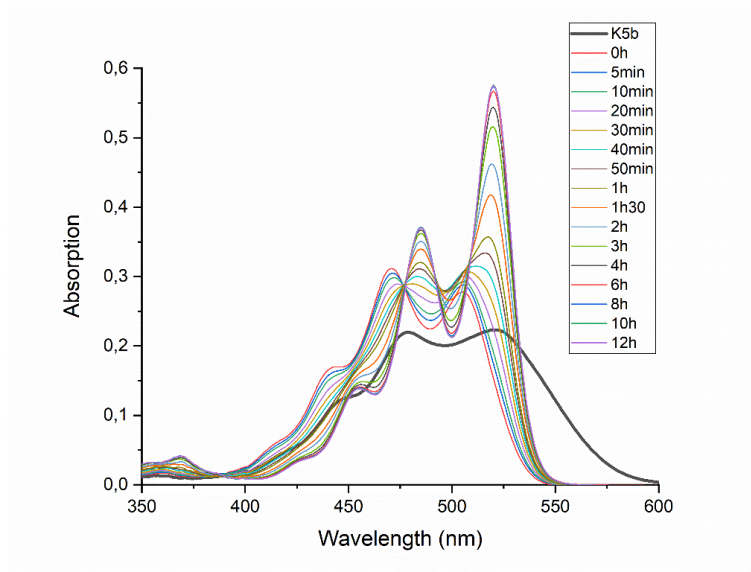
B)
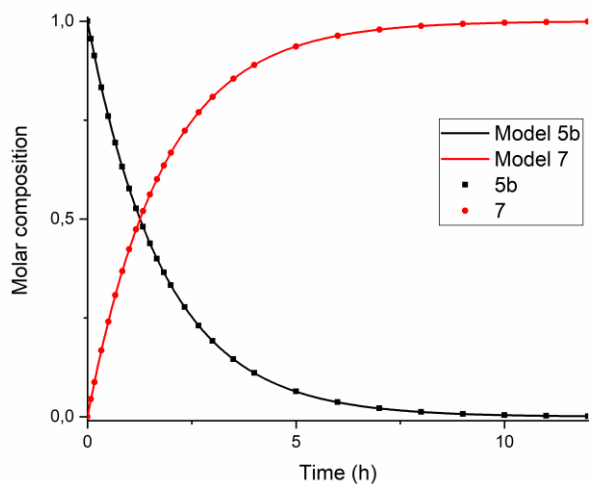
Figure S6. *(A) Absorption spectra of the acidification and hydrolysis of amic acid **5b** with 50 µl 3M HCl in DMF at room temperature. The black line represents **K5b** before acidification, λ_{max} = 521 nm. The final spectrum at 12 hours represents PMIMA **7**. Isobestic points are at 477 nm. **(B)** Composition of the reaction mixtures obtained from* UV-VIS spectra. Solid lines represent the theoretical fitting cuves obtained using a fist-order decay. From this the rate constant is calculated at $1.5*10^{-4}$ s^{-1}.
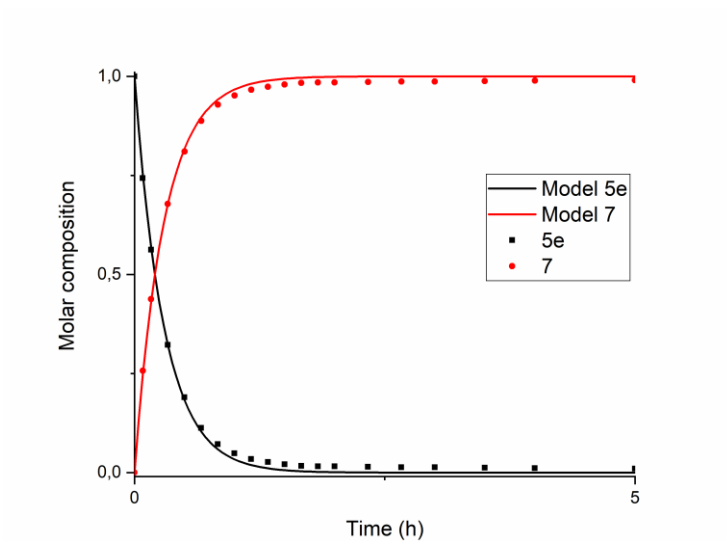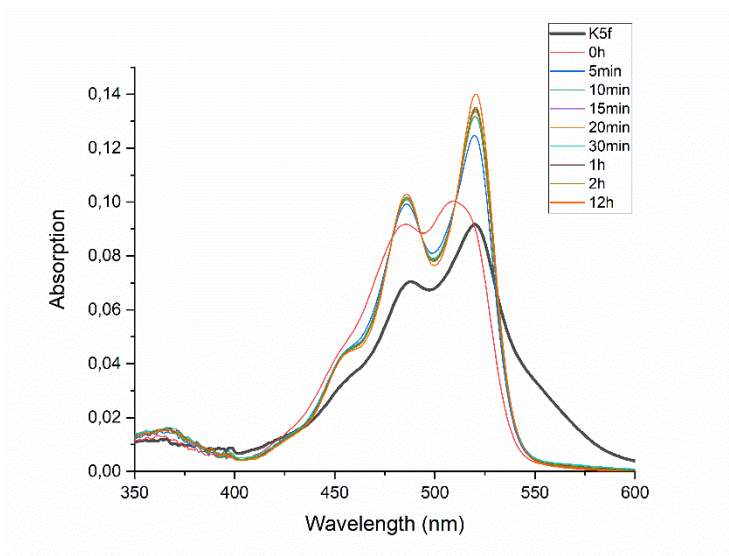
A)
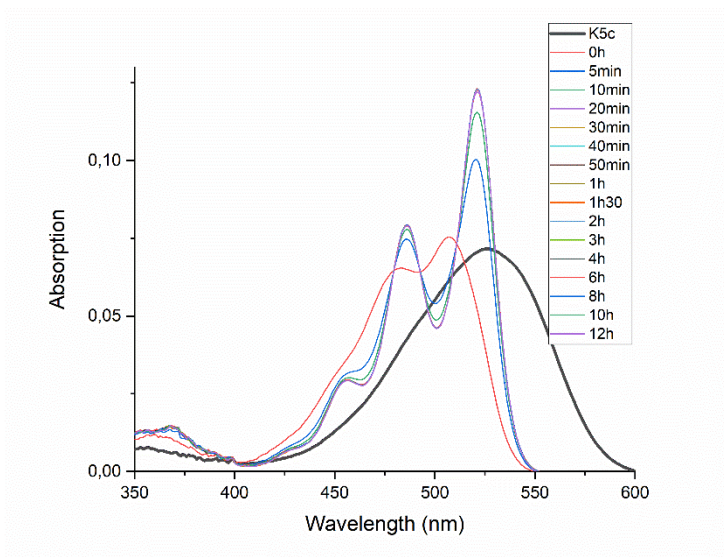
B)

Figure S7. (A) *Absorption spectra of the acidification and hydrolysis of amic acid **5c** with 50 µl 3M HCl in DMF at room temperature. The black line represents **K5c** before acidification, λ_{max} = 525 nm. The final spectrum at 12 hours represents PMIMA **7**. Isobestic points are at 479, 492 and 510 nm. **(B)** Composition of the reaction mixtures obtained from UV-VIS spectra. Solid lines represent the theoretical fitting cuves obtained using a fist-order decay. From this the rate constant is calculated at $3.7*10^{-3}$ s^{-1}.*

A)

B)

Figure S8. (A) *Absorption spectra of the acidification and hydrolysis of amic acid **5d** with 50 μl 3M HCl in DMF at room temperature. The black line represents **K5d** before acidification, λ_{max} = 524 nm. The final spectrum at 12 hours represents PMIMA **7**. Isobestic points are at 479, 492 and 510 nm. **(B)** Composition of the reaction mixtures obtained from UV-VIS spectra. Solid lines represent the theoretical fitting cuves obtained using a fist-order decay. From this the rate constant is calculated: $4.5*10^{-4}s^{-1}$.*
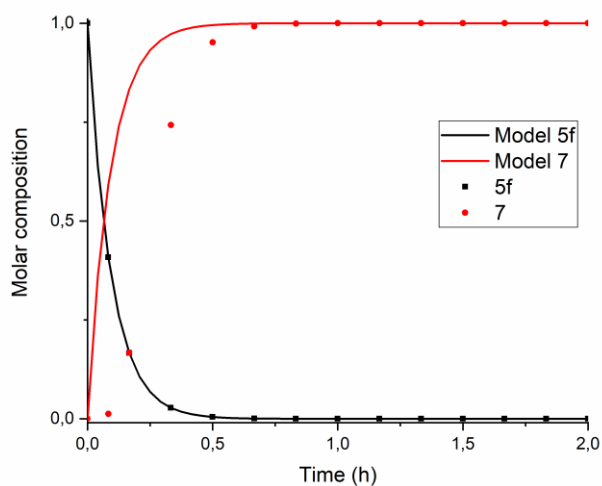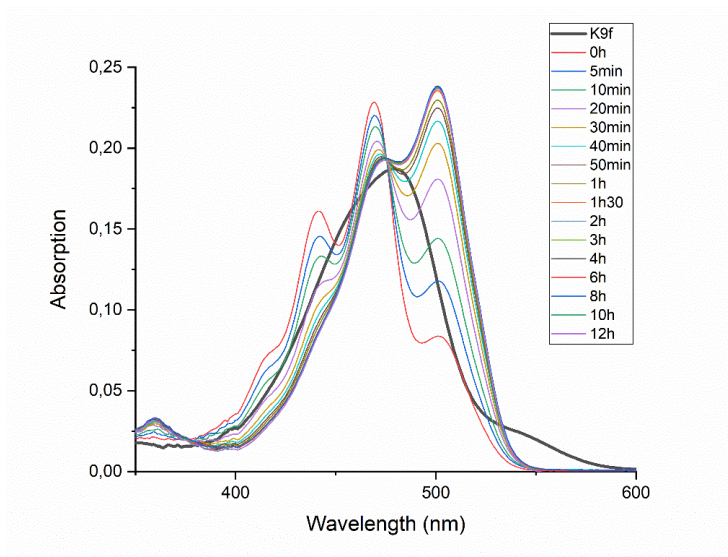
A)

B)

*Figure S9. (A) Absorption spectra of the acidification and hydrolysis of amic acid **5e** with 50 µl 3M HCl in DMF at room temperature. The black line represents **K5e** before acidification, λ_{max} = 486 and 520 nm. The final spectrum at 12 hours represents PMIMA **7**. Isobestic points are at 478, 492 and 510 nm. (B) Composition of the reaction mixtures obtained from UV-VIS spectra. Solid lines represent the theoretical fitting cuves obtained using a fist-order decay. From this the rate constant is calculated at $9.4*10^{-4}$ s^{-1}.*

A)

B)

Figure S10. (A) *Absorption spectra of the acidification and hydrolysis of amic acid* ***5f*** *with 50 µl 3M HCl in DMF at room temperature. The black line represents* ***K5f*** *before acidification, λ_{max} = 487 and 520 nm. The final spectrum at 12 hours represents PMIMA 7. Isobestic points are at 479, 492 and 510 nm. **(B)** Composition of the reaction mixtures obtained from UV-VIS spectra. Solid lines represent the theoretical fitting cuves obtained using a fist-order decay. From this the rate constant is calculated at $3.0*10^{-3}$ s^{-1}.*
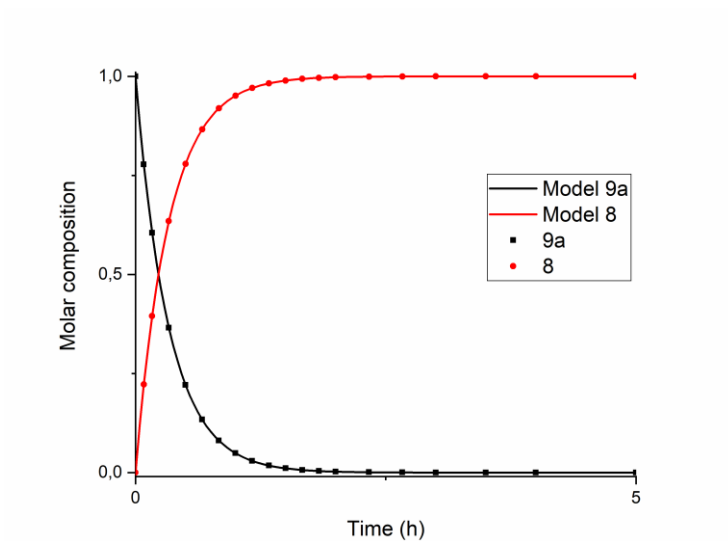
A)

B)

*Figure S11. (A) Absorption spectra of the acidification and hydrolysis of amic acid **9a** with 50 µl 3M HCl in DMF at room temperature. The black line represents **K9a** before acidification, λ_{max} = 479 nm. The final spectrum at 12 hours represents PMADE **8**. Isobestic points is at 475 nm. (B) Composition of the reaction mixtures obtained from UV-VIS spectra. Solid lines represent the theoretical fitting cuves obtained using a fist-order decay. From this the rate constant is calculated at $8.4*10^{-4}$ s^{-1}.*
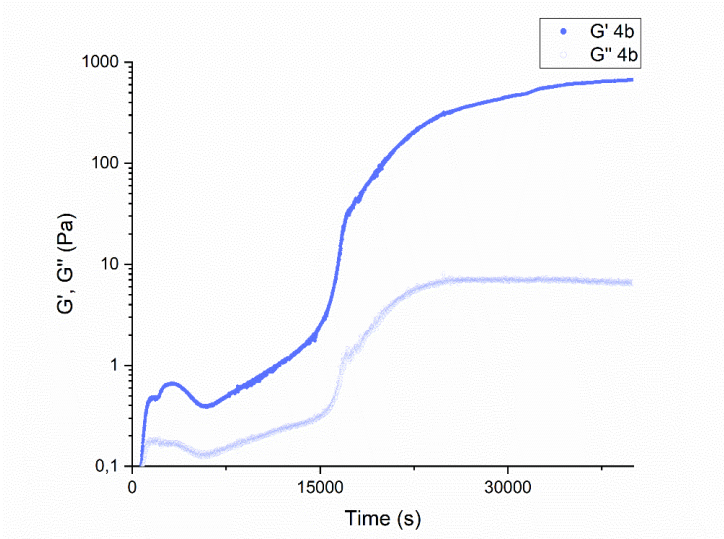
3.5.3. Rheology

Figure S12. *Rheological time-sweeps of G' and G'' of 1 mM aqueous gels of **K₄4b** with 0.05 M glucono-δ-lactone*

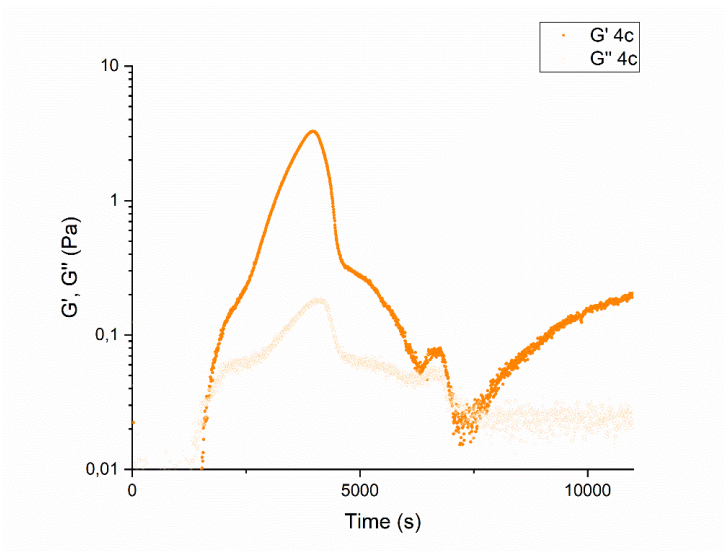***Figure S13.*** *Rheological time-sweeps of G' and G'' of 1 mM aqueous gels of **K₄4c** with 0.05 M glucono-δ-lactone*

Figure S14. *Rheological time-sweeps of G' and G'' of 1 mM aqueous gels of **K₄4d** with 0.05 M glucono-δ-lactone*

Figure S15. *Rheological time-sweeps of G' and G'' of 1 mM aqueous gels of **K₄4e** with 0.05 M glucono-δ-lactone*

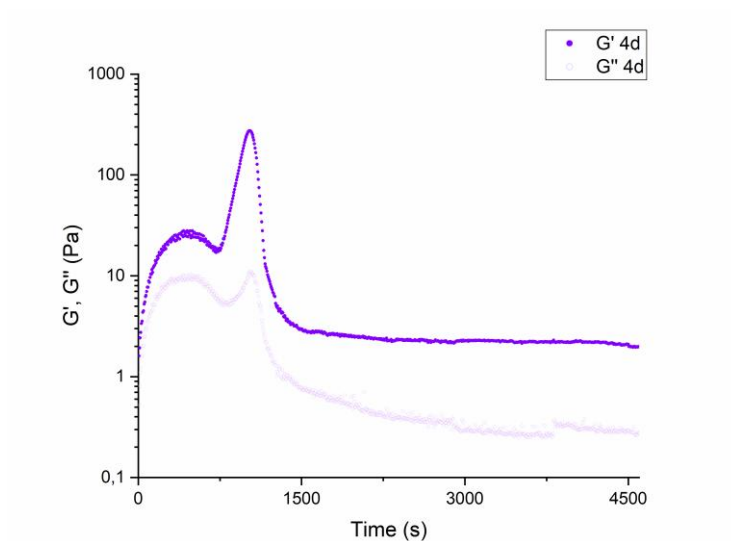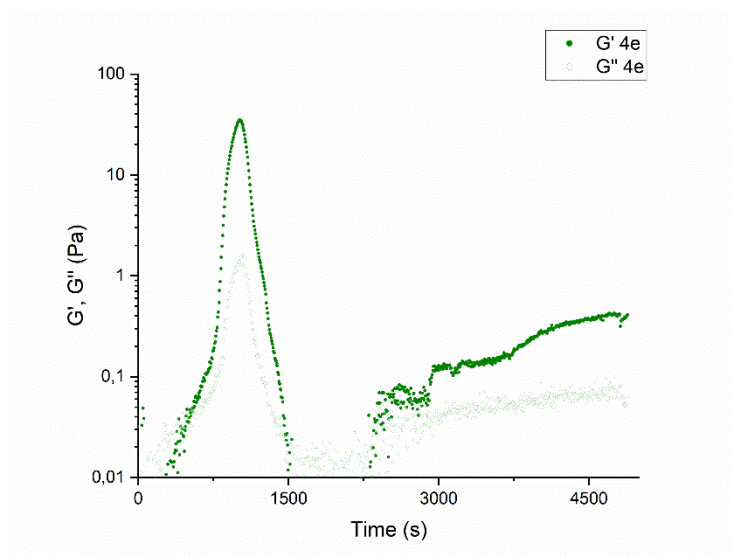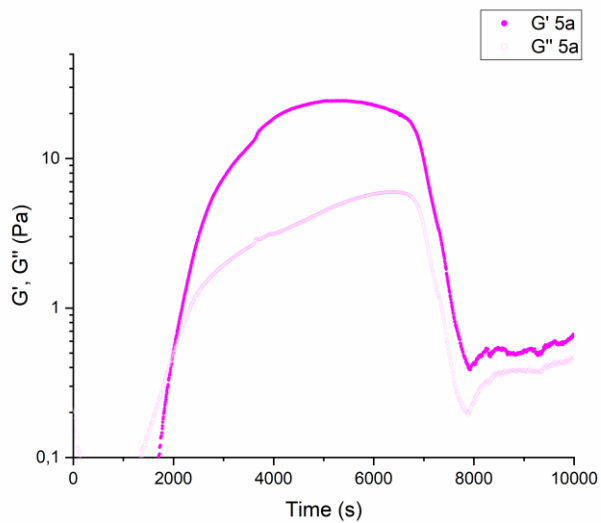*Figure S16. Rheological time-sweeps of G' and G'' of 1 mM aqueous gels of **K5a** with 0.05 M glucono-δ-lactone*
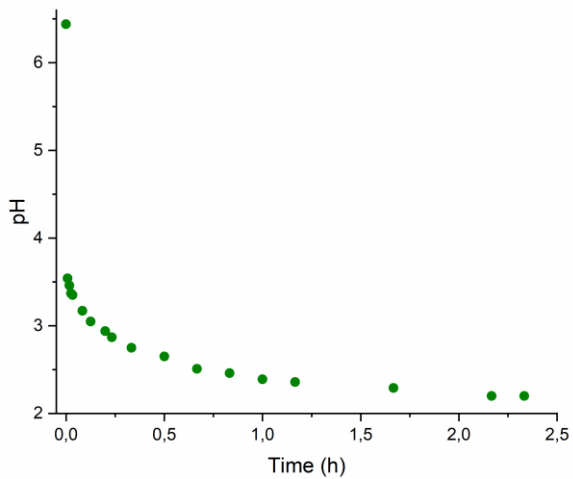

Figure S17. pH of a 0.05 M GdL solution over time.

3.5.4. Photos of hydrogels

Figure S18. *Gelation of crude amic acid reaction mixtures. The hydrogels contain 0.5-1% w/w amic acid, DBU-Cl salts, excess amine and ~10% DMF.*
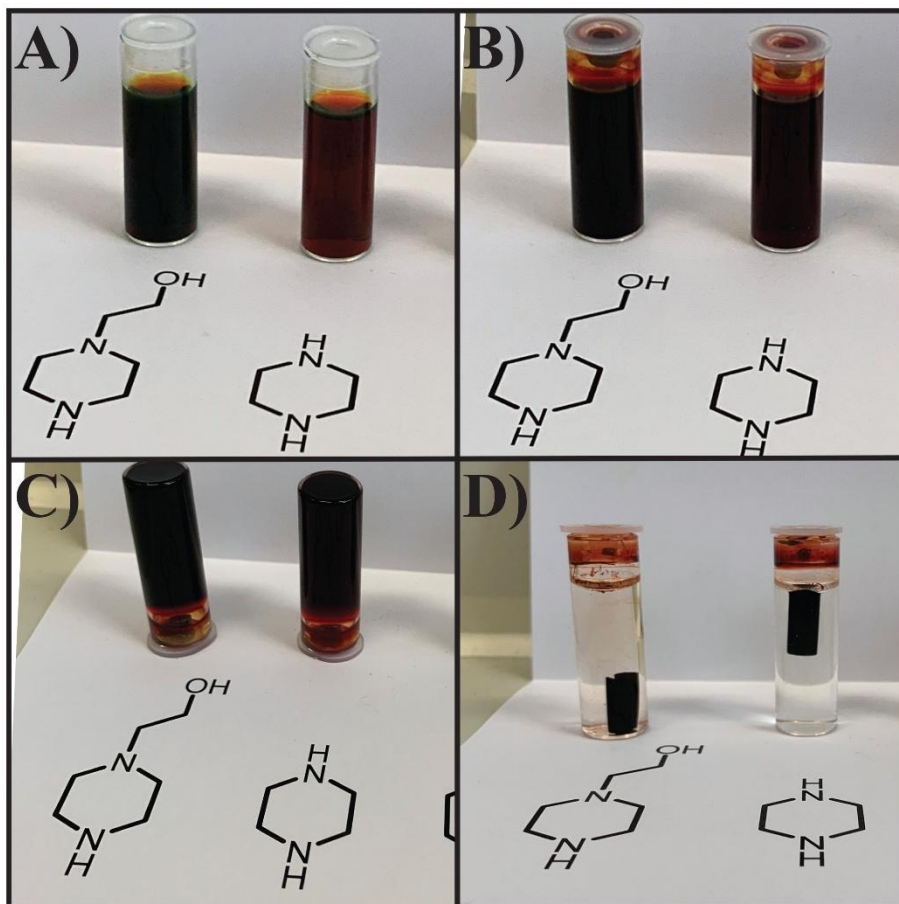
Figure S19. *Gelation of crude amic acid reaction mixtures. The hydrogels contain 0.5-1% w/w amic acid, DBU-Cl salts, excess amine and ~10% DMF.* **A)** *Solutions directly after adding HCl;* **B)** *Solutions after careful mixing;* **C)** *Solution have gelated, 25 minutes after acidification;* **D)** *Shrunken gels, 19h and 30min after acidification.*
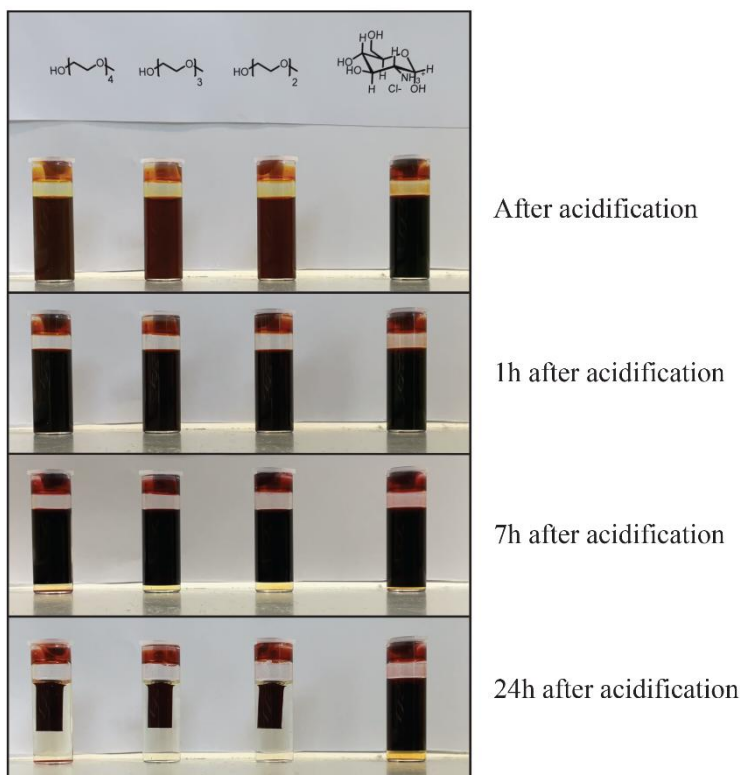
Figure S20. *Gelation of crude amic acid reaction mixtures. The hydrogels contain 0.5-1% w/w amic acid, DBU-Cl salts, excess amine/alcohol and ~10% DMF.*

Figure S21. *Gel inversion experiment of 2.5 * 10^{-3} M **K$_2$4a** in 0.25 M AcOH buffer of pH 4, 1 hour and 45 minutes after acidification.*

3.5.5. NMR spectra

Figure S22. *^{1}H-NMR spectrum of K$_{24}$a in CD$_3$OD.*

Figure S23. *^{13}C-NMR spectrum of K$_{24}$a in CD$_3$OD.*

Figure S24. *¹H-NMR spectrum of **K₂4b** in CD₃OD.*

Figure S25. *¹³C-NMR spectrum of **K₂4b** in CD₃OD.*

Figure S26. *^{1}H-NMR spectrum of* ***K₂4c*** *in CD₃OD.*

Figure S27. *^{1}H-NMR spectrum of* ***K₂4d*** *in CD₃OD.*

Figure S28. *¹³C-NMR spectrum of **K₂4d** in CD₃OD.*

Figure S29. *¹H-NMR spectrum of **K₂4e** in CD₃OD.*
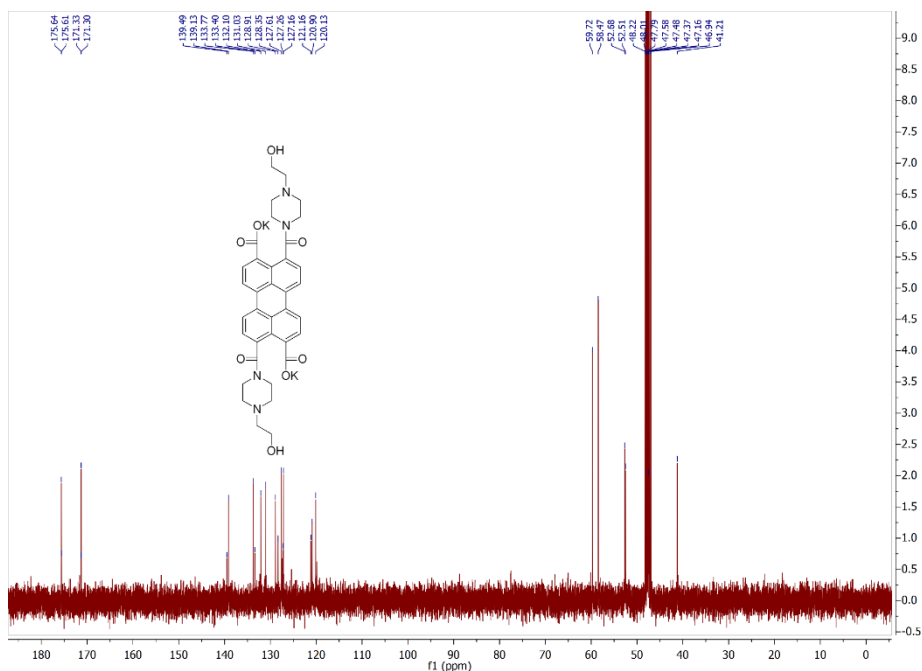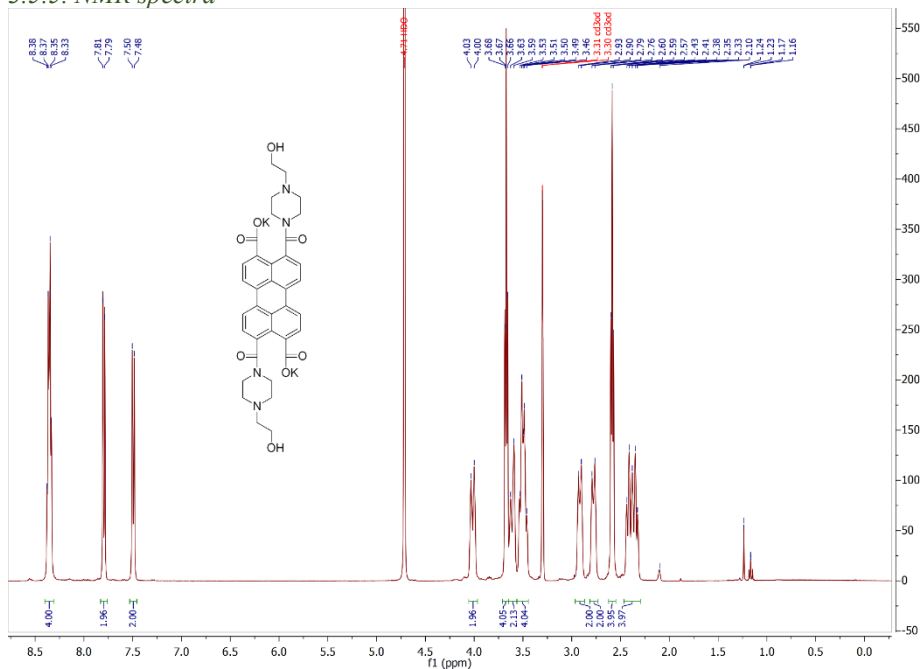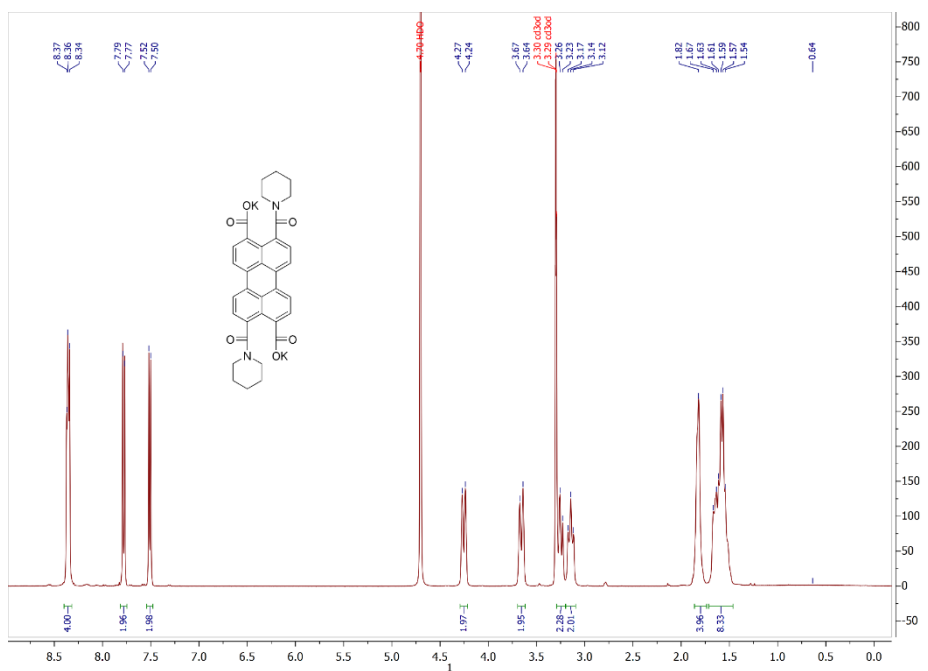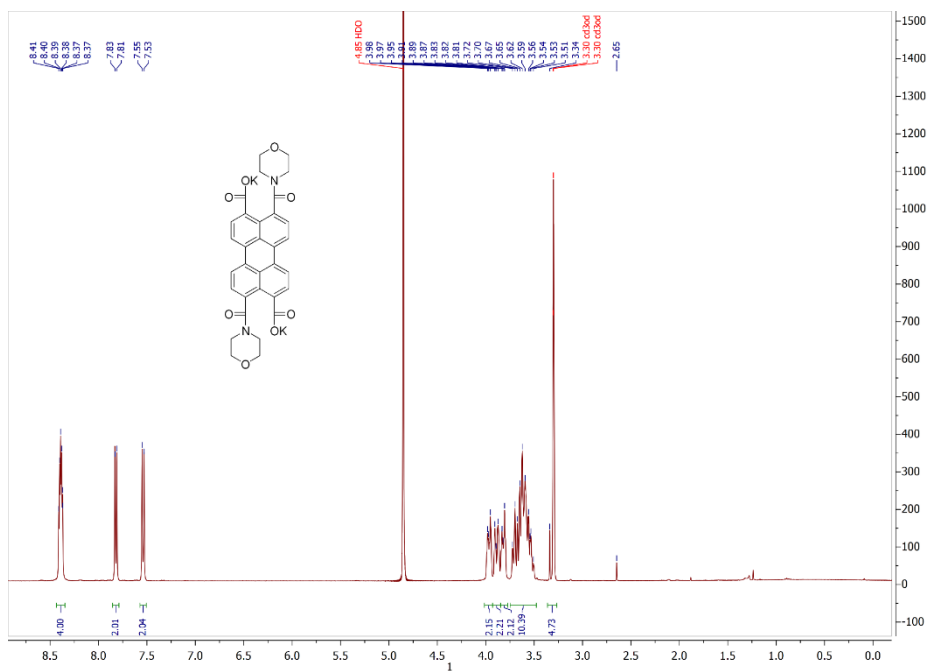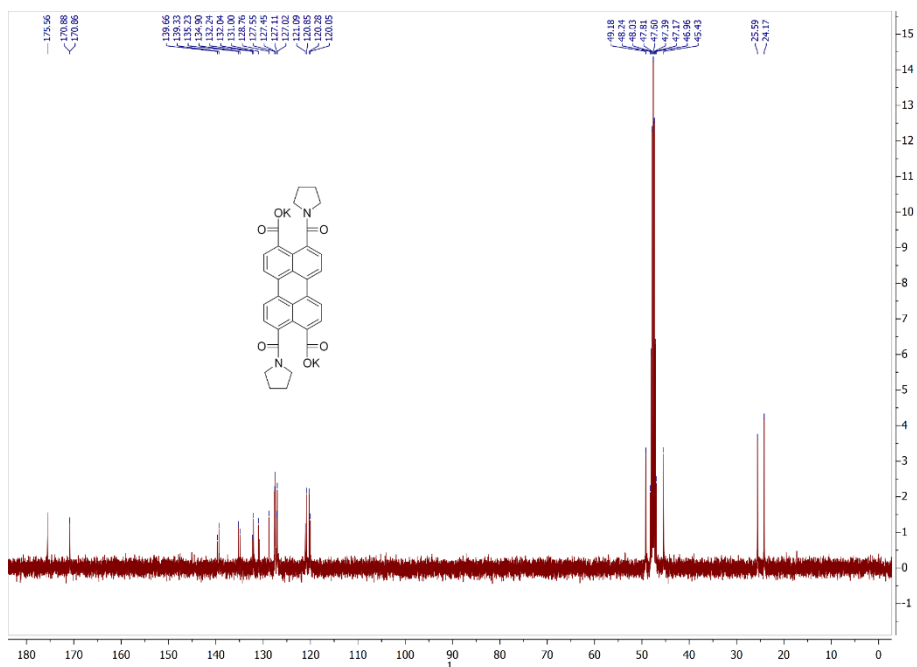
Figure S30. *${}^{13}C$-NMR spectrum of **K₂4e** in CD₃OD.*

Figure S31. *${}^{1}H$-NMR spectrum of **K₂4f** in CD₃OD.*

Figure S32*. ^{1}H-NMR spectrum of 1-(2-hydroxyethyl)piperazine (**2a**) in D$_2$O.*

3.6 References

(1)   Kardos, M. Über Einige Aceanthrenchinon- Und 1.9-Anthracen-Derivate. *Berichte Dtsch. Chem. Ges.* **1913**, *46* (2), 2086–2091. https://doi.org/10.1002/cber.191304602126.

(2)   Herbst, W.; Hunger, K.; Wilker, G. *Industrial organic pigments: production, properties, applications*; Wiley-VCH: Weinheim, 2004.

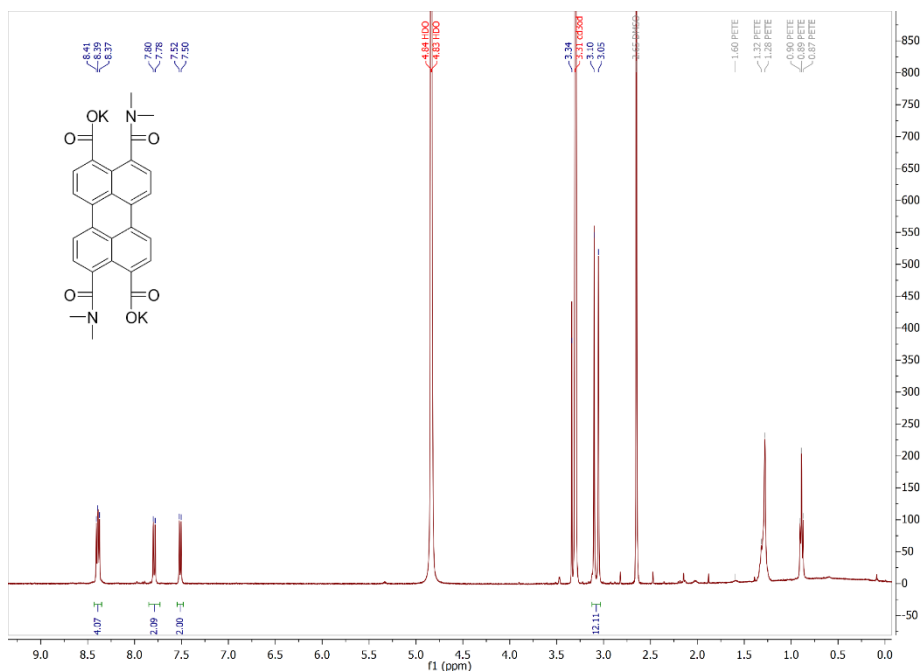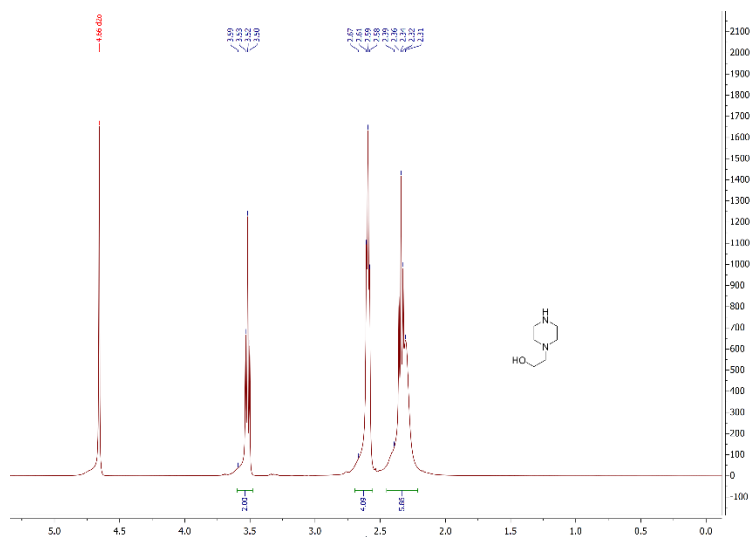(3)   Nielsen, C. B.; Holliday, S.; Chen, H.-Y.; Cryer, S. J.; McCulloch, I. Non-Fullerene Electron Acceptors for Use in Organic Solar Cells. *Acc. Chem. Res.* **2015**, *48* (11), 2803–2812. https://doi.org/10.1021/acs.accounts.5b00199.

(4)   Liu, Z.; Wu, Y.; Zhang, Q.; Gao, X. Non-Fullerene Small Molecule Acceptors Based on Perylene Diimides. *J. Mater. Chem. A* **2016**, *4* (45), 17604–17622. https://doi.org/10.1039/C6TA06978A.

(5)   Zink-Lorre, N.; Font-Sanchis, E.; Sastre-Santos, Á.; Fernández-Lázaro, F. Perylenediimides as More than Just Non-Fullerene Acceptors: Versatile Components in Organic, Hybrid and Perovskite Solar Cells. *Chem. Commun.* **2020**, *56* (27), 3824–3838. https://doi.org/10.1039/D0CC00337A.

(6)   Soto Perez, G.; Dasgupta, S.; Żuraw, W.; Fuentes Pineda, R.; Wojciechowski, K.; Krishnan Jagadamma, L.; Samuel, I.; Robertson, N. Solution-Processable Perylene Diimide-Based Electron Transport Materials as Non-Fullerene Alternatives for Inverted Perovskite Solar Cells. *J. Mater. Chem. A* **2022**, *10* (20), 11046–11053. https://doi.org/10.1039/D2TA01321E.

(7)   Xiao, J.; Yu, H.-J.; Xie, D.-X.; Shinohara, A.; Fan, T.; Yi, J.; Lin Lai, J. Y.; Shao, G.; Yan, H. Organic Photovoltaic Performance and Structural Relationship of Non-Fullerene Small Molecule Acceptors Based on a Tetraarylphenazine Core and Perylene Diimide. *Sustain. Energy Fuels* **2023**, *7* (1), 294–299. https://doi.org/10.1039/D2SE01218A.

(8)   Kelley, R. F.; Shin, W. S.; Rybtchinski, B.; Sinks, L. E.; Wasielewski, M. R. Photoinitiated Charge Transport in Supramolecular Assemblies of a 1,7,N,N‘-Tetrakis(Zinc Porphyrin)-Perylene-3,4:9,10-Bis(Dicarboximide). *J. Am. Chem. Soc.* **2007**, *129* (11), 3173–3181. https://doi.org/10.1021/ja0664741.

(9)   Hurenkamp, J. H.; Browne, W. R.; Augulis, R.; Pugžlys, A.; Loosdrecht, P. H. M. van; Esch, J. H. van; Feringa, B. L. Intramolecular Energy Transfer in a Tetra-Coumarinperylene System: Influence of Solvent and Bridging Unit on Electronic Properties. *Org. Biomol. Chem.* **2007**, *5* (20), 3354–3362. https://doi.org/10.1039/B711681K.

(10)   Fujitsuka, M.; Harada, K.; Sugimoto, A.; Majima, T. Excitation Energy Dependence of Photoinduced Processes in Pentathiophene−Perylene Bisimide Dyads with a Flexible Linker. *J. Phys. Chem. A* **2008**, *112* (41), 10193–10199. https://doi.org/10.1021/jp805350d.

(11)   Wasielewski, M. R. Self-Assembly Strategies for Integrating Light Harvesting and Charge Separation in Artificial Photosynthetic Systems. *Acc. Chem. Res.* **2009**, *42* (12), 1910–1921. https://doi.org/10.1021/ar9001735.

(12)   Blas-Ferrando, V. M.; Ortiz, J.; Bouissane, L.; Ohkubo, K.; Fukuzumi, S.; Fernández-Lázaro, F.; Sastre-Santos, Á. Rational Design of a Phthalocyanine–Perylenediimide Dyad with a Long-Lived Charge-Separated State. *Chem. Commun.* **2012**, *48* (50), 6241–6243. https://doi.org/10.1039/C2CC31087B.

(13)   Frischmann, P. D.; Mahata, K.; Würthner, F. Powering the Future of Molecular Artificial Photosynthesis with Light-Harvesting Metallosupramolecular Dye Assemblies. *Chem. Soc. Rev.* **2013**, *42* (4), 1847–1870. https://doi.org/10.1039/C2CS35223K.

(14)   Ghosh, I.; Ghosh, T.; Bardagi, J. I.; König, B. Reduction of Aryl Halides by Consecutive Visible Light-Induced Electron Transfer Processes. *Science* **2014**, *346* (6210), 725–728. https://doi.org/10.1126/science.1258232.

(15)   Dubey, R. K.; Inan, D.; Sengupta, S.; Sudhölter, E. J. R.; Grozema, F. C.; Jager, W. F. Tunable and Highly Efficient Light-Harvesting Antenna Systems Based on 1,7-Perylene-3,4,9,10-Tetracarboxylic Acid Derivatives. *Chem. Sci.* **2016**, *7* (6), 3517–3532. https://doi.org/10.1039/C6SC00386A.

(16)   Zeman, C. J. I.; Kim, S.; Zhang, F.; Schanze, K. S. Direct Observation of the Reduction of Aryl Halides by a Photoexcited Perylene Diimide Radical Anion. *J. Am. Chem. Soc.* **2020**, *142* (5), 2204–2207. https://doi.org/10.1021/jacs.9b13027.

(17)   Iordache, A.; Delhorbe, V.; Bardet, M.; Dubois, L.; Gutel, T.; Picard, L. Perylene-Based All-Organic Redox Battery with Excellent Cycling Stability. *ACS Appl. Mater. Interfaces* **2016**, *8* (35), 22762–22767. https://doi.org/10.1021/acsami.6b07591.

(18)   Ranque, P.; George, C.; Dubey, R. K.; van der Jagt, R.; Flahaut, D.; Dedryvère, R.; Fehse, M.; Kassanos, P.; Jager, W. F.; Sudhölter, E. J. R.; Kelder, E. M. Scalable Route to Electroactive and Light Active Perylene Diimide Dye Polymer Binder for Lithium-Ion Batteries. *ACS Appl. Energy Mater.* **2020**, *3* (3), 2271–2277. https://doi.org/10.1021/acsaem.9b01225.

(19)   Yan, C.; Barlow, S.; Wang, Z.; Yan, H.; Jen, A. K.-Y.; Marder, S. R.; Zhan, X. Non-Fullerene Acceptors for Organic Solar Cells. *Nat. Rev. Mater.* **2018**, *3* (3), 1–19. https://doi.org/10.1038/natrevmats.2018.3.

(20)   Würthner, F. Perylene Bisimide Dyes as Versatile Building Blocks for Functional Supramolecular Architectures. *Chem Commun* **2004**, No. 14, 1564–1579. https://doi.org/10.1039/B401630K.

(21)   Seki, T.; Lin, X.; Yagai, S. Supramolecular Engineering of Perylene Bisimide Assemblies Based on Complementary Multiple Hydrogen Bonding Interactions. *Asian J. Org. Chem.* **2013**, *2* (9), 708–724. https://doi.org/10.1002/ajoc.201300025.

(22)   Gershberg, J.; Fennel, F.; H. Rehm, T.; Lochbrunner, S.; Würthner, F. Anti-Cooperative Supramolecular Polymerization: A New K 2 – K Model Applied to the Self-Assembly of Perylene Bisimide Dye Proceeding via Well-Defined Hydrogen-Bonded Dimers. *Chem. Sci.* **2016**, *7* (3), 1729–1737. https://doi.org/10.1039/C5SC03759J.

(23)   Nişancı, B.; Daştan, A.; Bozdemir, Ö. A. Aromatic Stacking of a Perylenetetracarboxylic Tetraester: Self-Assembly in Both Water and Chloroform. *Tetrahedron Lett.* **2018**, *59* (39), 3558–3562. https://doi.org/10.1016/j.tetlet.2018.08.037.

(24)   Wilson-Kovacs, R. S.; Fang, X.; Hagemann, M. J. L.; Symons, H. E.; Faul, C. F. J. Design and Control of Perylene Supramolecular Polymers through Imide Substitutions. *Chem. – Eur. J.* **2022**, *28* (3), e202103443. https://doi.org/10.1002/chem.202103443.

(25)   Roy, S.; Maiti, D. K.; Panigrahi, S.; Basak, D.; Banerjee, A. A New Hydrogel from an Amino Acid -Based Perylene Bisimide and Its Semiconducting, Photo-Switching Behaviour. *RSC Adv.* **2012**, *2* (29), 11053–11060. https://doi.org/10.1039/C2RA21319B.

(26)   Datar, A.; Balakrishnan, K.; Zang, L. One-Dimensional Self-Assembly of a Water Soluble Perylene Diimide Molecule by PH Triggered Hydrogelation. *Chem. Commun.* **2013**, *49* (61), 6894–6896. https://doi.org/10.1039/C3CC43359E.

(27)   R. Draper, E.; Wilbraham, L.; J. Adams, D.; Wallace, M.; Schweins, R.; A. Zwijnenburg, M. Insight into the Self-Assembly of Water-Soluble Perylene Bisimide Derivatives through a Combined Computational and Experimental Approach. *Nanoscale* **2019**, *11* (34), 15917–15928. https://doi.org/10.1039/C9NR03898A.

(28)   Adams, V.; Cameron, J.; Wallace, M.; Draper, E. R. Mechanoresponsive Self-Assembled Perylene Bisimide Films. *Chem. – Eur. J.* **2020**, *26* (44), 9879–9882. https://doi.org/10.1002/chem.202001805.

(29)   Egan, J. G.; Brodie, G.; McDowall, D.; Smith, A. J.; Edwards-Gayle, C. J. C.; Draper, E. R. Impact of Subtle Change in Branched Amino Acid on the Assembly and Properties of Perylene Bisimides Hydrogels. *Mater. Adv.* **2021**, *2* (15), 5248–5253. https://doi.org/10.1039/D1MA00470K.

(30)   Sukul, P. K.; Malik, S. Co(II) Induced Aggregation of Chiral Perylene Derivatives and Macroscopic Formation of Supramolecular Networks. *Chem. Lett.* **2018**, *47* (4), 576–579. https://doi.org/10.1246/cl.171192.

(31) Bettini, S.; Syrgiannis, Z.; Ottolini, M.; Bonfrate, V.; Giancane, G.; Valli, L.; Prato, M. Supramolecular Chiral Discrimination of D-Phenylalanine Amino Acid Based on a Perylene Bisimide Derivative. *Front. Bioeng. Biotechnol.* **2020**, *8*.

(32) Draper, E. R.; Greeves, B. J.; Barrow, M.; Schweins, R.; Zwijnenburg, M. A.; Adams, D. J. PH-Directed Aggregation to Control Photoconductivity in Self-Assembled Perylene Bisimides. *Chem* **2017**, *2* (5), 716–731. https://doi.org/10.1016/j.chempr.2017.03.022.

(33) Pocker, Y.; Green, Edmond. Hydrolysis of D-Glucono-.Delta.-Lactone. I. General Acid-Base Catalysis, Solvent Deuterium Isotope Effects, and Transition State Characterization. *J. Am. Chem. Soc.* **1973**, *95* (1), 113–119. https://doi.org/10.1021/ja00782a019.

(34) Adams, D. J.; Butler, M. F.; Frith, W. J.; Kirkland, M.; Mullen, L.; Sanderson, P. A New Method for Maintaining Homogeneity during Liquid–Hydrogel Transitions Using Low Molecular Weight Hydrogelators. *Soft Matter* **2009**, *5* (9), 1856–1862. https://doi.org/10.1039/B901556F.

(35) Icil, H.; Icli, S. Synthesis and Properties of a New Photostable Polymer: Perylene-3,4,9,10-Tetracarboxylic Acid-Bis-(N,N′-Dodecylpolyimide). *J. Polym. Sci. Part Polym. Chem.* **1997**, *35* (11), 2137–2142. https://doi.org/10.1002/(SICI)1099-0518(199708)35:11<2137::AID-POLA3>3.0.CO;2-V.

(36) Konieczkowska, J.; Janeczek, H.; Kozanecka-Szmigiel, A.; Schab-Balcerzak, E. Poly(Amic Acid)s and Their Poly(Amide Imide) Counterparts Containing Azobenzene Moieties: Characterization, Imidization Kinetics and Photochromic Properties. *Mater. Chem. Phys.* **2016**, *180*, 203–212. https://doi.org/10.1016/j.matchemphys.2016.05.066.

(37) Gnida, P.; Bujak, K.; Janeczek, H.; Schab-Balcerzak, E.; Konieczkowska, J. Poly(Amic Acid)s vs. Polyimides with π-Conjugated –NN- Units: Cis-Trans Isomerization Reaction and Kinetics of Thermal Imidization. *Opt. Mater.* **2020**, *104*, 109931. https://doi.org/10.1016/j.optmat.2020.109931.

(38) Budy, S. M.; V Rose III, J.; Gibson, C.; Son, D. Y. Synthesis, Characterization and Nanoparticle Formation of Polyarylene Poly(Amic Acid)s and Polyimides Containing Fluorescent Dye Moieties. *Polym. Int.* **2021**, *70* (6), 759–767. https://doi.org/10.1002/pi.6125.

(39) Kwakernaak, M. C.; Koel, M.; Berg, P. J. L. van den; Kelder, E. M.; Jager, W. F. Room Temperature Synthesis of Perylene Diimides Facilitated by High Amic Acid Solubility. *Org. Chem. Front.* **2022**. https://doi.org/10.1039/D1QO01723C.

(40) Kreuz, J. A.; Edman, J. R. Polyimide Films. *Adv. Mater.* **1998**, *10* (15), 1229–1232. https://doi.org/10.1002/(SICI)1521-4095(199810)10:15<1229::AID-ADMA1229>3.0.CO;2-B.

(41) de Barros, T. C.; Filho, P. B.; Loos, M.; Politi, M. J.; Chaimovich, H.; Cuccovia, I. M. Formation and Decomposition of N-Alkylnaphthalimides: Experimental Evidences and Ab Initio Description of the Reaction Pathways. *J. Phys. Org. Chem.* **2011**, *24* (5), 385–397. https://doi.org/10.1002/poc.1768.

(42) Souza, B. S.; Mora, J. R.; Wanderlind, E. H.; Clementin, R. M.; Gesser, J. C.; Fiedler, H. D.; Nome, F.; Menger, F. M. Transforming a Stable Amide into a Highly Reactive One: Capturing the Essence of Enzymatic Catalysis. *Angew. Chem.* **2017**, *129* (19), 5429–5432. https://doi.org/10.1002/ange.201701306.

(43) Langhals, H. Control of the Interactions in Multichromophores: Novel Concepts. Perylene Bis-Imides as Components for Larger Functional Units. *Helv. Chim. Acta* **2005**, *88* (6), 1309–1343. https://doi.org/10.1002/hlca.200590107.

(44) Demmig, S.; Langhals, H. Leichtlösliche, lichtechte Perylen-Fluoreszenzfarbstoffe. *Chem. Ber.* **1988**, *121* (2), 225–230. https://doi.org/10.1002/cber.19881210205.

(45) Alternatively Reactions Were Conducted Overnight (16h) at Room Temperature.

(46) Chen, Z.; Fimmel, B.; Würthner, F. Solvent and Substituent Effects on Aggregation Constants of Perylene Bisimide π-Stacks – a Linear Free Energy Relationship Analysis. *Org. Biomol. Chem.* **2012**, *10* (30), 5845–5855. https://doi.org/10.1039/C2OB07131B.

(47) Ran, G.; Zeb, J.; Song, Y.; Denis, P. A.; Ghani, U.; Zhang, W. Photoinduced Symmetry Breaking-Charge Separation in the Aggregated State of Perylene Diimide: Effect of Hydrophobicity. *J. Phys. Chem. C* **2022**, *126* (8), 3872–3880. https://doi.org/10.1021/acs.jpcc.1c10712.

(48) Balakrishnan, K.; Datar, A.; Naddo, T.; Huang, J.; Oitker, R.; Yen, M.; Zhao, J.; Zang, L. Effect of Side-Chain Substituents on Self-Assembly of Perylene Diimide Molecules: Morphology Control. *J. Am. Chem. Soc.* **2006**, *128* (22), 7390–7398. https://doi.org/10.1021/ja061810z.

(49) Görl, D.; Zhang, X.; Würthner, F. Molecular Assemblies of Perylene Bisimide Dyes in Water. *Angew. Chem. Int. Ed.* **2012**, *51* (26), 6328–6348. https://doi.org/10.1002/anie.201108690.

(50) Zhang, X.; Rehm, S.; Safont-Sempere, M. M.; Würthner, F. Vesicular Perylene Dye Nanocapsules as Supramolecular Fluorescent PH Sensor Systems. *Nat. Chem.* **2009**, *1* (8), 623–629. https://doi.org/10.1038/nchem.368.

4

Controlled halogenation and imidization of perylene dianhydride

Abstract

Complete control over substitution behavior of perylene diimides (PDIs) is needed to achieve its full potential in photovoltaics, photocatalysis and battery electrode chemistry. To achieve this, new methods of halogenation are required, that deliver high yield products with greater control. Here, we describe a study on the boundary conditions at which controlled halogenation takes place. This then gives a route towards dichlorinated perylenes at moderate yields, while also giving a new route towards tetrabrominated perylenes. We also report on mix halogenated perylenes, a perylene monoimide diester (PMIDE) with two bromides (1 and 7) and two chlorides (6 and 12). We explore the difference in reactivity between chloride and bromide substituents, were we find that bromide is more reactive towards pyrrolidine.

4.1 Introduction

Although perylene diimides (PDIs) are known in chemistry for more than 100 years,[1] their synthesis remains largely archaic. High temperatures and corrosive reagents are used to fabricate PDIs. This is detrimental to selectivity and yield, also for their environmental and economic costs. Which is unfortunate, since PDIs are a class of valuable organic dyes that have a diverse amount of industrial and academic applications.[2] They are also used in photovoltaics,[3–7] photocatalysis,[8–16] electrode materials in batteries[13,17,18] and fluorescence probes[19–21].

PDI synthesis typically starts with perylene dianhydride (PDA), which undergoes an imidization and a halogenation,[22,23] followed by substitution of the halogens with groups that are desired.[11,12,24–26] The interplay of all 12 positions on the perylene core (Scheme 1) determines the photo- and electrochemical properties of the end product. The substitution is mainly done through nucleophilic aromatic substitution, while metal-catalyzed cross coupling reactions are also possible. Total control of all 12 positions is required to get full access to all the properties PDIs have to offer. In the last decade, efforts have successfully been made in elucidating the exact reaction conditions needed to get selective and high yielding transformations of PDIs.
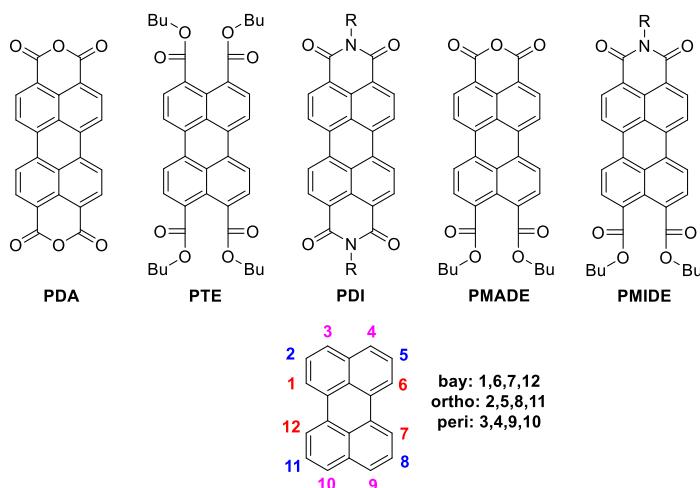
Scheme 1. *Perylene and its nomenclature.*

Two main approaches are taken in literature for selective and high yielding halogenation, chlorination of the 1,6,7 and 12 positions[19] and bromination of the 1 and 7 positions.[27] Both pathways use ester groups as temporal solubilizing and protecting groups, perylene tetraester (PTE). Especially the solubilizing effect of ester groups is needed, since PDAs and PDIs are known for their low solubility. In the chlorination, PDA is dissolved in chlorosulfonic acid together with iodide and heated to 66ºC for 16 hours (Scheme 2B). After reaction completion, the resulting PDA undergoes an esterification and repeated crystallization. This yields pure 1,6,7,12-tetrachloro-PTE in 60% from PDA. Bromination starts with the esterification of PDA, which goes quantitatively. This PTE is than dissolved in dichloromethane, together with bromine and potassium carbonate for 24 hours at room temperature (Scheme 2A). After reaction completion, the mixture is
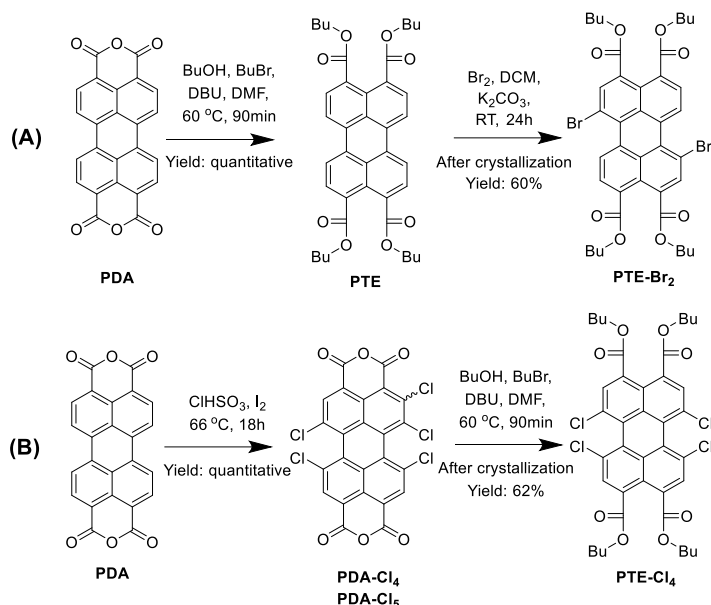
Scheme 2. *High yielding halogenation of PDA.*[19,27]

crystalized repeatedly, which yields pure 1,7-dibromo-PTE in 62% from PDA. Both PTE-Cl$_4$ and PTE-Br$_2$ can then be further transformed towards the desired end products. These methods allow for selective halogenation in good yields and can be easily scaled up due to the purification by crystallization.

Selective imidization of one anhydride can be directly achieved by hydrolyzing both anhydrides in a basic aqueous solution, followed by careful acidification to condense one anhydride, yielding a perylene monoanhydride-diacid.[28] The crude is then treated with an amine and potassium carbonate, yielding a perylene monoimide-monoanhydride in a >95% yield from PDA. Although this seems very promising, the product cannot be examined for its purity, since the solubility is so low. Also, this approach can only be used for unsubstituted PDA, because halogens are sensitive towards hydrolysis in the basic conditions used here. In a different approach, PTE and p-TsOH are dissolved in a toluene:heptane mixture, and stirred for 5 hours at 90°C, yielding 75% perylene monoanhydride diester (PMADE).[29] Heptane is used as a 'bad' solvent for PMADE, inhibiting its further hydrolysis towards PDA. This approach has been successfully modified for the synthesis of PMADE-Cl$_4$ and PMADE-Br$_2$, confirming the compatibility of the halogens with the used conditions.

Halogenated PMADEs are the true starting compounds for synthetic strategies that modify as many perylene positions as possible. Dubey et al. showed an imide and ester functionality on the peri position can be used to differentiate between chlorides in the bay area.[21] Through this effect, they are able to synthesize a perylene with 5 different substituents. The same strategy can be used for brominated perylenes.[30] With the currently described PMADEs in literature, five is the limit for now. To expand further to six or more substituents, new PMADEs, with new halogenation patterns are needed. It also requires the use of different halogens and discrimination between them. In this work

we will introduce these new PMADEs and explore the difference in reactivity between chloro- and bromo PTEs.

4.2 Results and discussions

Halogenation of PDA occurs through electrophilic aromatic substitution. When halogenating PDA, the energy barrier increases with each successive halogen, but not in equal amounts. The bay area is the most reactive and therefore the first halogen will be positioned there. This will make the perylene core more electron poor, lowering its reactivity. The second halogen will also be positioned in the bay area, due to steric hindrance, the 6 or 7 positions are therefore most preferred. The third halogen will also be positioned in the bay area, but the steric hindrance from the halogens already there will create an energy barrier that needs to be overcome, while the fourth halogen has to overcome a similar barrier. Halogenation of the 1 and 12 position will have a reversed trend, where the introduction of a third halogen on the 6 or 7 position is supposed to be easy. The ortho positions are less reactive, but do not have steric hindrance. Therefore, when the bay area is fully occupied, the ortho positions will be filled, and they will experience slightly different energy barriers. Based on this, one can see that only certain halogenated PDAs can be the main components of a mixture when controlling the reaction conditions. Mono-, di-, tetra- and octa substituted PDAs can be reliably synthesized. This can be seen in the established conditions for the tetrachlorination of PDA.[19] It has to be performed at 66°C for 18 hours in chlorosulfonic acid in the presence of iodide. This temperature and time are required, since a lower temperature will result in more trichlorinated PDA, while a higher temperature will yield higher chlorinated PDA. The same holds true for dibromination of PTE, where both the temperature and bromine concentration have to be controlled to obtain pure PTE-Br$_2$. See Scheme 3 for an overview of all reaction paths.

This understanding is the entire reasoning behind all the following discussed halogenation reactions. By controlling the temperature, reaction time and reactant concentrations, some energy barriers can be overcome, while others cannot.
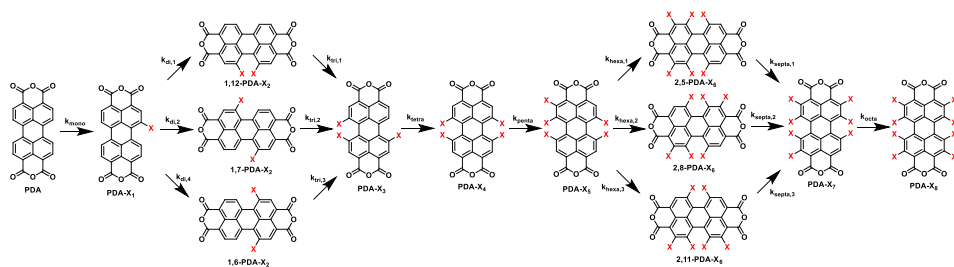
Scheme 3. *Different reaction pathways for halogenation of PDA.*

4.2.1. 1,7-dichloro-PTE

In order to synthesis 1,7-PTE-Cl$_2$, we used the tetrachlorination of PDA as a starting point, which, as discussed before, occurs at 66°C. Since that is a rather low temperature, lowing of reactant concentrations was applied here first. Chlorosulfonic acid was diluted with sulfuric acid (1:1), while the iodide catalyst remained at the same amount. The reaction was performed at temperatures between 30 and 70°C for 18 hours. After reaction
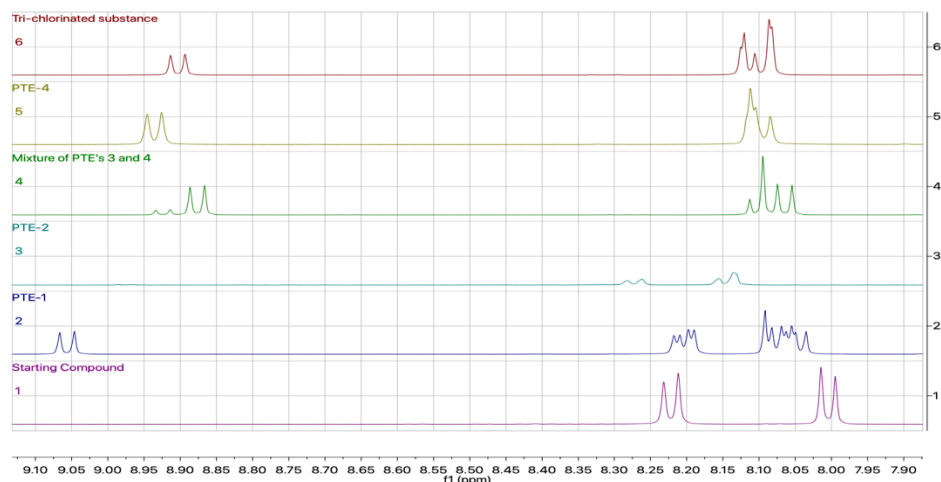
Figure 1. ^1H NMR of different chlorinated PTEs.

completion, the resulting chlorinated PDAs underwent an esterification. The mixtures were than analyzed by TLC and ^1H HNMR.

At 30-45°C, mainly PTE-Cl$_1$ was present in the mixture, with a small amount of PTE-Cl$_2$, but no PTE-Cl$_3$. At 50°C, mainly PTE-Cl$_1$ and PTE-Cl$_2$ were found in the same order of magnitude. However, at 60 and 70°C, still PTE-Cl$_1$ and PTE-Cl$_2$ were present, but also some PTE-Cl$_3$. Starting material was detected in all reaction mixtures. It is interesting to see that all mixtures contained a large fraction of starting material. Important to note is that no PTE-Cl$_4$ was found, due to this dilution. Next, the available chlorosulfonic acid in the mixture was halved and the reaction was performed at 40, 50 and 60°C for 18 hours. This made the chlorination less potent. Here, PTE-Cl$_3$ was not found anymore, while for 50 and 60°C, only small amounts of PTE-Cl$_2$ were formed. At 40°C, the main compound in the mixture was starting material, with only a minor fraction of PTE-Cl$_1$. Lastly, doing the reaction at the original dilution at 50°C for 72 hours, yielded PTE-Cl$_2$ as the major

Tabel 1. Reaction compositions in chlorination of PDA under different conditions. For clarity, reactions done at 50°C are highlighted in grey.

T(°C)	Time (h)	EQ ClHSO$_3$	PTE	PTE-Cl$_1$	PTE-Cl$_2$ (1,12)	PTE-Cl$_2$ (1,6/1,7)	PTE-Cl$_3$
70 °C	18	35.4	0%	16%	2%	51%	31%
60 °C	18	35.4	17%	44%	1%	33%	4%
50 °C	18	35.4	29%	47%	6%	18%	0%
45 °C	18	35.4	47%	41%	3%	8%	0%
40 °C	18	35.4	54%	37%	3%	6%	0%
30 °C	18	35.4	75%	20%	3%	2%	0%
60 °C	18	17.7	58%	25%	6%	10%	0%
50 °C	18	17.7	83%	17%	0%	0%	0%
40 °C	18	17.7	97%	3%	0%	0%	0%
50 °C	24	35.4	27%	40%	3%	28%	2%
50 °C	72	35.4	0%	7%	0%	61%	32%

fraction, without any starting material in the mixture (7% PTE-Cl$_1$, 61% PTE-Cl$_2$, 32% PTE-Cl$_3$). All the reaction composition estimates from ^{1}H-NMR (Fig. 1) can be seen in Table 1. Then, crystallization was done, in the same way literature reports it for PTE-Br$_2$.[27] This gave a mostly pure 1,7-PTE-Cl$_2$ in a 50% total yield.

4.2.2. 1,6,7,12-tetrabromo-PMIDE

Tetrabromination of PDA is a known reaction that requires harsh conditions, in sulfuric acid with bromine and iodide around 100°C for 12 to 24 hours.[31–33] Although this yields pure PDA-Br$_4$ excellently, it is still in our interest to explore alternative reaction pathways to gain this interesting analogue of PDA-Cl$_4$. PTE-Br$_2$ is made in dichloromethane with bromine and potassium carbonate at room temperature in 24 hours.[27] Using a similar approach as for PTE-Cl$_2$, the reaction temperature and reactant concentrations were increased in order to obtain PTE-Br$_4$. By refluxing PTE in bromine and using potassium bicarbonate as a base, PTE-Br$_4$ can be synthesized, although at a low yield of 26% after purification with column chromatography. This is lower than the known tetrabromination of PDA from literature. The instability of the ester groups seem to be the main reason for this. When potassium carbonate is used as a base, the yield is even lower, again hinting at the stability of the esters. Also the ester groups seem to be unstable against the silica used in the column chromatography.

Asymmetrization of the peri positions was done with pTsOH in refluxing n-heptane for 48 hours. The resulting mixture underwent several washing steps and a crystallization. This yielded the desired PMADE-Br$_4$ with a purity of 90%, the major contamination being PDA-Br$_4$. Subsequently, PMADE-Br$_4$ underwent an imidization with methylamine, according to standard procedures from literature, and characterization by ^{1}H NMR, see Figure 2.
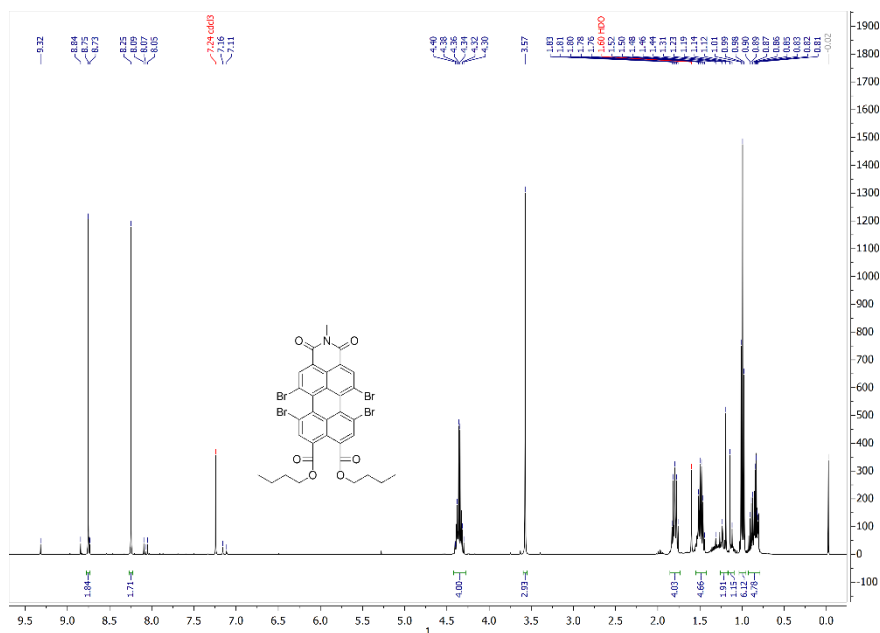

Figure 2. ^{1}H NMR of PMIDE-Br$_4$

4.2.3. 1,7-dibromo-6,12-dichloro-PMADE

In order to gain more control over the substitution pattern of the perylene scaffold, we sought to introduce different halogens in the bay area. This has to be done in a thoughtful way, otherwise complex mixtures can be formed. To date two different approaches have been tried, the bromination of PTE-Cl$_2$ and the chlorination of PDA-Br$_2$. Only the latter proved feasible so far. It is important to note that PDA-Br$_2$ is produced by hydrolysis of PTE-Br$_2$ with pTsOH in toluene for 48 hours, hydrolysis with sulfuric acid yielded product that failed to proceed to the desired PTE-Br$_2$-Cl$_2$. The reason for that remains unknown, but it is feasible it is due to side products that are left in the mixture after work up.

In the chlorination of PDA-Br$_2$, the reaction conditions for the preparation of PDA-Cl$_4$ were used as a starting point. The reactivity of the perylene core in an electrophilic aromatic substitution is similar, but the steric hindrance is larger, due to two bromides already present in the bay area. Dissolving PDA-Br$_2$ in chlorosulfonic acid with a catalytic amount of iodine and stirring it for 16 hours at 70°C, yielded a majority of PDA-Br$_2$-Cl$_2$. The crude than underwent an esterification, which yielded 91% PTE-Br$_2$-Cl$_2$. Analysis was done by ^{1}H NMR, see Figure 3.
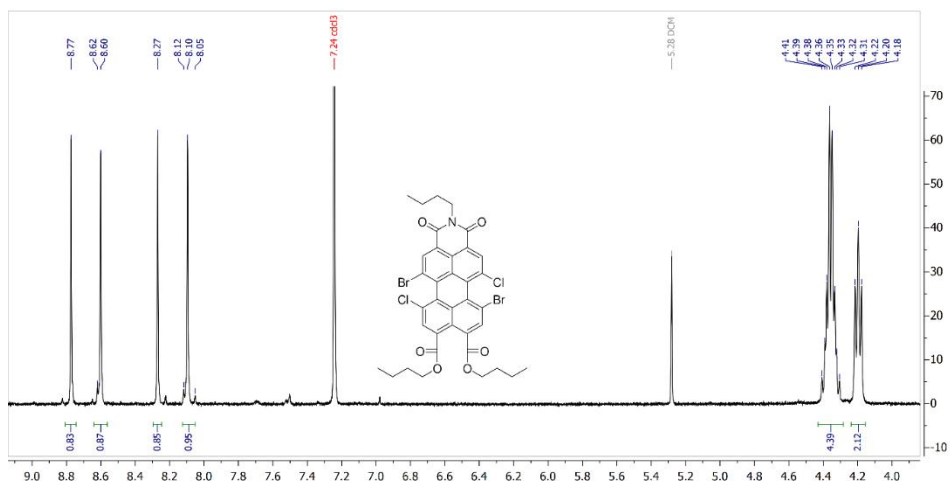

Figure 3. *^{1}H NMR of PTE-Br$_2$-Cl$_2$*

Next, PTE-Br$_2$-Cl$_2$ underwent a partial hydrolysis with the same conditions described before with PTE-Br$_4$, yielding PMADE-Br$_2$-Cl$_2$ in 48% after column chromatography. This was followed by an imidization with n-butylamine under standard conditions from literature.[21]

PMADE-Br$_2$-Cl$_2$ is a very desirable starting material for the synthesis of complex PDIs. Like PMADE-Cl$_4$, the ester and anhydride/imide positions will influence halogen reactivity, but this can be exacerbated with the difference in reactivity between bromide and chloride. This is especially important for the 1 and 6 positions, since these two positions could not be regioselectively substituted by Dubey *et al*. A proposed substitution pathway can be seen in Scheme 4.
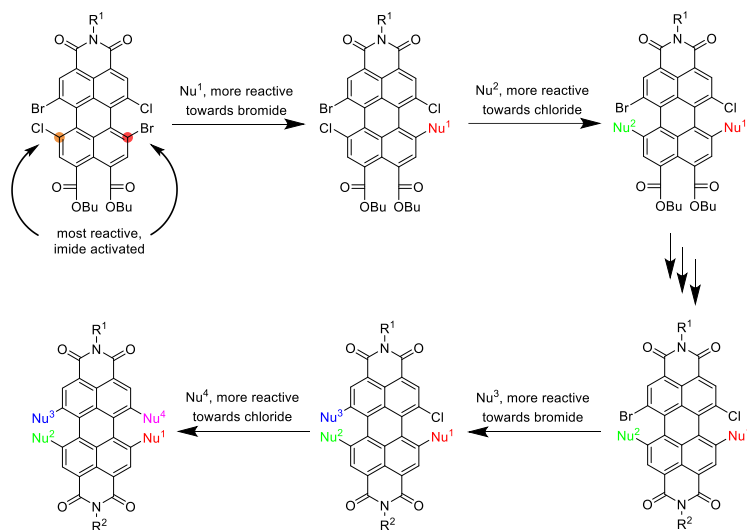
Scheme 4. *Proposed reaction pathway for complex substitution of PMADE-Br$_2$-Cl$_2$, resulting in 6 unique groups.*

4.2.4. Reaction kinetics

For this proposed reaction pathway to work, bromide and chloride need to have a rather grand difference in reactivity towards nucleophiles. Different nucleophiles can also have different reactivity's towards the halogens according to the 'hard and soft, Lewis acids and bases' concept. We chose three categories of nucleophiles to investigate, phenols, thiophenols and cyclic amines. PTE-Br$_2$ and PTE-Cl$_2$ were chosen as model reagents here. When subjected towards standard NAS conditions from literature, no substantial difference in reactivity's can be found for phenol and thiophenols towards chloride or bromide. However, deactivating cyclic amines do show a different reactivity towards the halogens. Here, a monosubstitution with pyrrolidine can be performed at room temperature with PTE-Br$_2$ and PTE-Cl$_2$. PTE-Br-Pyr is formed almost quantitatively, while PTE-Cl-Pyr still contains a lot of starting material and needs extensive purification. A second pyrrolidine can react with the other halogen at elevated temperatures. The same trend is observed here, PTE-Br-Pyr reacts quantitatively, while PTE-Cl-Pyr does not. Since the first substitution already occurs are room temperature, and PTEs are very UV-VIS active, this reaction can be followed real-time. PTE-Br$_2$ and PTE-Cl$_2$ were diluted to $1.4 * 10^{-5}$ M concentrations, pyrrolidine was added in a 10^5 times excess. PTE-Br$_2$ reacted approximately twice as fast with pyrrolidine compared to PTE-Cl$_2$. Figure 4 shows the absorptions and conversation over time. Clear isosbestic point can be seen, indicating that the reaction proceeds from one product to another selectively. PTE-X$_1$ and PTE-X$_3$ were also tested and the bromide is subsequently faster reacting, see the SI. Since one of the reactants is in extreme excess, we can assume that the reaction follows first order kinetics. Table 2 shows the calculated rate constants for the measured reactions.

Although we see a difference in reactivity between chloride and bromide, the difference is not very large. If this were to be exploited in a lab scale reaction, the reaction conditions need to be very well chosen and one can expect to find many side products in the mixture.
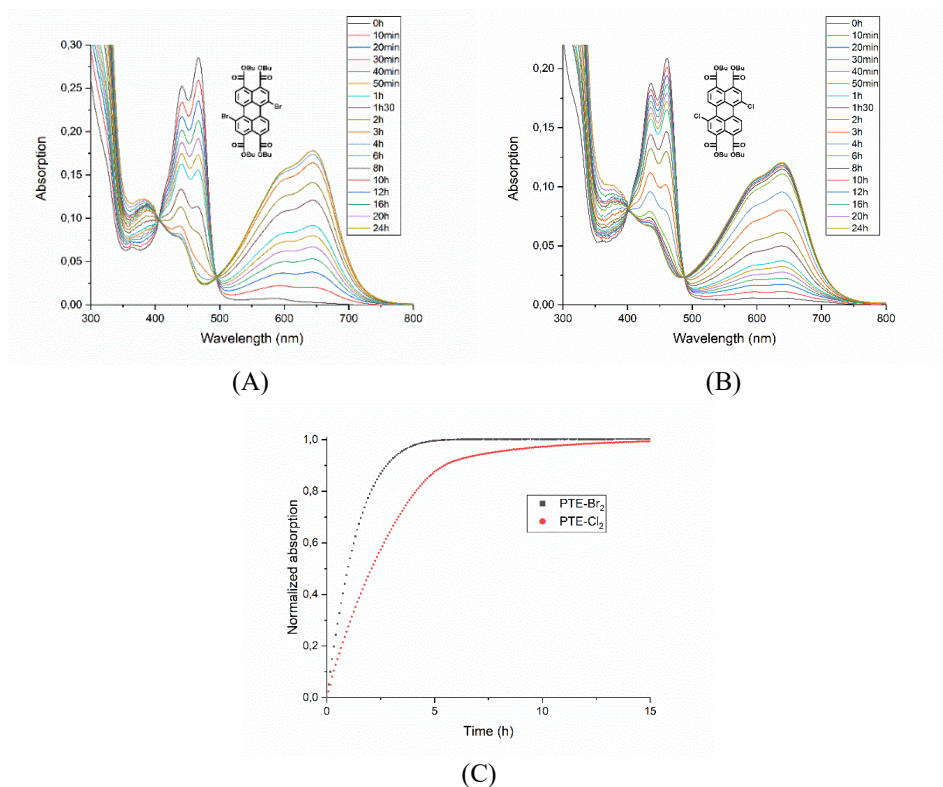
(A)

(B)

(C)

Figure 4. *A) UV-VIS spectra of PTE-Br$_2$ in the presence of pyrrolidine over time. Isosbestic point at 495 nm. B) UV-VIS spectra of PTE-Cl$_2$ in the presence of pyrrolidine over time. Isosbestic point at 489 nm, C) Normalized absorption of (A) and (B) at 645 nm and 640 nm respectively over time.*

Other nucleophiles will have other reactivity's towards the halogens, but this remains unknown at the moment of writing, but as written above, the lab scale reactions did not show a big difference.

To see whether this difference in reactivity still holds in a lab scale reaction we tried two different reactions with PTE-Br$_2$-Cl$_2$, a metal catalyzed cross coupling and a NAS with pyrrolidine. Metal catalyzed cross coupling reactions are known to react more readily with bromides. Literature reports show Suzuki reactions done with PDI-Br$_2$.[34] In our lab, Suzuki was also successfully done with PTE-Br$_2$. However, we were unable to perform a

Table 2. *Rate constants of reaction between pyrrolidine and PTE-X$_y$, calculated from UV-VIS experiments.*

Amount of halogens	Br	Cl
1	k = 0.48 h^{-1}	k = 0.39 h^{-1}
2	k = 0.80 h^{-1}	k = 0.42 h^{-1}
3	k = 1.85 h^{-1}	k = 0.59 h^{-1}

Suzuki with PTE-Br$_2$-Cl$_2$. That might be, due to steric hindrance or ester instability. The attempts always ended with a mixture of unidentifiable compounds. To date we have not yet done a Suzuki with PDI-Br$_2$-Cl$_2$. NAS with pyrrolidine was only partially successful. The reaction was performed in pure pyrrolidine at room temperature, the same conditions used for PTE-X$_2$. The reaction time was extended from 24 hours to 75 hours to compensate for the slower reaction kinetics caused by the steric hindrance of 4 halogens in the bay area. The reaction was monitored with TLC, which showed the formation of many different products. After 75 hours, a work up and purification by column chromatography was done, yielding only ~1 mg of reasonable pure compound. Other fractions from the column chromatography were unidentifiable. After ^{1}H NMR analysis, it was concluded that this was PTE-X$_2$-Pyr$_2$, see Figure 5. The spectrum shows two distinct singlets, which indicates that the molecule is symmetric in 1 plane. Since we have seen that bromide reacts faster than chloride and in the absence of a mass spectrum of this sample, we could carefully conclude that this is PTE-Cl$_2$-Pyr$_2$.

Poor ester stability might be to blame for this low reaction yield, just like we have seen with PTE-Br$_4$. Although it was not done in our lab yet, performing these same reactions with the diimide or monoimide might circumvent this problem. This would certainly be the next step in this project.

4.3 Conclusions

New halogenated perylene derivatives were successfully synthesized and characterized. PTE-Br$_4$ was synthesized with a novel method, while PTE-Cl$_2$ and PMIDE-Br$_2$-Cl$_2$ were never reported in the literature before. Reaction temperature, concentration and time have a direct effect on the extent of halogenation. Milder conditions will result in a lower
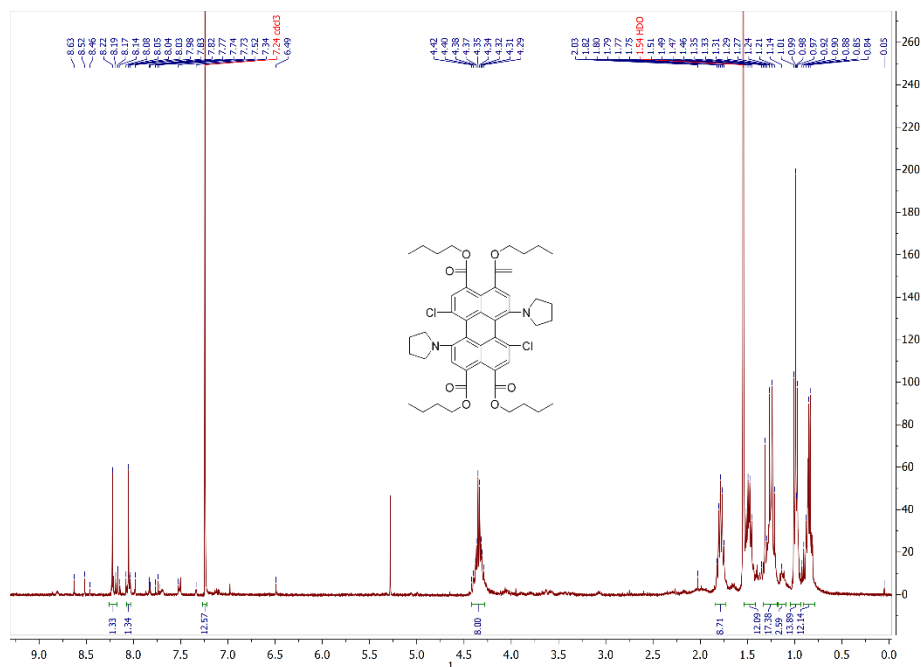

Figure 5. *^{1}H NMR spectrum of PTE-Cl$_2$-Pyr$_2$, with impurities.*

degree of halogenation, while harsher conditions will result in a higher degree of halogenation. Mono-, di-, tetra- and octa- halogenation products are kinetically and energetically favored. Here, only a relevant different in halogen reactivity was seen towards pyrrolidine. PTE-Cl$_2$ shows a lower reactivity towards the cyclic amine, compare to PTE-Br$_2$. This was observed in lab scale reactions and in UV-VIS experiments. Bromide was more reactive, compared to chloride. We have tried to exploit this different with the substitution of PTE-Br$_2$-Cl$_2$ with pyrrolidine, but this was only partially successful and yielded PTE-Cl$_2$-Pyr$_2$. However, we did see again a different reactivity in the halogens. In the future, this can be used in PMIDE-Br$_2$-Cl$_2$ and PDI-Br$_2$-Cl$_2$, thereby obtaining more complex PDIs, where total control of all perylene positions is necessary.

4.4 Experimental
Synthesis of 1,7-dichloro-PTE

PDA (2.00 g, 5.098 mmol), I$_2$ (0.332 g, 1.310 mmol) were added to a round bottom flask together with a stirring bar. A mixture of chlorosulfonic acid and sulfuric acid was prepared in a 1:1 ratio. This mixture (6 mL) was added to the solids in the flask, which was transferred to a reflux condenser with a CaCl$_2$ tube on top. The mixture was heated at 40°C for 120 hours. After which, the mixture was left to cool to room temperature. The contents were poured over ice and left to stand until the ice was completely melted. The solids were filtered off and washed with copious amounts of water. The crude was left to dry under air and later transferred to a vacuum oven to further dry, yielding a dry red powder. The dry powder was put in a round bottom flask again and DMF (50 mL), DBU (2.802 g, 18.407 mmol), BuOH (2.713 g, 36.600 mmol) and BuBr (5.070 g, 37.005 mmol) were added. The resulting suspension was left to stir over night at 40°C. After reaction completion, the crude was precipitated out in water (500 mL) and filtered off. This was again followed by drying under air and vacuum oven. The dry crude was dissolved in DCM (20 mL), to which ACN (140 mL) was added. After 4 days, crystals were visible and the suspension was filtered again. This yielded the pure orange product.

Yield: 1.486 g, 41%. ^{1}H NMR(400 MHz, CDCl$_3$): δ = 8.94 (d, 2H), 8.08 (m, 4H), 4.32 (m, 8H), 1.77 (m, 8H), 148 (m, 8H), 0.98 (t, 12H).

Synthesis of 1,6,7,12-tetrabromo-PTE

To a stirring suspension of Br$_2$ (6 mL), I$_2$ (97.2 mg, 0.383 mmol) and KHCO$_3$ (1.059 g, 7.660 mmol), PTE (1.00 g, 1.532 mmol) was added. The mixture was stirred at 55°C for 48 hours. After reaction completion, the mixture was cooled to room temperature and the remaining bromine was quenched with NaS$_2$O$_5$ in water. The contents of the round bottom flask were transferred to a separatory funnel, to which DCM was added. The organic phase was collected and dried on magnesium sulfate. After filtration, the solvent was removed, which yielded the crude product. Following this, the product was purified by column chromatography (1:1 DCM:hexane → 100% DCM). This yielded the pure orange product.

Yield: 394.1 mg, 25.7%. ^{1}H NMR(400 MHz, CDCl$_3$): δ = 8.23 (s, 4H), 4.36 (m, 8H), 1.80 (quin, 8H), 1.50 (sex, 8H), 1.01 (t, 12H).

Synthesis of 1,6,7,12-tetrabromo-PMADE

PTE-Br$_4$ (1.50 g, 1.55 mmol) and p-toluenesulfonic acid monohydrate (0.30 g, 1.58 mmol) were dissolved in n-heptane (7 mL) and stirred for 48 hours at reflux temperature. After that the mixture was cooled to 70°C and hexane (15 mL) was added to the mixture, which was left to stir for 1 hour. The resulting suspension was filtered and the solids were washed with a few portions of a water:ACN (1:1) mixture. This was then followed by drying of the solids in a vacuum oven. The crude was then added to ACN (35 mL) and sonicated for 5 minutes. The solids were filtered off and dried again. This yielded the product with 90% purity. Silica column chromatography was avoided for larger scale synthesis, since the product tend to degrade on the silica.

Yield: 0.95 g, 65%. ^{1}H NMR (400 MHz, CDCl$_3$): δ = 8.80 (s, 2H), 8.28 (s, 2H), 4.38 (m, 4H), 1.82 (m, 4H), 1.49 (m, 4H), 1.01 (t, J = 8.0 Hz, 6H). ^{13}C NMR (100 MHz, CDCl$_3$): δ = 166.53, 158.57, 137.77, 135.19, 134.04, 131.59, 129.10, 125.76, 124.03, 123.28, 118.04, 66.32, 30.52, 19.19, 13.75.

Synthesis of 1,6,7,12-tetrabromo-PMIDE
A mixture of toluene (4 mL) and acetic acid (0.2 mL) were prepared in a round bottom flask. To the stirring solution, PMADE-Br$_4$ (0.231 g, 0.276 mmol) and methylamine (0.034 g, 1.104 mmol, 9.8 M in methanol) is added. The resulting solution is left to stir at 100°C overnight. After reaction completion was confirmed by TLC, the reaction mixture was cooled to room temperature and the solvent was removed by rotary evaporation. The crude was than purified by column chromatography (DCM:PETE 1:1), which yielded an orange-red product.

Yield: 95.1 mg, 40%. ^{1}H NMR (400 MHz, CDCl$_3$): δ = 8.75 (s, 2H), 8.25 (s, 2H), 4.40-4.30 (m, 4H), 3.57 (s, 3H), 1.80 (quin, 4H), 1.50 (quin, 4H), 0.99 (t, 6H).

Synthesis of 1,7-dibromo-6,12-dichloro-PTE
In a 25 mL round bottom flask equipped with a stirring bar, PDA-Br$_2$ (0.550 g, 1.000 mmol), I$_2$ (55 mg, 0.217 mmol) and chlorosulfonic acid (8 mL) were added. The flask was placed on a reflux condenser equipped with a CaCl$_2$ tube and heated to 90°C while stirring for 48 hours. After cooling to room temperature the reaction mixture was poured on ice, filtered and washed with plenty of water. This yielded crude PDA-Br$_2$-Cl$_2$ as a red solid. In a 10 mL round bottom flask equipped with a stirring bar the crude was suspended in DMF (3.2 mL) and subsequently BuOH (0.380 g, 5.127 mmol), BuBr (0.710 g, 5.182 mmol) and DBU (0.380 g, 2.496 mmol) were added. The reaction was stirred for 24 hours at room temperature. The solidified reaction mixture was poured into water (40 mL), filtered and washed with water. This yielded a brown-green solid.

Yield: 520 mg, 91%. ^{1}H NMR(400 MHz, CDCl$_3$): δ = 8.22 (s, 2H), 8.05 (s, 2H), 4.40-4.31 (m, 8H), 1.82-1.75 (m, 8H), 1.51-1.46 (m, 8H), 1.01-0.97 (m, 12H). ^{13}C NMR (100 MHz, CDCl$_3$): δ = 166.96, 166.86, 134.92, 133.88, 132.84, 132.04, 130.72, 130.21, 129.38, 128.25, 123.35, 123.15, 77.30, 76.99, 76.67, 66.02, 30.53, 19.19, 13.75.

Synthesis of 1,7-dibromo-6,12-dichloro-PMADE
In a 25 mL pear shaped flask, PTE-Br$_2$-Cl$_2$ (100 mg, 0.11 mmol) and p-toluenesulfonic acid monohydrate (26 mg, 0.14 mmol) were mixed with n-heptane (1 mL), resulting in a inhomogeneous reaction mixture. The reaction was kept at reflux (90°C) for 26 hours without stirring. Instead, the mixture was manually homogenized on a regular basis. The

reaction progress was monitored by TLC. The crude reaction mixture was purified with column chromatography (1:5 DCM:PETE →100% DCM). The product was isolated as a red solid.

Yield: 48 mg, 48%. ^{1}H NMR(400 MHz, CDCl$_3$): δ = 8.79 (s, 1H), 8.63 (s, 1H), 8.28 (s, 1H), 8.11 (s, 1H), 4.41-4.31 (m, 4H), 1.84-1.77 (m, 4H), 1.52-1.47 (m, 4H), 1.02-0.98 (m, 6H). ^{13}C NMR (100 MHz, CDCl$_3$): δ = 166.61, 166.51, 158.64, 158.55, 137.67, 135.11, 134.69, 134.28, 133.97, 133.04, 132.17, 131.84, 131.57, 131.50, 128.05, 126.96, 125.43, 124.73, 123.87, 123.66, 118.47, 118.03, 77.30, 76.99, 76.67, 66.29, 30.51, 19.18, 13.74.

Synthesis of 1,7-dibromo-6,12-dichloro-PMIDE
PMADE-Br$_2$-Cl$_2$ (48 mg, 0.064 mmol), n-butylamine (7 mg, 0.096 mmol) and propionic acid (2 mL) were loaded into a 25 mL pear shaped flask equipped with a magnetic stirrer. The flask was attached to the reflux column and heated to 100°C. The reaction progress was monitored with TLC. After 7-8 hours, the heating was switched off and the reaction mixture was allowed to cool down to room temperature. The mixture was poured into water, filtered with a Buchner filter and extensively washed with water. Afterwards, the product was isolated as an orange solid.

Yield: 17 mg, 33%. ^{1}H NMR (400 MHz, CDCl$_3$): δ = 8.77 (s, 1H), 8.60 (s, 1H), 8.27 (s, 1H), 8.09 (s, 1H), 4.41-4.31 (m, 4H), 4.22-4.18 (m, 2H), 1.83-1.76 (m, 4H), 1.73-1.76 (m, 2H), 1.52-1.42 (m, 4H), 1.31-1.24 (m, 2H), 1.01-0.96 (m, 9H). ^{13}C NMR (100 MHz, CDCl$_3$): δ = 166.79, 166.69, 162.42, 162.36, 135.80, 135.04, 133.88, 133.71, 133.53, 132.83, 132.12, 131.52, 131.42, 130.97, 130.27, 128.64, 127.52, 123.92, 123.91, 123.66, 123.32, 122.58, 122.10, 77.31, 77.00, 76.68, 66.16, 40.60, 31.90, 30.53, 30.17, 29.67, 29.33, 22.66, 20.30, 19.19, 14.09, 13.79, 13.74.
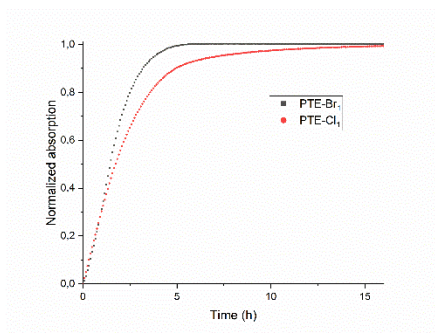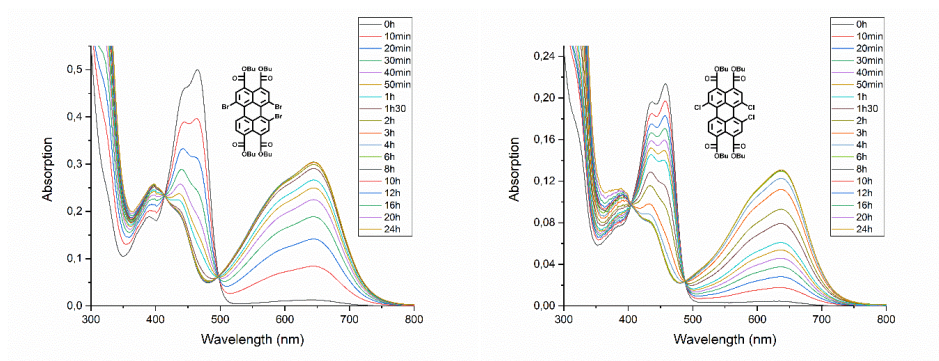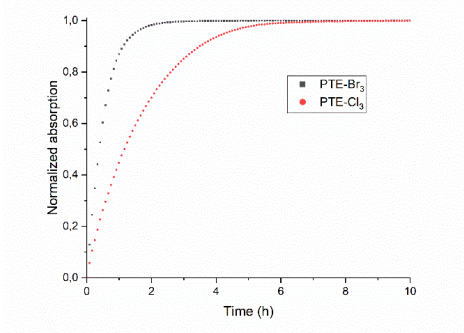
4.5 Supporting information
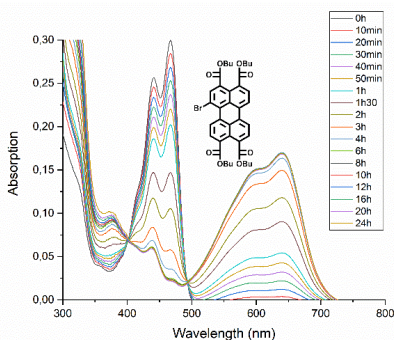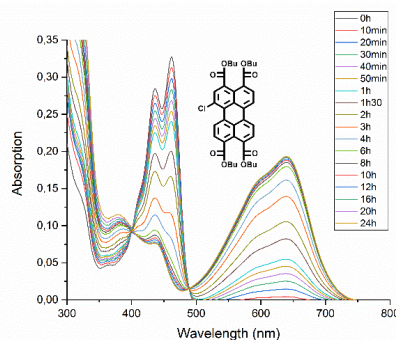
(A)   (B)

(C)

Figure S1. A) UV-VIS spectra of PTE-Br$_1$ in the presence of pyrrolidine over time. Isosbestic point at 493 nm. B) UV-VIS spectra of PTE-Cl$_1$ in the presence of pyrrolidine over time. Isosbestic point at 489 nm, C) Normalized absorption of (A) and (B) at 640 nm over time.

(A)

(B)

(C)

Figure S2. A) UV-VIS spectra of PTE-Br$_3$ in the presence of pyrrolidine over time. Isosbestic point at 497 nm. B) UV-VIS spectra of PTE-Cl$_3$ in the presence of pyrrolidine over time. Isosbestic point at 489 nm, C) Normalized absorption of (A) and (B) at 645 nm and 634 nm respectively over time.
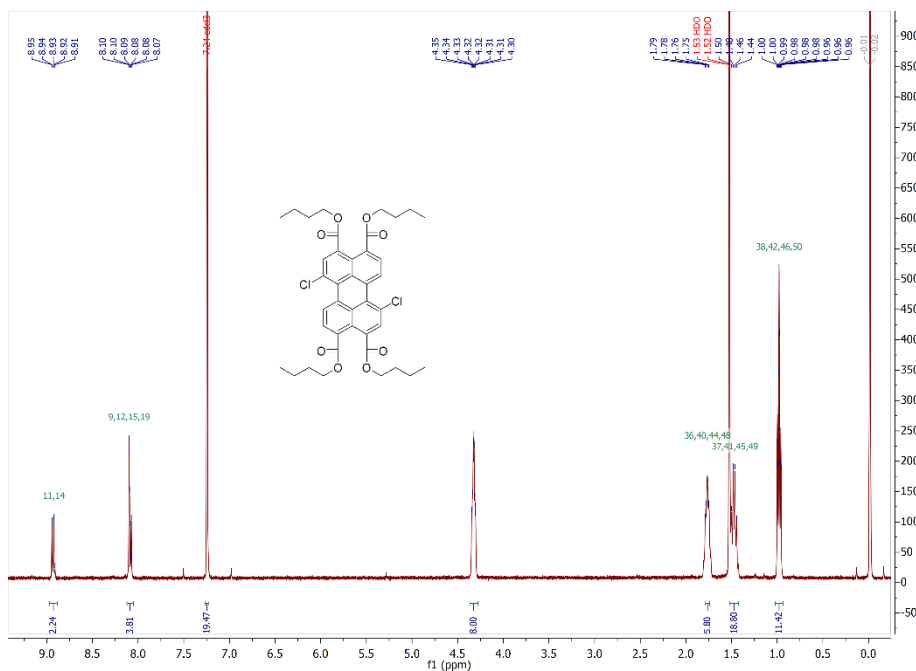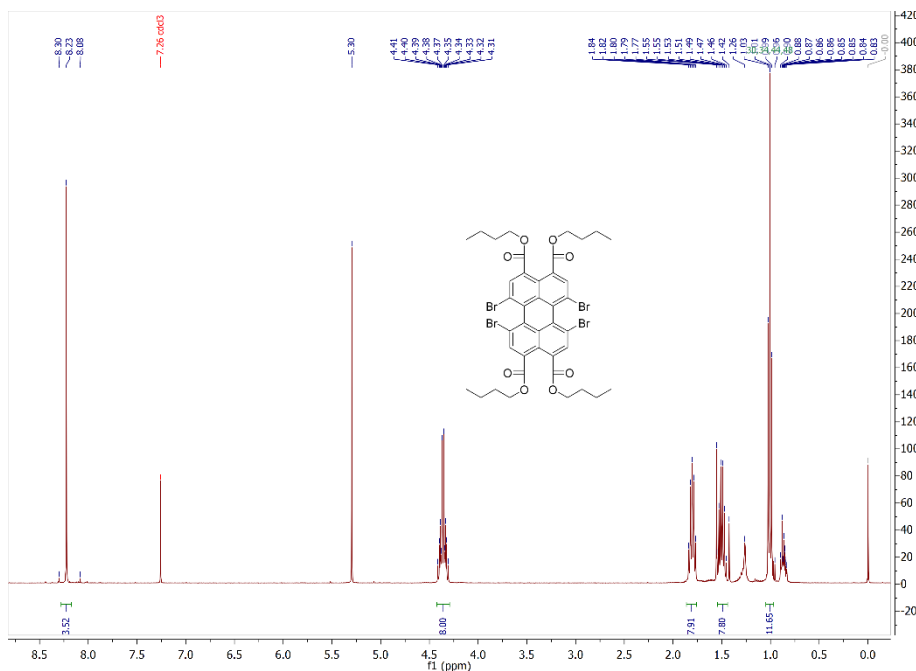
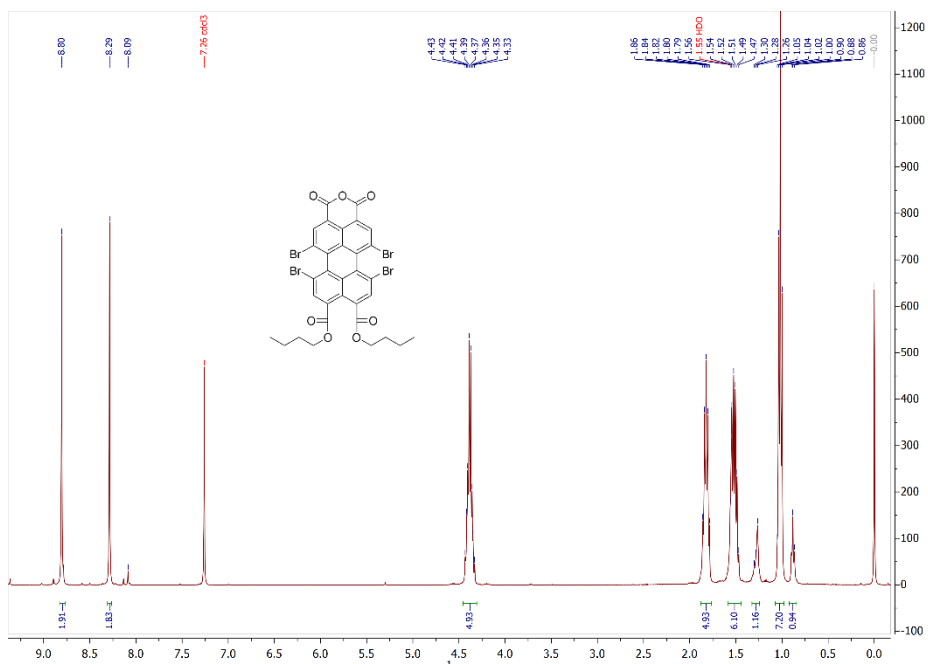128

Figure S3. *¹H NMR of PTE-Cl₂.*

Figure S4. *¹H NMR of PTE-Br₄.*

Figure S5. *^{1}H NMR of PMADE-Br$_4$.*
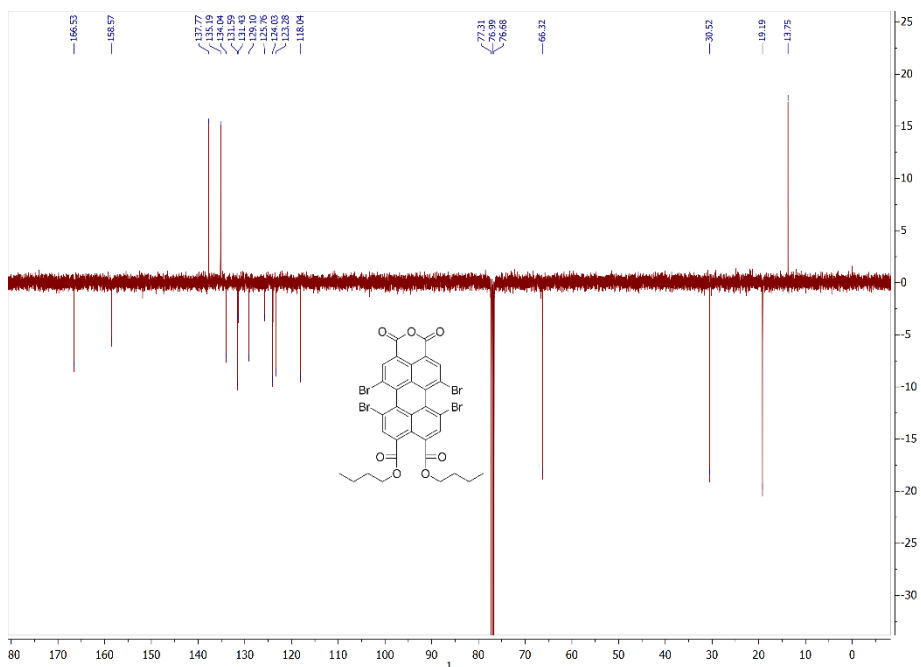
Figure S6. *^{13}C NMR of PMADE-Br$_4$.*
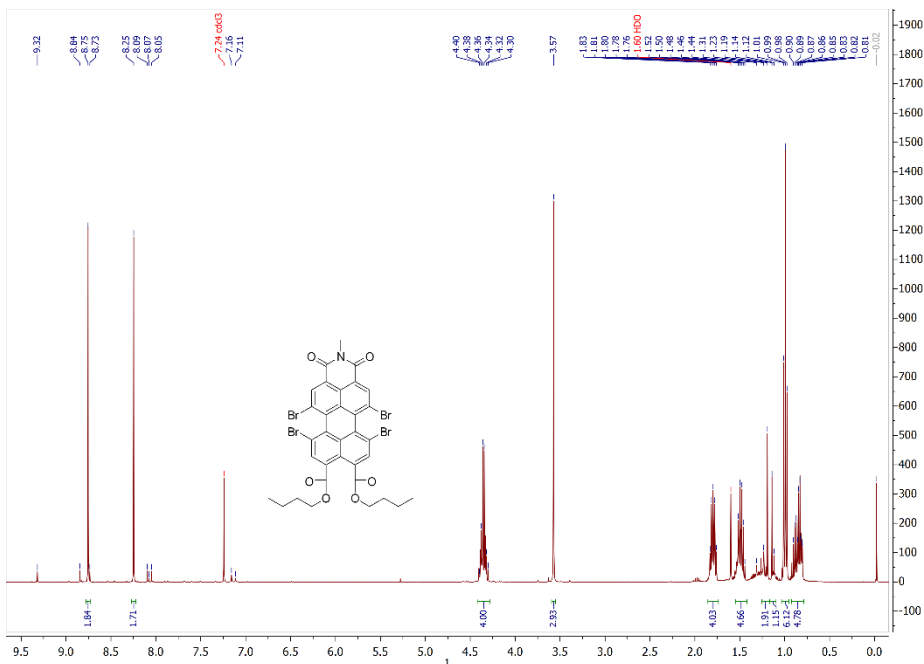
Figure S7. *${}^1H$ NMR of PMIDE-Br${}_4$.*
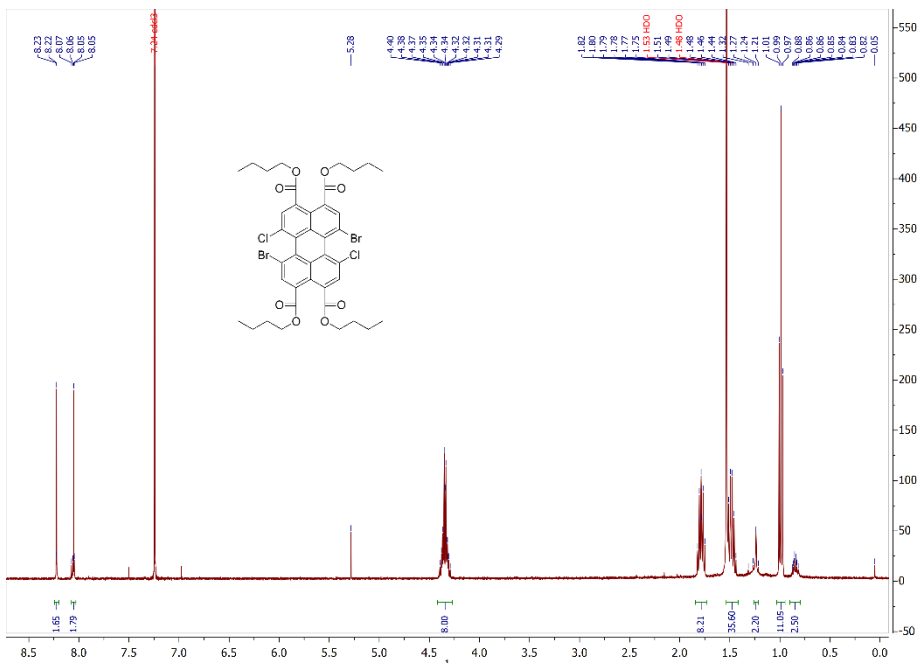
Figure S8. *${}^1H$ NMR of PTE-Br${}_2$-Cl${}_2$.*
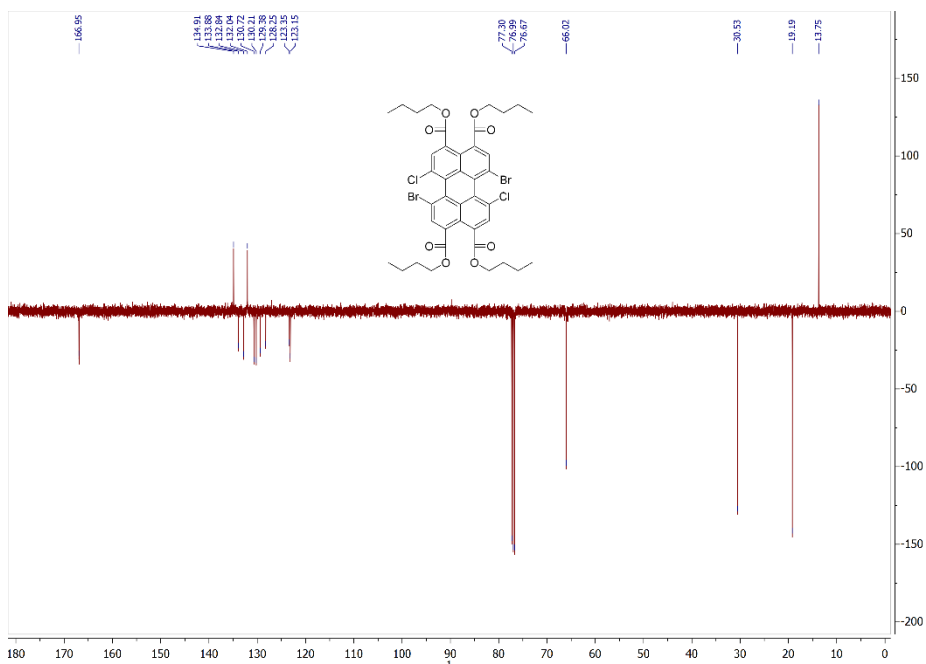
Figure S9. *¹³C NMR of PTE-Br₂-Cl₂.*

Figure S10. *¹H NMR of PMADE-Br₂-Cl₂.*

Figure S11. *¹H NMR of PMIDE-Br₂-Cl₂.*

4.6 References

(1) Kardos, M. Über Einige Aceanthrenchinon- Und 1.9-Anthracen-Derivate. *Berichte Dtsch. Chem. Ges.* **1913**, *46* (2), 2086–2091. https://doi.org/10.1002/cber.191304602126.
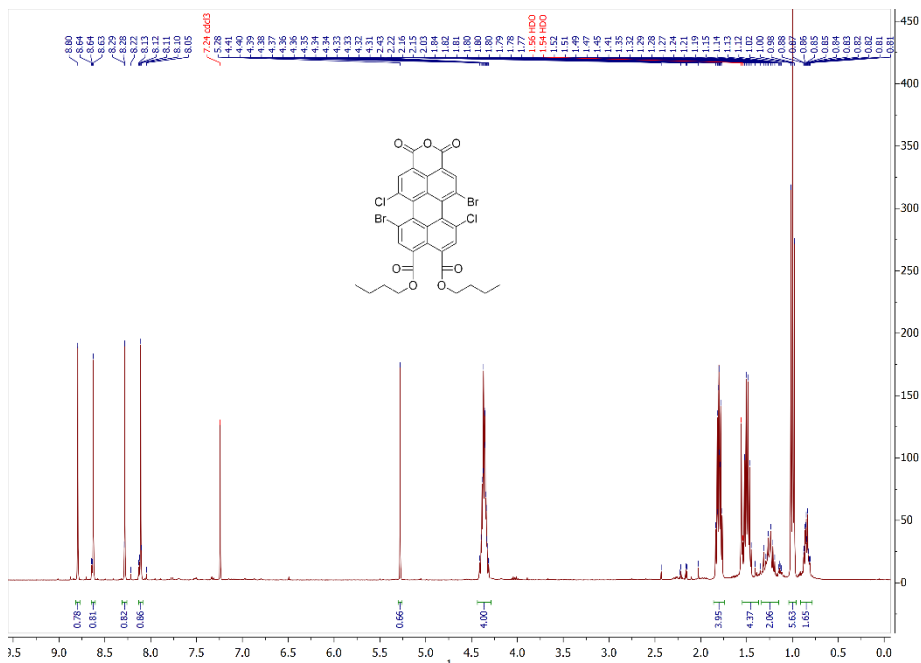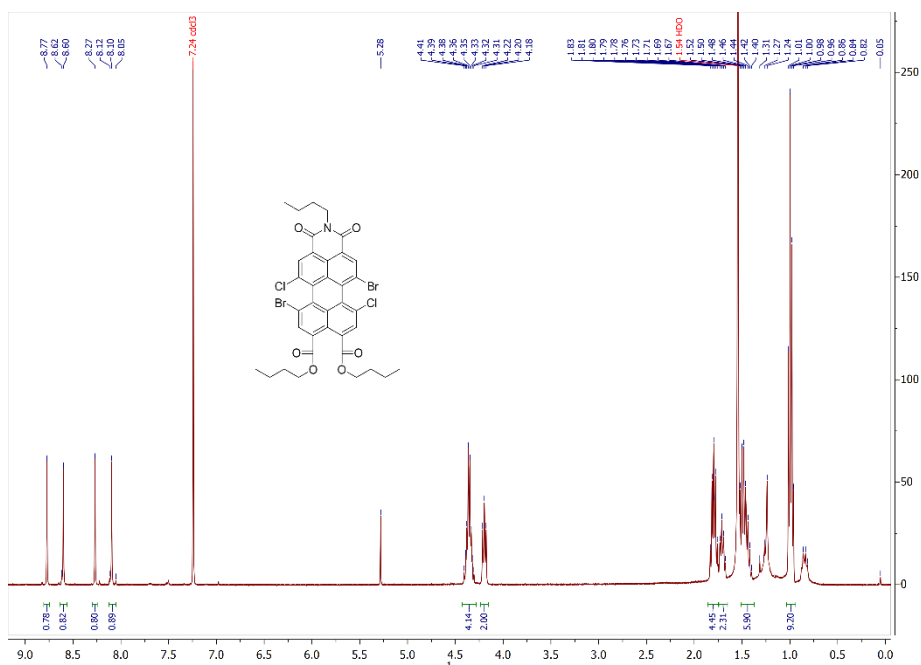
(2) Herbst, W.; Hunger, K.; Wilker, G. *Industrial organic pigments: production, properties, applications*; Wiley-VCH: Weinheim, 2004.

(3) Nielsen, C. B.; Holliday, S.; Chen, H.-Y.; Cryer, S. J.; McCulloch, I. Non-Fullerene Electron Acceptors for Use in Organic Solar Cells. *Acc. Chem. Res.* **2015**, *48* (11), 2803–2812. https://doi.org/10.1021/acs.accounts.5b00199.

(4) Liu, Z.; Wu, Y.; Zhang, Q.; Gao, X. Non-Fullerene Small Molecule Acceptors Based on Perylene Diimides. *J. Mater. Chem. A* **2016**, *4* (45), 17604–17622. https://doi.org/10.1039/C6TA06978A.

(5) Zink-Lorre, N.; Font-Sanchis, E.; Sastre-Santos, Á.; Fernández-Lázaro, F. Perylenediimides as More than Just Non-Fullerene Acceptors: Versatile Components in Organic, Hybrid and Perovskite Solar Cells. *Chem. Commun.* **2020**, *56* (27), 3824–3838. https://doi.org/10.1039/D0CC00337A.

(6) Soto Perez, G.; Dasgupta, S.; Żuraw, W.; Fuentes Pineda, R.; Wojciechowski, K.; Krishnan Jagadamma, L.; Samuel, I.; Robertson, N. Solution-Processable Perylene Diimide-Based Electron Transport Materials as Non-Fullerene Alternatives for Inverted Perovskite Solar Cells. *J. Mater. Chem. A* **2022**, *10* (20), 11046–11053. https://doi.org/10.1039/D2TA01321E.

(7) Xiao, J.; Yu, H.-J.; Xie, D.-X.; Shinohara, A.; Fan, T.; Yi, J.; Lin Lai, J. Y.; Shao, G.; Yan, H. Organic Photovoltaic Performance and Structural Relationship of Non-Fullerene Small Molecule Acceptors Based on a Tetraarylphenazine Core and Perylene Diimide. *Sustain. Energy Fuels* **2023**, *7* (1), 294–299. https://doi.org/10.1039/D2SE01218A.

(8) Kelley, R. F.; Shin, W. S.; Rybtchinski, B.; Sinks, L. E.; Wasielewski, M. R. Photoinitiated Charge Transport in Supramolecular Assemblies of a 1,7,N,N'-Tetrakis(Zinc Porphyrin)-Perylene-3,4:9,10-Bis(Dicarboximide). *J. Am. Chem. Soc.* **2007**, *129* (11), 3173–3181. https://doi.org/10.1021/ja0664741.

(9) Hurenkamp, J. H.; Browne, W. R.; Augulis, R.; Pugžlys, A.; Loosdrecht, P. H. M. van; Esch, J. H. van; Feringa, B. L. Intramolecular Energy Transfer in a Tetra-Coumarinperylene System: Influence of Solvent and Bridging Unit on Electronic Properties. *Org. Biomol. Chem.* **2007**, *5* (20), 3354–3362. https://doi.org/10.1039/B711681K.

(10) Fujitsuka, M.; Harada, K.; Sugimoto, A.; Majima, T. Excitation Energy Dependence of Photoinduced Processes in Pentathiophene–Perylene Bisimide Dyads with a Flexible Linker. *J. Phys. Chem. A* **2008**, *112* (41), 10193–10199. https://doi.org/10.1021/jp805350d.

(11) Wasielewski, M. R. Self-Assembly Strategies for Integrating Light Harvesting and Charge Separation in Artificial Photosynthetic Systems. *Acc. Chem. Res.* **2009**, *42* (12), 1910–1921. https://doi.org/10.1021/ar9001735.

(12) Blas-Ferrando, V. M.; Ortiz, J.; Bouissane, L.; Ohkubo, K.; Fukuzumi, S.; Fernández-Lázaro, F.; Sastre-Santos, Á. Rational Design of a Phthalocyanine–Perylenediimide Dyad with a Long-Lived Charge-Separated State. *Chem. Commun.* **2012**, *48* (50), 6241–6243. https://doi.org/10.1039/C2CC31087B.

(13) Frischmann, P. D.; Mahata, K.; Würthner, F. Powering the Future of Molecular Artificial Photosynthesis with Light-Harvesting Metallosupramolecular Dye Assemblies. *Chem. Soc. Rev.* **2013**, *42* (4), 1847–1870. https://doi.org/10.1039/C2CS35223K.

(14) Ghosh, I.; Ghosh, T.; Bardagi, J. I.; König, B. Reduction of Aryl Halides by Consecutive Visible Light-Induced Electron Transfer Processes. *Science* **2014**, *346* (6210), 725–728. https://doi.org/10.1126/science.1258232.

(15) Dubey, R. K.; Inan, D.; Sengupta, S.; Sudhölter, E. J. R.; Grozema, F. C.; Jager, W. F. Tunable and Highly Efficient Light-Harvesting Antenna Systems Based on 1,7-Perylene-3,4,9,10-Tetracarboxylic Acid Derivatives. *Chem. Sci.* **2016**, *7* (6), 3517–3532. https://doi.org/10.1039/C6SC00386A.

(16) Zeman, C. J. I.; Kim, S.; Zhang, F.; Schanze, K. S. Direct Observation of the Reduction of Aryl Halides by a Photoexcited Perylene Diimide Radical Anion. *J. Am. Chem. Soc.* **2020**, *142* (5), 2204–2207. https://doi.org/10.1021/jacs.9b13027.

(17) Iordache, A.; Delhorbe, V.; Bardet, M.; Dubois, L.; Gutel, T.; Picard, L. Perylene-Based All-Organic Redox Battery with Excellent Cycling Stability. *ACS Appl. Mater. Interfaces* **2016**, *8* (35), 22762–22767. https://doi.org/10.1021/acsami.6b07591.

(18) Ranque, P.; George, C.; Dubey, R. K.; van der Jagt, R.; Flahaut, D.; Dedryvère, R.; Fehse, M.; Kassanos, P.; Jager, W. F.; Sudhölter, E. J. R.; Kelder, E. M. Scalable Route to Electroactive and Light Active Perylene Diimide Dye Polymer Binder for Lithium-Ion Batteries. *ACS Appl. Energy Mater.* **2020**, *3* (3), 2271–2277. https://doi.org/10.1021/acsaem.9b01225.

(19) Dubey, R. K.; Westerveld, N.; Sudhölter, E. J. R.; Grozema, F. C.; Jager, W. F. Novel Derivatives of 1,6,7,12-Tetrachloroperylene-3,4,9,10-Tetracarboxylic Acid: Synthesis, Electrochemical and Optical Properties. *Org. Chem. Front.* **2016**, *3* (11), 1481–1492. https://doi.org/10.1039/C6QO00374E.

(20) Dubey, R. K.; Knorr, G.; Westerveld, N.; Jager, W. F. Fluorescent PET Probes Based on Perylene-3,4,9,10-Tetracarboxylic Tetraesters. *Org. Biomol. Chem.* **2016**, *14* (5), 1564–1568. https://doi.org/10.1039/C5OB02540K.

(21) Dubey, R. K.; Eustace, S. J.; van Mullem, J. S.; Sudhölter, E. J. R.; Grozema, F. C.; Jager, W. F. Perylene Bisimide Dyes with up to Five Independently Introduced Substituents: Controlling the Functionalization Pattern and Photophysical Properties Using Regiospecific Bay Substitution. *J. Org. Chem.* **2019**, *84* (15), 9532–9547. https://doi.org/10.1021/acs.joc.9b01131.

(22) Gao, J.; Xiao, C.; Jiang, W.; Wang, Z. Cyano-Substituted Perylene Diimides with Linearly Correlated LUMO Levels. *Org. Lett.* **2014**, *16* (2), 394–397. https://doi.org/10.1021/ol403250r.

(23) Jozeliūnaitė, A.; Striela, R.; Labanauskas, L.; Orentas, E. Practical Preparation of Octa- and Tetrabromoperylene Diimides and Derivatives Thereof. *Synthesis* **2017**, *49* (23), 5176–5182. https://doi.org/10.1055/s-0036-1589088.

(24) Zhao, Y.; Wasielewski, M. R. 3,4:9,10-Perylenebis(Dicarboximide) Chromophores That Function as Both Electron Donors and Acceptors. *Tetrahedron Lett.* **1999**, *40* (39), 7047–7050. https://doi.org/10.1016/S0040-4039(99)01468-9.

(25) Zhang, X.; Pang, S.; Zhang, Z.; Ding, X.; Zhang, S.; He, S.; Zhan, C. Facile Synthesis of 1-Bromo-7-Alkoxyl Perylene Diimide Dyes: Toward Unsymmetrical Functionalizations at the 1,7-Positions. *Tetrahedron Lett.* **2012**, *53* (9), 1094–1097. https://doi.org/10.1016/j.tetlet.2011.12.080.

(26) Baier, M. C.; Huber, J.; Mecking, S. Fluorescent Conjugated Polymer Nanoparticles by Polymerization in Miniemulsion. *J. Am. Chem. Soc.* **2009**, *131* (40), 14267–14273. https://doi.org/10.1021/ja905077c.

(27) Sengupta, S.; Dubey, R. K.; Hoek, R. W. M.; van Eeden, S. P. P.; Gunbaş, D. D.; Grozema, F. C.; Sudhölter, E. J. R.; Jager, W. F. Synthesis of Regioisomerically Pure 1,7-Dibromoperylene-3,4,9,10-Tetracarboxylic Acid Derivatives. *J. Org. Chem.* **2014**, *79* (14), 6655–6662. https://doi.org/10.1021/jo501180a.

(28) Huth, K.; Heek, T.; Achazi, K.; Kühne, C.; Urner, L. H.; Pagel, K.; Dernedde, J.; Haag, R. Noncharged and Charged Monodendronised Perylene Bisimides as Highly Fluorescent Labels and Their Bioconjugates. *Chem. – Eur. J.* **2017**, *23* (20), 4849–4862. https://doi.org/10.1002/chem.201605847.

134

(29)   Xue, C.; Sun, R.; Annab, R.; Abadi, D.; Jin, S. Perylene Monoanhydride Diester: A Versatile Intermediate for the Synthesis of Unsymmetrically Substituted Perylene Tetracarboxylic Derivatives. *Tetrahedron Lett.* **2009**, *50* (8), 853–856. https://doi.org/10.1016/j.tetlet.2008.11.084.

(30)   Philip, A. M.; Hsu, C. C.; Wei, Z.; Fridriksson, M. B.; Grozema, F. C.; Jager, W. F. Directing Charge Transfer in Perylene Based Light-Harvesting Antenna Molecules. *J. Chem. Phys.* **2020**, *153* (14), 144302. https://doi.org/10.1063/5.0021454.

(31)   Queste, M.; Cadiou, C.; Pagoaga, B.; Giraudet, L.; Hoffmann, N. Synthesis and Characterization of 1,7-Disubstituted and 1,6,7,12-Tetrasubstituted Perylenetetracarboxy-3,4:9,10-Diimide Derivatives. *New J. Chem.* **2010**, *34* (11), 2537–2545. https://doi.org/10.1039/C0NJ00240B.

(32)   Fan, L.; Xu, Y.; Tian, H. 1,6-Disubstituted Perylene Bisimides: Concise Synthesis and Characterization as near-Infrared Fluorescent Dyes. *Tetrahedron Lett.* **2005**, *46* (26), 4443–4447. https://doi.org/10.1016/j.tetlet.2005.04.137.

(33)   Zhou, M.; Zhu, L.; Sun, Z.; Yang, Z.; Cao, D.; Li, Q. Tri-Petal Lilac-Like Perylene: Asymmetrical Substituted Platform for Regioselective Ether-Exchange Reaction. *Synlett* **2017**, *28* (16), 2121–2125. https://doi.org/10.1055/s-0036-1590808.

(34)   Pagoaga, B.; Giraudet, L.; Hoffmann, N. Synthesis and Characterisation of 1,7-Di- and Inherently Chiral 1,12-Di- and 1,6,7,12-Tetraarylperylenetetracarbox-3,4:9,10-Diimides. *Eur. J. Org. Chem.* **2014**, *2014* (24), 5178–5195. https://doi.org/10.1002/ejoc.201402625.

5

Magnesium alginate as an electrolyte for magnesium batteries

Abstract

We present magnesium alginate as an aqueous polymer electrolyte for use in magnesium batteries. Alginates are polysaccharides extracted from algae, that form hydrogel materials when subjected to divalent and trivalent cations. They are renewable, non-toxic, biocompatible materials that are widely used in the food- and pharma industries. Mg^{2+} is weakly bound to the alginate polymer, which results in a hydrogel-like material that contains mobile magnesium ions. We propose that this is the ideal situation for an electrolyte that behaves in a similar way as a 'water-in-salt' system. Our models confirm that Mg^{2+} is only weakly bound to alginate in the presence of water. Magnesium alginate was successfully synthesized and characterized by FTIR, XRD and PDF. Ionic conductivity was proven with EIS measurements, a 2 wt% magnesium electrolyte shows a conductivity of 1.8 mS/cm. During conductivity experiments, we noticed the formation of a black layer on the magnesium electrodes, which can improve the ionic conductivity of the electrolyte. We carefully characterized this layer with XPS and saw that it mainly consists of alginate derivatives.

5.1 Introduction

In recent decades, extensive research has been done on magnesium and magnesium ion batteries. To date this has not let to a successful commercialization. This is very unfortunate, since magnesium chemistry has promising properties that could bring a magnesium battery in direct competition with present lithium-ion batteries. Magnesium is the 5th most abundant element on the planet's crust, and approximately 1000 times more abundant compared to lithium and it also offers more possible mining locations which enables supply chain diversification.[1,2] The theoretical energy densities of lithium and magnesium are comparable. The success of lithium-ion batteries can be explained by a delicate interplay between the correct cathode, an intercalating graphite anode and an electrolyte that is tolerant towards both. This is due to the solid electrolyte interface (SEI).[3] The development of an electrolyte stable against magnesium is the main obstacle in the development of magnesium batteries. Most organic solvents and simple magnesium salts ($Mg(SO_3CF_3)_3$ and $Mg(ClO_4)_2$ e.g.) will form a surface film on the electrodes, which shows no conductivity for magnesium ions.[4] Ethereal electrolytes with Grignard reagents do not form surface films, but are strongly reducing and therefore have a low anodic stability.[5]

Salts play an integral role in electrolytes. They allow for ionic conductivity and therefore the proper operation of a battery. A higher concentration of salts is generally considered good for both oxidative and reductive stabilities of electrodes. This has been shown in conventional lithium-ion batteries.[6] The general principle behind this, is that solvent molecules are coordinated to ions and thereby stabilizing them when in close proximity of the electrodes. In aqueous electrolytes, this gets an extra dimension, since water needs to be stabilized enough to widen beyond the traditional electrochemical stability window of water at 1.23 V. When the concentration of salts gets high enough, the water content gets lower than the salt content, creating a 'water in salt' electrolyte. Suo *et al.* have demonstrated a successful application of the water-in-salt concept in a lithium-ion battery.[7] They dissolved LiTFSI to such an extent that for every Li^+ there were only 2.6 water molecules on average. This widened the electrochemical stability window of water to ~3.0 V. The low water mobility diminished the degradation of water, and a formed SEI further decreased degradation. Leong et al. have shown a similar approach in an aqueous water-in-salt magnesium battery.[8] They have shown that magnesium chloride can be used to stabilize the magnesium anode against water degradation. They are able to cycle their battery over 700 cycles with a discharge plateau at 2.4-2.0 V.

There is no clear concentration definition of what constitutes a water-in-salt electrolyte. However, it is understood that water is bound and organized around ions in the solution to such an extent that little to no free water is present. A similar situation can occur in hydrogels, where water molecules are organized around hydrophilic polymer chains.[9–11] The water dynamics in hydrogels are very complex and change for different hydrogels, but water molecules are either tightly bound, loosely bound or free.

Alginates are polysaccharides that can be harvested from algae. They are extensively used in the food- and pharma industries, since they exhibit biocompatibility and excellent mechanical properties.[12] Alginates are composed of two different monomers that differ in whether the carboxylate is situated in the axial or equatorial positions (G- and M monomers respectively). When these carboxylates are exposed to divalent or trivalent
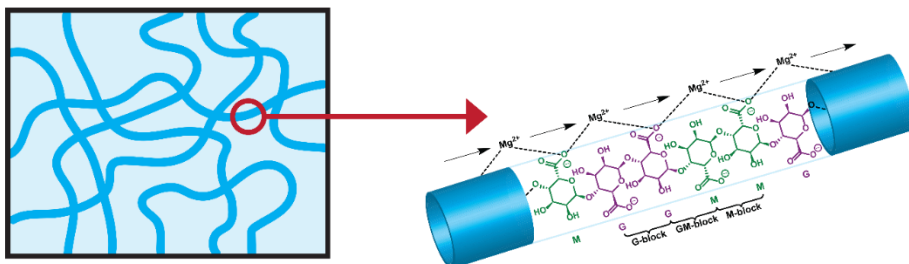
Figure 1. Schematic overview over Mg^{2+} 'hopping' between carboxylates.

Because this convergence of properties, we investigate the use of magnesium alginate as an electrolyte in magnesium batteries. This work will explain the synthesis of magnesium alginate, explore its use as an electrolyte and give a computational understanding of its inner workings.

cations, they can form a crosslink.[13] Through this, the alginate can form a hydrogel. The best known example is with calcium, which forms a strong and robust hydrogel, where calcium ions are in a dissolved-like state.[14] Magnesium ions cannot induce such strong gelation of alginate, the bonds between the ions and carboxylate is weaker and the magnesium is therefore more mobile in the solution, see Figure 1.[15] For an electrolyte, the ionic mobility must be maintained for its proper function.

5.2 Results and Discussion
5.2.1. X-ray Diffraction (XRD) Analysis
To check whether the synthesis of magnesium alginate was successful, XRD was used to determine whether Mg(OH)$_2$ was still present in the synthesized Mg-alginate samples. This was done by analysing both the synthesized products and the initial reagents. The results are presented in Figure 2.
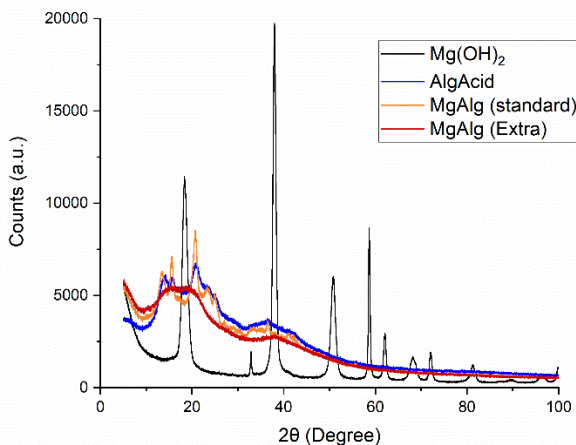

Figure 2. XRD analysis results of Mg-Alg and the initial reagents.

$Mg(OH)_2$ is crystalline and is characterised by peaks at 18.4°, 33.3°, 38.0°, 50.7°, 58.8°, 68.2°, and 72.0° corresponding to the $Mg(OH)_2$ brucite structure.[16] The spectra for $Mg(OH)_2$ in Figure 2 has distinct peaks that correspond to $Mg(OH)_2$ structure. The Alg-acid is mostly amorphous and so produces smaller peaks. Since none of the synthesized Mg-Alg samples have the distinctive peaks that can be attributed to $Mg(OH)_2$, it can be concluded that $Mg(OH)_2$ is not present in the samples. The Mg-Alg samples produce a similar curve to that of the alginic acid, suggesting that the alginic acid did retain its structure. The Mg-Alg, standard ratio (all G-monomer carboxylates are bound by magnesium) sample shows a good correlation with the Alg-acid compared to the Mg-Alg, extra Mg ratio (all G and M-monomer carboxylates are bound by magnesium) sample implying the amount of Mg influences the alginate structure.

5.2.2. Pair Distribution Function (PDF)

Pair Distribution Function results are shown in Figures 3a and 3b, where the X-ray diffraction data from Mg-Alg in 2θ-space are shown (Fig. 3a), and used for the calculations of the pair distribution function (Fig. 3b). The X-ray diffraction data from Mg-Alg in Q-space, with the background subtracted, and the reduced structure factor F(Q) of Mg-Alg, can be found in the supporting information.
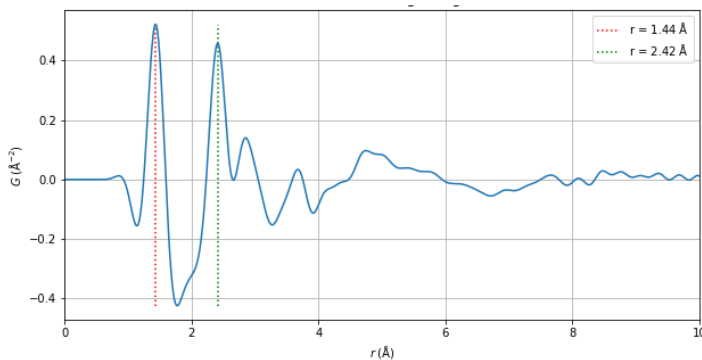
(A)
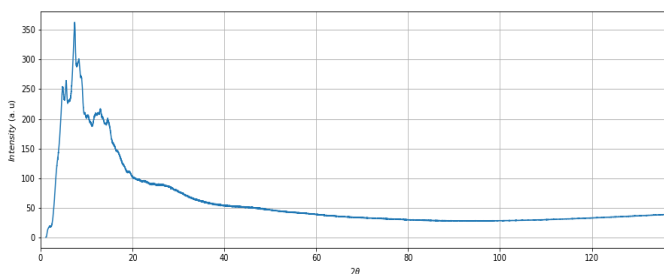
(B)

Figure 3. (a) X-ray diffraction data from Mg-Alg in 2θ-space. (b) The pair distribution function G(r) of Mg-Alg. The X-ray diffraction data from Mg-Alg in Q-space, with the background subtracted, and the reduced structure factor F(Q) of Mg-Alg, can be found in the supporting information.

The results show two main peaks at 1.44 Å and 2.42 Å. The first peak can be attributed to the C-C, C-O distances which are typically in this order. The peak at 2.42 Å is thus assigned by the distance between a Mg^{2+} ion and the carboxyl group. This number is longer than often seen for Mg^{2+}-ligand bond lengths, which are typically in the order of 2.15 Å to 2.25Å.[17] However the elongation can be understood by the binding energy as discussed by Rutkowska-Zbik et al. They found that Mg^{2+}-H_2O bonds are longer and weaker in chelates than in the complexes with water, which was explained by the binding energy being proportional to the electron density of the chelating ligand. The negative charge at the carboxylate group in the alginate is delocalized over two oxygen's reducing the electron density and thus giving an even longer bond length, as found here for the alginate ligand. The other peaks are then related to Mg^{2+}-C and other Mg^{2+}-O distances. This elongated bond length, and thus a reduced binding energy toward the alginate ligand, gives rise to the solubility behavior of the magnesium alginate, hence, allowing magnesium ions to be dissociated from the alginate ligand once it is brought in contact with water.

Modelling with GROMOS[18] showed that in all cases studied, the Mg^{2+} ion is surrounded by six oxygen atoms, but the origin of the oxygen is strongly dependent on the water content.

Table 1: *Distribution of the ligand oxygen atoms arising from water and alginate, see Figure 4.*

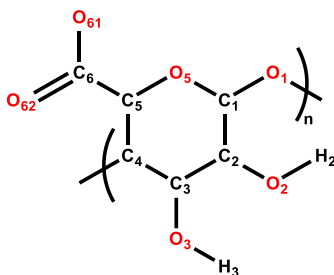| H_2O: Mg^{2+} ratio	O_{61} (Carboxyl)	O_{62} (Carboxyl)	O_3 (Hydroxyl)	O_2 (Hydroxyl)	O_5 (Ether)	O_1 (Ether)	O (H_2O)
0	2.07 ± 0.05	2.09 ± 0.05	0.5 ± 0.03	0.95 ± 0.04	0.12 ± 0.02	0.05 ± 0.01	-
6	0.86 ± 0.04	1.00 ± 0.03	0.034 ± 0.007	0.103 ±0.014	0.007 ± 0.003	-	4.01 ± 0.01
12	0.27 ± 0.02	0.42 ± 0.03	0.041 ± 0.009	0.146 ± 0.016	-	-	5.1 ± 0.08
24	0.062 ± 0.008	0.062 ± 0.008	0.027 ± 0.011	0.094 ± 0.013	-	-	5.74 ± 0.07

Figure 4. *Chemical structure of an alginate residue with numbering of atoms.*

In a dry system, the carboxyl group (O51 and O52, see Table 1 and Figure 4) provides the most ligand atoms (43%) followed by the hydroxyl group (15%). A small percentage has been found for the O5 and O1 oxygen atoms. Once, water is introduced, the oxygen ligand will come mainly from the water molecules, with a strong decrease of the carboxyl and hydroxyl groups as ligand. The oxygen ligands O4 and O1 do not participate as ligands anymore. The obtained results agreed quite well with earlier observed results where an alginate system containing Mg^{2+} does not show any gelation effects, which can

be attributed to the cation's high affinity for water (solvation free energy). The interaction with water is so strong that most cations will be entirely surrounded by water molecules, or will only bind to a carboxylate anion in a mono-dentate configuration (mono complex). If the cation is bound in a mono-dentate configuration, crosslinks cannot be formed between alginate polymers.[11] Another study by Perić-Hassler and Hünenberger showed that Mg^{2+} might bind loosely to the carboxylate group.[19] The carboxylate oxygens are positioned in the second hydration shell around the cation in a loose binding configuration. The carboxylate group and the cation share the same water molecule (which is positioned in between them) as a solvation molecule. This means the cation is surrounded by water while maintaining a connection to the carboxylate group. The influence of loose binding on gelling properties is unclear.

5.2.3. Characterization using Fourier Transform InfraRed Spectroscopy (FTIR)

To further understand the structure of Mg-Alg, FTIR was used to investigate the chemical bonds that were present in the samples. Spectra were taken for Mg-Alg and Alg-acid and these are shown in Figure 5. Several peaks were shifted or changed in intensity compared to Alg-acid, in particular the –C–O (~1000 cm^{-1}) and –COO^- (~1400 –1600 cm^{-1}) bands. The Mg-Alg samples exhibit a peak at 1419 cm^{-1} that is absent in the Alg-acid, likely represents $-COO^-$ stretching due to the presence of Mg^{2+}. Alg−acid and Mg-Alg (standard ratio) sample shows a peak that corresponds to the free acid –C=O stretch (~1700 cm^{-1}) which is absent in the Mg-Alg (extra Mg ratio) sample spectra. The "standard" Mg-Alg sample was prepared such that the amount of Mg was just enough to bind to the carboxylate group of the G-residue. The "extra'' Mg-Alg sample had additional Mg to bind to the carboxylate group of both the G and M- residues which would explain why the sample does have the free acid –C=O peak. All these stretch vibrations correspond to bonds that are involved in the binding of the metal to alginate polysaccharide.

5.2.4. Electrolyte Preparation and Cell Assembly

To investigate the electrochemical performance of the Mg-Alg electrolyte different concentrations of the electrolyte were prepared. The Mg-Alg powder that was obtained from the drying process was used to prepare the electrolyte. The concentrations of the
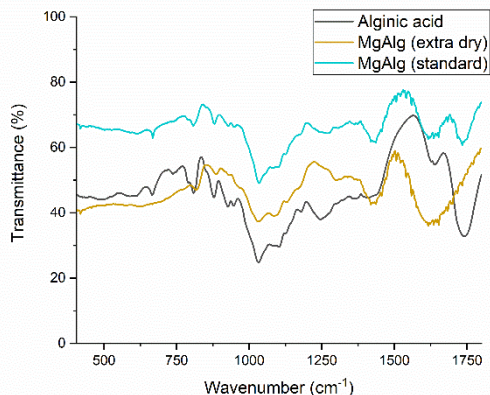

Figure 5. *FTIR Spectra of the Mg-Alg samples against the Alg-Acid*

electrolyte prepared were 2 wt%, 25 wt%, 50 wt%, 75 wt% and 100 wt%. To prepare the 2 wt% and 5 wt%, Mg-Alg was weighed and a proportionate amount of water was added using a pipet to achieve the required concentration. This solution was then placed in a vial and allowed to mix overnight. For the 50 wt% and 75 wt%, the proportionate amounts of powder and water were mixed in a mortar and pestle. The mixture were than pressed at 8 tons for 3 minutes, resulting in pellets of ~0.9 mm thickness and a diameter of 13 mm.

To assemble the test cells, magnesium plates were used as electrodes. The electrolyte solution was first placed onto one electrode (magnesium plate), the separator was then added (fibre glass separators), followed by some more electrolyte. This was then topped off by the second electrode (magnesium plate), after which the assembly was placed within the external housing. The rubber seal was then added so that the housing could be closed hermetically. This would then be connected to a galvanostat/ potentiostat equipped with an impedance meter for testing. The electrodes were sanded before the experiment. The different components can be seen in Figure 6.
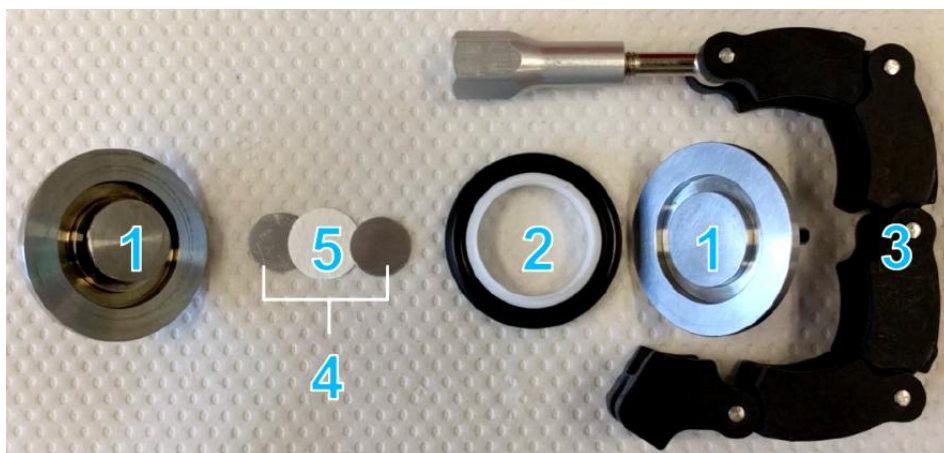

Figure 6. *Cell Assembly: (1) External housing; (2) Rubber seal; (3) Clamp; (4) Two electrodes (magnesium plates) and; (5) Electrolyte and separator*

5.2.5. Electrolyte Conductivity
The cell assembly in Figure 6 was connected to the potentiostat (Metrohm Autolab PGSTAT12) so as to measure the resistance of the electrolyte. The conductivity (σ) was then calculated according to Equation 1; using the electrolyte resistance (R_{el}), the thickness of the electrolyte layer (L) and the active area (A). The conductivity was taken at different temperatures for the different concentrations of electrolyte (Fig. 7). Mg-Alg concentration influences the electrolyte conductivity to a large extent, with lower concentrations (2 wt% and 25 wt%) exhibiting higher conductivities compared to the electrolyte with 50 wt%, 75 wt% and 100 wt%. Conductivity of lower concentration electrolytes are not significantly influenced by an increase of temperature, while the higher concentrations electrolytes are. The conductivity of the electrolyte seems to be influenced largely by the ionic conductivity as opposed to electronic conductivity. This is evidenced by the fact that addition of more charge carriers (Mg-Alg) does not significantly improve the conductivity of the electrolyte. In Figure 7b, conductivity is

converted to activation energy, using Arrhenius plots. A clear trend can be seen, where the activation energy changes according to the phase of the magnesium alginate.

$$\sigma = \frac{L}{A}\left(\frac{1}{R_{el}}\right)\left(\frac{S}{cm}\right) \hspace{2cm} \{EQ\ 1\}$$
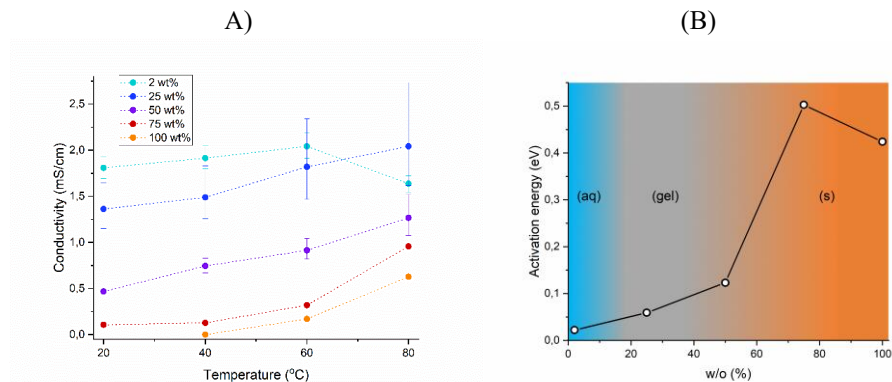
A)
(B)

Figure 7. (a) Conductivity of electrolytes at different concentrations. (b) Conductivities from Figure 6a converted to activation energies. Colors scheme shows different phases of the material, in solution, hydrogel-like, solid.

5.2.6. Electrochemical impedance spectroscopy (EIS) Profiles

EIS was carried out to measure the internal resistance of the electrolyte and the interfacial resistance between the electrolyte and the magnesium electrodes. While running the EIS experiment a dark layer was observed on the pristine magnesium electrodes (Figure 8). This layer became more apparent with each experiment and so, the effect the layer had on the system was investigated.

Figure 8. Bare magnesium surface compared with surface covered by the black layer after contact with Alginate solution

There is a significant change in the overall impedance due to the formation of the black coating in Figure 9a. The charge resistance before the formation of the black layer (~ 1200 Ω) is higher compared to resistance after the formation of the black layer (~ 700 Ω). The black layer seems to reduce the charge transfer resistance causing a subsequent reduction in the impedance but introduces a new process with its own time constant, which can be seen by the additional semicircle formed in the high frequency range. This new process could be indicative of the black coating formation. In Figure 9b, the increased number of charge carriers (25 wt%) results in a general reduction in the

impedance compared to the Figure 8a. However, there's an observed increase in the charge transfer resistance after the formation of the layer. Here also, there's a noticeable new process in the higher frequency range. Further increasing the charge carriers (50 wt%; Fig. 9c) causes a significant increase in both the charge transfer and interfacial resistance, with the new process becoming more prominent. It could be that this layer is made from the Mg-Alg in the electrolyte which would reduce the amount of charge carriers hence increasing the resistance. This would also explain why the layer seems to improve charge kinetics (decreasing interfacial resistance) in lower concentration (2 wt% and 25 wt%) electrolytes.

The blue EIS curves for 2 wt%, 25 wt% and 50 wt% indicate that an increase in the amount of charge carriers (from 2 to 25 wt%) in the electrolyte to some extent is beneficial for reducing interfacial resistances, however, continued increase (50 wt%) in the amount charge carriers causes a substantial increase in the resistance. Implying that ionic conductivity of the electrolyte plays a major role in improving the interfacial resistances of the cell.
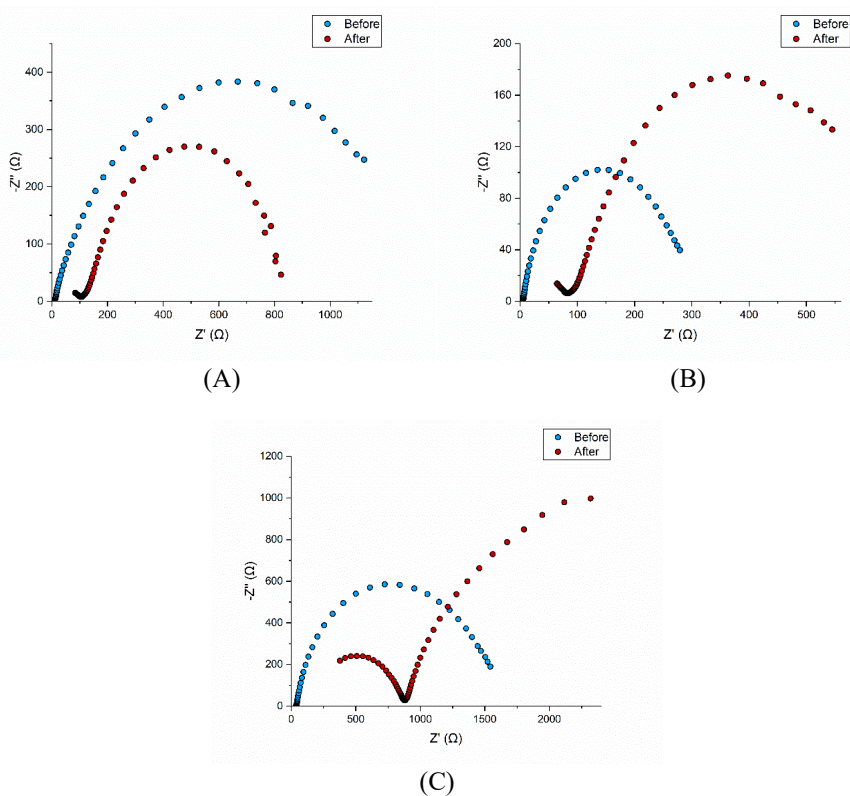
(A)

(B)

(C)

Figure 9. *EIS Curves: (a) EIS results for the 2 wt% Mg-alginate electrolyte before (blue) and after (red) forming of the black layer. (b) EIS results for the 25 wt% Mg-alginate electrolyte before (blue) and after (red) forming of the black layer. (c) EIS results for the 50 wt% Mg-alginate electrolyte before (blue) and after (red) forming of the black layer*

5.2.7. Surface Analysis using X-Ray Photoelectron Spectroscopy (XPS)

XPS was used to determine the surface chemistry of the magnesium plate before cycling in a cell (blue) and then also after cycling in a cell (red). A basic elemental analysis was performed as well as a more detailed analysis of the oxygen, magnesium and carbon bonds on the layer.

The relative ratios of C 1s : O 1s : Mg 2s change drastically during cycling (before: 62:21:17 vs after: 21:52:27)(Fig. 10). The magnesium at the surface before cycling consists of mainly magnesium hydroxide bonds with a small amount of metallic magnesium, compared to, after cycling that consists of mainly metallic magnesium with a small amount of magnesium bound to oxygen (more magnesium oxide than magnesium hydroxide). The carbon (bonded mainly in the 'C-C' configuration) present on the electrode before cycling is unexpected and maybe due to some contamination during testing. Conversely, the carbon present on the electrode after cycling contains 'C-C', 'O-C=O', 'C-OH' which are bonds indicative of an alginic structure. This suggests that the black layer formed on the electrodes after cycling has an alginate structure and would explain the improved charge kinetics observed by the EIS experiments after the formation of the black layer.
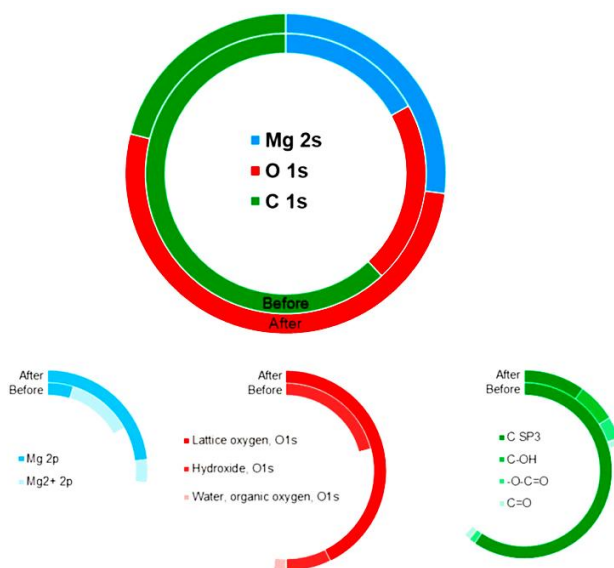

Figure 10. *Relative ratios of C 1s: O 1s: Mg 2s found during the different scans with the XPS. In the top centre is the survey analysis. The bottom from left to right: Mg2s Scan, O1s Scan, C1s Scan*
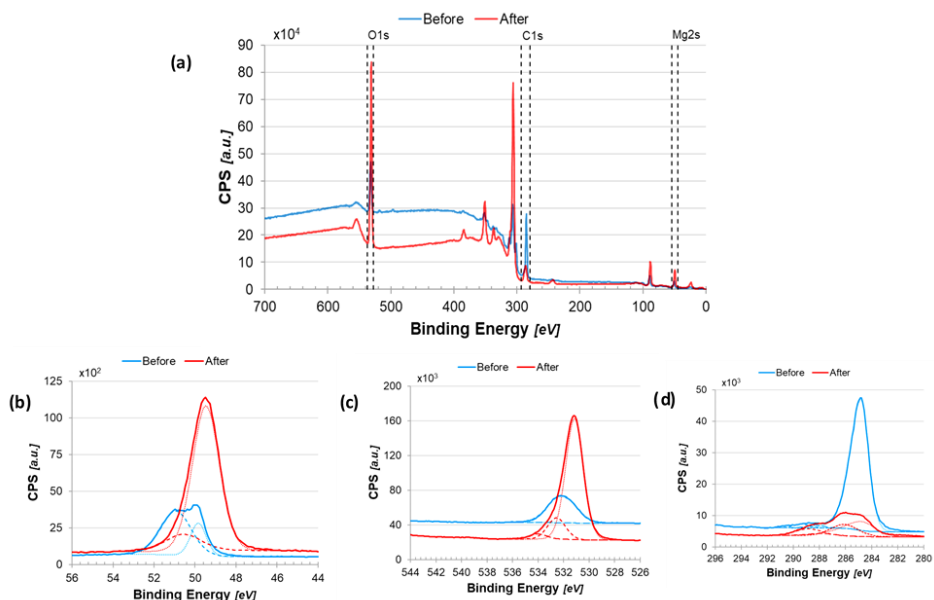
Figure 11. *(a) Survey analysis of the electrodes before (blue) and after (red) cycling; (b) Magnesium 2s scan results; (c) Oxygen 1s scan results and; (d) Carbon 1s scan results*

5.2.8. Modelling

Upon the introduction of water molecules, oxygen atoms (from water, carboxylate- and hydroxyl groups) are competing to form a bond with the cation. In simulations with a water content of 21.1 and 34.8 wt%, all cations could still form crosslinks between polymers. However, at 51.6 wt%, all divalent cations were almost entirely surrounded by water molecules in their first hydration shell. As a result, oxygen atoms from alginate are pushed away toward the second shell and form a solvent-bridged ion pairing with the cation. This increases the diffusivity of the cation. However, the structure could still be a hydrogel.

5.3 Experimental
5.3.1. Materials and methods

Magnesium alginate was synthesised using alginic acid (Alg-acid; Sigma Aldrich) and magnesium hydroxide ($Mg(OH)_2$; Sigma Aldrich). The Alg-acid used had a composition of 61% M-block residues and 39% G-block residues.

XRD was performed with an X'Pert Pro PANalytical, PDF analysis was done with PDF-getX and Highscore, FTIR was performed with a Thermo Scientific Nicolet iS50 FTIR, EIS was performed with a Metrohm Autolab PGSTAT12 and XPS was performed with a Thermo scientific K-Alpha

5.3.2. Synthesis of Magnesium Alginate

G-monomers have the higher affinity for binding cations. This was used to synthesize two different magnesium alginates. One where only the G-monomers is bound to magnesium (standard ratio) and one were all monomers are bound to magnesium (extra Mg ratio).

Alginic acid (1g) was added to a round bottom flask together with water. The solution was left to stir overnight. Following this, magnesium hydroxide (0.049 g for the 'standard ratio', 0.165 g for the 'Extra Mg ratio') was added to the solution. The solution was left to stir overnight again. After reaction completion, the solution was transferred to a beaker and left in an oven at 110 °C until all water had evaporated. The remaining solid were crushed with mortar and pestle to yield a fine powder.

5.3.3. Pair Distribution Function (PDF)

The X-ray diffraction measurements were carried out with a PANalytical Empyrean Alpha 1 diffractometer, with a silver X-Ray tube as source having a wavelength λ of 0.559 Å, as this provides a large Q-window, compared to for instance a copper source. This is necessary to achieve a high resolution pair distribution function, as the Fourier transform integral is thus done over a larger interval - a maximum 2θ of 140° and a λ of 0.559 Å, results in $Q_{max} = 21.1$ Å^{-1}.

Measurements were performed on Mg-Alg powder in a glass capillary, and an empty capillary for subtracting the contribution of the glass. The measurements were done in a time span of 20 hours. In order to obtain a pair distribution function (PDF), the X-ray Diffraction measurement data are collected and then processed in the program "PDFgetX3". This program has a build-in option to subtract the background diffraction pattern, which in our case is the glass capillary.

When configuring the program "PDFgetX3" the following parameters were chosen: a minimum Q-value of 0.8 Å^{-1}, as Q-values smaller than 0.8 showed too much noise. The maximum Q-value is determined by the wavelength of the X-rays and the maximum angle that is measured, which gave $Q_{max} = 21.1$ Å^{-1}. The maximum frequency in the so-called F(Q) correction polynomial was set to 1.7.

5.3.4. Modelling

Modelling was then done using the GROMOS software, where Lennard-Jones-parameters (LJ-parameters) must be chosen such that the ion reproduces several structural and thermodynamic data like the ion-to-oxygen distance in water, the first shell coordination number (CN), and the hydration free energy.[20] The LJ-parameter of Mg^{2+} is well defined by the GROMOS force field. A detailed description of the simulations is further described in the supporting information. The structure of an alginate chain used in the simulation consists of 12 G-monomers. M-monomers were not considered since they are not involved in the formation of the egg box structured cavities where the cation can reside. To avoid the presence of chain-end effects during the simulation, the chain is made infinitely long by linking the two terminal monomers, using periodic boundary conditions. This might eliminate chain-end effects, and may introduce restrictions regarding the longitudinal and torsional flexibility of the chain, where actually the longitudinal effects are expected to be limited since the persistence length of the polymer is about 40 residues.[21] Notice that the persistence length is defined as the distance over which the correlation in the direction of the tangent is lost and is exponentially decaying.

Because the chain consists of only 12 monomers, which is significantly shorter than the persistence length, a rigid rod can approximate the chain's behaviour. Also the effect on torsional flexibility is expected to be minimal since the 12 monomers are compatible with two- and three-fold helix structures.[19] The polymer structure was created using POLYS 2.0 software.[22]

To determine the structural and ionic properties of Mg^{2+} in multiple aqueous environments, four simulations with different water content were carried out. The H_2O : Mg^{2+} ratios considered were: 0, 6, 12 and 24. As explained in the supporting information, three simulation boxes are used to cope with the computational time.

5.4 Conclusions

We have investigated the use of magnesium alginate, as an electrolyte for magnesium batteries. We have successfully synthesized and characterized magnesium alginate by FTIR and XRD; no residual magnesium hydroxide is in the samples. PDF measurements show an elongated bond length between Mg^{2+} and alginate, which already indicates a weaker bond. Calculations with the GROMOS force field confirm this, when water is introduced in the system, the magnesium almost completely dissociates from the alginate. Ionic conductivity of magnesium was proven with EIS (1.8 mS/cm for 2 wt% Mg-Alg), higher concentrations of alginate give lower conductivities. When in a high concentration regime, the conductivity becomes temperature dependant and increases with higher temperatures. The black layer that is formed during the conductivity experiments was analysed by XPS, which indicates that the layer is composed of alginate derivatives. Overall, we can conclude that magnesium alginate is a promising and interesting electrolyte for magnesium batteries. It can be used in different concentrations and we see the development of a passivation layer that can improve the performance of the electrolyte. The hydrogel-like material can be used as a 'water-in-salt' system. Although not discussed in this paper, we are currently already working on finding suitable electrode materials to produce the first batteries that use magnesium alginate as an electrolyte.

5.5 References

(1)   Johnson, I. D.; Ingram, B. J.; Cabana, J. The Quest for Functional Oxide Cathodes for Magnesium Batteries: A Critical Perspective. *ACS Energy Lett.* **2021**, *6* (5), 1892–1900. https://doi.org/10.1021/acsenergylett.1c00416.

(2)   Yoo, H. D.; Shterenberg, I.; Gofer, Y.; Gershinsky, G.; Pour, N.; Aurbach, D. Mg Rechargeable Batteries: An on-Going Challenge. *Energy Environ. Sci.* **2013**, *6* (8), 2265. https://doi.org/10.1039/c3ee40871j.

(3)   Winter, M.; Barnett, B.; Xu, K. Before Li Ion Batteries. *Chem. Rev.* **2018**, *118* (23), 11433–11456. https://doi.org/10.1021/acs.chemrev.8b00422.

(4)   Lu, Z.; Schechter, A.; Moshkovich, M.; Aurbach, D. On the Electrochemical Behavior of Magnesium Electrodes in Polar Aprotic Electrolyte Solutions. *J. Electroanal. Chem.* **1999**, *466* (2), 203–217. https://doi.org/10.1016/S0022-0728(99)00146-1.

(5)   Yagi, S.; Tanaka, A.; Ichikawa, Y.; Ichitsubo, T.; Matsubara, E. Effects of Water Content on Magnesium Deposition from a Grignard Reagent-Based Tetrahydrofuran Electrolyte. *Res. Chem. Intermed.* **2014**, *40* (1), 3–9. https://doi.org/10.1007/s11164-013-1449-9.

(6)   Shen, Y.; Liu, B.; Liu, X.; Liu, J.; Ding, J.; Zhong, C.; Hu, W. Water-in-Salt Electrolyte for Safe and High-Energy Aqueous Battery. *Energy Storage Mater.* **2021**, *34*, 461–474. https://doi.org/10.1016/j.ensm.2020.10.011.

(7)   Suo, L.; Borodin, O.; Gao, T.; Olguin, M.; Ho, J.; Fan, X.; Luo, C.; Wang, C.; Xu, K. "Water-in-Salt" Electrolyte Enables High-Voltage Aqueous Lithium-Ion Chemistries. *Science* **2015**, *350* (6263), 938–943. https://doi.org/10.1126/science.aab1595.

(8)   Leong, K. W.; Pan, W.; Wang, Y.; Luo, S.; Zhao, X.; Leung, D. Y. C. Reversibility of a High-Voltage, Cl--Regulated, Aqueous Mg Metal Battery Enabled by a Water-in-Salt Electrolyte. *ACS Energy Lett.* **2022**, *7* (8), 2657–2666. https://doi.org/10.1021/acsenergylett.2c01255.

(9)   Shapiro, Y. E. Structure and Dynamics of Hydrogels and Organogels: An NMR Spectroscopy Approach. *Prog. Polym. Sci.* **2011**, *36* (9), 1184–1253. https://doi.org/10.1016/j.progpolymsci.2011.04.002.

(10)   McConville, P.; Whittaker, M. K.; Pope, J. M. Water and Polymer Mobility in Hydrogel Biomaterials Quantified by 1H NMR: A Simple Model Describing Both T1 and T2 Relaxation. *Macromolecules* **2002**, *35* (18), 6961–6969. https://doi.org/10.1021/ma020539c.

(11)   El Hariri El Nokab, M.; Lasorsa, A.; Sebakhy, K. O.; Picchioni, F.; van der Wel, P. C. A. Solid-State NMR Spectroscopy Insights for Resolving Different Water Pools in Alginate Hydrogels. *Food Hydrocoll.* **2022**, *127*, 107500. https://doi.org/10.1016/j.foodhyd.2022.107500.

(12)   Lee, K. Y.; Mooney, D. J. Alginate: Properties and Biomedical Applications. *Prog. Polym. Sci.* **2012**, *37* (1), 106–126. https://doi.org/10.1016/j.progpolymsci.2011.06.003.

(13)   Kiriinya, L. K.; Kwakernaak, M. C.; Van den Akker, S. C. D.; Verbist, G. L. M. M.; Picken, S. J.; Kelder, E. M. Iron and Manganese Alginate for Rechargeable Battery Electrodes. *Polymers* **2023**, *15* (3), 639. https://doi.org/10.3390/polym15030639.

(14)   Sikorski, P.; Mo, F.; Skjåk-Bræk, G.; Stokke, B. T. Evidence for Egg-Box-Compatible Interactions in Calcium−Alginate Gels from Fiber X-Ray Diffraction. *Biomacromolecules* **2007**, *8* (7), 2098–2103. https://doi.org/10.1021/bm0701503.

(15)   Topuz, F.; Henke, A.; Richtering, W.; Groll, J. Magnesium Ions and Alginate Do Form Hydrogels: A Rheological Study. *Soft Matter* **2012**, *8* (18), 4877. https://doi.org/10.1039/c2sm07465f.

(16)   Kurosawa, R.; Takeuchi, M.; Ryu, J. Fourier-Transform Infrared Analysis of the Dehydration Mechanism of Mg(OH)2 and Chemically Modified Mg(OH)2. *J. Phys. Chem. C* **2021**, *125* (10), 5559–5571. https://doi.org/10.1021/acs.jpcc.0c08696.

(17)   Rutkowska-Zbik, D.; Witko, M.; Fiedor, L. Ligation of Water to Magnesium Chelates of Biological Importance. *J. Mol. Model.* **2013**, *19* (11), 4661–4667. https://doi.org/10.1007/s00894-012-1459-3.

(18)   Christen, M.; Hünenberger, P. H.; Bakowies, D.; Baron, R.; Bürgi, R.; Geerke, D. P.; Heinz, T. N.; Kastenholz, M. A.; Kräutler, V.; Oostenbrink, C.; Peter, C.; Trzesniak, D.; van Gunsteren, W. F. The GROMOS Software for Biomolecular Simulation: GROMOS05. *J. Comput. Chem.* **2005**, *26* (16), 1719–1751. https://doi.org/10.1002/jcc.20303.

(19)   Perić-Hassler, L.; Hünenberger, P. H. Interaction of Alginate Single-Chain Polyguluronate Segments with Mono- and Divalent Metal Cations: A Comparative Molecular Dynamics Study. *Mol. Simul.* **2010**, *36* (10), 778–795. https://doi.org/10.1080/08927021003752853.

(20)   Poset, A. M. du; Zitolo, A.; Cousin, F.; Assifaoui, A.; Lerbret, A. Evidence for an Egg-Box-like Structure in Iron(II)–Polygalacturonate Hydrogels: A Combined EXAFS and Molecular Dynamics Simulation Study. *Phys. Chem. Chem. Phys.* **2020**, *22* (5), 2963–2977. https://doi.org/10.1039/C9CP04065J.

(21)   Perić, L.; Pereira, C. S.; Pérez, S.; Hünenberger, P. H. Conformation, Dynamics and Ion-Binding Properties of Single-Chain Polyuronates: A Molecular Dynamics Study. *Mol. Simul.* **2008**, *34* (4), 421–446. https://doi.org/10.1080/08927020701759699.

(22)   Engelsen, S. B.; Hansen, P. I.; Pérez, S. POLYS 2.0: An Open Source Software Package for Building Three-Dimensional Structures of Polysaccharides. *Biopolymers* **2014**, *101* (7), 733–743. https://doi.org/10.1002/bip.22449.

6

Iron and Manganese Alginate for Rechargeable Battery Electrodes

Abstract

We present a sustainable, inherently safe battery chemistry that is based on widely available and cheap materials, that is, iron and manganese hosted in alginate biomaterial known from the food and medical industry. The resulting battery can be recycled to allow circularity. The electrodes were synthesised by the alginate caging the multivalent metals to form a hydrogel in an aqueous environment. Characterisation includes FTIR, XPS and Mössbauer spectroscopy. The electrochemical performance of the electrodes was investigated by performing cyclic voltammetry (CV) and (dis)charge experiments. Mn and Fe ions show good co-ordination with the alginic acid with higher oxidation states demonstrating complex bonding behaviour. The non-optimised iron and manganese alginate electrodes already exhibit a cycling efficiency of 98% and 69%, respectively. This work shows that Fe and Mn atomically disperse in a bio-based host material and can act as electrodes in an aqueous battery chemistry. While demonstrated at cell level, it is furthermore explained how these materials can form the basis for a (semi-solid) flow cell.

6.1 Introduction

The global energy demand is expected to increase by 48% in the next 20 years partly because of the strong growth in world population.[1] Fossil fuels still provide the highest contribution to the world's energy demand, accounting for 84% of the current energy consumption.[2] There has been a global drive to switch to energy sources that have a lower carbon footprint. Renewable energy presents an opportunity to decarbonise our energy consumption with benefits ranging from a reduction in greenhouse gas emissions to the diversification of energy supplies and a reduced dependency on fossil fuels. However, the fluctuations in electricity demand and supply requires the use of batteries with novel battery chemistries that can provide safe, sustainable and affordable energy storage to overcome this intermittency.

To cope with the above requirements, materials for the negative and positive electrodes need to be low cost, environmental friendly, highly stable and have an acceptable energy density. Organic and bio-based electrodes have gained popularity because of their green and sustainable production and use, as well as their potential for application in large-scale energy storage. This is particularly important once aqueous electrolytes are considered.

More recently, the most studied organic electrode materials have been organic carbonyl compounds. Examples are quinone, naphthalene dianhydride and perylene dianhydride derivatives. When polymerised, these compounds show excellent stability in a lithium-ion battery, providing good capacity.[3]

Alginic acid is a polysaccharide that is abundantly available, environmentally friendly, cost effective and nontoxic. It is well-known for its ability to bind multivalent cations, very efficiently forming alginate hydrogels in aqueous environments.[4] This gelation ability has given alginic acid applications in the (bio)medical and food industries.[5] The ability to capture/cage cations inside its structure is of particular interest for battery applications. Iron and manganese ions are attractive candidates for novel electrode materials because of their abundance, low cost and low toxicity, and are well-known for their electron storage ability that is due to the possible changes in oxidation state. Hence, this work investigates the electrochemical properties of iron alginate (Fe-Alg) and manganese alginate (Mn-Alg) for use in rechargeable batteries.

Alginic acid is found in the cell walls of brown algae and is composed of two anionic monomers: (1,4) linked α-L guluronic acid (G) and (1,4) linked β-D-mannuronic acid (M) (Figure 1). The carboxyl group in the G- monomer has the same orientation as the hydroxyl group, whereas in the M- monomer the carboxyl group is oriented perpendicular to the hydroxyl group. Upon deprotonation, the negatively charged carboxylate can chelate with cations. Multivalent cations can crosslink the alginate polymer chains. This will increase the viscosity of the solution and in most cases results in the formation of a hydrogel. The cation's affinity towards the alginate varies depending on its charge, affinity to water, ionic radius and chemical affinity with the alginate. Bivalent alkaline earth cations (Mg^{2+}, Ca^{2+} and Sr^{2+}) form ionic bonds, whereas bivalent transition metal ions (Mn^{2+}, Co^{2+}, Cu^{2+}, Fe^{2+} and Zn^{2+}) and trivalent metal cations (Fe^{3+}, Cr^{3+}, Al^{3+}, Ga^{3+}, Sc^{3+} and La^{3+}) form complex uronates via strong coordination–covalent bonds.[6] Alginates display a good affinity for transitional metal ions with the affinity being greater for the trivalent metal cations than for divalent cations.[6] Divalent cations tend to bind to two
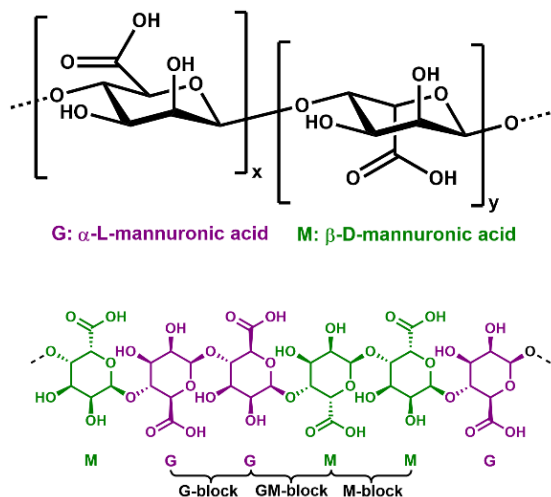
Figure 1. *Structural properties of alginate polymers with monomer units: mannuronic (M) and guluronic (G) residues and the configuration of M-, G- and GM-blocks.*

alginate chains. Trivalent cation bonding appears to be more complex; one might expect trivalent cations to bind to three alginate chains. However, some studies have shown that trivalent cations tend to bind to two alginate chains.[7,8] The remaining positive charge is then compensated for by other groups or ions.
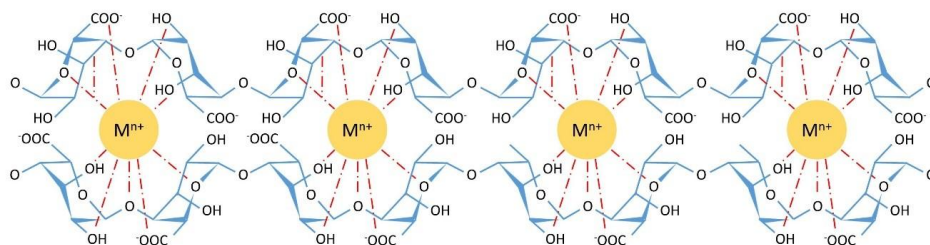

Figure 2. *Orientation of a multivalent cation in the egg-box structure; the possible chelate bonds are the dotted red lines.*

Differences in the M/G ratio also affect the chelating capability and gel strength.[9,10] Gel formation has been shown to be greatly influenced by the interactions of the G-blocks. The linkage of two G-monomers creates a cavity, making it an ideal place (cage) for a multivalent cation to reside. The crosslinking of the G-blocks by multivalent cations creates a tightly held junction, popularly referred to as 'egg-box model' (Figure 2).[11] Haug et al. experimentally showed that precipitated parts of the alginates are richer in guluronic acid compared to mannuronic acid[11]. Polymers with high M- or MG-block content produce a more elastic and flexible gel while a high G-block content gives stronger and more brittle gels.[12] Cations can also demonstrate preferential bonding to the G and M diads: Sr^{2+} ions only bind to G-blocks, whereas Ca^{2+} binds to G- and GM-blocks and Ba^{2+} only to G- and M-blocks[13]. Here, we will focus on iron(III) alginate (Fe(III)-Alg) and manganese(II) alginate (Mn(II)-Alg).

6.2 Methods and discussion

6.2.1. Synthesis and characterization

The synthesis of powders of Fe(III)-Alg and Mn(II)-Alg was successfully performed at larger scale. To that end, we used the exchange of the loosely bound sodium ions by multivalent cations. It was noticed that during the synthesis and drying process, it is important to avoid temperatures above 40 °C to minimise alginate decomposition.

In more detail, a solution of sodium alginate (2% *w/w*) was added dropwise to a vigorously stirring solution of iron(III)chloride (1 M) or manganese(II)nitrate (1 M). The solution turned into a suspension of fine gel particles and was left to stir for an hour at room temperature. After this, vacuum filtration was used to obtain these gel particles. This was followed by extensive washing of the gel residue with distilled water until the filtrate was colourless. The gel residue was initially dried by washing with ethanol and further dried in a vacuum oven at 30 °C. The dried Fe and Mn alginates were crushed into a powder via ball milling at 240 rotations/min for 5 h (Pulverisette 7, Planetary Micro Mill, Ede, the Netherlands). This yielded the final alginate powders. Reagents for synthesis were purchased at Sigma-Aldrich, Schnelldorf, Germany. Only Manganese(II)nitrate was purchased at Alfa Aesar.

6.2.2. Fourier Transform InfraRed Spectroscopy (FTIR)

Using FTIR (Frontier FT-IR, PerkinElmer) we investigated whether sodium counter-ions were successfully replaced by iron or manganese ions. Spectra were taken for Fe(III)-Alg, Mn(II)-Alg and Na-alginate and these are presented in Figure 3. Several peaks were shifted or changed in intensity compared to Na-alginate, in particular the –OH (~3200 cm^{-1}) and –COO$^-$(~1400–1600 cm^{-1}) bands. In addition, the Fe(III)-Alg shows a new peak that corresponds to the free acid –C=O stretch (~1700 cm^{-1}). All these stretch vibrations correspond to bonds that are involved in the binding of the metal to alginate polysaccharide. Although it is not possible to quantify the amount of sodium replacement, it can be observed that it has happened to a major extent. It is further interesting to see that the free –C=O stretch observed for Fe(III)-Alg might indicate a more loosely bound Fe^{3+} ion compared to the other measured divalent ions.
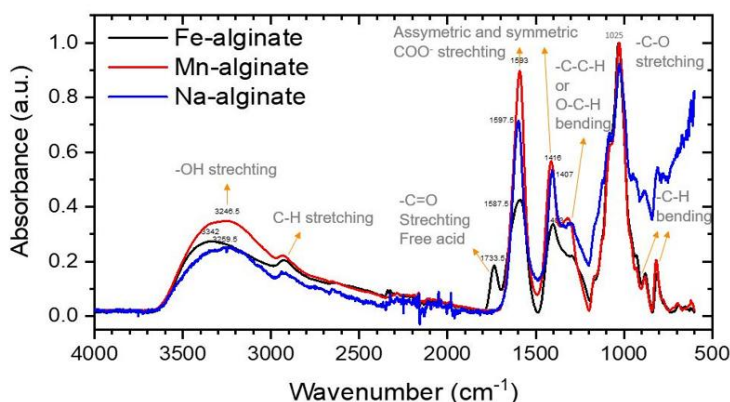

Figure 3. *IR spectrum for Fe-Alg-P, Mn-Alg-P and Na-Alg powder. Resolution 2 cm–1, 16 scans averaging.*

6.2.3. X-ray Photoelectron Spectroscopy (XPS)

X-ray photoelectron spectra provides (K-Alpha, ThermoFisher) a detailed insight into the composition of the Fe(III)-Alg and Mn(II)-Alg, as well the oxidation states of the ions. However, one should keep in mind that XPS is predominantly a surface analysis technique. The results for Fe can be seen in Figure 4. First of all, the atomic ratio between Fe and C (C:Fe) is fairly low compared to what we expected. C:Fe was measured at 68:1, while a pure Fe(III)-Alg should give a ratio between 18:1 and 12:1. A similar ratio was measured for C and Mn (63:1), which is much lower compared to the ratio of a pure Mn(II)-Alg (C:Mn 12:1). However, this could be due to the fact that XPS scans the surface of a sample and we expect ions to be wrapped inside the polysaccharide chains, inside the 'egg-box structure'. The same explanation might apply to the relatively high sodium content. The sodium ion is not necessarily bound to an 'egg-box structure' and can therefore exist on the surface. It does show that the synthesis of the Fe(III)-Alg powder is not fully complete, meaning parts at the carboxyl groups are still compensated for by sodium ions, rather than being exchanged with iron ions. The Fe and Mn content in the alginates is approximately the same, which could imply a similar crosslinking efficiency. The chloride content in the Fe(III)-Alg is also surprising and it indicates to
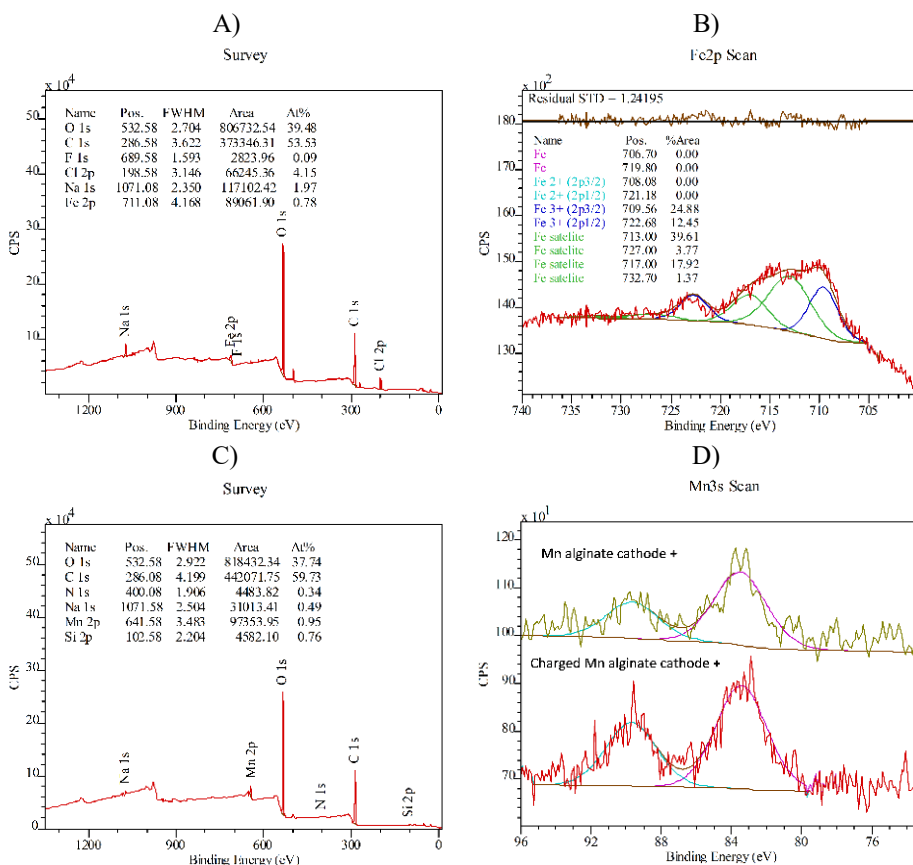

Figure 4. XPS spectra of Fe(III)-Alg (*A, B*) and Mn(II)-Alg (*C, D*).

what extent Fe^{3+} is bound to the alginate chain. It would be sterically challenging for Fe^{3+} to bind to three carboxylate groups of the alginate. This result could indicate that Fe^{3+} binds to two carboxylates and one chloride anion. Iron is observed exclusively as Fe^{3+}, while manganese shows more complex behaviour. Figure 5 shows the results of the Mn2p and Mn3s peaks before and after the charging of Mn(II)-Alg. Before charging, the peak separation $\Delta E = 6.14$ eV and the satellite feature both confirm that the oxidation state of manganese is 2+. After charging, the oxidation state was again determined to be 2+. The difference between the two measurements is the lower amount of counts per second, which implies that when the oxidation state of the manganese increases, it leaves the electrode and dissolves most likely in the aqueous electrolyte.

6.2.4. Mössbauer Spectroscopy

Mössbauer spectroscopy (Made in house at Delft University of Technology) measures the recoilless nuclear resonance fluorescence and can probe the chemical environment of an atom. This is based on the absorption and emission of gamma photons from deep orbitals that are sensitive to the ionic charge. Not all elements can be measured through Mössbauer spectroscopy; Fe can, but Mn cannot. A 'free' atom will have a lower quantum yield compared to a tightly packed atom, since some absorption energy of the 'free' atom will be changed to kinetic energy. In this paper, we use Mössbauer spectroscopy to determine the oxidation state of iron in our alginate samples. For Fe(III)-Alg, we could see 100% Fe^{3+} (Figure 5). For comparison, we also prepared a sample of Fe^{2+} ions in alginate giving Fe(II)-Alg, using $Fe_2SO_{4\ (aq)}$ as the exchange solvent. It is seen that this Fe(II)-Alg oxidises partly to Fe(III)-Alg during the synthesis.
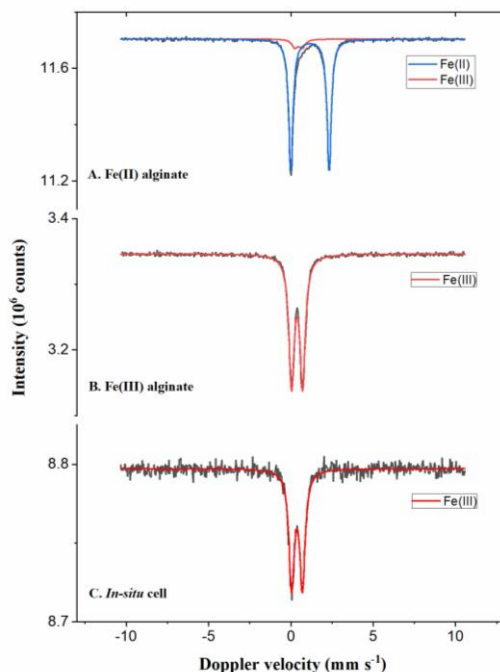

Figure 5. *Mössbauer spectra for Fe-Alg powder; (**A**) Fe(II)-Alg powder; (**B**) Fe(III)-Alg powder; (**C**) Fe(III)-Alg in an in situ cell.*

6.2.5. Thermogravimetric Analysis (TGA)

A thermogravimetric (TGA4000, PerkinElmer) analysis will give detailed information about the decomposition of the Fe(III)-Alg and Mn(II)-Alg at high temperature and various oxidative conditions. During the measurement, the weight of the compound is continuously measured (Figure 6). First, from room temperature to 175 °C, we see a decrease in sample mass of 10 wt% and 11 wt% for Fe(III)-Alg and Mn(II)-Alg, respectively, mainly caused by the release of water vapour, small organic molecules and other volatiles. Second, from 175 °C to 350 °C, decomposition of the alginate backbone and hydroxyl groups takes place. This further decreases the samples' masses by 39 wt% and 37 wt%, respectively. Third, from 350 °C to 600 °C, decarboxylation takes place, reducing the sample masses further by 13 wt% and 15 wt%, respectively. Fourth, from 600 °C to 800 °C, some minor decomposition takes place. Finally, the samples are put under aerobic conditions, while maintaining the temperature at 900 °C where all remaining organics are combusted, leaving in the end 12 wt% residual mass from Fe(III)-Alg and 12 wt% of Mn(II)-Alg, reflecting iron oxide and manganese oxide, respectively. Combining these results with the composition data obtained from XPS, we can approximate the theoretical capacities that these alginates can provide, i.e., 53 mAh/g for Fe(III)-Alg and 61 mAh/g for Mn(II)-Alg.
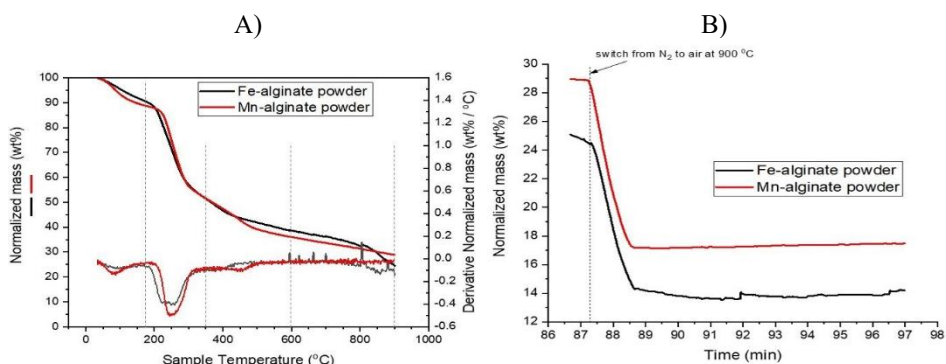
A)   B)

Figure 6. *TGA of Fe(III)-Alg (A) and Mn(II)-Alg powder (B).*

6.2.6. Electrode Preparation and Battery Assembly

To investigate the electrochemical performance of the transition metal alginates, two different electrodes were prepared: (i) with an alginate hydrogel and (ii) with the alginate powders.

The electrodes with the alginate hydrogels were made via dip coating of the hydrogel on carbon paper (CP), thus giving with an Fe(III)-Alg or Mn(II)-Alg hydrogel layer. The CP was first dipped into a 2% *w/w* Na-alginate solution and after 15 min of absorption, the CP with Na-alginate was then then placed in 0.5 M $FeCl_3$ to form the Fe(III)-Alg hydrogel layer or in 0.5 M $Mn(NO_3)_2$ to form the Mn(II)-Alg hydrogel layer for another 15 min.

(ii) The electrodes containing the alginate powders were made by casting a thin layer. This thin layer consisted of active material (synthesised Fe(III)-Alg powder or Mn(II)-Alg powder, 80 wt.%), a binder (PVDF, 10 wt.%) and conductive materials to provide a network for electrons to move freely (KS4 7 wt.%, carbon black (CB) 3 wt.%). NMP was used as the solvent. The ratio of the weight of all powders combined vs. the weight of NMP was approximately 1:1. This formed a thick slurry, which was then spread onto the

current collector substrates with a doctor blade to achieve a 150 µm thick film. Aluminium and carbon paper were used as substrates. The substrates with the slurry coating were then dried in a vacuum oven and cut to the desired shape using a paper punch (diameter ~1.27 cm).

The two types of electrodes required different battery setups. The reference electrode used for both setups was Ag/AgCl and the electrolyte was Na-alginate with different concentrations running from 1–5 *w/w* Na-alginate, possibly with the co-addition of sodium chloride (0.25 M). The battery setup for the dip-coated electrodes was as shown in Figure 7.

The thin-layer-coated electrode experiments were conducted in a test cell as shown in Figure 8. Here, two inert titanium plates acted as current collectors on which the electrodes were placed (Figure 8A). To prevent short circuiting between the electrodes, the electrolyte was placed in a mat between them (Figure 8A). The test cell was then closed (Figure 8B) and the reference electrode inserted (Figure 8C).
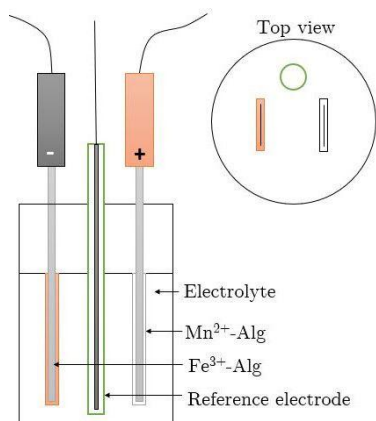

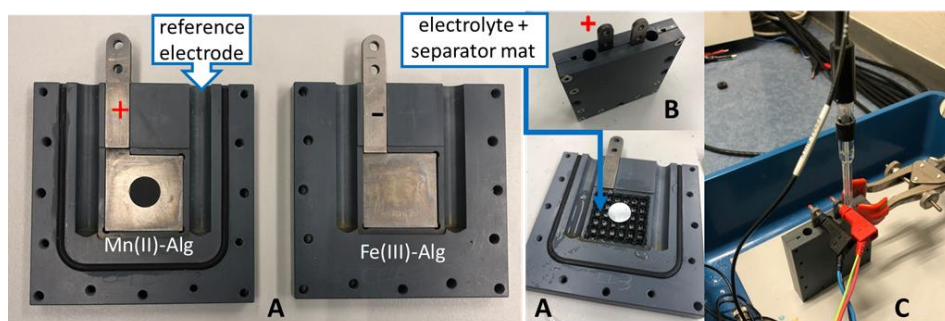*Figure 7. Battery Assembly for the Dip-Coated Electrode.*

Figure 8. Test cell: (A) open test cell; (B) closed test cell with the electrodes; and (C) closed test cell with the reference electrode.

Both battery setups, as shown in Figures 7 and 8, were then connected to a battery cycler (MACCOR 4000, Tulsa, U.S.A. or Autolab Potentiostat PGSTAT302N device, Metrohm, Barendrecht, the Netherlands) and measured via the standard software package to perform the electrochemical experiments.

6.2.7. Cyclic Voltammetry (CV)

CV was used to investigate the reversibility of the hydrogels. The electrochemical cell with the dip-coated battery electrodes was connected to the Metrohm Autolab Potentiostat PGSTAT302N cycler (Autolab) for cycling. Both hydrogels, Mn(II)-Alg and Fe(III)-Alg, show reversibility (see Figure 9), implying that they can accept and donate electrons, though Fe(III)-Alg hydrogel exhibits a higher efficiency compared to Mn(II)-Alg hydrogel. The lower efficiency for Mn(II)-Alg hydrogel indicates that some of the electrons are lost because of unwanted side reactions. This supports the findings of the XPS that manganese after charging oxidises to higher states, which then leave the electrode. The Mn(II)-Alg hydrogel voltammogram shows the anodic peak (oxidation) at 1.07 V and the cathodic peak (reduction) at 0.6 V. The Fe(III)-Alg hydrogel voltammogram shows the cathodic peak (reduction) at 0.2 V and two anodic peak (oxidation) at 0.5 V and 1.2 V, respectively. This is indicative of the complex bonding nature of Fe^{3+}, as was also observed from the XPS spectra.

6.2.8. Charge/Discharge Profiling

The electrochemical cell with the electrodes containing the alginate powders (Figure 8) was connected to the Maccor cycler to (dis)charge the cell at a constant current. Figure 10B shows that the Mn(II)-Alg powder has an oxidation potential of 0.98 V and reduction potential of 0.63 V. This is comparable with the potentials exhibited by the Mn(II)-Alg hydrogel (see Figure 9A); therefore, it is plausible that the same reaction occurs in both the hydrogel and powder, and an average reduction potential of the Mn^{2+}/Mn^{3+} redox couple is approximately 0.8 V. The reduction potential for Fe(III)-Alg powder is seen at 2.0 V (Figure 10A) with two anodic peaks at 0.43 V (averaged from 2.5 h to 3 h) and 0.9 V (averaged from 3 h to 3.5 h). This is also comparable with potentials exhibited by the Fe(III)-Alg hydrogels (see Figure 9). The differences in the potential between the
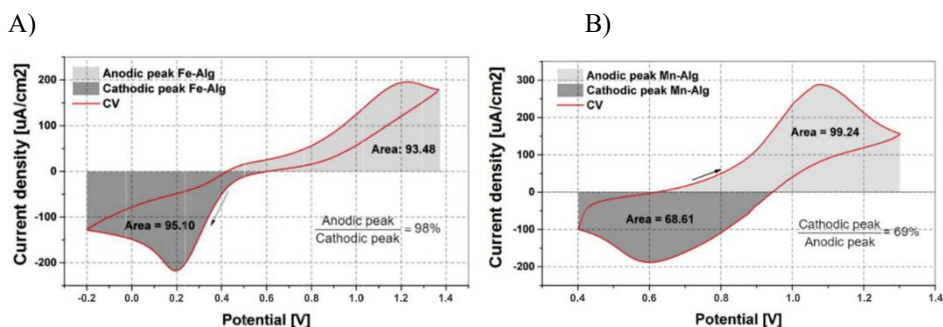
A)   B)

Figure 9. Cyclic voltammogram of (**A**) Fe(III)-Alg hydrogel. Scan rate n = 5 mV/s, 1% w/w Na-alginate electrolyte and (**B**) cyclic voltammogram of Mn(II)-Alg hydrogel. Scan rate n = 5 mV/s, 1% w/w Na-alginate electrolyte. The arrow shows the direction of the scan.

hydrogels and the powders can be attributed to differences in the internal resistances (impedance) of the systems; since the hydrogels are non-conductive, the resistance is

greater, resulting in higher overpotentials. Hence, the actual redox potential is difficult to define because of the high and somewhat changing internal resistance of the electrode.

Figure 10 also gives the specific charge of Mn(II)-Alg powder and Fe(III)-Alg powder electrodes as 80 mAh/g and 16 mAh/g, respectively. For Mn(II)-Alg powder, this is 1.3 times higher than the TGA-derived capacity (61 mAh/g for one electron transfer), implying that the redox reaction may involve the transfer of two electrons (122 mAh/g for two electron transfer). Losses can be attributed to limitations by electrical and ionic conductivity. Figure 11A does show that the conductivity of Mn(II)-Alg powder is greatly influenced by ionic conductivity. The addition of more charge carriers (Na-Alg) in the electrolyte significantly improves the specific charge capacity of the Mn(II)-Alg electrode.

The specific capacity of Fe(III)-Alg powder (16 mAh/g) is much lower than the TGA capacity of 53 mAh/g. This suggests that the Fe(III)-Alg electrode is considerably affected by limited conductivity, which could be either ionic or electrical in nature.
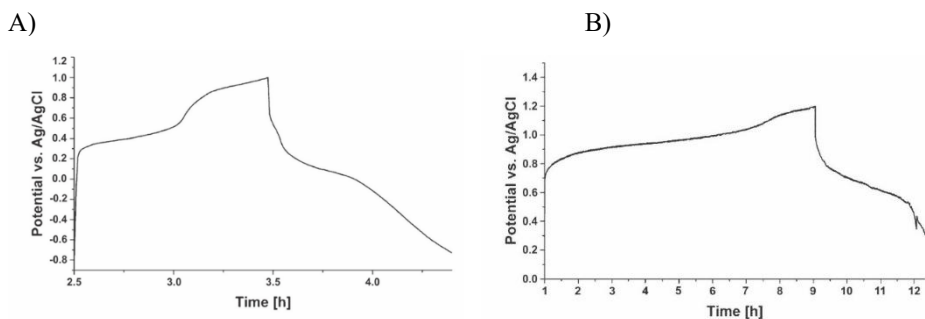
A)   B)

Figure 10. *The cycle behaviour of (**A**) Fe(III)-Alg electrode from powder for 1 cycle at 0.1 mA in 1% w/w Na-alginate electrolyte and (**B**) Mn(II)-Alg electrode from powder for 1 cycle at 0.1 mA in 1% w/w Na-alginate electrolyte.*
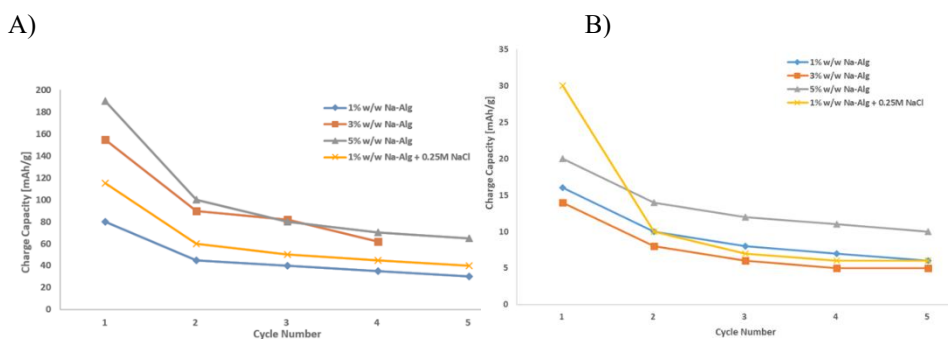
A)   B)

Figure 11. *Specific capacity of: (**A**) Mn(II)−Alg electrodes from powder for different compositions of the electrolyte and (**B**) specific capacity Fe(III)−Alg electrodes from powder for different compositions of the electrolyte. I = 0.1 mA.*

From the XPS analysis of Fe(III)-Alg, the amount of Cl^- ions is substantial; they are located closely and partially bound to the Fe^{3+} ion and, hence, form part of the overall internal resistance of the electrode. This suggests that the conductivity in the Fe(III)-Alg

powder might be considerably affected by the Cl⁻ ionic conductivity. The literature indicates that trivalent cations form complex and irregular structures with alginates [7,8] as evidenced by the XPS spectra (see Figure 4): electrons "wrapped" up in this structure are less mobile, affecting the electronic conductivity. Figure 11B additionally illustrates that the addition of more charge carriers (Na-Alg) in the electrolyte does not significantly improve the specific charge capacity of Fe(III)-Alg powder (contrary to Mn(II)).

To analyse the internal resistance (impedance), relaxation measurements were carried out, as presented in Figure 12. The Mn(II)-Alg cells were charged for 2 h and then allowed to rest for 1 h. Obviously, a significant drop in the voltage (about 0.1 V after 0.01 mA charge) is observed as a result of the charge overpotential, from which the impedance can be estimated to be 10 kΩ. A similar relaxation measurement was recorded for the Fe(III)-Alg cell, where the voltage drop is about three times higher, giving an impedance of about 30 kΩ. This significant difference in voltage drop has a clear impact on the obtained capacity, and thus it is obvious that the capacity of the Mn(II)-Alg found in our cell is much higher than the capacity found for the Fe(III)-Alg cell. Hence, the utilised capacity is strongly determined by the impedance of the cell. It is stressed, however, that we did not optimise these electrodes for the cells, and most likely we have to adjust the carbon-to-alginate-powder ratio, which will be explored further in the future.

Figure 13 shows the cycling of a Mn(II)-Alg powder electrode vs. an Fe(III)-Alg powder electrode, the arrangement of the intended battery of this research. Since the possible utilised capacity is much lower for the Fe(III)-Alg powder compared to the Mn(II)-Alg powder, the cut-off potentials are adjusted to the Fe(III)-Alg powder electrode to prevent electrolyte degradation. Here too, we can observe the huge influence of the impedance of the Fe(III)-Alg electrode. It is stressed that the negative overall potential is thus a result of the way the electrode potentials have been measured versus the reference electrode. Nevertheless, we see that the Fe(III)-Alg powder electrode is reversible, as the cycle behaviour stays the same with increasing cycling number. For the Mn(II)-Alg powder electrode, very stable behaviour is observed, but the capacity decreases as the cycle number increases.
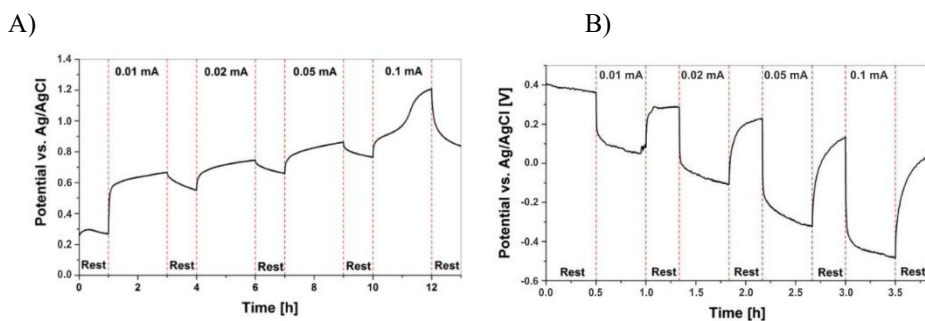
A)   B)

Figure 12. *Stability of (**A**) Mn(II)−Alg powder for different values for I as indicated in the figure in 1% w/w Na−alginate electrolyte and (**B**) Fe(III)−Alg powder for different values for I as indicated in the figure in 1% w/w Na−alginate electrolyte.*
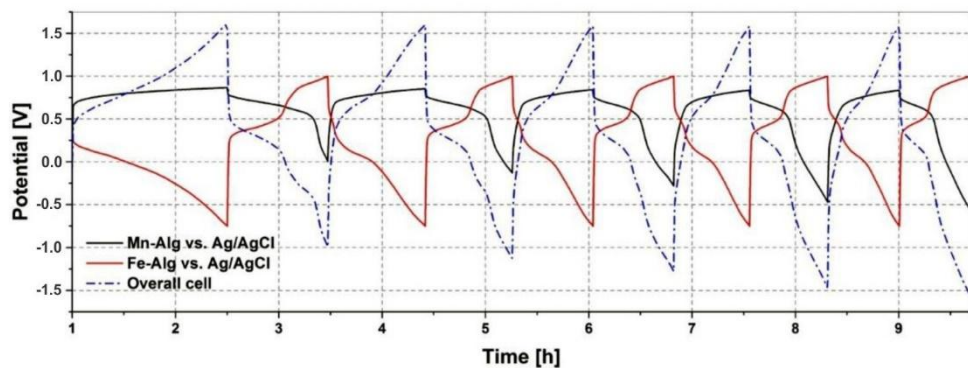
Figure 13. *Cycle behaviour of a Mn(II)−Alg electrode from powder vs. an Fe(III)−Alg electrode from powder, 1% w/w Na−alginate electrolyte, at a charge/discharge current I = 0.1 mA.*

This is in line with the findings from Figures 10–12. The increase in the charging potential seen in Figure 12A, at 11 h, is most likely a result of the Mn^{3+}/Mn^{4+} redox couple. This is in contrast to the potential increase in the Fe(III)-Alg electrode in Figure 13 where the increase was a result of a change in internal resistance caused by Cl^- conductivity.

6.3 Conclusions

Fe(III) and Mn(II) alginate have been successfully synthetised and characterised; albeit, the ion exchange is not yet fully optimised. It appears that Fe(III)-Alg is charge compensated with one chloride ion and two alginate carboxylates, analogous to Ca-Alg and other divalent alginates. Similarly, Mn^{2+} behaves analogous to Ca^{2+} in alginate. Despite the room for further improvement, we have shown that both transition metal alginates can be used as electrode materials in a rechargeable battery with Fe(III)-Alg as the negative electrode and Mn(II)-Alg as the positive electrode, which is highly encouraging considering the low cost and low toxicity of this type of system. We have found a redox potential for Mn^{2+}/Mn^{3+} in the Mn(II)-Alg electrode of 0.8 V versus Ag/AgCl. For the Fe(III)-Alg electrode, the internal resistances lead to a hard-to-interpret potential curve, which makes it difficult to define a proper reduction potential for Fe^{2+}/Fe^{3+} in the Fe(III)-Alg electrode. In conclusion, although there is plenty of room for improvement, based on our current results, we find that Fe/Mn-alginate is a highly interesting platform for nontoxic, biocompatible and cheap electrochemical storage systems. Although not the topic of the current paper, we could remark that we might be able to use these two transition metal alginates as positive electrodes in a metal-ion battery, e.g., based on Mg or Zn.

6.4 References

(1) *International Energy Outlook - U.S. Energy Information Administration (EIA)*. https://www.eia.gov/outlooks/ieo/index.php (accessed 2022-11-22).

(2) *Our World in Data.* https://ourworldindata.org/energy (accessed 2022-11-22).

(3) Lu, Y.; Chen, J. Prospects of Organic Electrode Materials for Practical Lithium Batteries. *Nat. Rev. Chem.* **2020**, *4* (3), 127–142. https://doi.org/10.1038/s41570-020-0160-9.

(4) Grant, G. T.; Morris, E. R.; Rees, D. A.; Smith, P. J. C.; Thom, D. Biological Interactions between Polysaccharides and Divalent Cations: The Egg-Box Model. *FEBS Lett.* **1973**, *32* (1), 195–198. https://doi.org/10.1016/0014-5793(73)80770-7.

(5) Draget, K. I.; Taylor, C. Chemical, Physical and Biological Properties of Alginates and Their Biomedical Implications. *Food Hydrocoll.* **2011**, *25* (2), 251–256. https://doi.org/10.1016/j.foodhyd.2009.10.007.

(6) Brus, J.; Urbanova, M.; Czernek, J.; Pavelkova, M.; Kubova, K.; Vyslouzil, J.; Abbrent, S.; Konefal, R.; Horský, J.; Vetchy, D.; Vysloužil, J.; Kulich, P. Structure and Dynamics of Alginate Gels Cross-Linked by Polyvalent Ions Probed via Solid State NMR Spectroscopy. *Biomacromolecules* **2017**, *18* (8), 2478–2488. https://doi.org/10.1021/acs.biomac.7b00627.

(7) Bruchet, M.; Mendelson, N. L.; Melman, A. Photochemical Patterning of Ionically Cross-Linked Hydrogels. *Processes* **2013**, *1* (2), 153–166. https://doi.org/10.3390/pr1020153.

(8) Davis, J.; McLister, A.; Cundell, J.; Finlay, D. *Smart Bandage Technologies: Design and Application*; Elsevier/AP, Academic Press is an imprint of Elsevier: Amsterdam ; Boston, 2016.

(9) Topuz, F.; Henke, A.; Richtering, W.; Groll, J. Magnesium Ions and Alginate Do Form Hydrogels: A Rheological Study. *Soft Matter* **2012**, *8* (18), 4877. https://doi.org/10.1039/c2sm07465f.

(10) Phillips, G. O.; Williams, P. A. *Handbook of Hydrocolloids*, 2nd ed.; Woodhead publishing in food science, technology and nutrition; CRC press Woodhead publ: Boca Raton (Fla.) Oxford, 2009.

(11) Haug, A.; Smidsrød, O.; Larsen, B.; Gronowitz, S.; Hoffman, R. A.; Westerdahl, A. The Effect of Divalent Metals on the Properties of Alginate Solutions. II. Comparison of Different Metal Ions. *Acta Chem. Scand.* **1965**, *19*, 341–351. https://doi.org/10.3891/acta.chem.scand.19-0341.

(12) Szekalska, M.; Puciłowska, A.; Szymańska, E.; Ciosek, P.; Winnicka, K. Alginate: Current Use and Future Perspectives in Pharmaceutical and Biomedical Applications. *Int. J. Polym. Sci.* **2016**, *2016*, e7697031. https://doi.org/10.1155/2016/7697031.

(13) Paredes Juárez, G. A.; Spasojevic, M.; Faas, M. M.; de Vos, P. Immunological and Technical Considerations in Application of Alginate-Based Microencapsulation Systems. *Front. Bioeng. Biotechnol.* **2014**, *2*.

7
Summary

As the world decarbonizes the energy systems, energy storage is an important pillar that cannot be ignored. Renewable energy sources are intermittent and non-flexible. Therefore, energy needs to be stored for shorter and longer periods. Since most renewable energy sources provide electricity, chemical battery storage is the most obvious first choice for storage.

And indeed, for short- and medium-term storage, chemical battery storage is economically feasible. However, the current reigning technology, the lithium-ion battery, is far too expensive for world-wide deployment for grid-scale storage. This comes down to material cost, which is connected to resource abundancy. Lithium, nickel, cobalt and other metals are too expensive. One should also not forget that their concentration in only a few places on Earth, makes for a weak supply chain.

New battery chemistries need to be found, that are solely based on abundant and/or renewable materials. Sodium, magnesium, iron, zinc and aluminum are metals that could replace lithium in batteries, while expensive transition metal oxides might be replaced by easily synthesized organic molecules. This thesis explores a few examples of materials that could be used in magnesium batteries.

In **chapter 2** perylene diimides are introduced. These versatile and robust molecules have shown promise as battery electrode material. This chapter describes a new and mild synthesis route towards them, the mild imidization. Traditionally perylene diimide synthesis requires harsh conditions, high temperature and corrosive solvents. In this new approach, one only needs the biocompatible solvent DMSO and potassium carbonate at 100 ºC. Also, a room temperature variant of the procedure has been developed that uses DBU as a base. The resulting products are also easily obtained through a simple precipitation in water, without the need for purification. The reaction kinetics and substrate scope are also investigated.

Perylene diamic acids, a sister compound to perylene diimides, are described in **chapter 3**. These are the intermediates in the imide synthesis. When the reaction is done with a secondary amine, the imide cannot be formed, and one is left with a water-soluble salt. The high solubility in water makes this class of molecules stand out in the perylene family. When diamic acids are exposed to acid, the reaction is undone and perylene dianhydride is formed. This compound is very insoluble in water. Chapter 3 shows that very controlled acidification can yield highly colored hydrogels. The gels are characterized by different techniques. The hydrogels might be of interest to material scientists, since they undergo uniform shrinkage over time. In their soluble form, perylene diamic acids are of interest as water-soluble compound in aqueous batteries.

The perylene family is known to be 'redox tunable'. By changing the side groups of the perylene, one can change the redox potential at which it reacts, which determines the potential at which a battery operates. **Chapter 4** looks into a new way to gain more control over the substitution of perylene tetraesters, by making a dibromo-dichloro perylene tetraester. In theory, this gives more control over the substitution pattern compared to tetrachloro and tetrabromo derivatives. This chapter investigates the kinetics of substitution reactions.

Chapter 5 presents a new aqueous polymer electrolyte for magnesium batteries, magnesium alginate. Alginate is a biopolymer that is harvested from algae. It is a polysaccharide of two monomers that both contain carboxylate groups. The difference between the monomers is only the spatial orientation of the carboxylate group. When an alginate solution is mixed with a solution that contains a multivalent cation, it will form a hydrogel. The carboxylate group from crosslinks with the cations, making a covalent-link hydrogel. Magnesium ions, two plus charged, are an exception, judged on the macroscale, they do not form a hydrogel. However, it is known that magnesium makes microscopic instable hydrogels that constantly form and break apart. From this, we can say that although magnesium is mobile in the solution, it is still heavily associated with the alginate backbone, and this is an indication that this electrolyte can act as a 'water-in-salt' electrolyte. Chapter 5 shows that magnesium alginate can have good ionic conductivity, even at very low water content. After some cycling, a black layer forms on the magnesium electrodes. This layer enhances the stability of magnesium in water.

Alginate hydrogels can also be used as matrices to encapsulate transition metal cations. **Chapter 6** brings a new approach to make a 'simple' manganese-iron battery. By encapsulating manganese(II) on one electrode and iron(III) in alginate, we were able to cycle this simple ion pair multiple times. This material might have applications in semi-solid flow battery.

Summary in Dutch

Nu de wereld de energiesystemen aan het vergroenen is, zien we dat energieopslag steeds belangrijker wordt. Duurzame energiebronnen zijn niet constant en niet flexibel. Daarom is het belangrijk dat energie voor kortere en langere periodes wordt opgeslagen. Doordat de meeste duurzame energiebronnen elektriciteit leveren, is energieopslag in een chemische batterij het meest logisch.

Dat zien we ook, voor korte en middellange periodes is opslag in een chemische batterij economisch haalbaar. De lithium-ion batterij is op dit moment het meest ontwikkelde batterij systeem. Het zal echter niet mogelijk zijn om deze technologie te gebruiken voor alle electriciteitsopslag wereldwijd, omdat de prijs van lithium-ion batterijen daar te hoog voor is. Dit komt voornamelijk door de hoge materiaalkosten van deze batterij, die weer gekoppeld zijn aan het voorkomen van deze materialen op aarde. Lithium, nikkel en kobalt zijn te duur. Ook moet niet vergeten worden dat deze materialen slechts op een aantal plekken voorkomen op aarde. Dat kan resulteren in een zwakke toeleveringsketen.

Nieuwe chemische reactie moeten worden gevonden die we kunnen gebruiken in nieuwe batterijen. Deze reacties moeten materialen gebruiken die veel voorkomen op aarde of volledig hernieuwbaar zijn. Natrium, magnesium, ijzer, zink en aluminium zijn metalen die lithium kunnen vervangen in een batterij. Organische stoffen zouden de dure transitiemetaaloxides in elektrodes kunnen vervangen. In dit proefschrift worden enkele materialen beschreven die kunnen worden gebruikt in een magnesium batterij.

In **hoofdstuk 2** worden peryleenbisimides geïntroduceerd. Deze veelzijdige en robuuste moleculen zijn goede kandidaten voor batterijmaterialen. Dit hoofdstuk beschrijft een nieuwe en milde synthesemethode om ze te bereiden, de milde imidizatie. Deze nieuwe methode gebruikt een biocompatibel oplosmiddel, DMSO, en kaliumcarbonaat op 100 ºC. Het hoofdstuk beschrijft ook een procedure waarin de reactie plaatsvindt op kamertemperatuur, met DBU als base. Met een simpele neerslag in water kan het eindproduct worden geïsoleerd. Er is geen zuiveringsstap nodig. De reactiekinetiek en substraatbereik worden ook onderzocht in dit hoofdstuk.

Peryleenbisamidezuren, een zusterverbinding van peryleenbisimides, worden beschreven in **hoofdstuk 3**. Deze stoffen zijn de intermediairen van de imide synthese. Wanneer een imidizatie wordt gedaan met een secundair amine, dan kan een imide niet vervormd worden. Dit resulteert in een wateroplosbaar zout. Peryleenbisamidezuren zijn bijzonder door hun hoge oplosbaarheid in water, andere leden van de peryleenfamilie zijn namelijk zeer slecht oplosbaar in water. Wanneer de bisamidezuren worden blootgesteld aan zuren, dan wordt de reactie ongedaan gemaakt en vormt zich het startmateriaal, peryleenbisanhydride. Hoofdstuk 3 bekijkt het gecontroleerd toevoegen van zuur. Hierbij kunnen dan kleurrijke hydrogels gevormd worden. De gels worden geanalyseerd met verschillende technieken. Materiaalwetenschapper kunnen geïnteresseerd zijn in deze hydrogels, omdat zij homogeen krimpen over de tijd. In de opgeloste vorm kunnen peryleenbisamidezuren interessant zijn als wateroplosbare batterijmaterialen.

De peryleenfamilie staat bekend om haar 'redoxinstelbaarheid'. Wanneer men zijgroepen aanpast, dan past men ook de redoxpotentiaal aan waar het molecuul reageert. Dit heeft uiteindelijk invloed op de voltage waarop een batterij werkt. **Hoofdstuk 4** bekijkt een nieuwe manier om meer controle te krijgen over de substitutiereactie van

peryleentetraesters. Dit wordt gedaan met dibromo-dichloro-peryleentetraester. In theorie zou deze stof gecontroleerder een substitutiereactie moeten kunnen doen dan de tetrachloro en tetrabromo varianten. Dit hoofdstuk kijkt ook naar de kinetiek van deze reactie.

Hoofdstuk 5 introduceert een nieuw waterig polymeerelektrolyt voor magnesiumbatterijen, magnesiumalginaat. Alginaat is een biopolymeer dat wordt gewonnen uit algen. Het is een polysacharide die uit twee monomeren bestaat. De monomeren bevatten beide een carboxylaatgroep en de monomeren verschillen in de ruimtelijke oriëntatie van die carboxylaatgroep. Wanneer men een alginaatoplossing mengt met een oplossing die een meervoudig geladen kation bevat, dan vormt zich een hydrogel. De carboxylaatgroepen maken koppelingen tussen polymeerketen door te binden aan de kationen. Hierdoor vormt zich een covalentachtige hydrogel. Magnesiumionen, twee plus geladen, zijn de uitzondering op deze regel. Op een macroscopisch niveau maken zij geen hydrogel. Echter is bewezen dat op microscopisch niveau wel een instabiele hydrogel wordt gevormd. Deze gels worden continue gevormd en afgebroken. Vanuit dit alles kunnen we zeggen dat magnesium mobiel is in de oplossing, maar dat het nog steeds een associatie heeft met de alginaatpolymeren. Dit is een indicatie dat we hier te maken kunnen hebben met een 'water-in-zout' elektrolyt. Hoofdstuk 5 laat zien dat magnesiumalginaat een goede ionische geleiding heeft, zelfs bij een zeer lage hoeveelheid water. Na een aantal keer de elektrolyt te gebruiken zien we een zwarte laag die zich vormt op de elektrodes. Deze laag beschermt magnesium tegen water.

Alginaathydrogels kunnen ook gebruikt worden als matrices om transitiemetaalionen te encapsuleren. **Hoofdstuk 6** laat een nieuwe manier zien om een 'simpele' mangaan-ijzer batterij te maken. Het was mogelijk om een batterij een aantal keer te laden en te ontladen waarin mangaan(II) en ijzer(III) geëncapsuleerd zijn in alginaathydrogels. Deze materialen zouden toepassingen kunnen hebben in het gebied van semi-vaste redox flowbatterij.

8

Acknowledgement

I would like to thank all people who have contributed to this thesis in any shape or form. Big and small contributions were all needed to come to this result. So many people have contributed to my work. My apologies if I have forgotten you in this text. You are still in my mind and heart.

First, I would like to thank my promotor, Erik, and copromotor, Wolter. Toen ik aankwam op mijn eerste dag stonden mijn vaardigheden echt nog in de kinderschoenen. Ik was nog onervaren en wist eigenlijk niet zo goed waar ik aan begon. Stiekem zou je kunnen zeggen dat ik, als 24-jarige, nog niet 100% volwassen was. Echter heb ik het gevoel dat ik vanaf dag 1 een volwaardig lid van het team was. Ik werd overal mee naartoe genomen en overal in betrokken. **Erik**, je hebt mij over mijn koudwatervrees heen geholpen in het begeleiden van studenten. Ik had nog niet door hoe geweldig en belangrijk het begeleiden van studenten is. Zonder hen was dit proefschrift een heel stuk dunner. Ook heb je mij wijs gemaakt hoe je moet samenwerken met partners, zowel vanuit de universiteit als de industrie. Jouw passie en meningen over batterijen hebben vaak mijn ogen geopend. Je trok mij ook af en toe vanuit de details terug naar het grote plaatje, waarom doen we dit en wat zijn de belangrijke experimenten? **Wolter**, jij hebt mij juist de passie voor het allerkleinste detail meegegeven. Op het oog onbelangrijke zaken, zijn juist de dingen die leiden tot hele nieuwe inzichten en studies. De "cans of worms" die wij samen opgetrokken hebben, zijn ontelbaar en hebben tot veel prachtig onderzoek geleid. Dingen waar we zeker nog 10 jaar mee doorkunnen! Je houdt standaarden hoog en zorgt ervoor dat er gewoon degelijk en goed werk wordt verricht. Hopelijk kan ik op een dag jouw prachtige manier van schrijven emuleren, op dit moment is het vooral proberen na te doen.

I want to thank **Ciqing**, **Dai**, **Francesca**, **Frank**, **Hugo**, **Jaco**, **Lucie**, **Marc**, **Roxanne**, **Tingxian**, **Victorio**, **Wessel** and **Willem**, for the beautiful time I had in Leiden during my master thesis. The things I learned and enjoyed made me consider doing a PhD.

Anand, **Benjamin**, **Benjamin**, **Daniel**, **Dennis**, **Dnyandevi**, **Eduardo**, **Elmira**, **Gijs**, **Hendrik**, **Irene**, **Jan**, **Laura**, **Marcel**, **Mark**, **Puck**, **Reece**, **Rienk**, **Sarah**, **Stephen**, **Tamar** and **Tessel** thank you for the amazing time I had with you in the ASM lab and in general at the university. For a long time during the pandemic, after Abbey left the group, I was alone in the lab and in the office. There were also not a lot of people in general in the ASM group. I did not have a lot of peers to laugh with and share frustrations. During the pandemic that was on design by the university, it was not a nice time. Luckily, I moved to the big office, and the labs were fully open again, which gave me back a lot of fun. Thanks again for that. I also want to thank **Abbey**, who started around the same time as me in the OMI lab. You were very kind and patient with me, I can be quite a storm to handle sometimes. You showed me how elegant and beautiful synthesis should be done. **Maryam**, we have always had a lot of fun in the lab and during our coffee breaks. It was amazing when you cooked delicious food for lunch with Wolter and me. I also really enjoyed the New Years celebration I had with your family. **Suellen**, we are now the 'oldest' in the office and of course we are also the wisest. It is always nice to have you around. Our (still running) plant experiment is one of my most cherished moments at ASM.

Ajay, **Albert**, **Alexandros**, **Anastasiia**, **Biffo**, **Chaofan**, **Hao**, **Lars**, **Luca**, **Lucas**, **Mark**, **Marnix**, **Meera**, **Michel**, **Pedro**, **Pier**, **Pranav**, **Shengnan**, **Swapna**, **Theo**, **Victor**, **Wenxuan**, **Xavier**, **Xuehang** and **Zhu** thank you for keeping me company during

my time in the reactor institute. Although my main spot was in building 58, I still spend quite some time with you in the SEE labs. During the group meetings specifically, I learned a lot, since I was just a simple organic chemist by training. My contributions to the meeting were always a little out of the ordinary for many of you, but I was always pleasantly surprised by the enthusiasm with which you received my presentations. **Peter**, as my former master student, now colleague, thank you for your contributions to chapters 2 and 3. Your project has done a lot to finish it up. I enjoyed our time together in the lab and we had a lot of laughs together. You are a kind and smart person, and it makes me happy that our joint publications will also be on the publication list in your thesis. I would like to thank **Remco** and **Hanan**. In one of my first days, I met Remco and Hanan. Thank you so much for your support and advice, especially when I started. You showed me the basics of battery making and showed me the way in the battery lab. I truly enjoyed our coffees through the years, and we had a lot of fun at the chains conference, although sometimes online during the pandemic, but we still made the best out of that!

Without Aleksandra, **Dan**, Duco, Esther, Frans, Katarina, **Nirmal**, Sietse and Stephen, I would still be looking and searching for things in the lab. Thank you so much! You were of immense importance for my work in this thesis. I am also grateful for all the patience you had with all my students. **Aleksandra**, you can find everything in the ASM labs! That is because you bring order and peace to the lab. I sometimes feel guilty to even work somewhere, because it is all so nice and tidy. **Duco**, your knowledge and enthusiasm have brought me so many insights on how I should do my research, and how to handle myself safely in the lab. You did this all with an amount of humor that made my day much brighter. **Esther**, we had so much fun in and outside the lab. In you I found a fellow chemist, and it was nice to work together on little projects in the lab. I still admire the beautiful Schlenk set-up that you built. Also, the time that we quenched a million unlabeled glovebox samples is something I will never forget. A little fire here, a little explosion there. We knew what we were doing and that we could count on each other. **Frans**, when I started my PhD, I quickly learned that you were the board computer that brought the research group to the moon. You knew where everything was, how everything worked and how to do things properly. We had quite a few laughs and I learned a lot from you. **Katarina**, it is good that we have different offices, because if we would share one, we would be constantly talking and do no work. You take your responsibilities seriously, and I value and respect that. Without you, the lab would be very different. **Sietse**, you are someone that is not afraid of real chemistry. You are one of the few people that do not look weird when I do a reaction in hot fuming sulfuric acid. I appreciate your calm approach and your chemical insights. **Stephen**, we had so much fun through the years, I cannot list them all here. Thank you for helping me with my NMR related problems and challenges. I really enjoyed the Saturgay evenings that you organized. You know all the good places in every city. Every time it amazes me! When Roland and I went to your place, I learned you can cook like the best! Apart from that, meeting you in the hallway or in the atrium can be a highlight of my day.

It is always nice to have a little chat with **Caroline**, **Els**, **Ilse**, **Martine**, **Nicole** and **Veby**. Thank you for your help in guiding me through the mazes of TU Delft. Whether it was contracts, declaring travel costs, getting student access to the lab or any of the many other things.

avonden moeten opvrolijken. Tijdens onze lange vriendschap heb jij je familie uitgebreid met eerst **Simran** en daarna met **John**, **Milan** en **Lily**. Jou, en ook hen, wil ik bedanken voor de afleiding en steun die ik soms nodig had de afgelopen jaren.

Bas en Peggy, mijn lieve paranimfen, jullie vertegenwoordigen de twee facetten van mijn academische leven. **Bas**, jij en ik zijn vrienden sinds de zomer van 2012. Wij zijn samen MST gaan doen en we reisde elke dag samen met de trein naar Leiden en Delft. Een van de periodes waar ik nog steeds om moet lachen is onze LO1 presentatie, toen jij de slappe lach kreeg. Dat was het zoveelste puberale moment dat wij gehad hebben tijdens dit project. Ondanks dat wij steeds meer verschillende studiekeuzes maakte, zijn we altijd verbonden gebleven voor onze liefde voor scheikunde en duurzaamheid. Eigenlijk ben ik met het doen van deze PhD weer dichter in de buurt gekomen van jou. Door de jaren heen hebben wij zo veel dingen gedaan. Van jouw trouwerij met Paco en je vrijgezellenfeest, tot avonden waarin we NOS-jaaroverzichten keken. Het maakt niet uit of het grote of kleine momenten zijn, wij hebben altijd lol en plezier. Ook jij hebt mij altijd gesteund de afgelopen jaren en je had grote interesse in wat ik deed. Je was mega enthousiast toen ik mijn eerste paper publiceerde. En nog steeds denk ik dat jij de meeste geïnteresseerde persoon bent in de inhoud van dit proefschrift. Misschien zelfs wel meer dan de commissie zelf. Duizendmaal dankt voor je steun, je vriendschap en voor het willen zijn van mijn paranimf. **Peggy**, jou ontmoette ik tijdens het doen van mijn PhD. Ik had je al in de verte zien zitten bij de groepsbesprekingen en zien lopen in de gang. Maar tijdens de pandemie ontdekte wij elkaars bizarre interesse voor het bijhouden van de statistieken over de pandemie. En eigenlijk, sinds dat we voor het eerst met elkaar zijn gaan praten, zijn we nooit meer uitgepraat. Ook denk ik dat we nog wel genoeg gesprekstof hebben voor een aantal decennia. Los van het feit dat je een geweldige vriendin bent, heb ik veel van je geleerd. Jij hebt mij laten zien hoe je een lab runt, hoe een schoon lab eruitziet, hoe je werkt naar resultaten en nog veel meer. Wat mij het meeste bijbleef was jouw pure en oprechte passie in je eigen project en scheikunde in het algemeen. Jij had je project met een zwaard verdedigd en dat vind ik inspirerend en bewonderingswaardig. Dat vuur voor het onderzoek heb ik sinds dat moment ook proberen te vinden in mijn werk. En ik kan je vertellen dat ik dat nu ook heb. Ook jij steunt mij altijd met mega veel enthousiasme en viert met mij de overwinningen die ik haal ik het lab. Peggy, ook jou wil ik duizendmaal bedanken voor je steun, je vriendschap en voor het willen zijn van mijn paranimf.

Ik kan in geen woorden uitdrukken hoe dankbaar ik mijn ouders, **Peter** en **Petra**, en mijn zusje, **Ariena**, ben voor alle steun en aanmoediging die ik altijd gekregen heb, niet alleen tijdens het doen van mijn PhD, maar mijn hele leven lang. Bij jullie mag ik altijd mijzelf zijn en jullie trekken mij weer naar de grond als ik te veel met mijn hoofd in de moleculen zit. Jullie laten mij altijd zien dat er nog een wereld buiten de universiteit is. Dat heb ik vaak nodig en dat doen jullie vaak zonder dat zelf te weten. Zonder jullie had ik deze PhD nooit gedaan en daarom wil ik dat jullie weten dat jullie namen onder de mijne op voorkant behoren te staan. Ik houd van jullie, bedankt.

Als laatste wil ik mijn lieve **Roland** bedanken. Door al die jaren heen heb je altijd vierkant achter mij gestaan. Als ik aan het mopperen was, hoorde je dat aan en hielp je me erdoorheen. En ondanks dat jouw fysische brein anders in elkaar zit dan mijn chemische, probeer je altijd te begrijpen wat ik allemaal aan het doen ben. Jij was de stille kracht die mij altijd rechtop hield en ik ben je daar eeuwig dankbaar voor.

9

List of publications

1. Kieltyka, R.E.; Kwakernaak, M.C.; Liu, T.; Tong, C. Tripodal Squaramide-Based Monomers. WO2019160419A1, August 22, 2019. (2019).

2. Liu, T.; van den Berk, L.; Wondergem, J.A.J.; Tong, C.; Kwakernaak, M.C.; ter Braak, B.; Heinrich, D.; van de Water, B.; Kieltyka, R.E. Squaramide-Based Supramolecular Materials Drive HepG2 Spheroid Differentiation. *Adv. Healthcare Mater.* **2021**, *10* (2001903). https://doi.org/10.1002/adhm.202001903

3. Kwakernaak, M.C.; Koel, M.; van den Berg, P.J.L.; Kelder, E.M.; Jager, W.F. Room temperature synthesis of perylene diimides facilitated by high amic acid solubility. *Org. Chem. Front.* **2022**, *9* (1090). https://doi.org/10.1039/D1QO01723C

4. Tong, C.; Wondergem, J.A.J.; van den Brink, M.; Kwakernaak, M.C.; Chen, Y.; Hendrix, M.M.R.M.; Voets, I.K.; Danen, E.H.J.; Le Dévédec, S.; Heinrich, D.; Kieltyka, R.E. Spatial and Temporal Modulation of Cell Instructive Cues in a Filamentous Supramolecular Biomaterial. *ACS Appl. Mater. Interfaces* **2022**, *14* (17042). https://doi.org/10.1021/acsami.1c24114

5. Kiriinya, L.K.; Kwakernaak, M.C.; van den Akker, S.C.D.; Verbist, G.L.M.M.; Picken, S.J.; Kelder, E.M. Iron and manganese alginate for rechargeable battery electrodes. *Polymers* **2023**, *15* (639). http://doi.org/10.3390/polym15030639

6. Legerstee, W.J.; Kiriinya, L.K.; Kwakernaak, M.C.; Kelder, E.M. Magnesium Transfer between Atomic Force Microscopy Probes and Metal Electrodes in Aqueous Alginate Electrolytes. *Polymers* **2024**, *16* (1615). https://doi.org/10.3390/polym16121615

7. Kwakernaak, M.C.; Koel, M.; van den Berg, P.J.L.; Strik, N.; Jager, W.F. Perylene dianhydride hydrogels obtained from accessible perylene diamic acid salts by a versatile protonation-hydrolysis mechanism. *RSC Adv.* **2025**, *15* (10183). https://doi.org/10.1039/D5RA00372E

8. Kwakernaak, M.C.; Kiriinya, L.K.; Legerstee W.J.; Berghmans W.M.J.; Hofman C.G.T.; Kelder, E.M. Magnesium Alginate as an Electrolyte for Magnesium Batteries. *Batteries* **2025**, *11* (16). https://doi.org/10.3390/batteries11010016

10
Curriculum vitae

2023-now   Postdoctoral researcher at Delft University of Technology.

2019-2023   PhD in Chemistry
                Dissertation: Organic materials for magnesium batteries
                Promotor: Erik M. Kelder; Copromotor: Wolter F. Jager
                Delft University of Technology, Netherlands

2015-2018   Master Chemistry
                Specialization: Chemical Biology
                Thesis: Dynamic crosslinking of 1,2-dithiolane in supramolecular
                squaramide-containing hydrogels.
                Leiden University, Netherlands

2012-2015   Bachelor in Molecular Science and Technology
                Major: Chemistry
                Minor: Advance Molecular Science and Technology
                Thesis: Diarylsquaramide based organocatalysis and self-assembly in
                water.
                Leiden University and Delft University of Technology, Netherlands

2006-2012   Secondary school VWO (athenaeum)
                Comenius College, Capelle aan den IJssel, Netherlands

11-08-1994   Born in Capelle aan den IJssel, Netherlands